Electronic properties of titania (and AZO) and its interface to organic acceptor materials

Zur Erlangung des akademischen Grades Doktor-Ingenieur (Dr.-Ing.)
genehmigte Dissertation von Dipl.-Ing. Philip Reckers aus Darmstadt
Tag der Einreichung: 14.12.2017, Tag der Prüfung: 25.04.2018
Darmstadt — D 17

1. Gutachten: Prof. Dr. Wolfram Jaegermann
2. Gutachten: Prof. Dr. Thomas Riedl (BU Wuppertal)

TECHNISCHE UNIVERSITÄT DARMSTADT

Fachbereich Materialwissenschaft
Surface Science

Electronic properties of titania (and AZO) and its interface to organic acceptor materials

Genehmigte Dissertation von Dipl.-Ing. Philip Reckers aus Darmstadt

1. Gutachten: Prof. Dr. Wolfram Jaegermann
2. Gutachten: Prof. Dr. Thomas Riedl (BU Wuppertal)

Tag der Einreichung: 14.12.2017
Tag der Prüfung: 25.04.2018

Darmstadt — D 17

Bitte zitieren Sie dieses Dokument als:
URN: urn:nbn:de:tuda-tuprints-85599
URL: http://tuprints.ulb.tu-darmstadt.de/8559

Dieses Dokument wird bereitgestellt von tuprints,
E-Publishing-Service der TU Darmstadt
http://tuprints.ulb.tu-darmstadt.de
tuprints@ulb.tu-darmstadt.de

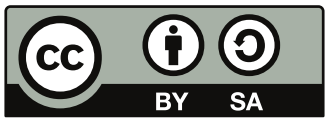

Die Veröffentlichung steht unter folgender Creative Commons Lizenz:
Namensnennung – Weitergabe unter gleichen Bedingungen 4.0 International
http://creativecommons.org/licenses/by-sa/4.0/

Abstract

The focus of this work is on the investigation of the electronic structure at interfaces of inverted organic solar cells and energetic states in the band gap of the anatase (101) surface.

Inverted organic solar cells are a promising alternative to conventional inorganic solar cells, regarding the potentially low production costs and its variety in possible applications. Inverted organic solar cells sometimes exhibit S-shaped I-V characteristics instead of diode-like I-V characteristics, which results in a decrease of the efficiency of the solar cells. The electronic alignment at the interface between the different materials within the solar cell influences strongly the functionality and efficiency of the solar cell. The contact formation between the materials depends on the materials itself, but also on the specific surface, e.g. adsorbates covering it. This work compares I-V characteristics of different solar cell device stacks with the respective energy diagrams. The investigation of the interface is mainly done by photoelectron spectroscopy, which is a powerful method to determine the electronic alignment at the interface between different materials. The shape of the I-V characteristics of inverted organic solar cells often depends on the used metal oxide (which acts as electron transporting layer) within the solar cell device stack. Typical electron transport layers are TiO_x and aluminum doped zinc oxide (AZO). Inverted organic solar cells with $PC_{61}BM$:P3HT as absorber material and AZO as electron transport layer show diode-like I-V characteristics, whereas solar cells with TiO_x as electron transport layer show S-shaped I-V characteristics. Using a bilayer consisting of TiO_x:AZO or AZO:TiO_x as electron transport layer, only solar cells where the TiO_x forms the interface to $PC_{61}BM$ show S-shaped I-V characteristics. In model experiments, C_{60} replaces $PC_{61}BM$ and the interface of C_{60} to TiO_x and AZO is determined by means of photoelectron spectroscopy. The interface energy diagram of the TiO_x/C_{60} interface displays a barrier for electron extraction, whereas the AZO/C_{60} interface does not. Interface experiments of C_{60} with *in situ* (adsorbate free) and *ex situ*

(adsorbate contaminated) cleaved anatase single crystals show the crucial influence of adsorbates on the formation of the electronic interface between the metal oxide and the organic absorber. Additional experiments show that the S-shaped I-V characteristics with TiO_x as electron transport layer transform into diode-like characteristics upon illumination with UV light. *In situ* UV illumination of the TiO_x/C_{60} interface with UV light induces changes of the band alignment, which result in a decrease of the electron extraction barrier at the TiO_x/C_{60} interface. Furthermore the reduction of the barrier is most probably caused by UV induced desorption of oxygen from the TiO_x surface.

The second part focuses on fundamental investigations of the anatase (101) surface. For this purpose, anatase single crystals are cleaved along the (101) surface plane by pliers and a clean (101) surface, without any further preparation methods such as sputtering and annealing, is obtained. Analyzing and comparing differently prepared titania samples by normal and resonant photoemission reveals the existence of shallow band gap states at the crystalline anatase surface. The origin of those shallow gap states is assigned to step edges of monoatomic height at the anatase (101) surface and respectively to the intersections of (101) surface planes of nanocrystalline anatase. In water adsorption experiments, the adsorption kinetics of water onto the anatase (101) surface are investigated in more detail.

Zusammenfassung

Diese Arbeit fokussiert sich auf die Untersuchung der elektronischen Struktur von Grenzflächen in organischen invertierten Solarzellen und die Untersuchung von elektronischen Zuständen in der Bandlücke an der Oberfläche der Anatas (101) Spaltfläche.

Invertierte organische Solarzellen sind eine vielversprechende Alternative zu konventionellen anorganischen Solarzellen in Bezug auf ihre potenziell niedrigen Kosten und der vielfältigen Anwendungsmöglichkeiten. Im Falle von invertierten organischen Solarzellen tritt es auf, das I-U Kennlinien anstatt einer Dioden-ähnlichen Form eine S-Form haben, was eine starke Reduktion der Effizienz bedeutet. Für die Funktionalität von Solarzellen im Allgemeinen spielt die elektronische Struktur an den Grenzflächen zwischen den Materialien eine entscheidende Rolle, da sie die Effizienz der Solarzelle maßgeblich beeinflusst. Die Kontaktausbildung ist vor allem durch das Material an sich, sowie auch durch dessen spezifische Oberfläche (z.B. Adsorbate) bestimmt. In dieser Arbeit erfolgt eine Korrelation von I-U Kennlinien verschiedener Solarzellenaufbauten mit Energiediagrammen verschiedener Grenzflächen. Die Untersuchung der entsprechenden Grenzflächen erfolgt hauptsächlich mittels Photoelektronenspektroskopie, welche es ermöglicht die elektronische Bandanpassung an der Grenzfläche zwischen Materialien zu bestimmen. Bei invertierten organischen Solarzellen wird insbesondere eine Abhängigkeit der Form der I-U Kennlinie (und damit auch der Effizienz) von dem verwendeten Metalloxid, welches als Elektronentransportschicht dient, beobachtet. Typische Elektronentransportschichten sind Titandioxid (TiO_x) und Aluminium dotiertes Zinkoxid (AZO). Invertierte organische Solarzellen mit $PC_{61}BM$:P3HT als Absorbermaterial und AZO als Elektronentransportschicht zeigen Dioden-ähnliche I-U Kennlinie Charakteristika, wohingegen Solarzellen mit TiO_x als Elektronentransportschicht I-U Kennlinien mit einer S-Form aufzeigen. Wird eine Doppelschicht bestehend aus TiO_x:AZO oder AZO:TiO_x als Elektronentransportschicht verwendet, zeigen nur Solarzellen, welche die TiO_x/$PC_{61}BM$ Grenzfläche aufweisen

eine S-Form in ihrer I-U Charakteristik. In Modellexperimenten wird $PC_{61}BM$ durch C_{60} ersetzt und die Grenzfläche von TiO_x und AZO zu C_{60} mittels Photoelektronenspektroskopie untersucht. Die elektronische Bandanpassung an der TiO_x/C_{60} Grenzfläche zeigt, dass es zu einer Barriere für Elektronenextraktion kommt, während diese Barriere an der AZO/C_{60} Grenzfläche nicht auftritt. Grenzflächenexperimente der C_{60} Grenzfläche mit *in situ* (Adsorbat freien) und *ex situ* (Adsorbat kontaminierten) gespaltenen Anatas Einkristallen weisen einen Einfluss von Adsorbaten auf die Ausbildung der Grenzfläche zwischen Metalloxid und organischem Absorber auf. Weitere Experimente an invertierten organischen Solarzellen mit TiO_x als Elektronentransportschicht zeigen, dass UV Licht zum Verschwinden der S-Form der I-U Kennlinie führt und Dioden-ähnliche I-U Kennlinien bewirkt. *In situ* Beleuchtung der TiO_x Grenzfläche mit UV Licht bewirkt eine Änderung der Bandanpassung, welche eine Reduktion der Elektronenextraktionsbarriere an der TiO_x/C_{60} Grenzfläche nach sich zieht. Weiterhin führt UV induzierte Desorption von Sauerstoff an der TiO_x Oberfläche sehr wahrscheinlich zu der Reduktion der Barriere für Elektronen.

Im Weiteren werden grundlegende Untersuchungen an der Anatas (101) Oberfläche durchgeführt. Hierfür werden Anatas Einkristalle entlang der (101) Oberfläche *in situ* mittels einer Zange gespalten, sodass saubere (101) Oberflächen ohne weitere Präperationsmethoden wie z.B. Sputtern und Annealen hergestellt werden. Analyse und Vergleich verschieden präparierter Titandioxid Proben mit normaler und resonanter Photoelektronenspektroskopie zeigen flach liegende Bandlückenzustände an der Oberfläche von kristallinem Anatas TiO_2. Die Herkunft dieser Bandlückenzustände wird durch das Vorhandensein von atomar hohen Stufen auf der Spaltfläche bzw. im Falle von nanokristallinem Anatas durch die Schnittpunkte der (101) Oberflächen erklärt. Zuletzt wird anhand von Wasseradsorptionsexperimenten, die Adsorbtionkinetik von Wasser auf der Anatas (101) Oberfläche genauer untersucht.

Contents

1 Introduction 13

I Theorie and Methods 17

2 Theoretical foundation 19

2.1 Inorganic and organic semiconductors . . . 19

2.1.1 General properties and the band structure of inorganic semiconductors . . . 19

2.1.2 Organic semiconductors . . . 20

2.1.3 Charge carriers of organic semiconductors . . . 21

2.1.4 Free charge carriers of organic semiconductors . . . 21

2.2 Interface and contact formation at metal/metal oxide/organic interfaces . . . 23

2.2.1 The Schottky model of the space charge region . . . 23

2.2.2 The metal/semiconductor contact . . . 24

2.2.3 The semiconductor/semiconductor heterocontact . . . 26

2.2.4 Interfaces with band bending and interface dipoles . . . 26

2.2.5 The Integer Charge-Transfer model . . . 28

2.3 Organic solar cells . . . 29

2.3.1 Basics of organic solar cells . . . 29

2.3.2 Absorber layers of organic solar cells - Exciton splitting . . . 30

2.3.3 Interfacial layers . . . 31

2.4 I-V characteristics of solar cells . . . 31

2.5 I-V curves of inverted organic solar cells with TiO_x as ETL . . . 35

3 Materials 37

3.1 Titanium dioxide . . . 37

3.1.1 Morphology of titanium dioxide . . . 37

3.1.2 Anatase surface structures . . . 37

3.1.3 Electronic structure . . . 39

3.1.4 Defect states . . . 39

3.2 Aluminum doped zinc oxide . . . 41

3.3 C_{60} and $PC_{61}BM$ . . . 41

4 Preparation Methods and experimental setup 43

4.1 Cleavage of anatase single crystals . . . 43

4.2 Atomic layer deposition . . . 44
4.3 Physical vapor deposition . . . 45
4.4 UV illumination, oxygen exposure and adsorption of water . . . 46
4.5 UHV systems . . . 46
4.5.1 Daisy-Fun . . . 46
4.5.2 SoLiAS . . . 47

5 Methods **49**
5.1 Photoelectron spectroscopy . . . 49
5.1.1 Working principle . . . 49
5.1.2 Radiation sources . . . 51
5.1.3 Analyzer . . . 52
5.1.4 Information contained in PES spectra . . . 52
5.1.5 Initial state and final state effects . . . 53
5.1.6 Resonant photoemission . . . 54
5.2 Low energy electron diffraction . . . 56
5.3 X-ray diffraction methods . . . 56
5.3.1 Laue diffraction . . . 57
5.3.2 X-ray powder diffraction . . . 58
5.4 Scanning electron microscopy . . . 58
5.5 Atomic force microscopy . . . 59
5.6 Optical absorption spectroscopy . . . 61

6 Aim of this work **63**

II Results and discussion I: Interfaces in inverted organic solar cells **65**

7 I-V characteristics of inverted organic solar cells **67**
7.1 I-V characteristics of IOSC with TiO_x and AZO as ETL . . . 67
7.2 I-V characteristics of TiO_x/AZO and AZO/TiO_x bilayers as ETL . . . 67
7.3 Unipolar devices with TiO_x or AZO interlayers and $PC_{61}BM$ or C_{60} as organic acceptor material . . . 69

8 The titanium dioxide - C_{60} interface **73**
8.1 TiO_x substrates - structure and morphology . . . 73
8.1.1 XRD and Laue diffraction of TiO_x . . . 73
8.1.2 SEM of TiO_x . . . 75
8.1.3 AFM of TiO_x . . . 75
8.1.4 LEED of TiO_2 sc-(101) . . . 76
8.1.5 UV-Vis of TiO_x 80 °C . . . 76
8.2 Photoemission spectroscopy on various TiO_x samples . . . 78
8.2.1 Photoemission of TiO_x: Fundamentals . . . 78
8.2.2 Influence of temperature and crystallinity . . . 81

8.3 Photoemission spectroscopy of C_{60} . . . 86
8.3.1 Comparison of the electronic structure of C_{60} and $PC_{61}BM$ . . . 89

9 Photoemission spectroscopy of the titanium dioxide - C_{60} interface and the effect of UV illumination 91
9.1 The TiO_x 80 °C/C_{60} interface and influence of UV illumination . . . 91
9.2 Energy diagram of the 80 °C TiO_x/C_{60} interface . . . 95
9.3 Influence of UV light on the TiO_x/C_{60} interface after UV pretreatment of the TiO_x substrate 99
9.4 Summary and discussion: The 80 °C TiO_x/C_{60} interface and the influence of UV illumination 102

10 Anatase (101)/C_{60} interface experiments 105
10.1 TiO_2 anatase *in situ*/C_{60} interface . . . 105
10.1.1 TiO_2 anatase *in situ*/C_{60} interface - influence of UV light . . . 107
10.2 TiO_2 anatase *ex situ*/C_{60} interface . . . 107
10.2.1 TiO_2 anatase *ex situ*/C_{60} interface - influence of UV light . . . 108
10.3 Analysis of the Ti $2p_{3/2}$ and C 1s line shape of synchrotron experiments . . . 109
10.4 Anatase/C_{60} interface diagrams determined from synchrotron experiments . . . 111
10.5 Discussion anatase/C_{60} interfaces . . . 112
10.6 Summary anatase/C_{60} interfaces . . . 114

11 The titania / air interface and the influence of UV light 117
11.1 Anatase single crystal: Influence of air and UV light . . . 117
11.1.1 Anatase single crystal *in situ*: Influence of air exposure and UV illumination . . . 117
11.1.2 Anatase single crystal: Influence of UV illumination on *in situ* and *ex situ* cleaved anatase . . . 118
11.1.3 Discussion of energy level positions of *in situ* and *ex situ* cleaved TiO_2 samples . . . 119
11.1.4 Influence of O_2 plasma on anatase . . . 121
11.1.5 Discussion anatase single crystal: Air and UV influence . . . 123
11.1.6 Conclusion and summary: Anatase and adsorbates . . . 129
11.2 ALD prepared *ex situ* TiO_x: Influence of air and UV light . . . 131
11.2.1 Origins of surface band bending upon X-ray/UV illumination . . . 132
11.2.2 Conclusion and summary: ALD prepared TiO_x . . . 137
11.3 Summary of air exposed titania interfaces . . . 138

12 Mechanistics for UV light induced changes at the TiO_x/C_{60} interface 141
12.1 Summary of previous results . . . 141
12.2 Deriving a mechanistic model to explain changes of theTiO_x/C_{60} interface . . . 142
12.2.1 Model I: UV induced oxygen desorption at the TiO_x surface - No further interactions between the TiO_x surface and C_{60} . . . 142
12.2.2 Model II: UV induced oxygen desorption at the TiO_x surface - Assuming interactions between the TiO_x surface and C_{60} . . . 144
12.3 Comparison and discussion of both mechanistic models . . . 144

13 Inverted organic solar cells without S-shaped I-V characteristics 147
13.1 Al:ZnO substrates - structure and morphology . . . 147
13.1.1 SEM and AFM of ZnO and AZO . . . 148
13.1.2 XRD of ZnO and AZO . . . 148
13.1.3 UV-Vis of AZO . . . 149
13.2 Photoemission of AZO and its interface to C_{60} . . . 149
13.2.1 UV influence on the AZO substrate and the AZO /C_{60} interface . . . 151
13.2.2 Energy diagram of the AZO/C_{60} interface . . . 151
13.3 Summary: AZO/C_{60} interface and the UV influence . . . 153

14 TiO_x/C_{60} and AZO/C_{60} interface obtained at synchrotron Bessy II 155

15 Comparing energy band diagrams and I-V characteristics 159
15.1 Comparison and discussion of I-V curves and derived energy band diagrams . . . 159
15.1.1 IOSC with 80 °C TiO_x . . . 160
15.1.2 Complete AZO/C_{60} energy band line-up . . . 164

16 Summary and Outlook of UV influence on interfaces in organic solar cells 167
16.1 Outlook . . . 169

III Results and discussion II: Investigation of gap states in TiO_2 171

17 Synchrotron induced study of gap states in TiO_2 173
17.1 Identification of gap states in different titania samples . . . 174
17.1.1 Valence band and gap state analysis of different titania samples . . . 174
17.1.2 Discussion: Gap states of different titania samples . . . 180
17.1.3 Summary and conclusion: Gap states of different titania samples . . . 181
17.2 Resonant photoemission of titania gap states . . . 182
17.2.1 Results and discussion: RESPES on amorphous TiO_x, nc-TiO_2 and sc-(101) surfaces 184
17.2.2 Discussion of the resonant photoemission measurements of the Ti 3p→3d transition. 188
17.2.3 RESPES of the Ti 2p→3d/4sp transition on the *in situ* cleaved sc-(101) anatase surface 189
17.2.4 Conclusion and summary of resonant photoemission measurements . . . 192
17.3 Water on TiO_2 sc-(101) surface plane . . . 194
17.3.1 Results and discussion: Water on LN-cooled sc-(101) surface . . . 194
17.3.2 In detail analysis of valence band feature evolution upon water adsorption . . . 198
17.3.3 Model of water adsorption onto the anatase sc-(101) surface plane . . . 199
17.3.4 Conclusion and Summary . . . 201

18 Summary of fundamental investigation on *in situ* and *ex situ* cleaved anatase (101) surfaces and outlook 203

A Appendix of part II 205
A.1 TiO_2 sc-(101) O1s - *ex situ* and *in situ* . . . 205

A.2 The 500 °C TiO_x/C_{60} interface 207
A.2.1 TiO_x 500 °C substrate 207
A.2.2 TiOx 500 °C/C_{60}: Influence of X-ray and UV radiation 209
A.2.3 Energy diagram of the 500 °C TiO_x interface before and after UV 211
A.2.4 Influence of UV light on the 500 °C TiO_x/C_{60} interface after UV pretreatment of the TiO_x substrate 212
A.2.5 Summary: TiO_x 500 °C/C_{60} interface and the UV influence 212

B Appendix of part III **217**
B.1 Resonant photoemission 217

Bibliography **221**

List of figures **241**

List of tables **246**

Index of abbreviations

χ Electron affinity

$\mathbf{E}_{CB}$ Conduction Band level

$\mathbf{E}_{CB}$ Valence Band level

$\mathbf{E}_{CNL}$ Charge Neutrality Level

$\mathbf{E}_{F}$ Fermi Energy

$\mathbf{E}_{G}$ Energy gap of inorganic and organic semiconductors

$\mathbf{E}_{Vac}$ Vacuum level

I_P Ionization potential

$\mathbf{V}_{O}$ Oxygen vacancy

AFM Atomic Force Microscopy

ALD Atomic Layer Deposition

CBM Conduction Band Maximum

CT Exciton Charge Transfer Exciton

DGS Deep Gap States

DOS Density of States

DSSC Dye-Sensitized Solar Cells

ETL Electron Transport Layer

HOMO Highest Occupied Molecular Orbital

HTL Hole Transport Layer

ICT Integer Charge Transfer model

IOSC Inverted Organic Solar Cells

IPES Inversed Photoelectron Spectroscopy

LEED Low energy electron diffraction

LUMO Lowest Unoccupied Molecular Orbital

OSC Organic Solar Cells

PES Photoelectron Spectroscopy

PVD Physical Vapor Deposition

RESPES Resonant Photoelectron Spectroscopy

SEM Scanning Electron Microscopy

SGS Shallow Gap States

STM Scanning Tunneling Microscopy

SXPS Synchrotron induced X-ray Photoelectron Spectroscopy

UV-Vis Ultraviolet-Visible Spectroscopy

VBM Valence Band Minimum

WF Work Function

XPS X-ray Photoelectron Spectroscopy

XRD X-ray Diffraction

1 Introduction

Mankind has a constantly increasing demand of energy. From 1990 to 2014 the world energy production increased from about 102TW h to 160TW h (terawatt-hours).[1] The increasing global population and the need to increase the standard of living all over the world will further increase the demand of energy and predictions assume an increase of 37 % of the energy consumption till 2035.[2] So far the main energy sources are fossil fuels like coal, gas and oil (in total about 80 %). According to the 2014 REN's report (Renewable Energy Policy Network for the 21st Century), in 2012 19 % of the energy worldwide was generated by renewable energy sources like e.g. wind energy (2 %), solar energy (2 %), hydro energy (3.8 %) or bioenergy (9 %) (like biofuels and waste). In 2013 the percentage of renewable energies contributing the electricity generation was worldwide about 22 %.[3] Due to the massive use of fossil fuels CO_2 is produced, which is widely accepted to be play a key role in the process of global warming.[4] In accordance with the increase of the energy demand of 37 %, CO_2 emission would increase by 25 %.[2] To limit the increase of the global warming to a maximum of 1.5 °C, 175 countries, including the USA and China, signed the Paris agreement in 2015. In order to achieve the goal of 1.5 °C temperature increase, fossil fuels have to be substituted by renewable energies by the year 2060.[5]

Solar energy is one of the most promising renewable energy as the energy of the sun send to earth per year, is about 3000 times the energy used on earth in one year,[6] and therefore an efficient harvesting of this energy could contribute enormously to worldwide energy production. Furthermore solar cells enable local energy supply, which is good for areas with no own power grid. The best known and longest investigated solar cells are based on silicon. The first practical crystalline silicon solar cell was presented by Bell Labs in 1954 with an efficiency of 6 %.[7] Besides single crystalline silicon solar cells also polycrystalline and amorphous silicon solar cell exist, where polycrystalline solar cell are the most produced ones nowadays and have an efficiency of about 14 %.[8] Also thin film solar exist, which allow thinner cells due to the use of semiconducting materials with a direct band gap. Most thin film solar cells either use cadmium telluride (CdTe) or copper indium gallium selenide (CIGS) as absorber material. Their efficiencies in commercial devices is about 17 %.[9] Furthermore, multijunctions solar cells based on the combination of several absorber materials with different band gaps exist, allowing a better harvesting of the solar energy spectrum and therefore an increased efficiency. Solar cells with two absorbers are called tandem solar cells, with three absorbed triple solar cells. More recently solar cells containing organic materials emerged. In 1988, Grätzel and O'Reagen invented a dye-sensitized solar cell (DSSC) based on an organic dye, which absorbs light, TiO_2, which accepts the generated electron and an electrolyte which recovers the dye.[10]
Another type of solar cells with organic absorber materials are based on organic semiconductors and commonly referred to as organic solar cells (OSC). The research of Alan J. Heeger et al. in the 1970's on conductive polymer enabled the research on replacing inorganic semiconductor materials in semiconductor devices like solar cell or light emitting diodes.[11] Till the 1980's organic solar cells only

reached efficiencies about 1 %, till Tang et al. had a breakthrough by combining p- and n-type organic semiconductors, which actually not increased the efficiencies but strongly increased the photocurrent of organic solar cells.[12] Organic solar cells have several advantages compared to common inorganic solar cell devices. They can be designed flexible, have a very low weight (500 g/ m^2), are thin (less than 1 mm), can be produced in several colors and are semitransparent (achieving up to 50 % light transmission with 6 % efficiency). These properties enable the use of OSC devices on facades of buildings, e.g. due to their semi transparency on glass, on big tents or also integrated in the car roof to charge the battery. Furthermore first commercial OSC devices have an energy payback of less than three month, are manufactured without any toxic material and contain no heavy metals in the solar cell. Heliatek is currently producing commercially available multijunctions organic solar cells with an efficiency of 7 to 8 %.[13]

OSC devices are divided into classic OSC devices and inverted OSC devices (IOSC), where the electrodes are switched compared to the classic device. The introduction of the inverted cell structure improves the stability of OSC devices and also facilitates the manufacturing of semitransparent OSC devices.[14,15] The improved stability arises from the possibility to use high work function metals like silver and metal oxides like titanium dioxide or zinc oxide as selective layers, which are much more air-stable compared to low work function metals like magnesium used in conventional devices.[14,15] Selective layers between the organic absorber and the electrode in OSC devices are used to increase the efficiency by favoring either the transport of electrons or holes. This electron or hole selectivity is achieved by proper alignment of the electric transport levels at the interface between the organic material and the selective layer. This alignment is crucial for a good functionality of a solar cell and will be investigated in this work.

A further focus of this work is also directed to different amorphous and crystalline titanium dioxide surfaces. Titanium dioxide is of special interest, as it has a wide range of application, for example it is used in solar cells as electron transport layer, as photocatalyst for water splitting or other organic materials, in paints as white pigment or as corrosion-protective and optical coating in light emitting devices.[16] In this work the energetic surface structure of differently prepared TiO_2 and TiO_{2-x} samples are investigated. An improved understanding of the electronic properties of TiO_2 and TiO_{2-x} surfaces helps to gain insights to the superior role of TiO_{2-x} surface as catalyst as well its beneficial role in organic solar cells and dye-sensitized solar cells.[10,17]

This work was conducted within the framework of the DFG (Deutsche Forschungsgemeinschaft) project "Inverted organic solar cells".[1] There is still a lack of understanding of the electronic structure occurring at the metal oxide/organic absorber interface and its consequences for the resulting I-V characteristics of inverted organic solar cells (IOSC). To get a better understanding of the electronic structure at the interfaces between the charge extraction layer and the organic absorber, interface experiments by photoelectron spectroscopy (PES) are conducted between various metal oxides and organic absorbers. The obtained results by PES are correlated to the I-V characteristics of corresponding unipolar devices and complete solar cells. In order to separate interface effects from changes of the bulk properties of the metal oxides, adsorbate free metal oxides and metal oxides with adsorbates are taken into

[1] Project number MA 2104/2-2 and RI1551/4-2

account as well as metal oxides with varying charge carrier concentrations (e.g. TiO_x and AZO). A special focus is put on the origin of the UV light induced transient I-V characteristics of IOSC with TiO_x as interfacial layers.
Furthermore an in depth study of gap states of different TiO_2 materials is performed. By synchrotron induced photoemission experiments a new gap state type just below the Fermi level is identified and further analyzed by resonant photoelectron spectroscopy. At last, water is adsorbed on to an *in situ* cleaved anatase (101) surface and a model of adsorption is derived.

Part I.

Theorie and Methods

2 Theoretical foundation

2.1 Inorganic and organic semiconductors

Solids materials are divided into different material classes, which are metals, semiconductors and insulators and have different electronic properties (see Fig. 2.1).
For optoelectronic devices, like solar cells, semiconducting materials are needed. Only semiconducting materials allow the adsorption of electromagnetic radiation and the separation of the generated charge carriers. As absorbing semiconductors, either organic or inorganic materials can be used. One of the major differences between organic and inorganic semiconductors is their conductivity which is 10^{-8} S/ cm^2 for e.g. C_{60}[18] and about 10^{-4} and 10^{0}S/ cm^2 for inorganic semiconductors like Si and Ge.[19] This differences arises from lower mobilities and lower charge carrier densities of organic semiconductors. In this section, the difference between organic and inorganic semiconductors will be described and the origin of the lower mobility and charge carrier density will be explained.

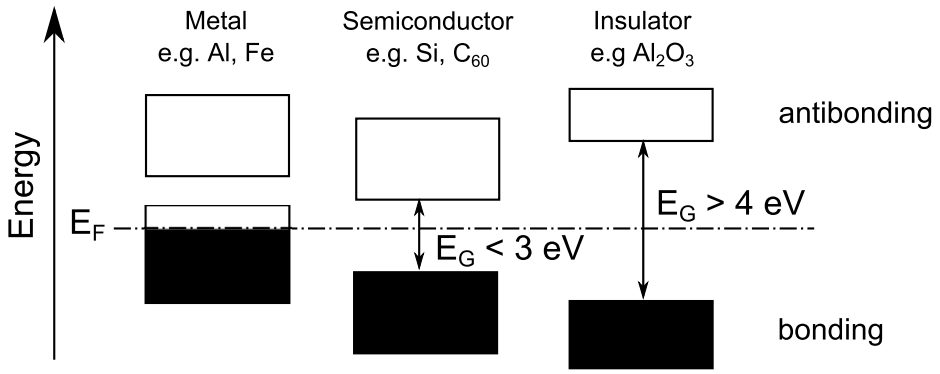

Figure 2.1. – Electronic band structure of a metal, a semiconductor and an insulator. In metals the Fermi level E_F lies within an energy band. Semiconductors and insulators have an energy gap between occupied and unoccupied energy bands.

2.1.1 General properties and the band structure of inorganic semiconductors

The electronic characteristics of a material are determined by the electronic band structure of the respective material. Due to the overlap of the atomic orbitals within a solid, molecular orbitals with discrete energy levels are formed. As an inorganic solid consists of about 10^{23} atoms per cm^3 the resulting energy levels are very close together and form quasi-continuous energy bands. The width of the energy bands in inorganic materials is about 2-8 eV and depends on the degree of the overlap of the respective atomic orbitals. While the overlap of small orbitals close to the core is reduced and hence only narrow bands are formed, large orbitals overlap more and the resulting bands are broader. This correlates well

with large band gaps between core bands, and small or no band gaps between valence bands. The filling of the energy bands with electrons is given by the Fermi-Dirac distribution function (Eq. (1.1)) and ascribes the probability that a state E is occupied for a given chemical potential μ and the product of the Boltzmann constant and temperature $k_B T$. The maximum electrochemical potential of the electrons μ is under thermodynamic equilibrium often set equivalent to the Fermi level E_F.

$$f(E) = \frac{1}{1 + e^{\frac{E-\mu}{k_B T}}} \tag{1.1}$$

In metals the energy bands are only partly occupied as shown in Fig. 2.1 and the DOS of electrons crosses E_F. At $T = 0$ K the energy bands of a semiconductors below E_F (valence band) is completely filled and its DOS of electrons does not cross E_F. Between the filled valence band and across E_F to the conduction band no empty states are existent and an energy gap E_G is formed between the valence band and the conduction band. If the energy gap is above 4 eV one talks about an insulator.

2.1.2 Organic semiconductors

As the name already says, organic semiconductors are based on carbon compounds. The basis for semiconducting organic materials is the sp^2- and sp^3 hybridization of C atoms. Upon the formation of sp^2- and sp^3 hybridizations, non-hybridized p-orbitals may remain. In the case of a sp^2 hybridization of a C atom, the $2s$-, the $2p_x$- and the $2p_y$-Orbitals form three sp^2 hybrid orbitals. By the overlap of those hybrid orbital bonding σ-molecular orbitals (MO) emerge and a strong bond is formed. The non-hybridized $2p_z$-orbitals form weaker π-type MO bondings and by this a double bond between the carbon atoms is established. A sp-hybridization occurs, when the $2s$- and $2p_x$ form two hybrid orbitals. The remaining $2p_y$- and $2p_z$-orbitals then form two π-bonds and this results in a triple bond. A molecule with alternating single and double bonds has a conjugated system. In a conjugated system the π bonds overlap across an intervening σ bond, such that the π electrons are not allocated at one atom, but are localized over a group of atoms. Two sp^2 molecular orbitals form a bond to a neighboring C atom, whereas the third sp^2 orbital either has a hydrogen atom or a functional group attached. With functional groups chemical and physical properties like absorption, reactivity or the growth mode can be influenced.[20]

Each atomic orbital of a single atom forms the same number of molecular orbitals, as the σ- and the π-molecular orbital split into a bonding and an antibonding orbital. The **H**ighest **O**ccupied **M**olecular **O**rbital (HOMO) consists of bonding π-molecular orbitals, the **L**owest **U**noccupied **M**olecular **O**rbital (LUMO) of antibonding π^*-molecular orbitals. In between the LUMO and the HOMO is an energy gap without any electronic states. The energy gap (E_G) corresponds to the band gap of inorganic semiconductors. In this work the band gap is always referred to as energy gap.
On a molecule in an organic solid, the exchange interaction in between the hybrid orbitals is high, whereas the exchange interaction between the molecules themselves is small, as usually only van der Waals forces interact. As a consequence organic solids do not have strongly delocalized band states (as inorganic semiconductors) and the width of the bands is only 4 to 300 meV (inorganic semiconductors:

2-8 eV). As a result valence electrons are located on a molecule but not in between them.[21]
Due to this fact the dispersion relation in organic semiconductors is shallow and the effective mass m^* of the electrons is high (compared to inorganic semiconductors). Thus charge carriers moving through the lattice scatter at many atomic cores and the formation of delocalized Bloch waves may not be an adequate description. Charge carrier transport therefore cannot be described by the classic band model of inorganic semiconductors, where electrons are delocalized over the whole solid. Other processes, like hopping between localized states, have to be considered (see Section 2.1.4).

2.1.3 Charge carriers of organic semiconductors

As in inorganic semiconductors, electrons on organic semiconductors can be excited across the energy gap as well. After the excitation of electrons from the HOMO to the LUMO, e.g. by photons with the respective energy, excitons are formed. An exciton is an electron-hole pair bound by the Coulomb force (see Eq. (1.2)).[21]

$$F_{coul} = \frac{e_0^2}{4\pi\epsilon\epsilon_0 \cdot r^2}, \tag{1.2}$$

where F_{coul} is the Coulomb force, e_0 the elementary charge, ϵ the permittivity of the solid, ϵ_0 the permittivity of the vacuum and r the distance between the charge carriers.
As F_{coul} is inverse proportional to the permittivity ϵ, a low permittivity results in a low screening between the single charges. Therefore the Coulomb force between the charge carriers is high, as is the exciton binding energy. Organic semiconductors have permittivities of 2-4 and exciton binding energies of about 0.5 to 0.7 eV. Heavily bound and localized excitons are typical for an organic semiconductor and are called Frenkel excitons. Their radius is only $\sim$10 Å and hence excitons are localized on one molecule. The permittivity of inorganic semiconductors varies from 10 to 15, thus the screening of the charge carriers is high and the exciton binding energy lower (0.01 eV). As the thermal energy at RT (0.025 eV) is sufficient to split excitons of inorganic semiconductors, free charge carriers result in inorganic semiconductors but not in organic ones. Weakly bound excitons are called Wannier excitons. For charge separation in organic semiconductors high electric fields above 10^6 V/cm are required, however, in organic solar cells only electric fields in the range of 10^4-10^5 V/cm are existent due to contact formation. Therefore there must be different mechanisms for an effective electron-hole separation (see Section 2.3.2 and Fig. 2.8).[22]

2.1.4 Free charge carriers of organic semiconductors

If charges separate and free charge carriers are present on the molecule, a polaron is formed. A polaron is a quasiparticle and describes the interaction of a charged particle and the self-induced polarization of its surroundings. The polarization originates from three different relaxations mechanisms, which occur around the free charge carrier and is summarized in Fig. 2.2.
The strongest and fastest relaxation is the electrical relaxation of the surrounding molecules. In this case, π electrons of the neighboring molecules get polarized due to the charge of the electron/hole. This relaxation takes place within 10^{-16} and 10^{-15} s and its contribution to the polarization is with

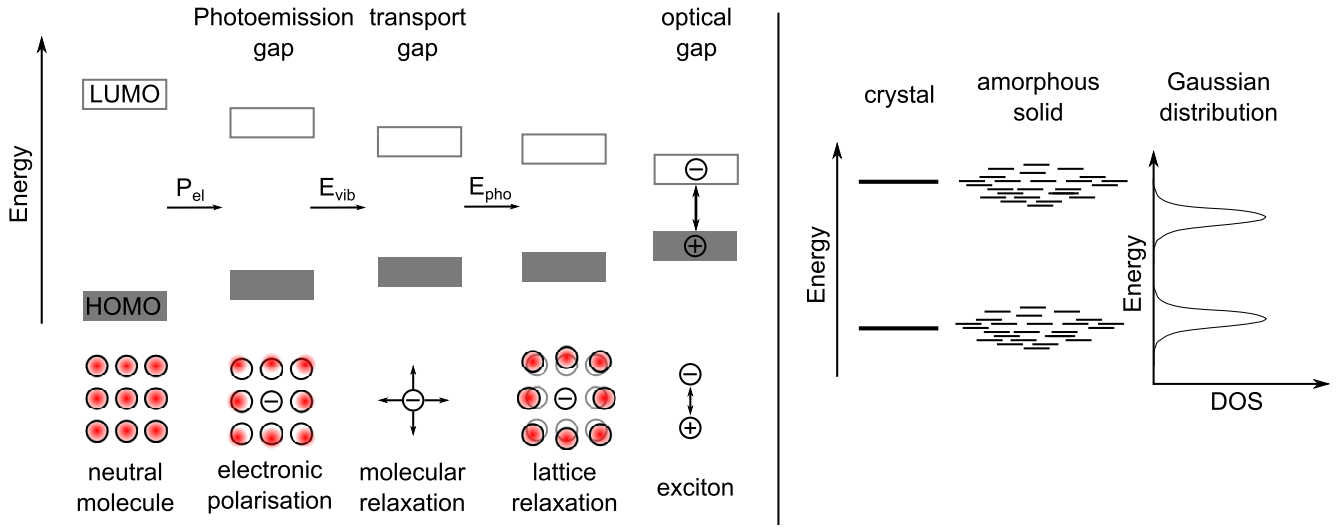

Figure 2.2. – Left: Schematic illustration of the energy gaps in organic semiconductors. Free charge carriers cause a polarization of the surroundings, which cause a decrease of the energy gap. The transport gap is about 200 meV smaller, than the photoemission gap, which is accessible by PES/IPES measurements. Right: Gaussian distribution of the energy levels of an organic solid. Adapted from Ref. [21, 24, 25].

$\sim$1 eV rather high.[21] The second relaxation process is the molecular relaxation. Here whole single molecules respond to the charge, which results e.g. in a change of the intramolecular bonding lengths. The molecular relaxation time is about 10^{-14} s and its contribution to the polarization 200 meV. The weakest ($\sim$10 meV) and slowest (10^{-13}-10^{-12} s) relaxation process is the lattice relaxation. It describes a distortion of the lattice due to the movement of the complete molecule. All these relaxation processes lead to an energetic change of the HOMO/LUMO positions in the organic semiconductor. Especially their time scale has to be taken into account as polarization effects are involved in PES as well as in charge transport.[21,23]

In PES the photoionization process takes about 10^{-14} s, though the electrical relaxation may be detected by PES, whereas the lattice relaxation is to slow to be detected. The molecular relaxation is at the same time scale as the photoionization process and therefore it is unknown if it is detected by PES. The photoemission energy gap measured by a combination of normal and inverse PES (IPES) represents therefore mainly the HOMO-LUMO gap after the electrical relaxation of the photohole in the valence band and the electron in the conduction band.[23]

For charge transport a different situation is present. As charge carriers in organic semiconductors are strongly localized, charge transport cannot be explained by the classic energy band model which is valid for inorganic semiconductors. The transport is instead described by a hopping process between the molecules. To hop from one molecule to another, the charge carrier has to overcome the potential barrier between the molecules. This can happen either thermally activated or by a tunneling process. The dwell time τ of the charge carrier on one molecule is about 10^{-12} s/hop, thus charge transport is sufficiently slow to allow all three relaxation mechanisms to occur. This gap therefore is also referred to as the transport gap for charge carriers. Experimentally the transport gap can be accessed for example, by cyclo-voltammetry, but often the PES/IPES gap is also assumed to be the transport gap.[26] By optical spectroscopic methods like UV-Vis spectroscopy only excitons and no free charge carriers are excited. As said before, the exciton binding energy is high

and thus the HOMO-LUMO gap determined from UV-Vis measurements is smaller, than the transport gap.

As every molecule or molecular chain in amorphous and polycrystalline organic semiconductors has different surroundings the exchange interaction for every molecule is different. As a consequence the polaron levels of every molecule depend on its surroundings and are different for every molecule. With the assumption of a Gaussian distribution of the molecular interaction a Gaussian distribution of the HOMO and LUMO energy levels is assumed (see Fig. 2.2 right).

2.2 Interface and contact formation at metal/metal oxide/organic interfaces

For solar cells the metal/semiconductor and semiconductor/semiconductor electronic interface alignment is crucial for its functionality as it governs the charge transport across the interface, which is important for the efficiency of a solar cell. The band alignment at inorganic interfaces (metal/semiconductor and semiconductor/semiconductor) is ascribed by the Schottky model.[27] Interface formation for the inorganic/organic and organic/organic interface formation is still under discussion. Braun et al. developed the Integer Charge-Transfer model (ICT-model) to describe the inorganic/organic and organic/organic interface.[28]

At the surface of different materials electronic potentials are existent as depicted in Fig. 2.3 and Fig. 2.4. Metals (see Fig. 2.3a) have only one surface potential, the work function (WF) φ, which is the distance of the Fermi level E_F to the vacuum level E_{Vac}. For semiconductors, where E_F is in between the energy gap, two other surface potentials are existent, the ionization potential I_P, which is the distance of the valence band (VB) to E_{Vac} and the electron affinity χ, which is the distance of the conduction band (CB) to E_{Vac} (see Fig. 2.3b). For a metal WF, I_P and χ are equivalent.

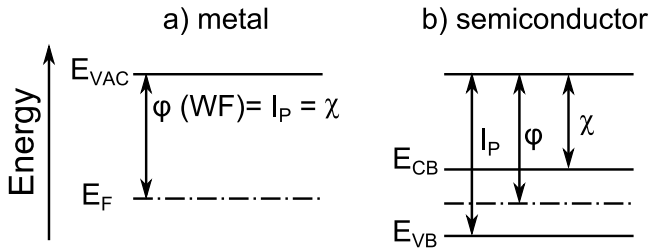

Figure 2.3. – Band diagram of a metal a) and a semiconductor b). I_P is the ionization potential, χ the electron affinity and φ the work function.

2.2.1 The Schottky model of the space charge region

In the case of semiconductors, potentials at surfaces or at the interface to other materials can be different to the potentials in the bulk, which has its origin in the low charge carrier concentrations of semiconductors. The charge carrier concentration at the surface of a semiconductor can change, e.g. if a contact to another material takes place or surface states are present. If this happens, band bending occurs at the surface/interface.

Figure 2.4 shows the contact formation of a p-type and a n-type semiconductor with the same energy gap. In Fig. 2.4a) the p- and n-type semiconductor are not in contact. E_D and E_A describe the ground state of the donor and acceptor states and are constant within the semiconductor. Upon contact formation of the p- and n-type semiconductor (see Fig. 2.4b) charges flow across the interface and the energy bands do bend at the interface. The area where band bending occurs is called the space charge region (d_{scr}). The band bending causes that in the p-type region E_A is pushed above E_F which causes an occupation (accumulation of electrons) of the donor states with electrons, while in the n-type region E_D is pushed below E_F, which causes an electron depletion of the acceptors states. The ionized species (negatively or positively charged atomic cores) are fixed in location. Figure 2.4c) shows the corresponding charge carrier concentration of ionized donors (N_D) and acceptors (N_A). The location-dependent concentration of ionized species, ρ, is defined by the distance to the conduction (n-type) or valence band (p-type). The width of the space charge region is defined by the Fermi level difference of both semiconductors and the charge carrier density of the semiconductor. The lower the charge carrier density the smaller becomes the screening of the transferred charges and the space charge region becomes broader. Non-degenerated semiconductors have a space charge region (d_{scr}) between 5-100 nm.[29] In Fig. 2.4d) and e) the electric field E and the potential φ are depicted. The potential φ has the reversed course of the band bending.

2.2.2 The metal/semiconductor contact

The metal/semiconductor interface can be ascribed by the Schottky model[27] and is often referred to as the Schottky contact. The band alignment is determined by the difference of the electron affinity χ of the metal and the semiconductor.

At contact formation between a metal and semiconductor, electron transfer occurs from the material with the lower WF to the higher WF. The transferred electrons causing a depletion region (space charge region) in the material with the lower WF, where the fixed charged atomic cores are the counter charges. The width of the space charge region, d_{scr}, depends on the transfered electrons (determined by the difference of the Fermi level position) and on the doping concentration (charge carrier concentration) of the respective material. Metals have a high charge carrier density of about 10^{22} cm^{-3} and the charged layer is screened after a few atomic layers. The doping concentration N_D of semiconductors is smaller (typical N_D: $\sim 10^{16}$ cm^{-3}). At constant charge carrier densities an increase of the band bending results in an increase of the width of the space charge layer. The height of the band bending (ϕ_{bb}) is equivalent to the χ difference of the metal and the semiconductor. If the metal has a higher χ, upward band bending occurs in the semiconductor towards the interface and if the metal χ is smaller, downward band bending occurs in the semiconductor towards the interface. The barrier height for electrons $\Phi_{B,n}$ at the interface is the difference of WF (or χ) of the metal and the χ_{sc} of the semiconductor. For holes, the barrier height $\Phi_{B,p}$ is the difference of $I_{P,sc}$ of the semiconductor and the WF of the metal (see Eq. (2.4)).[29–31]

$$\Phi_{B,n} = \varphi_m - \chi_{sc} \tag{2.3}$$

$$\Phi_{B,p} = I_{P,sc} - \varphi_m \tag{2.4}$$

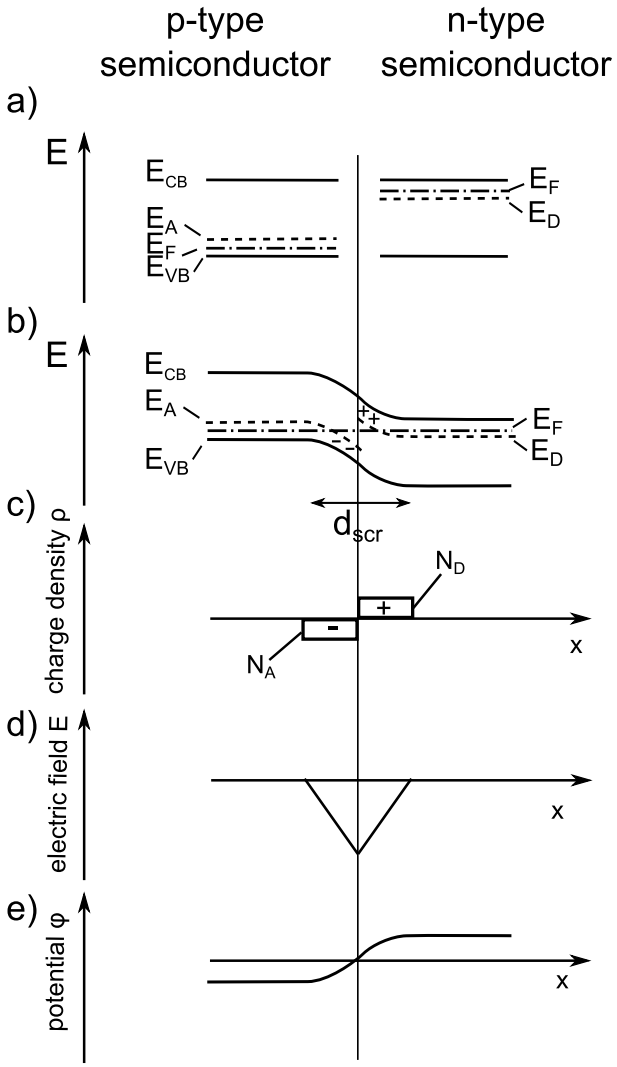

Figure 2.4. – (a): Band structure of a p- and n-type semiconductor before contact formation. E_D and E_A describe the ground state of the donors and acceptors. (b): After contact formation both semiconductor are in thermal equilibrium and the Fermi levels E_F are equalized. Electrons and holes flow across the interface and a space charge region is formed. Due to the band bending E_D and E_A cross E_F. At the interface E_A states become occupied by electrons and E_D states are depleted of electrons. (c): The location-dependent charge density ρ of ionized donors (N_D) and acceptors (N_A). (d and e): The electric field E and potential φ. The potential φ has reversed course of the band bending. Adapted from Ref. [29].

In Fig. 2.5a), contact formation between a metal (higher WF) and an n-type semiconductor (lower WF) is depicted.

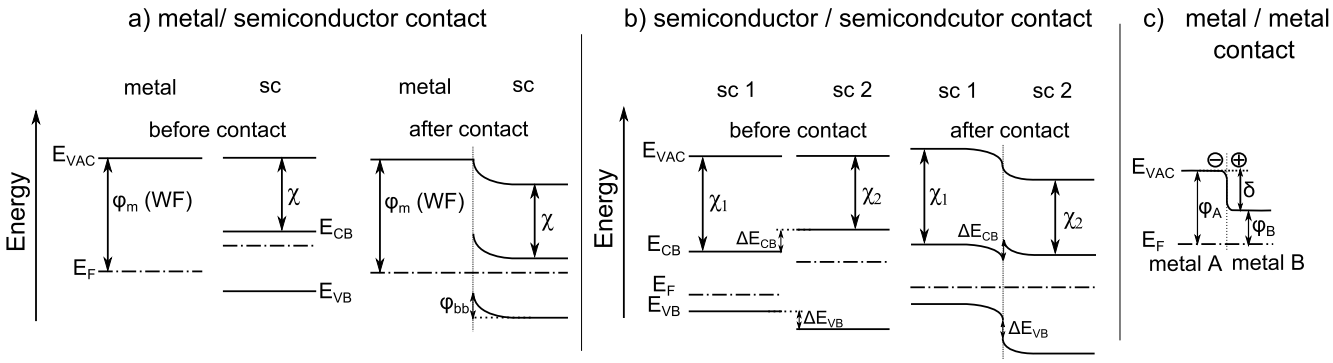

Figure 2.5. – Left: Metal/semiconductor contact. After contact the Fermi level aligns and charge transport at the interface takes place. As the charge carrier density in the semiconductor is low, band bending occurs. Middle: Semiconductor/semiconductor heterocontact. After contact both semiconductor bands bend towards the interface. This is also called Anderson model, as the formation of interface dipoles is not taken into account. Right: Contact between two metals with different work functions. Due to the equalization of E_F, electrons shift from metal B to metal A. Due to the high charge carrier density no space charge region is formed and the E_{Vac} offset is considered as interface dipole δ.

2.2.3 The semiconductor/semiconductor heterocontact

The semiconductor/semiconductor heterocontact interface alignment of two semiconductors with different energy gaps and can be ascribed by the Schottky model as well and is shown in Fig. 2.5b). As the energy gaps of the semiconductors are different, valence band and conduction band discontinuities exist at the interface, which match the difference of the energy gaps (Eqs. (2.5) and (2.6)).

$$\Delta E_{CB} = \chi_1 - \chi_2 \tag{2.5}$$

$$\Delta E_{VB} = I_{P,1} - I_{P,2} \tag{2.6}$$

Figure 2.5b) shows the interface alignment of an n-type and a p-type semiconductor following the Schottky model. First the vacuum levels align, and then the equalization of the Fermi level takes place. The electrons shift from the semiconductor with the smaller WF to semiconductor with the higher WF. As both semiconductors have a small charge carrier concentration, both materials display a band bending towards the interface. This description of the band alignment is also called the Anderson model and does not take the formation of interface dipoles into account.[29–31]

2.2.4 Interfaces with band bending and interface dipoles

The experimentally evidenced barrier height at metal/semiconductor or semiconductor/semiconductor interfaces often does not agree with the assumed barrier height from the Schottky or Anderson model. In many cases the barrier height is independent of the WF and E_A of the respective materials. This is

called Fermi level pinning. Origins of Fermi level pinning can be e.g. energetic states within the band gap at the surface (surface gap states) or metal induced surface states.

- **Surface gap states**:
  Gap states at the surface of semiconductors within the energy gap can origin from non-saturated chemical bonds, also named *dangling bonds*. *Dangling bonds* occur e.g. at the silicon surface, where unpaired valence electrons exist at the surface or due to oxygen vacancies at metal oxide surfaces like TiO_2. Oxygen vacancies introduce extra electrons, which reduce the oxidation state of titanium from 4+ to 3+. A surface state density has a mean electro-chemical potential as well, which is called charge neutrality level (E_{CNL}). If E_{CNL} is below E_F of the semiconductor, charges shift from the semiconductor to the surface states, which causes an upward band bending within the semiconductor, while the surface states become negatively charged. As the system has to be overall neutral, the charge of the space charge region has to compensate the charge of the surface states. If E_{CNL} is above E_F of the semiconductor, downward band bending towards the semiconductor surface occurs. The higher the surface state density the higher is the band bending. At surface state densities of about 10^{-13} to 10^{-15} states/ eV cm^2 the Fermi level position at the surface is independent of the doping of the semiconductor and only determined by the position of E_{CNL}. Then one talks about a pinned Fermi level.

- **Metal induced surface states (MIGS)**:
  At the metal/semiconductor interface, the metal wavefunction does not stop abruptly at the interface but decays as soon it enters the semiconductor to a certain depth. By this, metal induced gap states (MIGS) form at the interface.

The occurrence of interface states at the metal/semiconductor and semiconductor/semiconductor interfaces causes the formation of an interface dipole δ, which de- or increases the band bending at the interface. An example is given in Fig. 2.6, where the E_{CNL} of the surface states is below E_F of the semiconductor. The surface states are negatively charged and this charge is equalized by ionized donating atoms of the semiconductor, which cause an upward band bending towards the semiconductor surface. After contact with a metal with a higher WF, electrons shift from the semiconductor to the metal and band bending increases. When E_{CNL} of the surface states moves above E_F the electrons occupying the surface states shift into the metal and the surface state becomes positively charged. This induced positive charge adds up to the equalization of the contact potential and therefore the band bending of the semiconductor diminishes compared to the Schottky model.[31]

As Fermi level pinning often occurs at interfaces and the barrier height cannot always be predicted by the electron affinity rule. Therefore an equalization of the E_{CNL} proved to be more suitable to predict the barrier height at interfaces. For semiconductors the determination of E_{CNL} is difficult and not for all materials reliable values can be found in literature. By performing interface experiments and determining the line-up with PES measurement the barrier height can be accessed experimentally.

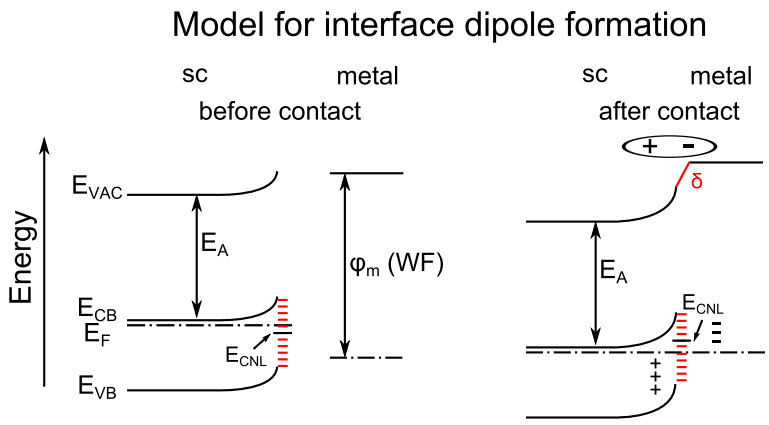

Figure 2.6. – Interface formation at the metal/semiconductor interface with electronic states within the band gap. As the surface states add an additional positive charge at the interface, a dipole forms at the interface.

2.2.5 The Integer Charge-Transfer model

According to Braun et al. band bending, as in inorganic semiconductors, is not expected in π-conjugated molecules forming an interface to metals, as organics do not have a band structure and rather localized electronic states. Only doped organic films, with a sufficiently high density of charges, e.g. due to impurities, can exhibit a "band-bending like effect".[28] Instead of classic band bending, Braun et al. assume a doping mechanism at inorganic-organic and organic-organic interfaces and developed the **I**nteger **C**harge-**T**ransfer (ICT) model to describe the interface alignment at inorganic-organic and organic-organic interfaces.

The ICT model assumes only a negligible amount of interaction between the π-orbitals of organic materials itself or of the organic semiconductor and the electronic wave functions of the inorganic substrate. Integer transfer states are the same as polaron levels, which occur if a charge carrier (hole or electron) is introduced in an organic semiconductor. E_{ICT+} is the hole polaron state above the HOMO and E_{ICT-} the electron polaron state below the LUMO. In the ICT model the position of those two states with respect to the Fermi level of the metal are relevant for the interface alignment. If the WF of the metal substrate is higher than E_{ICT+} or lower than E_{ICT-}, the Fermi level of the metal is pinned to E_{ICT+} or E_{ICT-} respectively. The barriers for the charge transport across the interface are independent of the WF of the metal and only determined by the polaron states of the organic material. In the second situation the WF of the metal is lower than E_{ICT+} and higher than E_{ICT-}. If this is the case, a vacuum level alignment occurs and the WF of the organic material scales with the WF of the substrate. Hence electron barriers at the interface scale as well with the metal WF and therefore can be tuned by the WF of the metal.[28]

In this work Fermi level shifts (respectively band bending) and the occurrence of a space charge layer within a C_{60} layer on various metal oxide substrates were obtained by means of photoelectron spectroscopy. Therefore the Schottky model appears to be valid for the metal oxide/C_{60} interface and is used in this work to determine the energy band line-up. Maibach et al. observed a formation of a space charge layer in DH6T at the $PC_{61}BM$/DH6T interface, as well.[32]

2.3 Organic solar cells

There exist two different main types of organic solar cells. On the one hand dye sensitized solar cells (DSSC)[10] and on the other hand organic solar cells (OSC) with a heterojunction of two different organic semiconductors. Recently a third type of OSC, with an organic halide perovskite as an absorber emerged. Perovskite solar cells advanced fast and efficiencies of over 20% are reached already.[33] In this section the device structure and important design rules of organic solar cells with a heterojunction to the absorber material are described and explained.

2.3.1 Basics of organic solar cells

The basic principles of solar cells, organic or inorganic, are the same. To generate charge carriers from sunlight a semiconducting absorber material is needed. Upon the incidence of light, electrons are excited above the energy gap of the absorber. In organic semiconductors no free charge carriers are generated, but strongly bound e-h pairs, i.e. excitons. The separation of those excitons is performed at an (in)organic-(in)organic donor/acceptor interface.[22] The free charge carriers are collected at the electrodes. To avoid the recombination of charge carriers at the wrong electrode and to enhance charge carrier extraction, electron transporting interfacial layers (ETL or hole blocking layer) and hole transporting interfacial layers (HTL or electron blocking layer) are inserted between the absorber and the electrodes. The interfacial layers are considered to be part of the electrodes.

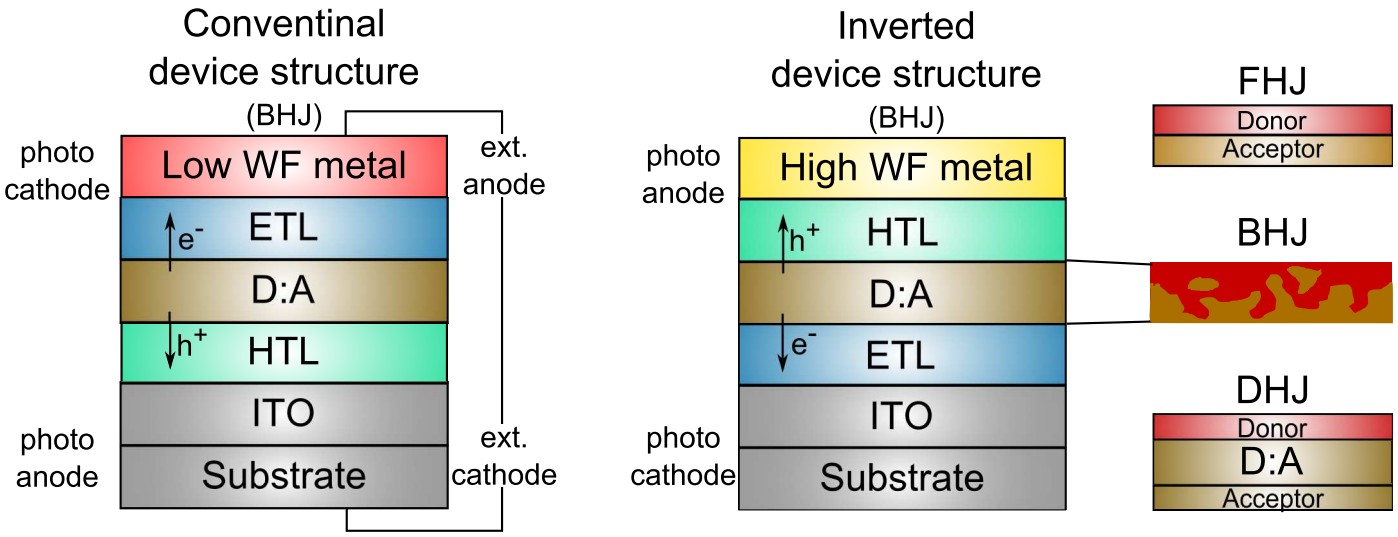

Figure 2.7. – Left: Conventional device structure of a heterojunction OSC with a low WF metal as top electrode and an ETL adjacent to the top electrode. Middle: Inverted device structure of a heterojunction OSC. The top electrode is now a high WF metal. Holes flow to the top electrode and electrons through adjacent ETL to the transparent ITO bottom electrode. Right: Different structures of the donor/acceptor absorber layer. A FHJ consists of bilayer structure, a BHJ consists of blend of the donor/acceptor system and DHJ is a combination of both device structures, where the donor/acceptor blend is embedded by an organic donor and an acceptor layer.

In Fig. 2.7 the conventional device structure (left) and the inverted device structure (middle) of OSC are depicted. In conventional OSC devices, a low WF metal is employed as top electrode and e.g.

ITO acts as bottom electrode. In the conventional device structure generated electrons flow to low WF metal, which acts as photo cathode and holes to the transparent photo anode. If the device is short circuited, photoinduced electrons and holes flow within an electronic circuit. In this case the photo anode becomes the cathode and the photo cathode becomes the anode, following the convention in electrical engineering.

In an inverted cell architecture the polarity of the cell is reversed. The cathode is now adjacent to the transparent substrate. As top electrode high work function metals are applied.[15] To ensure the change of the polarity n- (as ETL) and p-type (as HTL) interfacial layers are introduced. As low WF metals like Al, Mg or Ca have a low air stability compared the high WF metal like Au, Ag or Cu, inverted OSC are superior to conventional solar cells in terms of durability of the top electrode.[34] Furthermore inverted OSC show advantages in the manufacturing process compared to conventional OSC device structures.[35]

The absorber layers of OSC have different structures as well. It is distinguished between a flat heterojunction (FHJ) solar cell, bulk heterojunction (BHJ) and the diffuse bilayer heterojunction (DHJ). In a FHJ OSC the donor-acceptor system consists of a layer on top of each other, while in a BHJ OSC the absorber layer is a blend of the donor and acceptor material. Due to the blend the interface density between the donor and acceptor increases and exciton splitting is maximized. To improve the percolation path for the charge carriers to the electrodes, the blend can be embedded by the donor and the acceptor respectively, which results in a DHJ (see Fig. 2.7 right).[36]

2.3.2 Absorber layers of organic solar cells - Exciton splitting

The absorber layer in organic solar cells consists of an electron accepting (acceptor) and an electron donating (donor) organic semiconductor. As explained in Section 2.1.3 the exciton binding energy in organic semiconductors is high and the existing electric fields in the bulk of the organic materials are not high enough to separate them. Therefore the separation of excitons takes place at the interface of the donor and the acceptor (see Fig. 2.8). At this interface a normal bulk exciton can transform in a so called charge-transfer exciton (CT-Exciton). The formation of a CT-Exciton happens, if Eq. (3.7) is valid:

$$I_P - \chi - U_{C_{A,D}} < 0, \tag{3.7}$$

where I_P is the ionization potential of the donor, χ the electron affinity of the acceptor and $U_{C_{A,D}}$ the Coulomb energy of the respective exciton.
This means that the formation of a CT-Exciton only takes place, when $U_{C_{A,D}}$ is larger than the CT-Exciton binding energy, which is approximated by the difference of I_P and E_A. An effective formation of CT-Excitons takes place if the HOMO/HOMO or LUMO/LUMO difference is at least 0.3 eV. Although the charge carriers are on two different molecules after the CT-Exciton formation, they are not separated yet. The released energy upon CT-Exciton formation may be enough to separate electron and hole.[36]

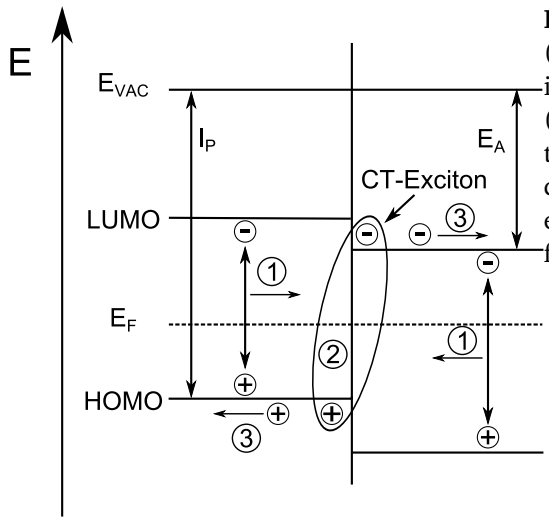

Figure 2.8 – Charge transfer exciton (CT-Exciton) formation at a donor/acceptor interface. The exciton travels to the interface (1), where it is transformed to a CT-Exciton, if the HOMO/HOMO or LUMO/LUMO difference is at least 0.3 eV (2). The released energy upon CT-Exciton formation can create free charge carriers (3).

2.3.3 Interfacial layers

To improve the efficiencies of organic cells interfacial layers between the absorber and the electrodes are introduced. Interfacial layers can establish ohmic contacts, act as charge selective contacts or exciton blocking layer and furthermore increase the stability of OSC devices.

Interfacial layers that improve the charge transport to the electrode by either forming an ohmic contact or acting as selective contact are divided into hole transport layers (HTL) and electron transport layers (ETL). ETL and HTL can either by organic or inorganic materials. The ETL is adjacent to the n-type organic semiconductor and has its LUMO/CBM on a similar electronic level as the LUMO of the acceptor, whereas the acceptor HOMO lies energetically much lower compared to the HOMO/VBM of the ETL. Due to this, the transfer of a hole to the ETL and the recombination of it is unlikely. The HTL just works the other way and the HOMO of the donor adjusts the VBM/HOMO of the HTL. Exciton blocking layers (EBL) have higher band gaps than the adjacent organic semiconductor and are reflecting the excitons, which increases the exciton dissociation probability. On the other hand, the large band gap of EBL induces energy barriers which hinder charge transport.[37,38]

Typical n-type interfacial layers for electron extraction (ETL) are TiO_x, SnO_x ZnO or AZO.[15,39,40] Beyond this, it was reported that TiO_2 as interfacial layer reduces the sensitivity of OSC to oxygen and water and improves the device stability.[41,42] Common p-type interfacial layers materials are PEDOT:PSS, MoO_x or WO_3[43–45] and bathocuproine (BCP) can act as an exciton blocking material.

2.4 I-V characteristics of solar cells

Figure 2.9 shows the I-V characteristics of a solar cell in the dark and under illumination. In the dark it equals the I-V characteristics of a diode and can be described by the common diode equation (Eq. (4.8)):

$$j_d = j_0 \cdot (e^{\frac{qV}{Ak_BT}} - 1), \tag{4.8}$$

where j_d is the dark current, j_0 the reverse leakage current, q the elementary charge, V the voltage and A the diode quality factor. Under illumination a photocurrent is induced in the diode inverse direction and the I-V characteristics shift down by the amount of the photocurrent density j_{ph}. The resulting I-V curve can be described by Eq. (4.9):

$$j = j_d - j_{ph} = j_0 \cdot (e^{\frac{qV}{Ak_BT}} - 1) - j_{ph} \tag{4.9}$$

The I-V curve proceeds between the short circuit current j_{sc} at zero voltage, where the solar cell is short-circuited and the open circuit voltage V_{oc} at zero current, where the electrodes are not connected. j_{ph} is directly dependent of the adsorbed photons. V_{oc} of inorganic solar cells is determined by the energy gap of the used semiconductor materials. The origin of V_{oc} of OSC is still under discussion. As organic semiconductors have an isolating behavior the metal-isolator-metal model (MIM-model)[30] is often used to describe I-V characteristics of OSC. In the MIM-model, the difference of the WF of the electrode materials is assumed as the origin of V_{OC}. However, experimental data showed that there are deviation of the model in the case of OSC and that V_{OC} is independent of the used electrode materials.[36,46,47] Instead it was proposed that the HOMO_{donor} and $\mathrm{LUMO}_{acceptor}$ difference is determining the value of V_{OC}.[48]

The solar cell is operated at the point of maximum power P_{max} and the respective current density j_{max} and voltage V_{max}. The fill factor FF is the quotient of the theoretical maximum power ($j_{sc} \cdot V_{oc}$) and P_{max} ($j_{max} \cdot V_{max}$) (see Eq. (4.10))

$$FF = \frac{j_{max} \cdot V_{max}}{j_{sc} \cdot V_{oc}} \tag{4.10}$$

The efficiency η of the solar cell is then defined by

$$\eta = FF \frac{J_{SC} \cdot V_{OC}}{P_{opt}} \cdot 100\,\%, \tag{4.11}$$

where P_{opt} is the power of the incident light.

In an equivalent circuit diagram (see Fig. 2.10 a), the current source is representative for photogenerated charge carriers within the absorber material and supplying the photocurrent j_{ph}. The diode is representative for the p-n junction of the absorber material. The photocurrent flows in reverse direction of the diode. In addition there are two resistors, one in series and one in parallel. The parallel resistor, also called shunt resistance R_{sh} represents losses e.g. due to leakage currents or recombination of charge carriers. R_{sh} is the slope of the I-V curve at current density j=0. In a good solar cell R_{sh} is as high as possible. The series resistance R_s is mainly determined by the resistivity of the absorber and the contacts

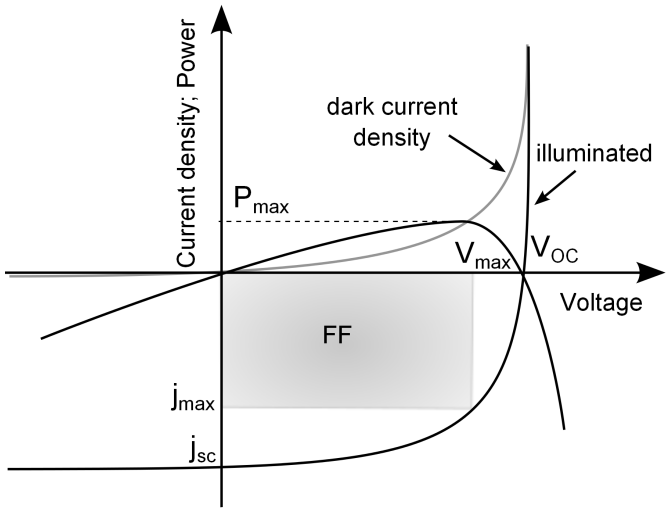

Figure 2.9. – I-V characteristic of a solar cell in the dark and under illumination. Under illumination the I-V curve shifts down by j_{ph} to j_{sc}. The solar cell is operated at the point of maximum power P_{max}, which also determines the FF of the solar cell. Adapted from Ref. [6].

and should be as low as possible. R_s is the slope of the I-V curve at $V=0$.[49] Including R_{sh} and R_s in the diode equation results in:

$$j = j_{ph} - j_d = j_{ph} - j_0\left[e^{\frac{q(V-j\cdot R_s)}{k_B T}} - 1\right] + \frac{V_{oc} - jR_s}{R_{sh}} \tag{4.12}$$

The influences of varying R_{sh} and R_s on the I-V curves are illustrated in Fig. 2.10 b) and c). A high shunt resistance R_{sh} decreases mainly the fill factor FF, whereas V_{oc} and j_{sc} stay more or less constant (see Fig. 2.10 b). In contrast a low R_s decreases V_{oc} and FF (see Eq. (4.12) and Fig. 2.10 c).

In addition, other cell properties, like barriers between the absorber material and the electrode/interlayer (ETL or HTL) or a reduced charge carrier extraction to the electrode can be the origin of a varying behavior of the I-V characteristics.[51–53] There are two kind of barriers for charge carriers, which can occur at a metal/semiconductor or a semiconductor/semiconductor interface: Injection barriers (φ_{inj}) and extraction barriers (φ_{ext}). In Fig. 2.11 the contact between the acceptor material and an ETL is depicted. An injection barrier for electrons exists, if the E_{CB} of the ETL is energetically below E_{CB} of the acceptor material (see Fig. 2.11 left). Visa versa, an electron extractions barrier exists, when electrons have to overcome a potential to flow to the adjacent layer (E_{CB} ETL above E_{CB} acceptor, see Fig. 2.11 right). Furthermore a high resistance of e.g. an interlayer can influence the I-V characteristics as it reduces the charge carrier extraction. Both barrier types and the resistance are under discussion to cause S-shaped I-V characteristics in organic solar cells.[51,53,54]
In the case of an extraction barrier, photogenerated charge carriers, e.g. electrons, are hindered to flow to the electrode, therefore the photocurrent decreases at a certain voltage region. Charges pile up and create a space charge, which causes an increase of the local field at the contact and causes charges to move more slowly through the organic semiconductor and that the probability for recombination of the charge carriers increases.[53,55] At sufficiently high voltages the electric field becomes high enough, that

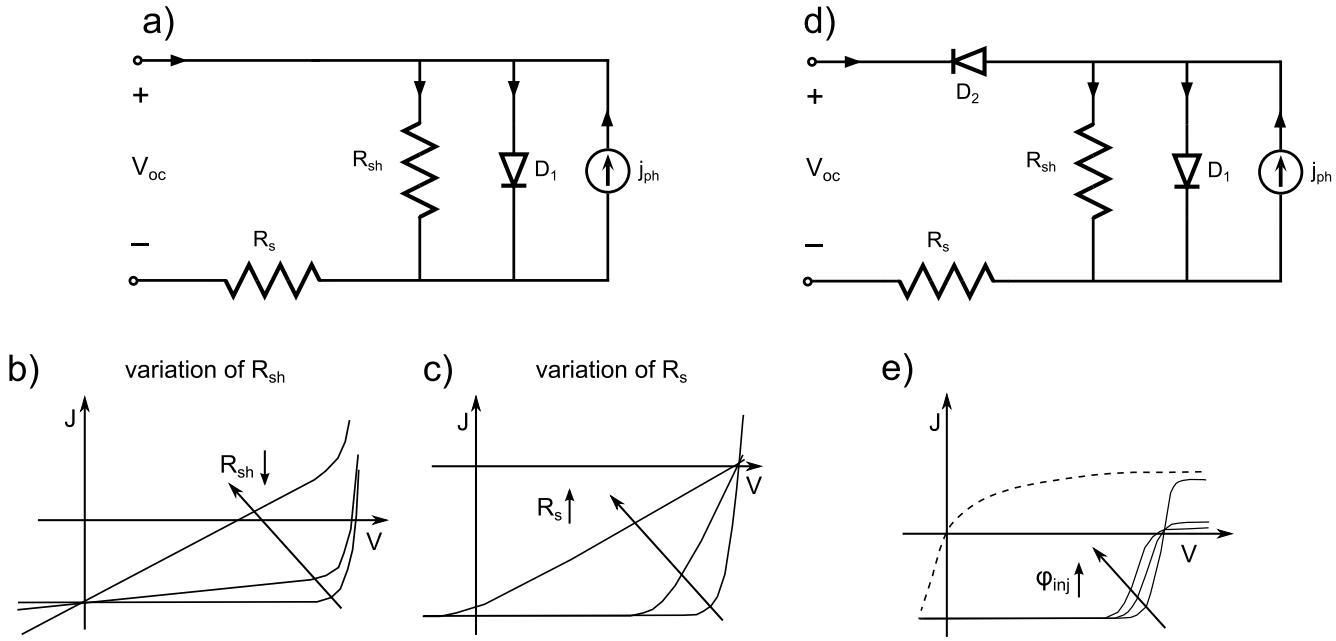

Figure 2.10. – a) Equivalent circuit diagram of an ideal solar cell. It consists of a diode (p-n junction), a source representative for the photocurrent and two resistors, the shunt resistance R_{sh} and a series resistance R_s. b) Influence of the variation of R_{sh} on the I-V characteristics. c) Influence of the variation of R_s on the I-V characteristics. d) Equivalent circuit diagram of a solar cell with an additional diode D_2 in reverse direction (counter diode). e) Influence of D_2 on the I-V characteristics of a solar cell. D_2 is a measure for a possible injection barrier, φ_{inj}, existing in the solar cell[50]

charge carriers can overcome φ_{ext} e.g. by tunneling through the barrier.

In case of injection barriers the origin of the S-shape is that the contact between the absorber and the

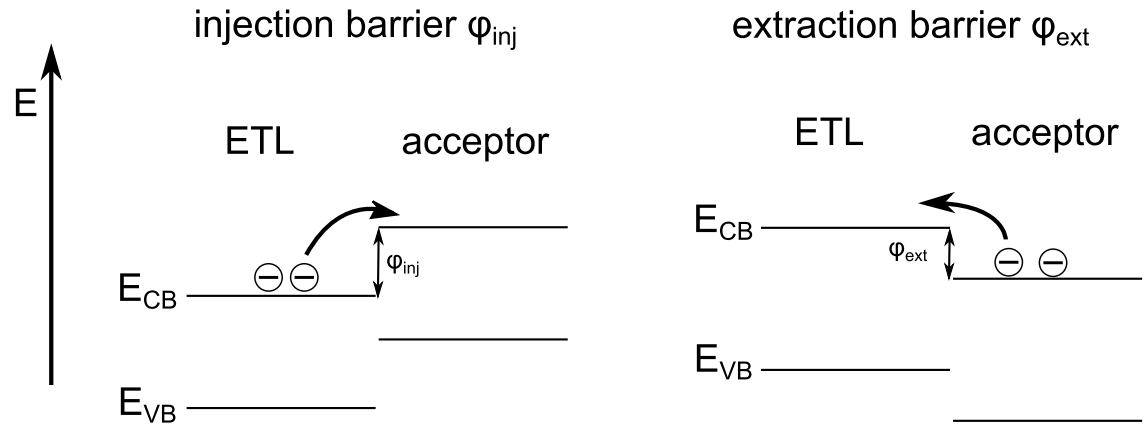

Figure 2.11. – Injection (left) and extraction (right) barrier for electrons.

electrode is a (Schottky-)diode in reverse direction to the photodiode as depicted in Fig. 2.10d). The current flowing over the barrier is described by Eq. (4.8) and the reverse leakage current $j_{D2(0)}$ is dependent of the barrier height φ_b, which is same as the φ_{inj} in Fig. 2.11. In Fig. 2.11 the ETL corresponds to the electrode. A diode in reverse direction is also referred to as counter diode.

$$j_{D2} = j_{D2(0)} \cdot (e^{\frac{qV}{Ak_BT}} - 1) \tag{4.13}$$

$$j_{D2(0)} = q \cdot N_V \sqrt{\frac{k_B T}{2\pi m^*}} \cdot e^{\frac{q\varphi_{inj}}{Ak_BT}} \tag{4.14}$$

The influence of an additional diode in reverse direction is depicted in Fig. 2.10e). The dashed line represents the I-V characteristic of D_2 in Fig. 2.10d) and adds up to I-V characteristics without D_2.

S-shaped I-V characteristics are observed e.g. for OSC,[51] IOSC,[15,53] and inorganic CdTe solar cells.[52] Tress et al. found out that S-shaped I-V characteristics in OSC can origin from injection and extraction barriers.[15] S-shaped I-V characteristics of CdTe and CIGS solar cells (often referred to as roll over) are usually attributed to injections barriers.[52,56]

2.5 I-V curves of inverted organic solar cells with TiO_x as ETL

An often observed phenomenon of IOSC are S-shaped I-V characteristics. Due to the S-shape the fill factor and the efficiency decreases. In order to improve the device performance of OSC it is important to understand the origin of S-shaped IV-curves. It seems that S-shaped I-V characteristics are related to the used ETL within IOSC with a $PC_{61}BM$:P3HT blend as absorber,[15] but also non-inverted organic solar cells, as e.g. systems with C_{60}/CuPc absorber, have S-shaped characteristics.[57] IOSC with TiO_x or ZnO prepared at low temperature (80-150 °C)[15,58] show S-shaped I-V curves, if the cells are not illuminated with UV light. After UV illumination IOSC with TiO_x or ZnO ETL's show both good I-V characteristics and high fill factors.[15,59–61]

In general the S-shaped I-V curves are attributed to an impaired extraction of majority charge carriers at the cathode (electrons) and the anode (holes).[62] Impaired extraction of majority charge carriers has been addressed to be caused e.g. by poor conductance of interlayers[54,63], imbalanced mobilities[64–67] or barriers for charge transport occurring in the device.[15,51,53,55,57,68–72] While imbalanced mobilities of the charge carriers are properties of the organic absorber material,[64] high resistivity of the interlayers or charge carrier barriers are dependent on the properties of the interlayer itself and its energy level line-up to adjacent layers.

Ecker et al. performed impedance measurements at an equivalent circuit system and proposed that the high resistivity of TiO_x causes S-shaped I-V curves. UV illumination reduces the resistivity of TiO_x and the S-shape disappears. Transient photoconductivity upon UV illumination of TiO_x was observed before by Pomoni et al.[73] The increased conductivity is attributed to the filling of trap states within the TiO_x upon electron-hole excitation due to UV illumination. Kim et al. attributed the disappearance of the S-shape upon UV illumination to an improved Fermi-level alignment at the ITO/TiO_x interface, due to UV induced trap filling in the TiO_x.[70] In literature mainly interfacial trap states and injection and

extraction barriers are discussed as origin of barriers causing S-shaped I-V curves. Wang et al. attributed S-shaped I-V curves of a conventional OSC with BCP as EBL[1] to interfacial recombination near the C_{60}/BCP interface[57] and Kuwabara et al. assigned the S-shaped I-V curve of IOSC, with TiO_x as ETL, to charge recombination centers near the TiO_x/P3HT:PC_{61}BM interface.[71] Others attributed the S-shape to a hindered charge transfer at one of the electrical contacts. Glatthaar et al. attributed the S-shape of classic OSC to a slow charge transport to the electrodes and presumed a corrosion of the aluminum cathode as one possible reason.[72] Wagenpfahl et al. artificially created S-shaped I-V curves of classic OSC devices by varying the ozone treatment time of the ITO electrode. Furthermore they simulated S-shaped I-V curves by varying the surface recombination velocity. Low surface recombination velocities are causing a S-shape and are assumed to be equivalent with an extraction barrier for the respective charge carriers.[53] Tress et al. investigated classic organic solar cells with different HTL and varied the offset of the absorber HOMO to the ETL HOMO. Thus they created injection and extraction barriers for holes within the device. They found out that both, injection and extraction barriers, can cause S-shaped I-V curves. Extraction barriers in OSC with FHJ and BHJ structure, cause both S-shape behavior, and their V_{OC} are independent of the barrier and just defined by the D/A system (effective energy gap). The influence of an injection barrier on I-V characteristics is different for FHJ and BHJ. While injection barriers in FHJ solar cells cause similar effects as extraction barriers (V_{OC} constant and decreasing FF), injection barriers in BHJ cells cause a decrease in V_{OC}. Already a HOMO mismatch of 0.2 eV caused strong S-kinks within the I-V curve of solar cells where V_{OC} was independent of the HTL.[55] Sundqvist et al. performed charge extraction by a linearly increasing voltage (CELIV) measurements on IOSC with TiO_x as ETL and S-shaped I-V characteristics (before UV illumination) and good diode characteristics after UV illumination. They addressed the S-shape to the high WF of the TiO_2 before UV illumination, which causes a low built-in potential, which allows a charge reservoir of holes, injected from the anode, to form in the organic layer at voltages close to V_{OC}. Upon exposure to UV radiation, the WF of the TiO_2 cathode decreases leading to an increased built-in potential and a reduced S-shape.[62]

[1] **E**xciton **B**locking **L**ayer

3 Materials

3.1 Titanium dioxide

Titanium dioxide has a wide range of applications and is used e.g. as white pigment for paint, as UV protection in sunscreen, as photocatalyst for water splitting, as well as in solar cells, either as electron transport layer or in dye sensitized solar cells for charge extraction.

3.1.1 Morphology of titanium dioxide

In nature, TiO_2 exists in three crystallographic structures: Anatase, rutile and brookite. The tetragonal rutile is thermodynamically the most stable polymorph and anatase (tetragonal) as well as brookite (rhombic) transform to rutile at elevated temperatures (anatase to rutile: 1188 K; brookite to rutile: 1023 K). The most prominent and for applications most relevant polymorphs are anatase and rutile.
Both, anatase and rutile crystallize in the tetragonal form, whereas their space group is different and $I4_1/amd$ and $P4_2/mmm$, respectively. The basic building block of rutile and anatase is a 6 fold coordinated Ti atom surrounded by oxygen atoms. The oxygen atoms are threefold coordinated. The two Ti-O bondings at the apexes of the octahedron are slightly longer and not all O-Ti-O bond angles are 90°, which leads to a slight distortion of the octahedron. Rutile has a hexagonal closed packing of oxygen atoms and half of the octahedral sites are occupied by Ti atoms. Anatase has cubic closed packing of oxygen atoms and half of the tetrahedral sites are occupied by Ti atoms. The energy gap of anatase is indirect and has a value of 3.2 eV, while rutile has a direct band gap with a value of 3.0 eV. In Fig. 3.1 the crystal structures of anatase (left) and (rutile) are displayed.[74]

3.1.2 Anatase surface structures

The anatase single crystal exposes the (101), (100) and (001) surfaces, where the (101) surface is thermodynamically the most stable and (001) the least stable surface and hence the anatase crystallite shape is dominated by (101) surface (see Fig. 3.2). According to the surface energy the (100) surface should be the surface with the second highest occurrence, but this is not the case in an equilibrium-shaped crystal, which is due to the formation of (101)-microfacets on the (100) surface, which creates similar local environments on the reconstructed (100) surface and the (101) surface.[77]

As the (101) surface is the most prevalent surface of anatase and discussed later in detail in the results and discussion part, only the anatase (101) surface structure will be considered here in detail. Using the concept of autocompensation a reasonable model for the (101) anatase surface was derived by Hebenstreit et al. The concept of autocompensation means, that for each Ti—O bond a O—Ti bond is

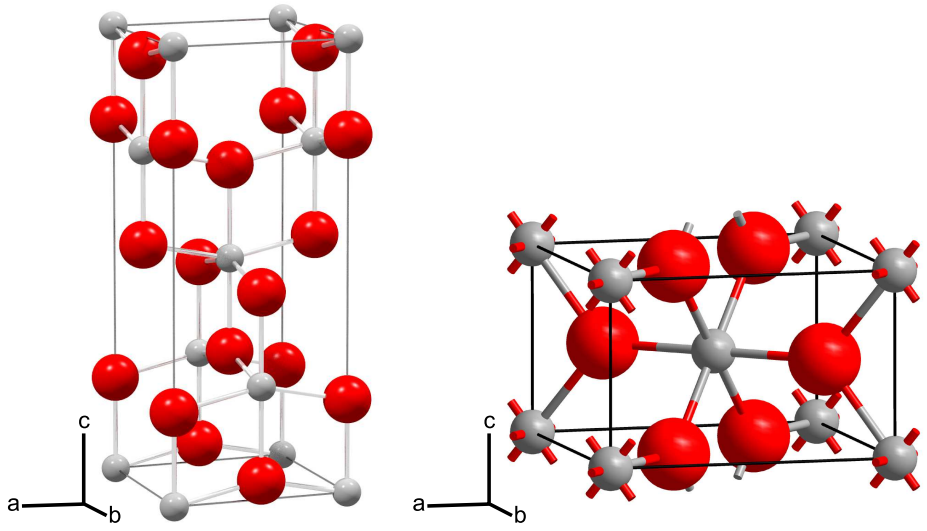

Figure 3.1. – Left: Unit cell of anatase. Right: Unit cell of rutile. Gray balls are titanium, red balls are oxygen atoms. The figure is taken from Ref. [75, 76].

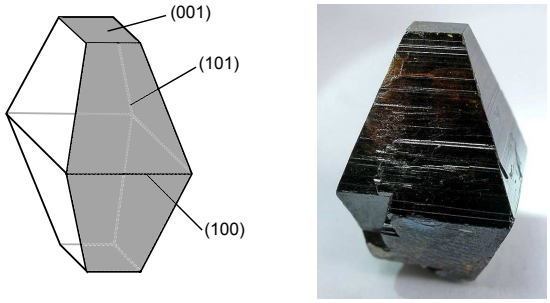

Figure 3.2. – Left: Sketch of the equilibrium-shape of an anatase single crystal (adapted from Ref. [78]). Right: Natural anatase single crystal similar to the used ones in this work. Taken from Ref. [79].

broken, when the crystal is cut along a certain direction.[80] Following this concept the anatase (101) surface has a sawtooth like structure build up by O-Ti-O double chains along the [101] direction as shown in Fig. 3.3a). At the ridges the oxygen atoms are twofold coordinated, whereas the rest of the oxygen is threefold coordinated, like in the bulk.[80,81] Titanium atoms in the bulk are sixfold coordinated. Depending on their positions at the surface, the titanium atoms on terraces are five -or sixfold coordinated, whereas at step edges titanium atoms are only fourfold coordinated.[77,80] Hebenstreit et al. performed a STM study of a sputter-annealed anatase (101) surface (a natural crystal was used) and reported the formation of a terrace/step structure on the (101) surface . The step structure consisted of monoatomic steps (of 4 Å height) with three preferred step orientations, which resulted in triangular shaped island (see Fig. 3.3b). Step edges form along the [010], [-1-11] and [-1-1-1] direction. Gong et al. made a detailed investigation of the formation energies and the stabilities of the different step edges on the anatase (101). By first-principles methods they calculated formation energies for the different step edges and confirmed the formation of trapezoidal islands (see Fig. 3.3c).[82]

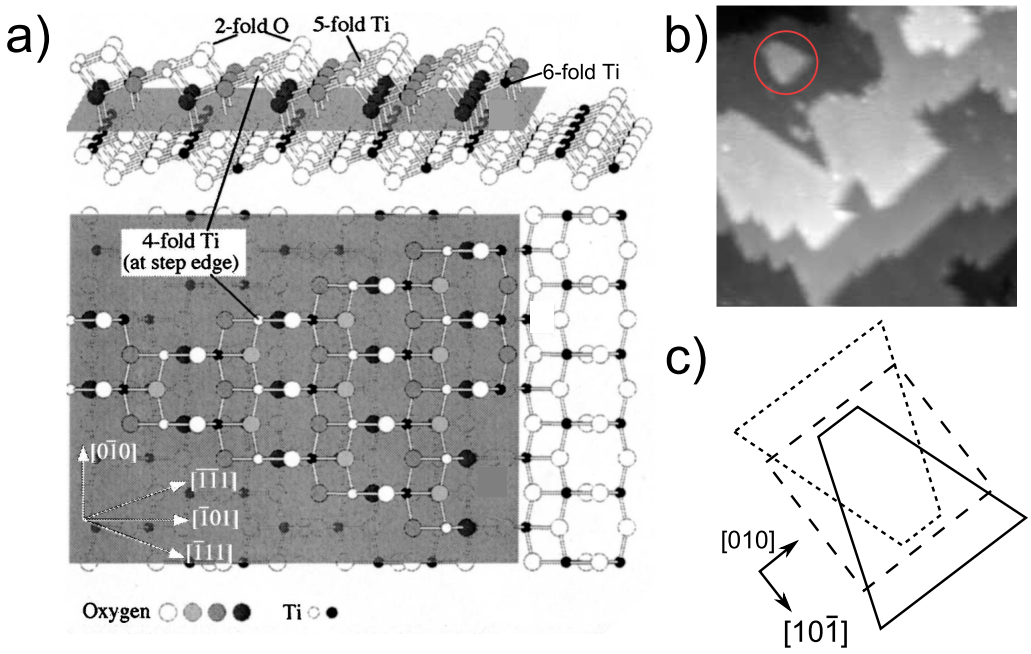

Figure 3.3. – a) Model of the autocompensated anatase (101) surface. The surface has a saw-tooth like structure, where the oxygen at the ridges are twofold coordinated and the titanium atoms five- or sixfold coordinated. At step edges on the (101) surface fourfold coordinated titanium atoms exist. b) STM image of a sputter annealed anatase (101) surface. Three step orientation can be seen which form trapezoidal islands on the surface. c) Sketch of possible island shapes. DFT calculations be Gong et al. showed that the formations of triangular shaped islands is preferred. Figures taken from Ref. [80, 82].

3.1.3 Electronic structure

Figure 3.4 left shows the calculated density of states (DOS) of anatase by Asahi et al.[83] compared to the valence spectrum of a sputter-annealed anatase (101) surface recorded by Thomas et al. (top spectrum)[84] On the right of Fig. 3.4 the molecular-orbital bonding diagram derived from a linear combination of atomic orbitals (LCAO) is displayed.[83]

The valence band is about 6 eV broad and is mainly derived by the O 2p atomic orbital, while the conduction band is mainly Ti 3d and Ti 4s derived. The upper valence band has almost no or only little Ti 3d and Ti 4s character and consists mainly of O 2p derived π-bonding states, while the lower valence band with its σ-bonding has an increased contribution of Ti 3d and Ti 4s atomic orbitals. The upper conduction band (above 8 eV) consists mainly of Ti orbitals with s and p character. The lower CB is mainly derived from Ti 3d states. The Ti 3d orbital exhibits crystal field splitting and the Ti 3d orbitals are split into a e_g and t_{2g} level.[83] Resonant photoemission measurements of the anatase (101) valence band confirmed the molecular orbital structure calculated by Asahi et al.[84,85]

3.1.4 Defect states

The most common defects on a TiO_2 surface are point defects due to oxygen vacancies (V_O). Mostly V_O are induced by ion bombardment or by annealing of the sample in UHV. If an oxygen vacancy, hence the removal of an oxygen atom takes place, the left electrons occupy Ti 3d orbitals. The occupied defect state corresponds to the population of Ti 3d orbitals around 1 eV below E_F. Resonant photoemission

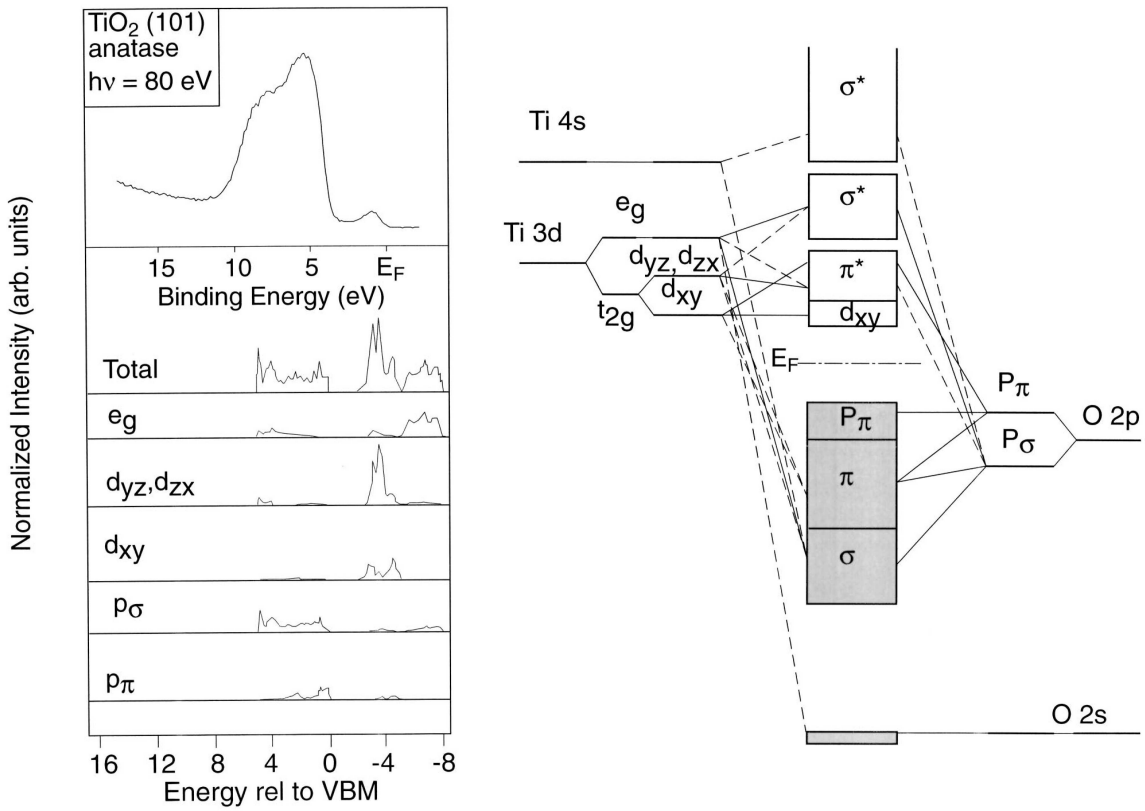

Figure 3.4. – Left: Photoemission spectrum of the valence band of a sputter annealed anatase (101) surface and the calculated band structure by Asahi et al.[83] Right: Molecular orbital diagram showing the contributions of the different atomic orbitals of Ti and O to the valence band and conduction band structure. Figures taken from Ref. [83] and [84].

measurements of the Ti 3p →Ti 3d transition showed the Ti 3d nature of the occupied gap states about 1 eV below E_F. The additional charge is also apparent in the Ti $2p_{3/2}$ core level as shoulder on the low binding energy side of the emission and is attributed to Ti^{3+} ions. While on the rutile (110) surface the induced V_O stay at the surface, V_O on anatase (101) migrate to subsurface sites. Removal of one twofold coordinated bridging oxygen results in two fourfold coordinated Ti^{3+} cations.

Another defect of anatase are the previously discussed step edges occurring on sputter-annealed and cleaved (101) surfaces as well as on the intersection of (101) planes of nanocrystalline materials. Step edges on the (101) surface and intersections of (101) of nanocrystals (see Fig. 3.2) planes both exhibit fourfold coordinated Ti sites. Nunzi et al. performed quantum mechanical DFT and DFT Tight-Binding calculations of TiO_2 nanocrystals of 3 nm diameter and observed localized states 0.3-0.4 eV below the delocalized conduction band originating from under-coordinated fourfold Ti atoms at the intersections of (101) surfaces[77,78] On sputter-annealed anatase (101) surfaces, triangular shaped islands, which exhibit step edges, were observed by STM measurements. Step edges are thought to be preferential adsorptions sites.[77,80,86]

3.2 Aluminum doped zinc oxide

The dominant method to deposit aluminum doped zinc oxide (AZO) films has been RF magnetron sputtering so far. As aluminum has a higher oxidation number (+III) than zinc (+II), doping of ZnO with Al, leads to n-doping and increased conductivity of AZO compared to ZnO. In recent years, AZO films were also deposited by ALD. To do so, alternating ZnO and Al_2O_3 layers are deposited.[87]

Lee et al. could verify a layered structure of ALD AZO film by TEM measurements, while Geng et al. reported hexagonal lattice structure with a preferred c-axis orientation of ALD ZnO and ALD AZO perpendicular to the substrate. Lee et al. reported a decrease of resistivity from $8 \cdot 10^{-3}\,\Omega\,\mathrm{cm}$ for ALD ZnO to $2.5 \cdot 10^{-3}\,\Omega\,\mathrm{cm}$ for ALD ZnO doped with about 2 at % aluminum. AZO films deposited by sputtering and PLD (pulsed laser deposition) exhibited the lowest resistivity with the incorporation of 2-3 at % as well, but showed a one order lower resistivity overall.[88] For ALD prepared AZO the crystal structure seems to be dependent on the amount of Al doping.[87,89]

3.3 C_{60} and $PC_{61}BM$

Fullerene and its derivatives are the most used acceptor materials in organic solar cell devices. Due to their low-lying LUMO level, they have excellent electron accepting properties and furthermore a unique fast charge transfer rate[90] and provide a low energy barrier for charge separation at the donor/acceptor interface,[91] which qualifies fullerenes as an excellent acceptor material in OSC.[41] Besides this, the fullerenes C_{60} and $PC_{61}BM$ are often used as model acceptor materials for OSC and therefore are extensively investigated.[41]

C_{60} (see Fig. 3.5 left) consists of 60 carbon atoms ordered in the shape of a soccer ball and is made of 12 pentagons and 20 hexagons. All C atoms are sp^2 hybridized and a conjugated π electron system is spanned over the whole molecule. In the year 1970 the stability of C_{60} was theoretically predicted by Osawa et al.[92] and first synthesized by Kroto et al. in 1985.[93] The diameter of C_{60} is about 7Å[93] and it can be evaporated at around 400 °C under UHV conditions. $PC_{61}BM$ is a derivative of C_{60}. It has an additional side chain consisting of a phenyl part and a methyl butanoate (see Fig. 3.5 middle). It was first synthesized in 1995 by Hummelen et al.[94] In contrast to C_{60}, $PC_{61}BM$ is soluble (in chlorobenzene), but cannot be evaporated without partial destruction.[95] Beside C_{60} and $PC_{61}BM$, many other fullerene derivatives with different amounts of carbon atoms exist. They differ in their HOMO/LUMO position and light absorption characteristics. As C_{70} and $PC_{70}BM$ absorb light stronger than C_{60} and $PC_{61}BM$, high PCE OSC are made with the C_{70} derivative.[41]

Inverted OSC referred to in this work were constructed with P3HT (Poly(3-hexylthiophene-2,5-diyl)) as organic p-type absorber (see Fig. 3.5 right). It is a standard p-type organic semiconductor for OSC devices.

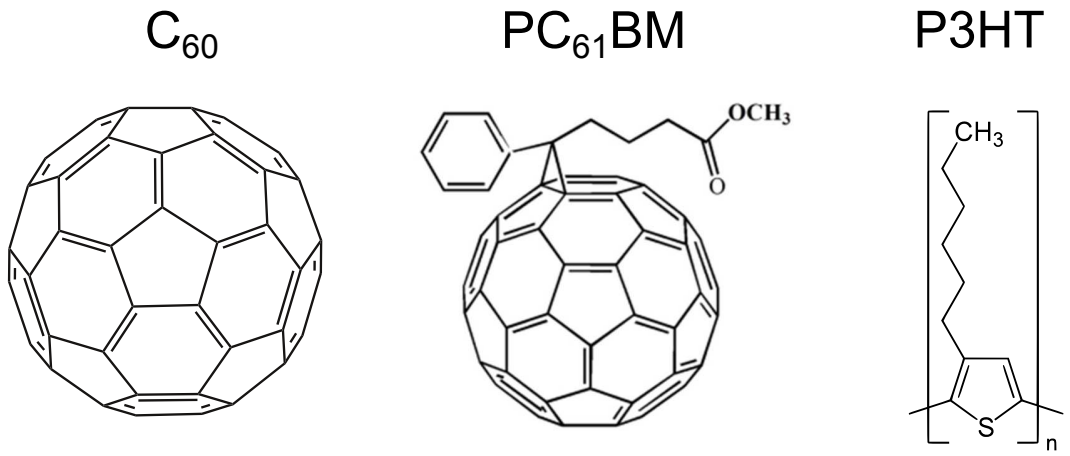

Figure 3.5. – Left: n-type organic absorber C_{60} molecule (Buckminster fullerene). Middle: $PC_{61}BM$ molecule with the additional phenyl and methyl butanoate part attached to the C_{60} molecule. Right: p-type organic semiconductor P3HT (Poly(3-hexylthiophene-2,5-diyl))

4 Preparation Methods and experimental setup

In this work titanium oxide (TiO_x) and aluminum doped zinc oxide (AZO) are used as substrate materials. TiO_x was prepared by atomic layer deposition (ALD) and by cleaving of a naturally grown anatase single crystal. AZO layers were deposited by ALD. All ALD prepared substrates were produced by Sara Trost and colleagues from our cooperations partner Bergische Universität Wuppertal, Germany. The ALD samples were packed in nitrogen atmosphere and send to Darmstadt, where they were stored in a nitrogen filled glove box. The ALD samples were shortly exposed to air in Wuppertal and Darmstadt. The cleavage of anatase single crystals is conducted at air (*ex situ*) and under UHV conditions (*in situ*). TiO_x, sc-TiO_2 and AZO were coated with C_{60} and the influence of UV light was investigated. For this purpose the sample was exposed *in situ* to UV irradiation and oxygen. Furthermore water was adsorbed to *in situ* cleaved anatase.

In this chapter all preparation methods are described. A focus is put on the newly applied *in situ* cleavage of anatase crystals. Furthermore the C_{60} deposition is briefly described and a short introduction into ALD is given.

4.1 Cleavage of anatase single crystals

To obtain clean TiO_2 surfaces, naturally grown anatase single crystals were cleaved *in situ* with pliers. The cleavage of crystals under UHV conditions enables the preparation of crystal surfaces without contaminations. The cleaving of crystals is often used in the case of materials with a layer lattice crystalline structure as WSe_2 or $MgBr_2$.[96] As only van-der-Waals interaction occurs between layers of such materials the cleavage is easy. Due to their 3D crystal lattice TiO_2 anatase single crystals are more difficult to cleave but still cleavage in the [100] and [011] directions is possible. While rutile crystals were already *in situ* cleaved by Bondarchuk et al.,[97] this was not reported for anatase crystals yet. Successful *ex situ* cleavage of anatase (101) was already demonstrated by Dulub et al.[98] The naturally grown single crystal used in this work have about edge lengths of 3 to 10 mm. After cleavage the surface appeared smooth by eye.

Figure 4.1 shows a sketch of the cleavage process. First the single crystal is positioned on the sample holder with the (101) surface pointing upwards and glued onto it with silver containing, conductive epoxy adhesive. In the beginning the (101) surface was determined by Laue spectroscopy, later, this was possible by a proper look on the crystal shape. When the epoxy was cured, a notch of about 1 mm depth was sawed in parallel to the (101) surface into the crystal. For sawing, a diamond wire saw was used (Fig. 4.1a). The notch improves the later cleaving process. Inside the UHV system the crystal was transferred into the cleavage chamber and positioned under the opened UHV pliers. The pliers were attached to an x-y-z manipulator and positioned at the crystal to perform the cleavage and then closed

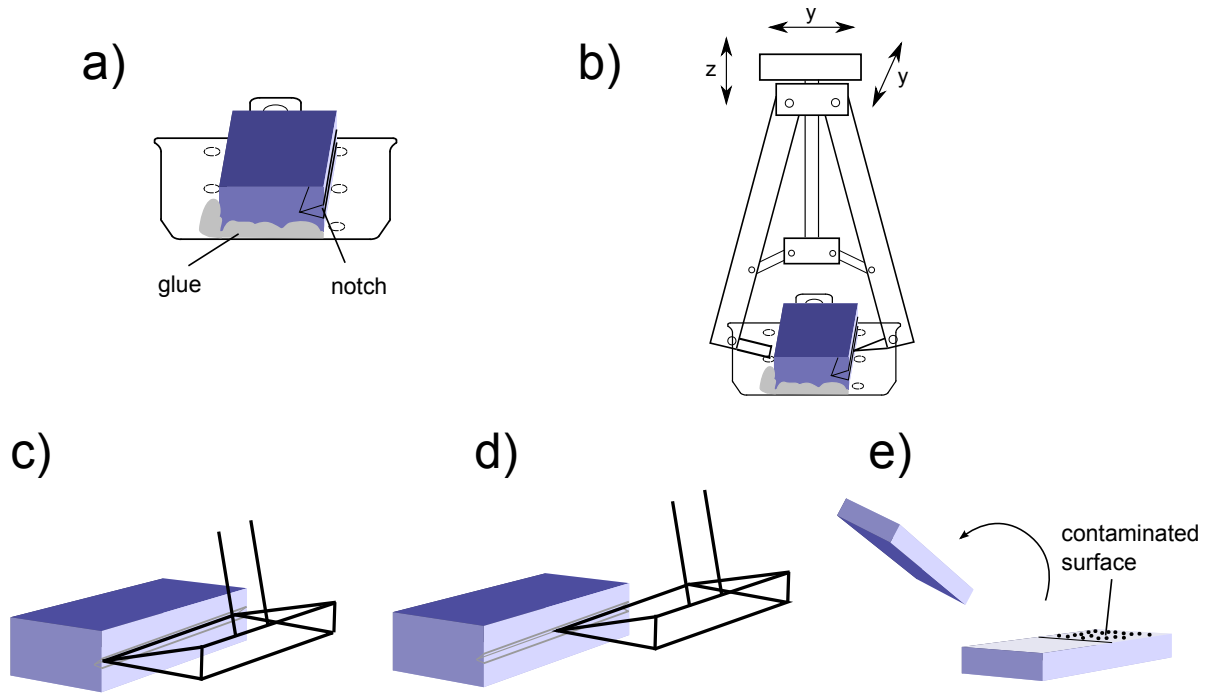

Figure 4.1. – Cleavage of an anatase single crystal: a) The crystal is glued with conductive Ag epoxy adhesive onto the sample holder and a notch is sawed into the crystal. b) The sample holder is positioned under the UHV pliers and the pliers are closed to cleave the crystal. To obtain a surface free of carbon contaminations the pliers are positioned not over the whole length of the crystal (c), but only till half of the crystal length (d). By this procedure a surface free of any contamination could be obtained (e). In this work, a clean anatase (101) surface was obtained by this method, but this method should enable to obtain as well other anatase surfaces, like the (100) surface.

(Fig. 4.1b). Despite successful cleavage of the anatase crystal, XP spectra of crystal surfaces still showed some amount of carbon. This contamination probably arises as the pliers are grazing over the surface, if the pliers are closing during the cleavage. This was avoided by positioning the pliers not over the complete length of the crystal (like in Fig. 4.1c)), but by positioning the pliers just till the half of the crystal length (like in Fig. 4.1d)). Despite the different aligning of the pliers, the crystal cleaved over the complete length. This resulted in a (101) surface, which showed carbon contaminations on one half, but was completely XPS clean on the other part of the crystal (like depicted in Fig. 4.1e)). Due to time limitations it was not possible to test this method also on the (100) surface of anatase.

4.2 Atomic layer deposition

All TiO_x and AZO films were deposited by atomic layer deposition (ALD), by our cooperation partner of the Bergische Universität Wuppertal. A brief introduction will be given here.

ALD was first carried out by Aleskovski in the 1960s and further developed by Suntola in the 1970s.[99,100] It is a variation of the much older technology of chemical vapor deposition (CVD).[101] ALD uses the fact that in a vacuum chamber a monolayer of a reactive gas retains on a substrate even if the gas is evacuated from vacuum chamber. When the first monolayer is exposed to an appropriate second reactive gas, a chemical reaction takes place, whose products form a solid monolayer of the

reagents. A repetition of this process allows a monolayer by monolayer film growth and therefore an outstanding control of the layer thickness, especially of only nanometers thick layers, and the deposition of homogeneous and uniform layers.[99] A further advantage is the possibility of alternating depositions of different materials, which was used in the case of the AZO films. A disadvantage of ALD are the general low deposition rates compared to a PVD process like evaporation or sputtering.

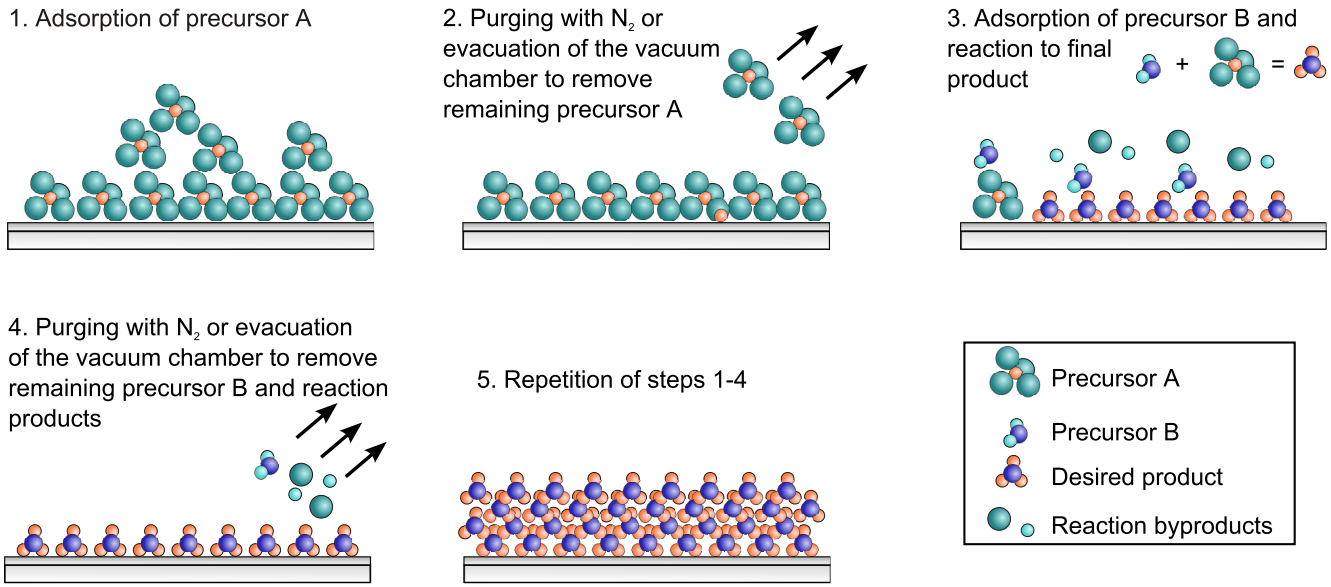

Figure 4.2. – Sketch of the atomic layer deposition (ALD) cycles. Adapted from Ref. [102].

A typical ALD preparation cycle is depicted in Fig. 4.2. First precursor A is let in to the vacuum chamber and a monolayer of the precursor attaches on to the substrate (step 1). To remove additional precursor species remaining on the substrate and the reaction chamber, the vacuum chamber is purged with an inert gas like N_2 and/or the vacuum chamber is evacuated. A single monolayer of precursor A remains on the surface (step 2). Then the second precursor B is introduced into the chamber and reacts with precursor A to the desired reaction product (step 3). Reaction byproducts in the gas phase or on the substrate are removed again by purging and/or an evacuation process and a monolayer of the desired material remains on the surface (step 4). Step 1 to 4 are repeated till the required layer thickness is reached (step 5).

In this work TiO_x was prepared from the precursors titanium isopropoxide and water at a substrate temperature of 80 °C. Al doped ZnO (AZO) layers were prepared as a nanolaminate consisting of a repeated deposition of 50 cycles ZnO and 2 cycles Al_2O_3. For ZnO diethyl zinc and water were used as precursors and for Al_2O_3 trimethylaluminium (TMA).[15] For AZO the substrate temperature was varied between 80 to 150 °C. For TiO_x and AZO the layer thickness was varied between 40 to 80 nm. The ALD deposition took place in a Beneq TFS 200 ALD reactor.

4.3 Physical vapor deposition

The C_{60} molecules were deposited under UHV conditions by physical vapor deposition (PVD) onto the various substrates. The deposition under UHV conditions strongly diminishes possible chemical

reactions of the evaporant and residual gas and therefore reduces impurities in the deposited layer. Furthermore the deposition rate increases as collisions with gas molecules are reduced and the mean free path of the evaporant increases.[103]

C_{60} was thermally evaporated from homemade effusion cells. The effusion cell was preheated about 1 h before the substrate was positioned in front of it. The effusion cells consist of an Al_2O_3 crucible, which is wrapped with tantalum heating wire. The tantalum wire is insulated with Al_2O_3 tubes. For the temperature control a nickel/chrome-nickel thermocouple was used, which was attached outside at the top of the Al_2O_3 crucible. A calibration with a second thermocouple inside the crucible showed, that the temperature is about 15-20 °C higher inside the crucible, than outside of the crucible.[104] Both, the tantalum wire and the thermocouple, were attached by a UHV feedthrough to the power supply and the thermometer.

4.4 UV illumination, oxygen exposure and adsorption of water

For the *in situ* UV illumination of the substrate materials with and without C_{60} on top of it, the sample was irradiated in UHV with a self-constructed UV lamp through a UV transparent MgF_2 window. The used UV LED emits a wavelength of 365 nm and has 11 W.[105] The UV light was focused with a lens in front of the LED. The UV light spot was covering the whole sample (sample size about 1 cm^2, LED spot about 2 cm^2)
Oxygen exposure was conducted in the MBE (see Fig. 4.3 left) or in a load lock by connecting an oxygen gas bottle to the venting valve.
Water adsorption on *in situ* cleaved anatase was performed at the SoLiAS endstation located at Bessy II in Berlin (see Fig. 4.3 right). At the SoLiAS the manipulator connects the analysis and the adsorption chamber. Furthermore the manipulator can be cooled by liquid nitrogen (LN_2) to cryogenic temperatures. For the water adsorption experiment, the cooled sample was transferred from the analysis chamber to the adsorption chamber and exposed to ultra clean water by opening a leak valve. The quantity of water was determined by the exposure time and pressure. Subsequently the sample on the manipulator was moved again to the analysis chamber and measured by XPS.

4.5 UHV systems

The experiments in this work were performed at the Daisy-Fun (**Da**rmstadt **I**ntegrated **Sy**stems for **Fun**damental Research) UHV system and at the SoLiAS (**So**lid/**Li**quid **A**nalyzing **S**ystem) located at the Synchrotron BESSY II in Berlin.

4.5.1 Daisy-Fun

The Daisy-Fun is located in Darmstadt and consists of three analyzing chambers, two load locks and several preparation chambers (see Fig. 4.3 left). The base pressure in all chambers is between 10^{-9} to 10^{-10} mbar.
The X-ray source used for photoemission has a silver and an aluminum anode, with characteristic

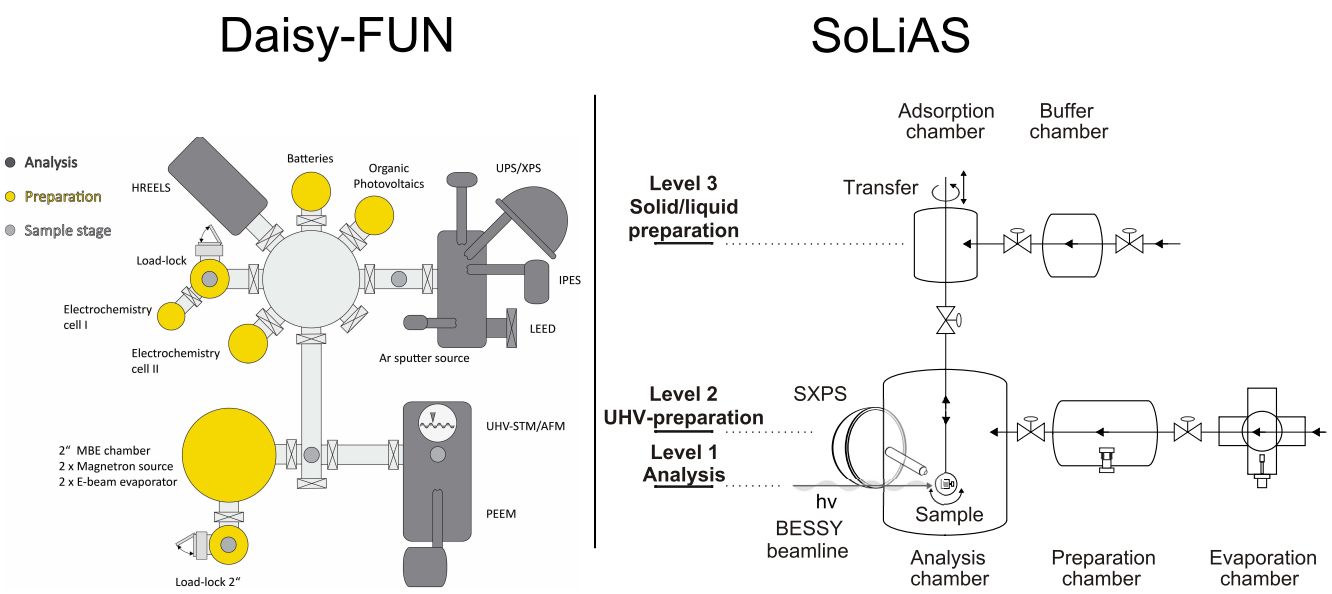

Figure 4.3. – Left: Sketch of the Daisy-Fun system in Darmstadt. Right: Sketch of the SoLiAS system situated at the synchrotron Bessy II in Berlin.

monochromatic excitation energies of 2984.3 eV for $Ag_{L\alpha}$ and 1486.6 eV for $Al_{K\alpha}$. Furthermore a Helium discharge lamp is attached to the chamber, which can emit photon energies of 21.2 eV (HeI) and 40.8 eV (HeII). For the detection of the photoelectrons a Phoibos 150 hemispherical electron energy analyzer from Specs is used. The energetic resolution of the Daisy-Fun is determined by the *fwhm* (20 to 80 %) of the Fermi edge of a clean (sputtered) silver foil. The resolution is for XPS($Al_{K\alpha}$)~0.35 eV and for UPS(HeI)~0.1 eV. The fit and the respective *fwhm* is directly determined by the SpecLab software used for recording of the photoemission spectra.
Additional to the photoemission system, equipment for inverse photoemission (electron gun and light detector), a LEED system and an argon sputter gun is attached to this chamber. For C_{60} deposition and UV illumination the organic photovoltaic chamber was used. Oxygen exposure took place either in the load-lock or in the MBE chamber.

4.5.2 SoLiAS

The SoLiAS system is located at the Synchrotron BESSY II in Berlin. The PES measurements performed in this work were performed at the U49-2/PGM-2 and the TGM-7 beamline. The U49-2/PGM-2 is a undulator beamline and provides photon energies from 90 eV to 1900 eV.[106] The TGM-7 is a dipole beamline and provides electrons with an energy of 8 eV to 120 eV.[107] The energetic resolution of the SoLiAS is determined by the *fwhm* (20 to 80 %) of the Fermi edge of a clean (sputtered) silver foil. The resolution is between 0.1 eV and 0.15 eV for excitation energies between 90 and 600 eV. The fit and the respective *fwhm* is directly determined by the SpecLab software used for recording of the spectra.

A scheme of the SoLiAS system is depicted in Fig. 4.3. The SoLiAS system is equipped with a Phoibos 150 analyzer (as the Daisy-Fun). The manipulator can be cooled with liquid nitrogen temperature (77 K). This allows the adsorption of water or solubles on the sample in the adsorption chamber and

the measurement with PES. C_{60} evaporation took place in the evaporation chamber and the pliers for cleaving were attached to the preparation chamber.

5 Methods

5.1 Photoelectron spectroscopy

Photoelectron spectroscopy (PES) is a non-destructive and surface sensitive method to investigate the chemical composition and the electronic structure of a material. It is based on the phenomena of the photoelectric effect, which was first observed by Hertz et al. in 1887[108] and first described quantum mechanically by Einstein in 1905.[109] The general setup of a photoemission spectrometer is depicted in Fig. 5.1. It consists of a radiation source, the sample, a photoelectron analyzer and a detector.

5.1.1 Working principle

The photoemission (PE) process describes a process, when a sample (solid or gas) is irradiated by a radiation source and electrons are excited above E_{Vac} and leave the sample with a certain kinetic energy (E_{Kin}). The electron has to overcome its own binding energy, which is its energetic distance to the Fermi energy (E_F) and the work function of the sample (Φ_s), which is the distance from E_F to E_{Vac}. E_{Kin} then depends on the energy of the incident photons, as all its energy is transmitted to the absorbing electron. This relation is shown in Eq. (1.1):

$$E_{Kin} = h\nu - E_{Bin} - \Phi_s \tag{1.1}$$

The photoemitted electron is called photoelectron and its kinetic energy can be detected by a spectrometer. On the way to the spectrometer the photoelectron has to overcome the potential difference Φ_s and the work function of the spectrometer Φ_{spec}. The spectrometer is in electrical contact with the sample and therefore the Fermi levels of the sample and spectrometer are equalized. As the work function of

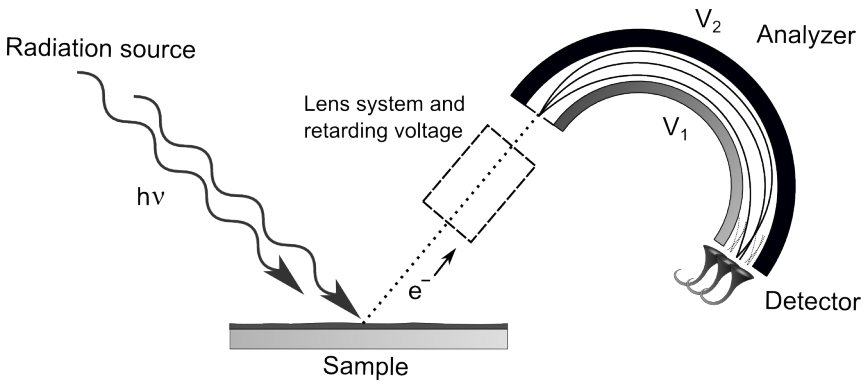

Figure 5.1. – Schematic setup for photoemission experiments including a radiation source, a sample, a system of focusing lenses (including a retarding voltage), an analyzer and a detector. Taken from Ref. [24].

the spectrometer Φ_{spec} is known, Eq. (1.1) can be rewritten to Eq. (1.2) and E_{Kin} becomes independent of work function of the sample Φ_s.

$$E_{Kin} = h\nu - E_{Bin} - \Phi_s + (\Phi_s - \Phi_{spec}) = h\nu - E_{Bin} - \Phi_{spec} \tag{1.2}$$

If photoelectrons leave the sample without any energetic losses peaks appear at distinct binding energy positions characteristic for different orbitals and elements. Binding energy values for each element and orbital are summarized in Ref. [110]. To determine the exact binding energy, a metal, like e.g. Ag, is measured and the position of the Fermi edge is determined. The kinetic energy position of E_F equals the kinetic energy of the exciting photons. The whole photoemission process taking place in the sample and the transfer to the detector is depicted in Fig. 5.2.

$$E_{Bin} = h\nu - E_{Kin} - \Phi_{spec} \tag{1.3}$$

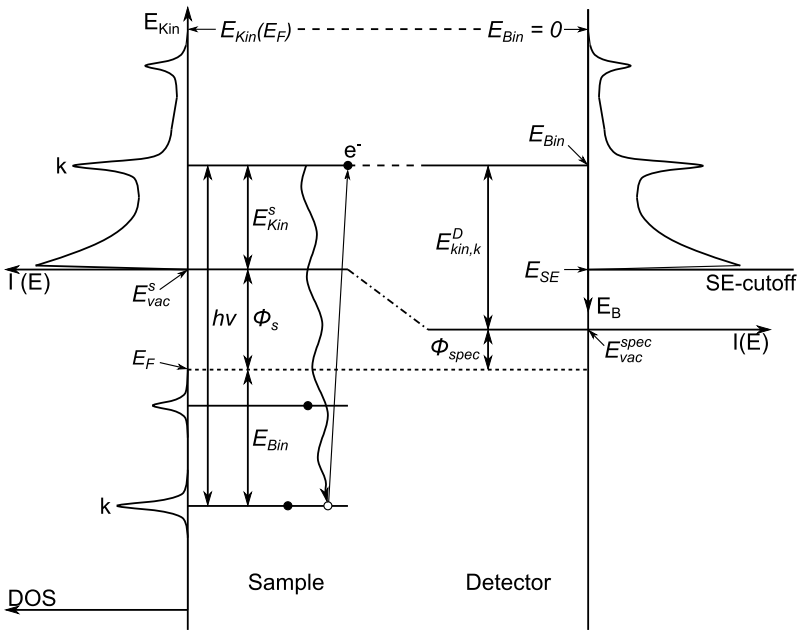

Figure 5.2. – Schematic illustration of the photoemission process within the sample and the transfer of the photoelectron to the detector. Detector and sample are in contact and their E_F position is equal. As Φ_{spec} is known, Φ_s is not needed to transfer the kinetic energy spectrum to a binding energy spectrum. The kinetic energy of the SE-cutoff equals the work function of the sample. The spectrum is a superposition of elastic scattered photo- and Auger electrons and a continuous background of inelastic scattered secondary electrons.[111] Adapted from Ref. [112].

Besides photoelectrons also Auger electrons can be excited during a photoemission process. An Auger electron occurs if the photohole, which forms due photoelectron emission, is occupied by an electron of an upper shell. The energy release during this drop may be high enough to excite another electron above E_{Vac}, which then is emitted from the sample. In contrast to the kinetic energy of photoelectrons the kinetic energy of Auger electrons is independent of the excitation energy $h\nu$. By varying the excitation

energy Auger and photoelectrons can easily be distinguished.
Furthermore secondary electrons occur if photoelectrons with high kinetic energy loose energy due to scattering processes. Secondary electron emission intensity increases strongly with decreasing E_{Kin} till its intensity abruptly drops at the secondary electron cutoff (see Fig. 5.2). The secondary electron cutoff is equal to the WF of the sample. It describes the point, where the secondary electrons just have enough energy to reach E_{Vac}. Further background electrons due to inelastic scattering appear at emission lines and add up to secondary electron emission. This results usually in a higher background at the high binding energy side of a core level emission.

5.1.2 Radiation sources

In this work $Al_{K\alpha}$ X-rays, a Helium discharge lamp and synchrotron radiation are used as radiation sources to obtain PE spectra. To produce $Al_{K\alpha}$ X-rays electrons are accelerated under UHV conditions from a cathode onto an Aluminum anode. The anode then emits its characteristics X-ray spectrum. To obtain a high resolution photoemission spectra, Al X-rays are monochromatized with a crystal monochromator that only transmits $Al_{K\alpha}$ X-rays. By varying the anode material and the settings of the monochromator different excitations energies can be produced.
A gas discharge lamp in general consist of a cathode and an anode. By applying a potential difference between the electrodes, a gas, in this case helium, is ionized. The electromagnetic spectrum of Helium plasma consists of several emissions and the ratio among them can be varied by changing the gas pressure and the currents between the electrodes. This way, HeI (21.2 eV) and HeII (40.8 eV) radiation can be produced. By using different gases like Neon the excitation energy can be varied as well.[111]
Synchrotron radiation forms when ions are deflected from straight propagation. The radiation is emitted tangential to the deflection of the ions. Synchrotron radiation is electromagnetic and covers a broad spectrum from microwaves (0.001 eV) to hard X-rays (up to 10 keV). A modern synchrotron, as Bessy II[1], accelerates electrons almost to speed of light and forces them to move in a circle. By using undulators, the electrons are forced to sinus like oscillations and the synchrotron radiation is emitted along the average direction of flight of the electrons. By varying the wavelength of the periodic motion of the electrons and the strength of the magnetic field, the wavelength of the emitted electromagnetic radiation can be adjusted. Characteristic for synchrotron sources is the possibility to select between a wide range of photon energies, the high photon flux and a high brilliance, which describes the amount of photons per second, solid angel and radiated area.

For the conducted experiments in this work, the easy variation between different photon energies at a synchrotron is the most relevant one. By varying the photon energies the mean free path of the photoelectrons in a solid and the information depth of the photoemission experiments can be tuned. In Fig. 5.3 the mean free path λ_e of the photoelectrons is plotted vs. their kinetic energy. The minimum of λ_e is about 5 Å at a kinetic energy of ~50 eV. The mean free path increases at kinetic energies lower or higher than 50 eV. At energies above 50 eV the higher kinetic energies cause a higher escape depth of the electrons and the mean free path is mainly determined by electron interactions. This means inelastic

[1] Parts of the following experiments were performed at Bessy II.

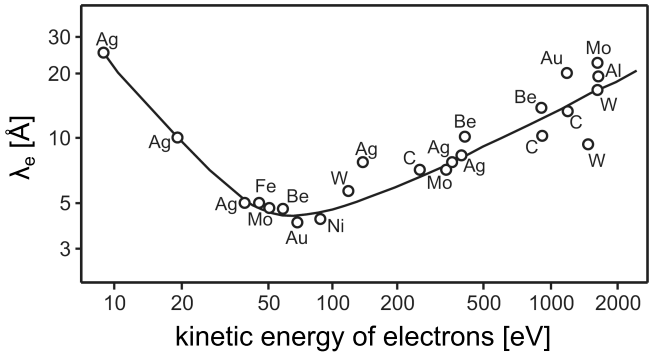

Figure 5.3. – Experimental data of the inelastic mean free path of electrons in dependence of their kinetic energy. The curve is a fit and is also called *bathtub curve*. Adapted from [24]

scattering at other electrons and the excitation of plasmons. At lower kinetic energies elastic scattering takes place, which leads to higher escape depth.[113]
Besides the mean free path of the photoelectrons also the cross section of each atomic orbital of each element varies with the photon energy. The cross section is the probability for a photoionization process at a given photon energy. Usually the cross section of photoelectrons increases with decreasing photon energies. Sometimes several photoionization channels can exist, which have different ionization probabilities. The different photoionization processes sum up, which can cause an amplification or an attenuation of the signal. In resonant photoemission (see Section 5.1.6) such an amplification takes place.[114]

5.1.3 Analyzer

The photoelectrons are detected energy-dispersive with the analyzer (see Fig. 5.1). Only photoelectrons with the certain adjustable energy, the pass energy E_{Pass}, pass through the analyzer. Before the photoelectrons enter the analyzer the photoelectrons are focused with a lens system and pass through a retarding voltage. The analyzer consists of two concentric hemispheres with a gap in between for the passing electrons. Between the hemispheres a voltage is applied, that only electrons with E_{Pass} can pass the analyzer. The constant E_{Pass} ensures an equally good resolution of the whole energetic spectrum. After leaving the hemispheres, electrons are detected with channeltrons, which amplify the signal.

5.1.4 Information contained in PES spectra

Layer thickness

PES enables the determination of layer thicknesses below the escape depth of photoelectrons, hence till about 10 nm. If a substrate is homogeneously covered with an adsorbate, photoelectrons of the substrate have to travel a through the adsorbate and their quantity decreases exponentially with the adsorbate layer thickness. For a homogeneous layer coverage the thickness can be calculated with Eq. (1.4), where I^0_{sub} is the intensity of a substrate emission line, I^d_{sub} the intensity of covered substrate emission line θ is the angle between the sample surface and the analyzer, λ_e the mean free path of the photoelectron in the adsorbate, and d the layer thickness of the adsorbate. The mean free path of photoelectrons is different

for different materials and can be calculated by the software "NIST Electrons Inelastic-Mean-Free-Path Database".[115] In the following interface experiments layer thicknesses were calculated by Eq. (1.4) and λ_e was calculated using the NIST software and the method of Gries.[116]

$$\frac{I_{sub}^{d}}{I_{sub}^{0}} = \exp - \left(\frac{d}{\lambda(e) \cdot \cos\theta} \right) \tag{1.4}$$

Stoichiometry

Moreover the stoichiometry can be calculated from the intensity ratios of the photoelectrons emissions. The recorded intensity of the photoelectron emission of a certain orbital depends on one hand on the amount of the specific element and in addition on the probability of the photoionization process, the cross section σ_{pi} and on the instrumental setup. Influences of the instrumental setup are given by a variation of the detection efficiency as a function of the kinetic energy, the angular dependence of the photoelectron emission, the analyzer transmission function, the mean free path of the photoelectrons (depends on the excitation energy) and the angle between analyzer and sample. All these factors, instrumental and the photoionization cross section σ_{pi} are included in the atomic sensitivity factor (ASF), which is specific for every instrumental setup, element and orbital. Thus, by using Eq. (1.5) the stoichiometry of a sample can be calculated.

$$\frac{n_A}{n_B} = \frac{I_A \cdot ASF_B}{I_B \cdot ASF_A} \tag{1.5}$$

5.1.5 Initial state and final state effects

In photoemission initial state effects and final state effects can influence the energetic position or width of an emission line. Initial state effects describe effects, which occur before and independent of the photoemission process. Final state effects occur after the photoionization process and have its origin in the formation of a photohole after photoelectron creation.

Initial state effects

Chemical shift: The chemical shift is an initial state effect and occurs if the electron charge density surrounding a nucleus is de- or increased. Such change of the electron charge density changes the static field each electron is experiencing. A change of the electron charge density can e.g. be caused by a change of the atomic oxidation state. If an electron is removed from the atom, the overall coulomb attraction of the positive nucleus to each electron increases and hence the electrons are bounded stronger to the nucleus. The energy to remove the electron and to form a photoelectron increases, thus the binding energy increases. In the case of adding an extra electron the binding energy of the electrons decreases. Another cause for a chemical shift can be a change of the chemical environment of an atom. This could be for example due to a morphology change of a crystal, while the stoichiometry stays the same. For ionic crystals, like TiO_2, the Madelung potential is used to describe the electrostatic potential of a single ion in a crystal.

Final state effects

Spin-orbit coupling and spin-spin coupling: Spin-orbit coupling describes the interaction of the angular momentum l of an electron and its spin s. Spin-orbit coupling causes a line splitting of the emission lines. In completely occupied atomic orbital spins are antiparallel, which results in a net spin $s = 0$. If one electrons is removed, the left-behind electron has a spin of $s = \pm 1/2$ and couples with the angular momentum of l, if $l \neq 0$. The resulting total angular momentum j is defined by $j = l \pm s$. The intensity ratio of the two resulting emissions is determined by the degeneracy of those final state, given by $2j + 1$. In the case of the Ti 2p orbital ($l = 1$) the unpaired electron has a total angular momentum j of $1/2$ and $3/2$. This result in an intensity ratio of 1:2.
Furthermore spin-spin coupling can exists, when unpaired electrons in the valence shell of an element are present. Then the unpaired electron and the total spin of the valence shell can couple.[117,118]

Plasmon excitation: Plasmons are collective excitations of the free electron gas. They occur when conduction electrons either screen a photohole and excite a plasmon or if the photoelectron interacts with the free electron gas.

Electron shake-up and Electron shake-off: Electron shake-ups and shake-offs happen if the photoelectron excites a second electron into an unoccupied state (shake-up) or above E_{Vac}, i.e. it is ejected from the sample (shake-off). A typical shake-up process is e.g. the excitation of a valence electrons across the energy gap into an unoccupied state. As shake-up and shake-off processes result in a loss of the kinetic energy of the photoelectron, they appear at higher binding energies.

5.1.6 Resonant photoemission

Resonant photoemission (RESPES) enables to de- or increase the intensity of certain parts of the photoemission spectrum. With the right choice of the excitation energy the total emission can be maximized by resonant transitions from the Ti 2p or Ti 3p orbital to the Ti 3d or the Ti 4sp orbital.
Figure 5.4 shows an illustration of the resonant photoemission process of the Ti 3p to Ti 3d transition. Resonant photoemission occurs, when a core level is excited with an energy near the adsorption threshold of the core level. The core electron is excited into an unoccupied state and then relaxes back into an unoccupied state (intermediate state). The energy the electron releases during falling back excites another electron from the valence band (final state). This causes additional emissions from the VB, which are overlapping with the photoelectrons from the direct photoemission process. The intensity of the overlap of both of this processes as function of the excitation energy is given by a Fano line shape. Figure 5.5 shows the resonant behavior of deep gap states in amorphous TiO_x. On the right a Fano profile (red) is added to a constant initial state (CIS) spectrum related to the emission intensity of a deep gap states (DGS), (where w describes the line width of the resonant energy and q the asymmetry of the Fano profile). The results of Fig. 5.5 are discussed in more detail in Section 17.2. The resonant process is a special case of an Auger process and is called a Super Coster-Kronig transition. While a classic Auger process describes an electron emission from another subshell of the same atom, a Coster-Kronig transition describes a process, where the primary hole is filled from a higher subshell. If the emitted electrons of the Auger transitions are on the same shell as well, it is called a Super Coster-Kronig transition.

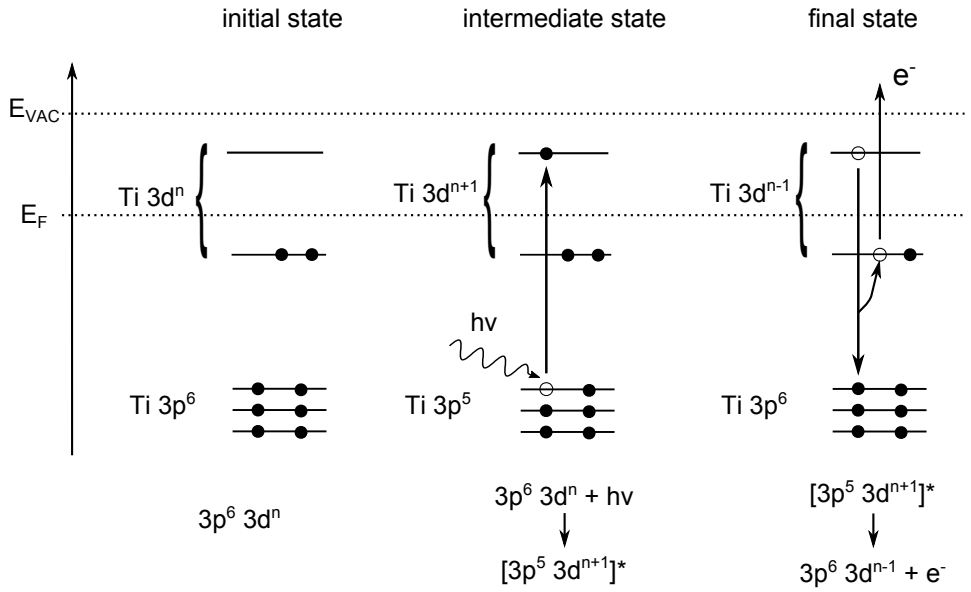

Figure 5.4. – Resonant photoemission process using the example of the $Ti\,3p \rightarrow Ti\,3d$. Left: Initial state of the $Ti\,3p$ and $Ti\,3d$ level. Middle: Intermediate state - a $Ti\,3p$ electron is excited into a $Ti\,3d$ state. Right: Final state, the excited electron falls back into the $Ti\,3p$ state and the released energy causes the excitation of a photoelectron from the valence band.

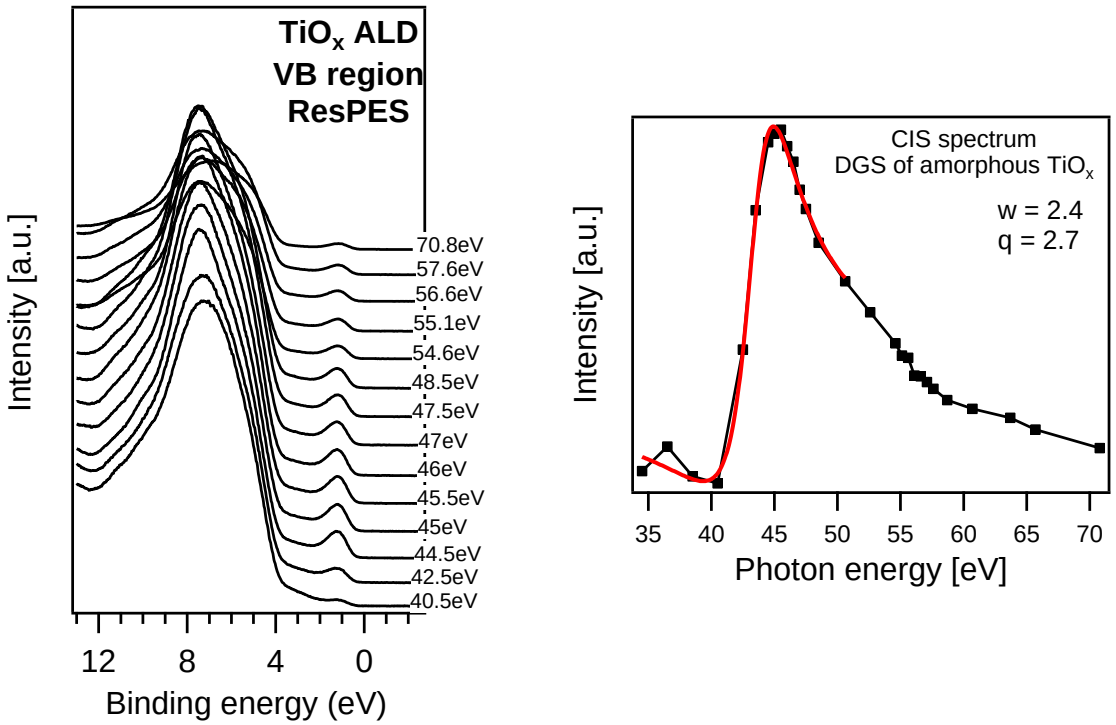

Figure 5.5. – Left: Valence band (VB) spectra of amorphous TiO_x prepared by ALD. The deep gap state (DGS) emission around 1 eV binding energy increases at photon energies around 45 eV. On the right the constant initial state (CIS) spectrum of the DGS emission is depicted and a Fano profile is added (red). These spectra are further discussed in Section 17.2.

5.2 Low energy electron diffraction

Low energy electron diffraction (LEED) is a standard method to determine the surface structure of crystalline materials and was first used in 1927 by Davisson and Germer.[119] To obtain a LEED diffraction pattern, a low energy electron beam with a fixed energy is focused on to a sample surface and the diffraction pattern of reflected electrons is reproduced on a fluorescent screen. Electron energies are usually between 20 and 500 eV,[120] which corresponds to a wave length of about 1 to 4 Å (calculated by the de-Broglie equation $\lambda = \frac{h}{mv}$[121]), which is in the range of the atomic distance of solids. The resulting diffraction pattern of the reflected electrons permits conclusions about the crystal symmetry in the range of the escape depth of the reflected electrons. The surface sensitivity of LEED is about twice as high as from photoemission (see Fig. 5.3), hence sharp LEED reflexes can be only obtained on very clean sample surfaces.

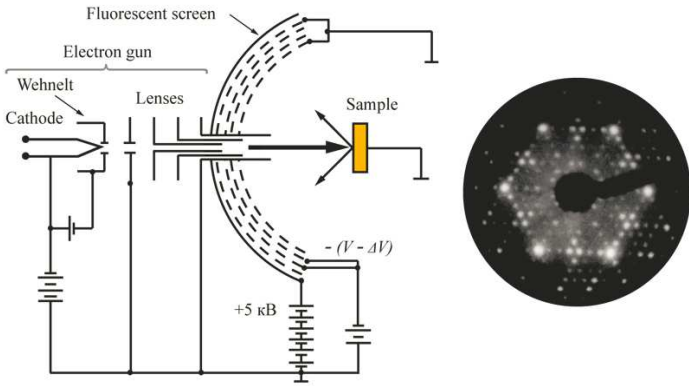

Figure 5.6. – Left: Schematic diagram of a standard four-grid LEED set-up (left) and LEED pattern of a Si(111)7×7 surface. Taken from Ref. [111].

In Fig. 5.6 a schematic drawing of the typical LEED setup is shown. Electrons are emitted from the cathode and focused by the Wehnelt cylinder and an electro-optical system. The electrons hit the sample at 90° and the backscattered electrons pass a system of three hemispherical concentric grids before impinging on the collector (fluorescent screen). The first grid is grounded as is the crystal, to obtain a field free region between the sample and the first grid. The second grid is at a negative potential compared to the first grid, which therefore repels inelastically scattered electrons. The third grid is at the same potential as the second grid, and improves the LEED pattern. LEED spots appear, when the diffracted electrons at the atomic planes interfere constructively and their pattern shows the reciprocal lattice of the surface. By increasing the electron beam energy the penetration depth of electrons increases and diffraction at more atomic planes inside the crystal takes place. As a result the LEED pattern includes more spots.[122]

5.3 X-ray diffraction methods

X-ray diffraction (XRD) is based on the diffraction of X-rays at ordered structures in crystalline materials. It is a non-destructive method to determine the structure of crystalline materials. It is based on the

Huygens-Fresnel principle, which says that every point reached by a wave front is the starting point of a secondary wave front with the same frequency and wavelength as the primary wave. In the case of XRD atoms are equivalent to points. The wavelength of X-rays is about 0.25 nm to 1 nm and therefore in the region of the spacing between the atomic planes.[123]
The foundation of XRD is the Bragg law (Eq. (3.6)). It describes the effect of the coherent and incoherent scattering of the incident X-rays under a certain angle θ and links the distance of the atomic planes d_{hkl}, the diffraction angle θ (between the atomic plane and the incident X-rays) and the wavelength λ of the X-ray source. n is an integral multiple of the wavelength.[124]

$$n\lambda = 2d_{hkl}sin\theta \tag{3.6}$$

Figure 5.7 shows the geometric description of the Bragg law. In dependence of incident angle θ of the X-ray the path difference δ of the two incident waves matches or not matches an integer of the wavelength and constructive or nonconstructive interference occurs. Hence constructive or deconstructive interference at a certain incident angle depends on the distance of the atomic planes. Thus the angles where reflexes appear enabls the determination of the crystal phase and the orientation of the crystal.[123]

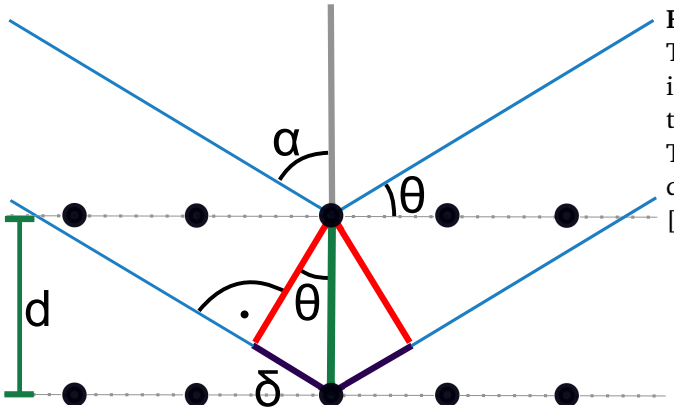

Figure 5.7 – Geometric illustration of the Bragg law. The blue lines represent the electromagnetic radiation incident on the crystal surface with a given angle α. θ is the complementary angle to α and is called Bragg angle. The distance between the atomic planes is d. The path difference 2δ is given by $2 \cdot \sin\theta$. Adapted from Ref. [125].

In general it is distinguished between X-ray diffractions methods for single crystalline and polycrystalline materials. For single crystals, e.g. Laue diffraction is used, while polycrystalline materials, are measured either in Bragg-Brentano geometry (reflection) or Debye Scherrer geometry (transmission). In this work Laue diffraction was used to determine the orientation of the cleaved anatase surface. For the determination of the crystalline phase of the ALD prepared TiO_x and AZO films, X-ray powder diffraction in the Bragg-Brentano geometry was used.

5.3.1 Laue diffraction

The Laue method is the oldest of all X-ray diffraction methods. It uses a continues (non-monochromatic) light source and usually uses the bremsstrahlung of the X-ray anode (in this case an Ag X-ray source), which is collimated and focused on a fixed crystal surface. If the Bragg law is satisfied a reflected beam is produced and recorded with a CCD image plate. As a non-monochromatic source is used, the different spots origin from different wavelengths and several planes can satisfy the Bragg law at the same time. Therefore Laue diffraction is faster compared to other X-ray diffraction methods with monochromatic

light sources. By using the free software "Cologne Laue Indexation Program" (CLIP)[126] Laue diffraction patterns for crystal surfaces can be simulated. By comparing the simulated pattern, with the recorded one, the orientation of the crystal surface can be determined.[127]

5.3.2 X-ray powder diffraction

To determine the crystal structure of a powder or polycrystalline films, X-ray powder diffraction is used. As the crystallites are statically distributed, it is not necessary to rotate the single crystal in every direction. To improve the statistics, the crystal is usually rotated in plane. In a typical powder diffraction pattern, the intensity is plotted against 2θ. From the position of the reflexes the crystal structure can be determined. The relative intensity of the reflexes allows determination of a texturing of the films and the *fwhm* of the reflexes allows the determination of the average crystallite sizes by applying the Debye-Scherrer equation:[128]

$$\tau = \frac{K\lambda}{\beta \cos(\theta)} \tag{3.7}$$

,where τ is the average size of the crystallites, K the shape factor of the crystallites, β the instrumental broadening, θ the Bragg angle and λ the wavelength of the X-rays.

5.4 Scanning electron microscopy

Scanning electron microscopy (SEM) is a method to image the surface morphology of solid objects. In contrast to other imaging methods like atomic force microscopy (AFM), the sample has to be conductive or, if not, has to be coated with a thin electrically conductive material. In a scanning electron microscope, a focused electron beam with a typical energy of 0.2 to 40 keV is scanning in a raster over the surface of the sample.

The incident electrons (primary electrons, PE) interact elastically and inelastically with the electrons and the core of the sample atoms, which results in the emission of electromagnetic radiation from the sample surface (see Fig. 5.8). For the imaging of the surface topography, the secondary electrons (SE) are used. Secondary electrons arise from inelastic scattering of PE with valence electrons and have an energy below 50 eV. In principle secondary electrons are formed within the whole pear shaped interaction volume of scanning electron microscopy, but due to their low kinetic energy SE have only a escape depth of below 10 nm and hence, the imaging of the surface is possible (see bathtub curve in Fig. 5.3). Another interaction with the sample is the elastic backscattering of the primary electrons (backscattered electrons, BSE). The intensity of BSE depends mostly of the atomic number of the sample material (higher atomic number = higher BSE intensity) and enables an atomic number dependent mapping of the sample surface. BSE electrons have an escape depth of 0.1 to 1 μm. At the ionization of inner-shell electrons, an electron from a higher energy can fall into the vacancy, resulting in either the release of an Auger electron or the emission of a X-ray photon. The energy of the X-ray photon is characteristic for the specific element and can be used to determine the chemical composition of the sample. One distinguishes between energy dispersive X-ray spectroscopy (EDX) and wavelength-dispersive X-ray

spectroscopy (WDX). Compared to EDX, WDX shows a higher resolution and is about one magnitude more sensitive than EDX. Characteristic X-rays origin from up to 2 μm sample depth. Further emitted electromagnetic radiation results from fluorescence to cathodoluminescence.[129]

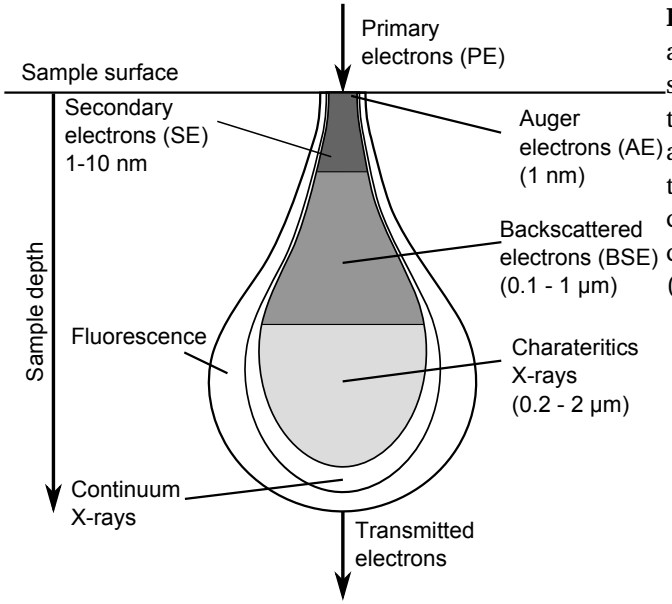

Figure 5.8 – Interactions of primary electrons (PE) with a solid. Secondary electrons are emitted from the near surface region only (10 nm) and are used to display the topography of the sample. Backscattered electrons allow a mapping of the surface (up to 1 μm) with respect of the atomic number of the elements of the sample and characteristics X-rays permit the determination of the chemical composition of the sample close to the surface (up to 2 μm). Adapted from Ref. [130].

5.5 Atomic force microscopy

The atomic force microscope (AFM) is a non-destructive method, which allows the determination of the surface topography of the sample surface even to an extend of atomic resolution. The principles of AFM are founded on the interactions of the measuring tip and the sample surface. In contrast to SEM (see Section 5.4) it is also possible to measure non-conductive surfaces and UHV conditions are not required. AFM was first introduced by Binning in 1986.[131]

Figure 5.9 left shows the setup of the AFM setup used in this work. It consists of a cantilever with a sharp tip (about 10-20 nm) at one end, which is screwed on a piezoelectric actuator. The actuator adjusts the height of the cantilever to the surface. Furthermore the sample is located on a piezoelectric actuator, which moves the sample underneath the tip and such enables the lateral measurement of the sample. The deflection of the cantilever is measured with an optical pointer. A laser beam is focused on the cantilever and a photodiode measures the reflection.

The interatomic force between the sample and tip causes a deflection of the cantilever. The interaction can be ascribed by the Lennard-Jones potential, which describes the interaction of neutral particles. At higher particle distances, van-der-Waals force causes an attraction between the particles, while at lower particle distances Pauli repulsion due to overlapping electron orbitals occurs. Due to the interaction of the measuring tip with the surface, the cantilever is bended and the strength of the displacement of the cantilever is used to determine the surface topography.

Figure 5.9 depicts the Lennard-Jones potential. At high distances (a few hundred nm) the tip is weakly deflected (green), getting closer to the surface van-der-Waals forces increase and cause a deflection of the cantilever (red). If the separation of the tip and sample becomes too small, tip and sample atoms

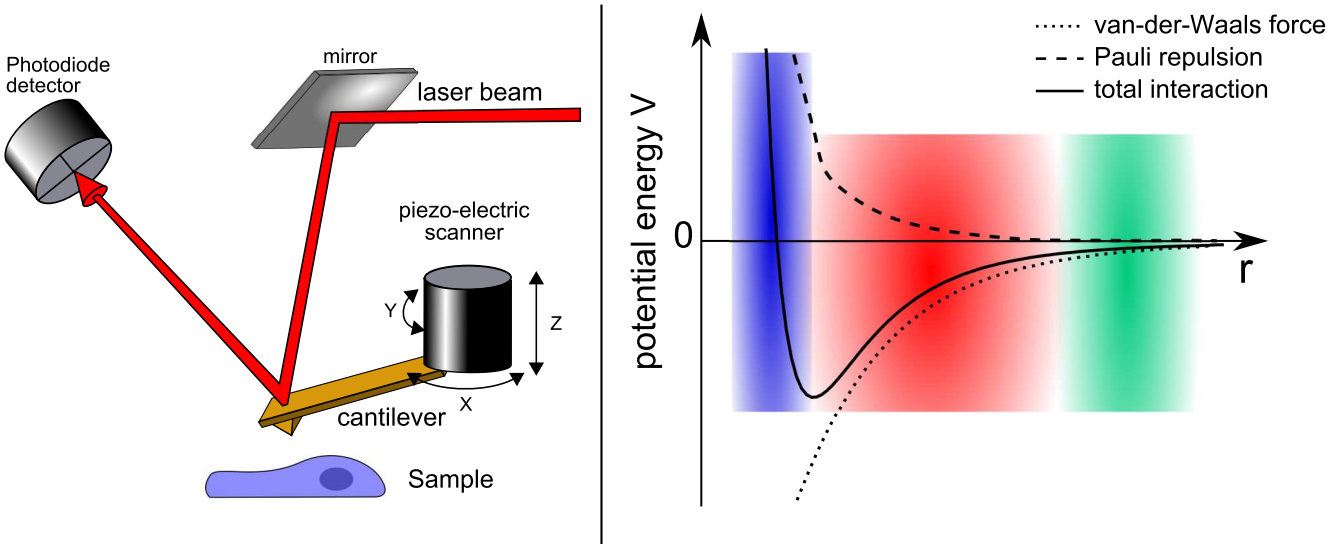

Figure 5.9. – Left: Sketch of an AFM. A piezo-electric scanner adjusts the height and the oscillation of the cantilever, while a photodiode measures the deflection of the cantilever. Right: Lennard-Jones potential, which describes the interaction of tip and the sample at certain distances.

repel and repulsive forces occur and the cantilever is pushed back (blue).[111]

The position of the tip relative to the surface defines the main imaging modes of an AFM:

- non-contact mode (red region)
- contact mode (blue region)
- tapping mode (both regions)

As the name already indicates, in contact mode the tip is touching the surface to image the surface. Regarding the Lennard-Jones potential, it is measured, which repulsive forces on the cantilever occur in dependence on the surface position. One distinguishes between *constant height mode* and *constant force mode*. In the case of constant height mode, the direct repulsive interaction is used as measuring signal. In the case of the constant force mode, the force on the cantilever is kept constant and a piezo crystal is used to change the height of the tip to obtain again the same force. The *constant height mode* is only suitable for smooth surface, while rougher surface should be measured in *constant force mode* instead.
The non-contact mode describes the process, where the cantilever is not touching the surface at all and only van-der-Waals forces occur. The cantilever oscillates at its resonant frequency and the van-der-Waals force is causing a damping of the oscillating cantilever and a feedback loop system maintains a constant oscillation frequency by varying the tip-to-sample distance. The non-contact mode is usually used to achieve true atomic resolution with the AFM.[131] As in the non-contact mode, sample and tip are not touching each other and a destruction of the cantilever is unlikely.
The third mode is the tapping mode and the most often used AFM mode. As the non-contact mode, the tapping mode uses attractive forces to image the surface. The cantilever is oscillating at frequencies slightly below it resonance frequency and its amplitude is up to 100 nm. In comparison to the non-contact mode, the tip may tap the surface at maximal deflection as it travels over the surface. A feedback loop system maintains a constant oscillation frequency by varying the tip-to-sample distance.[111,131]

5.6 Optical absorption spectroscopy

Optical absorption measurements are usually performed with an UV/Vis spectrometer and allow the determination of the energy gap of inorganic semiconducting materials. Due to the high exciton binding energy of organic semiconductors this is not possible for organic semiconductors.

In an UV-Vis spectrometer a sample of a certain thickness d is irradiated with electromagnetic radiation between 800 nm and 10 nm (UV-Vis). The electromagnetic radiation can be transmitted T, adsorbed A and reflected R. The transmission T is proportional to the thickness d of the sample. The relation between the intensity of the transmission T and the sample thickness d is given by the Beer-Lambert law (Eq. (6.8)). The Beer-Lambert law is also dependent on the specific adsorption coefficient, α_λ, of the respective material.

$$T = e^{-\alpha_\lambda \cdot d} \tag{6.8}$$

To determine the optical band gap of a semiconductor a Tauc plot is used.[132] At a Tauc plot, $(\alpha_\lambda h\nu)^{1/x}$ is plotted against the energy of light $h\nu$. The value x represents the nature of the transition occurring: For a direct transition x is 1/2 and for indirect transition x is 2.

6 Aim of this work

This work results from the joint DFG Project "Inverted organic solar cells" (MA 2104/2-2 and RI1551/4-2) by Prof. Thomas Riedl (Bergische Universität (BU) Wuppertal) and Dr. Thomas Mayer (Technische Universität (TU) Darmstadt). Thomas Riedl is professor of the chair of electronic devices at the department of Electrical Engineering, Information Technology and Media Technology of Bergische Universität (BU) Wuppertal. Among other electrical organic devices, the group of Thomas Riedl at BU Wuppertal is specialized in the manufacturing of inverted organic solar cell (IOSC) devices. One of their focuses is to deposit materials, which act as electron or hole transport layers in IOSC devices. The Surface Science group of the TU Darmstadt (Prof. Wolfram Jaegermann), focuses on the electronic properties of various semiconducting materials and, among others, has an in-depth knowledge of the investigation of metal and semiconductor surfaces and interfaces by photoemission spectroscopy.
This thesis is divided into two main parts. In the first part, the metal oxide/organic acceptor interface of inverted organic solar cells is investigated with regard to the influence of the metal oxide material and UV irradiation on the interface properties. In the second part a detailed study of defect states of the anatase (101) surface is performed.

Investigation on the origin of S-shaped I-V characteristics

As described in Section 2.5, IOSC devices with some specific ETL's exhibit S-shaped I-V characteristics.[15,71,133] Trost et al. observed that the S-shape of IOSC with TiO_x interlayers transforms into good diode characteristics after illumination of the IOSC device with UV light. Furthermore they observed, that IOSC devices with a ZnO ETL displays S-shaped I-V characteristics as well, which disappear after doping of the ZnO with Al_2O_3 (aluminum doped zinc oxide, **AZO**). Others, as Kuwabara et al. observed a transformation of S-shaped to diode like I-V characteristics upon using TiO_x, prepared at increased annealing temperatures, as ETL.[71] In order to clarify the origin of the S-shaped I-V curves, it shall be investigated, if the change of the I-V characteristics, by either changing the ETL or by illuminating with UV light, can be correlated with electronic interface contact properties of the ETL/organic interface in dependence of the ETL and/or UV irradiation.
All IOSCs manufactured from Sara Trost have a $PC_{61}BM$:P3HT blend as organic absorber, where the $PC_{61}BM$ forms the interface to the ETL.[134] As $PC_{61}BM$ cannot be evaporated without destruction[95] and a liquid preparation, e.g. by drop casting, leads to $PC_{61}BM$ layer thicknesses which are not sufficiently thin enough for the determination of an interface line-up,[24,104] C_{60} is used as model organic acceptor material. To investigate the comparability of $PC_{61}BM$ and C_{60} in terms of the interface formation to the ETL and electronic characteristics in IOSC devices, model experiments have to be performed. Interface experiments with TiO_x, AZO and annealed TiO_x will be conducted to check, if the energetic interface line-up differs for different ETL's. To determine the influence of UV light, interface experiment with UV illumination will also be conducted.

To investigate the origin of UV induced changes at the TiO_2/C_{60} interface, C_{60} deposition is performed on *in situ* and *ex situ* prepared TiO_2 interfaces and the influence of UV light on the respective interface is investigated. As surface preparation methods of TiO_2 like sputter annealing do not guarantee an adsorbate free surface,[135] a new preparation method to produce clean, adsorbate free TiO_2 surfaces is used. An anatase crystal is cleaved *in situ* with pliers, with the aim to achieve a clean surface without any pretreatment as sputter-annealing. By exposing the *in situ* cleaved crystal to UV light and different atmospheres like oxygen and air, the influence of adsorbates and UV on the TiO_x shall be investigated, to get further insight on the influence of UV illumination on the metal oxide/organic acceptor interface. From the gained results of the UV and adsorbate influence, energy diagrams are drawn to check if the energy level alignment explains the variations of I-V characteristics.

In depth investigation of defect states on the TiO_2 (101) surface

In order to obtain a clean, adsorbate free anatase TiO_2 (101) surface for the investigation of the ETL/organic interface in IOSC, a new preparation techniques for the (101) surface was developed. The anatase crystal was cleaved *in situ* with pliers. The new *in situ* preparation method enables the investigation of the anatase (101) surface without any further preparation processes like sputter annealing. Of special interest are gap states of TiO_x as they play a crucial role concerning charge transport in the bulk respectively across interfaces and for the catalytic activity as e.g. for water splitting. Hence an in depth analysis of defect states of the *in situ* cleaved anatase TiO_2 (101) surface by photoemission is performed and compared to other titania. To determine the origin of different gap states, differently prepared TiO_x/TiO_2 surfaces are investigated by SXPS and RESPES and the results are compared. Concerning a possible influence of water on the degradation of IOSC devices with TiO_2/TiO_x interfacial layers water is going to be adsorbed on the *in situ* cleaved, adsorbate free anatase (101) surface to gain information about water adsorption on (101) surface defect states and a possible catalytic activity of the (101) surface.

Part II.

Results and discussion I: Interfaces in inverted organic solar cells

7 I-V characteristics of inverted organic solar cells

Within the DFG project ”Inverted organic solar cells” (MA 2104/2-2 and RI1551/4-2) Sara Trost from BU Wuppertal performed I-V measurements of inverted organic solar cells (IOSC) with different ALD prepared electron transport layers (ETL). Besides the influence of different ETL's on I-V characteristics, she also investigated the influence of UV illumination on I-V characteristics of IOSC. Figure 7.1 shows the typical stack of the manufactured IOSC devices. It consists of a silver (100 nm) and ITO electrode, MoO_3 (15 nm) as HTL, P3HT:PC_{61}BM as organic absorber (200 nm) and varying ETL's (80 nm). As ETL ALD prepared individual TiO_x and AZO layers, as well as TiO_x/AZO bilayers were used. The influence of UV light was investigated by utilizing a UV filter for the solar light generator.

7.1 I-V characteristics of IOSC with TiO_x and AZO as ETL

In Fig. 7.2 I-V characteristics of IOSC with different ETL's and in dependence of the application of a UV filter for the solar light generator are displayed. Figure 7.2 shows I-V curves with the layer sequence ITO|TiO_x or AZO|P3HT:PC_{61}BM |MoO_3|Ag. The TiO_x and AZO layer are 80 nm thick. On the left of Fig. 7.2 I-V curves of the TiO_x and AZO IOSC, recorded with a UV filter, are displayed. While the IOSC with AZO as ETL (black) shows good, diode-like solar cell characteristics with a high FF, the solar cell with TiO_x as ETL (red), shows a S-shaped I-V curve and the FF is strongly reduced. On the right of Fig. 7.2 I-V curves recorded w/o an UV filter are displayed. The solar cells were illuminated by the solar light generator for 15 min before recording the I-V curve. Now also the solar cell with TiO_x as ETL shows good, diode-like, solar cell characteristics with a high fill factor.[15]
Summarizing, Sara Trost showed that inverted solar cells with ALD prepared AZO layers do have good, diode-like, I-V characteristics prior and after UV illumination, while IOSC with ALD prepared TiO_x as ETL do show S-shaped I-V curves prior UV illumination and good, diode-like, I-V curves after UV illumination.

7.2 I-V characteristics of TiO_x/AZO and AZO/TiO_x bilayers as ETL

Furthermore Sara Trost employed an ETL bilayer consisting of TiO_x and AZO in IOSC and varied the order of the layers. This means that once TiO_x was in contact to the organic acceptor-type absorber

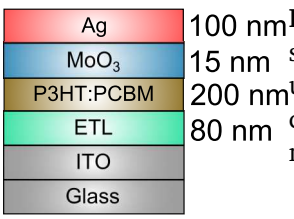

Figure 7.1 – Typical stack of IOSC devices used in this work to conduct I-V measurements.

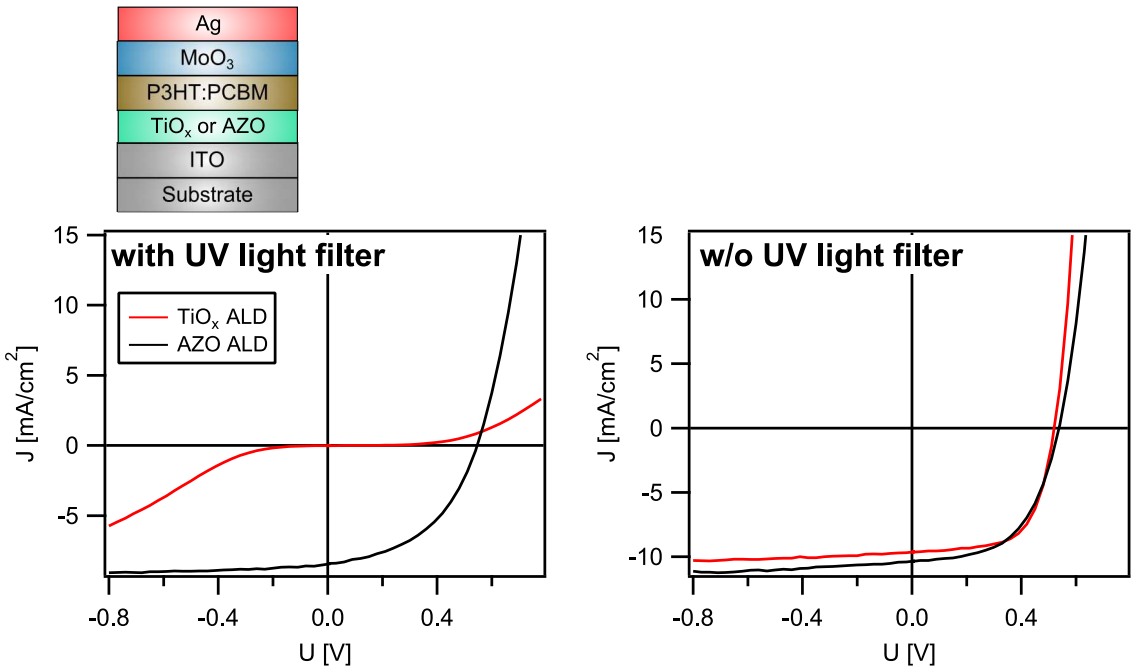

Figure 7.2. – I-V curves of IOSC with 80 nm thick TiO_x or AZO as ETLs are displayed. I-V curves on the left are recorded with a UV filter. The IOSC with TiO_x (red) shows a S-shaped I-V curve with a strongly reduced fill factor, while AZO (black) shows good diode characteristics. On the right I-V curves measured without UV filter are displayed. Now IOSC with TiO_x and AZO as ETL show both good diode characteristics. Adapted from Ref. [15].

and once AZO. In Fig. 7.3 IOSCs with a TiO_x and AZO ETL bilayer were used. The layer sequence of the TiO_x AZO bilayer was varied, which means that once TiO_x was at the bottom and AZO on top (TiO_x/AZO) and once AZO at the bottom and TiO_x on top (AZO/TiO_x). Hence in the former case, AZO forms the interface to the organic absorber and in the latter case TiO_x forms the interface to the organic absorber. On the left of Fig. 7.3 I-V curves of the respective layer sequences measured with a UV filter are displayed. While the solar cell with an AZO/TiO_x bilayer shows virtually no FF, the solar cell with the reversed bilayer sequence (TiO_x/AZO) shows good solar cells characteristics with a high fill factor. The I-V curves recorded without UV filter (Fig. 7.3 right), either with TiO_x or AZO forming the interface to organic absorber, show good solar cell characteristics with a high fill factor. The variation of the TiO_x and AZO sequence gives strong evidence, that the TiO_x/organic acceptor interface is responsible for the observed S-shaped characteristics of IOSC with TiO_x as ETL.

Summarizing, IOSC devices containing the TiO_x/organic acceptor-type absorber interface showed the same electronic behavior as IOSC with only TiO_x as ETL (S-shape prior UV illumination, no S-shape after UV illumination), IOSC devices with the AZO/organic acceptor-type absorber interface, showed the same electronic behavior as IOSC with only AZO as ETL (no S-shape prior and after UV illumination).

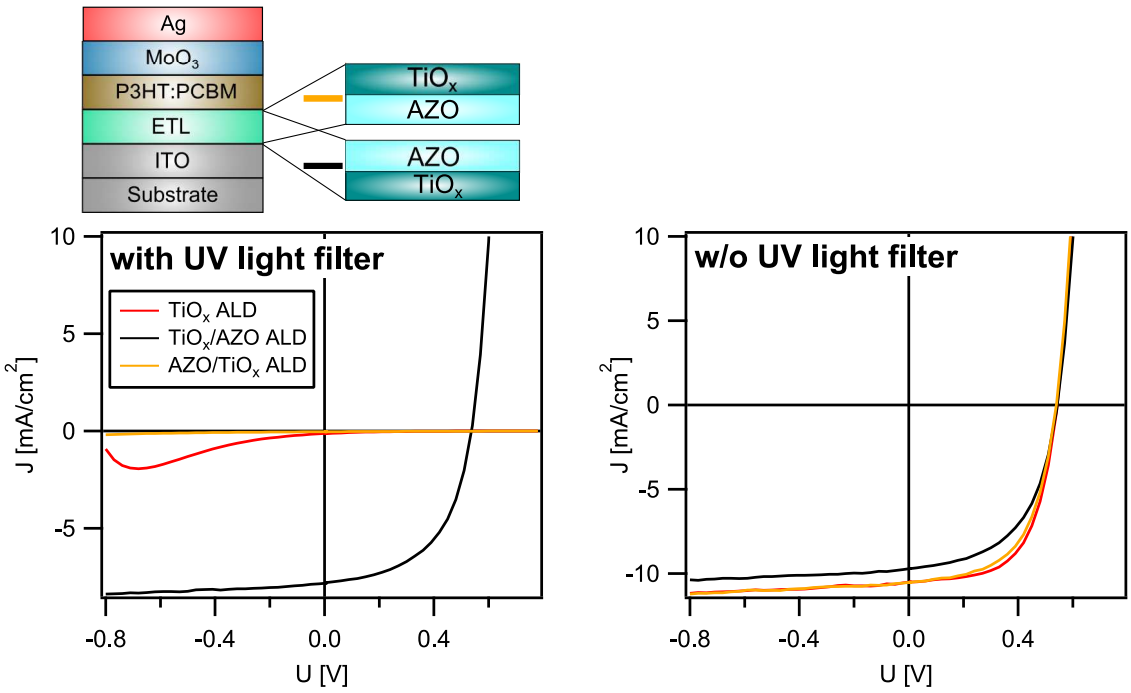

Figure 7.3. – The ETL consists of a TiO_x/AZO bilayer structure, where the sequence is varied. Each layer of the bilayer is 40 nm thick. On the left I-V curves recorded with a UV filter are displayed. In the case where TiO_x is on top and is making the contact to the organic absorber (yellow), the solar cell shows no diode character at all. In the case where AZO is on top and forms the contact to the organic absorber (black), the solar cell has again good diode characteristics. On the right I-V curves of solar cells with the same layer sequences are recorded without a UV filter. All I-V curves show diode-like I-V characteristics.

7.3 Unipolar devices with TiO_x or AZO interlayers and $PC_{61}BM$ or C_{60} as organic acceptor material

Furthermore I-V characteristics of unipolar, electron only devices with the layer sequence Glass/ITO/TiO_x/C_{60} or $PC_{61}BM$/Ca/Ag were recorded by Sara Trost (see Fig. 7.4 top and middle). By employing electron only unipolar devices the number of inorganic/organic interfaces is reduced to the TiO_x/C_{60}, respectively the TiO_x/$PC_{61}BM$ interface. The J-V curves of C_{60} and $PC_{61}BM$ show the same UV dependency. Before UV illumination almost no electrons, which are injected via the Ca/Ag electrode, are extracted and after UV illumination electron extraction is highly enhanced. Without UV the unipolar device with C_{60} shows a symmetric behavior and electron extraction (even though low) occurs in forward and electron injection in backwards polarity. $PC_{61}BM$ devices show only electron extraction in forward polarity and no electron injection in backwards direction. After UV illumination, both devices, with C_{60} and $PC_{61}BM$, show a symmetric electron current in forward and reverse polarity, indicating a much improved electron extraction/injection after UV irradiation. The electron extraction current of the C_{60} device is more than one magnitude higher, than the extraction current of the $PC_{61}BM$ device. In Fig. 7.4 bottom, unipolar, electron only devices with the layer sequence Glass/ITO/AZO/C_{60} or $PC_{61}BM$/Ca/Ag are displayed. Both show a similar and good electron extraction behavior before and after UV.

Summarizing the results from above, C_{60} shows similar I-V characteristics as $PC_{61}BM$ in unipolar devices. Thus C_{60} appears to be a suitable model acceptor material to transfer the obtained surface science results of the TiO_x/C_{60} interface to the measured I-V characteristics obtained of inverted organic solar cells with TiO_x as ETL and $PC_{61}BM$ as electron accepting material. The results on the electronic line-up of C_{60} and $PC_{61}BM$ are compared to each other in Section 8.3.1.

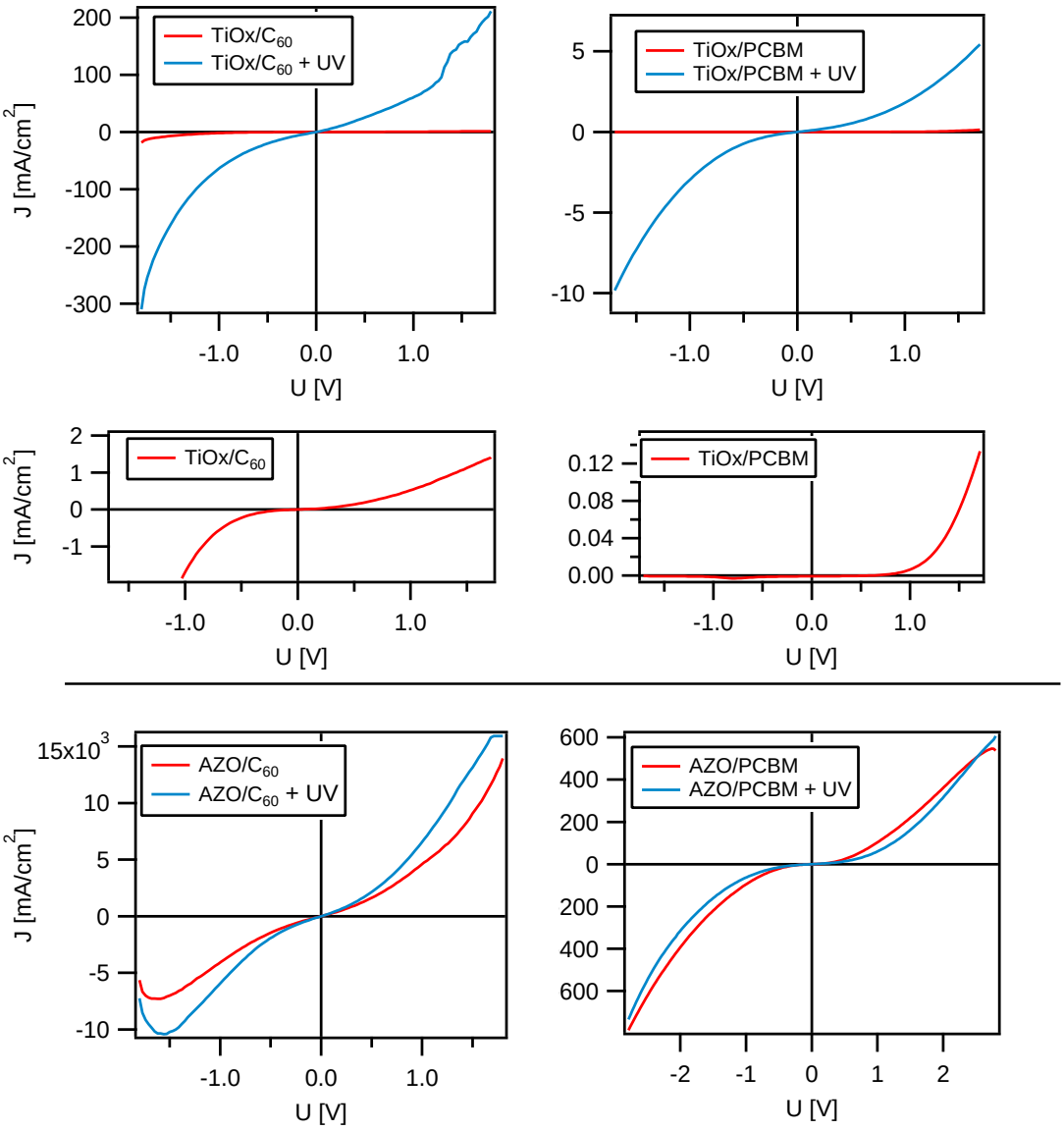

Figure 7.4. – Top: I-V curves of unipolar TiO_x/C_{60} and $TiO_x/PC_{61}BM$ devices. Both show the UV dependency and show bad electron extraction behavior before UV and good electron extraction behavior after UV radiation. Middle: Magnification of the TiO_x/C_{60} and $TiO_x/PC_{61}BM$ devices before UV radiation. Bottom: Unipolar AZO/C_{60} and $AZO/PC_{61}BM$ devices. Both show a similar and good electron extraction behavior before and after UV. The device stack is Glass/ITO/TiO_x (AZO)/C_{60} ($PC_{61}BM$)/Ca/Ag).

8 The titanium dioxide - C_{60} interface

8.1 TiO_x substrates - structure and morphology

In this work four differently prepared TiO_x surfaces were considered: Amorphous titania prepared by ALD at low temperatures, 500 °C post annealed ALD titania, nanocrystalline anatase out of slurry and naturally grown anatase single crystals. Besides the single crystal, all titania films were transparent. The color of the cleaved single crystal is dark blue (see Fig. 8.1). In the following paragraph, these substrates were investigated by SEM, AFM, and XRD. The single crystal was additionally investigated by Laue diffraction to determine the polymorph and cleavage plane, and by LEED to check the symmetry of the surface structure. The single crystal and the nanocrystalline anatase were not investigated by SEM.

8.1.1 XRD and Laue diffraction of TiO_x

Figure 8.2 A shows the Laue diffraction pattern of a cleaved anatase crystal. The recorded diffraction pattern (Fig. 8.2 A left) is in excellent agreement with the calculated diffraction pattern[1] displayed on the right of Fig. 8.2 A and confirms the intended cleavage at the (101) plane. The nanocrystalline sample, prepared out from a slurry, is pure anatase, which is indicated by the appearance of the (101), (004), (200), (105), (211), (204) reflexes in the XRD pattern B. The additional reflexes originate from the underlying FTO substrate and belong to SnO_2. From the *fwhm* of the (101) and (004) reflexes the crystallite size is calculated by the Scherrer equation (see Eq. (3.7)) to be 15 to 30 nm, which is in good agreement with the observed particle size by AFM in Fig. 13.2 b). The XRD measurement of the as deposited TiO_x sample was conducted on a sample with 150 nm TiO_x deposited on glass. The XRD pattern does not show any reflexes and hence the TiO_x is amorphous (see Fig. 8.2 D). The XRD pattern of the 500 °C annealed TiO_x is displayed in Fig. 8.2 C and displays reflexes, which are assigned to anatase. The intensity of the reflexes is low, which indicates only a partial transformation of the

[1] For the simulation of the anatase single crystal (101) surface Laue pattern, the free software Cologne Laue Indexation Program (CLIP) was used.

Figure 8.1. – Photograph of a cleaved naturally grown anatase single crystal as used in this work. Facing the camera is the (101) surface plane

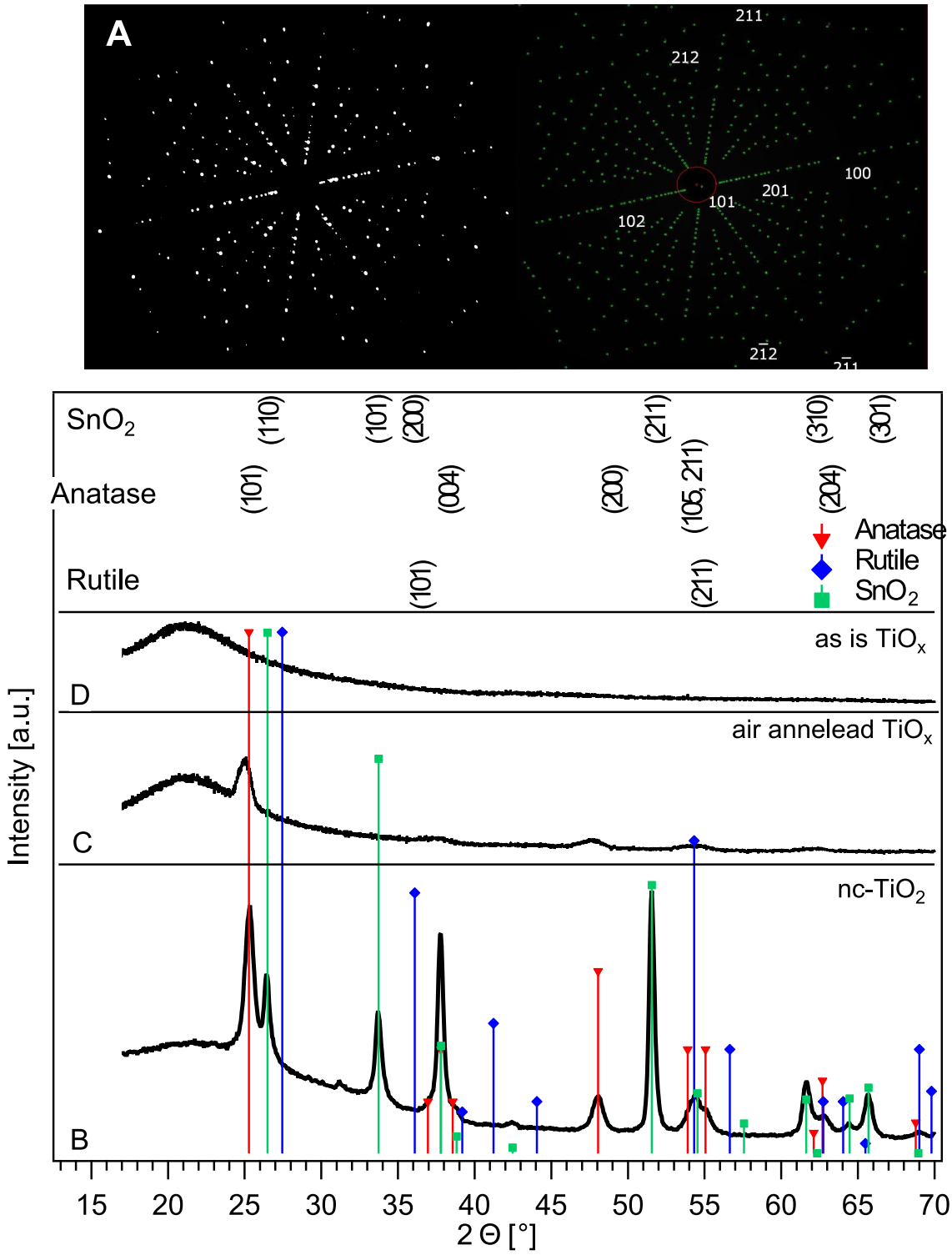

Figure 8.2. – (A) Laue diffraction pattern of the anatase single crystal cleavage plane (left) and the calculated diffraction pattern of the anatase (101) plane. (B) XRD patterns of a sintered, spin coated, nanocrystalline TiO_2 film (nc-TiO_2 bottom pattern B) and ALD titania as deposited (D) and post annealing (C). At the top, positions of reflexes expected in anatase, rutile, and SnO_2 of the FTO substrate are indicated. For the nc-film (B) anatase and additional substrate (SnO_2) reflexes appear. Before annealing, the ALD film (D) deposited at 80 °C, shows no reflexes. The broad feature with a maximum around 21° is caused by the glass substrate. After annealing (C) anatase reflexes appear. Taken from Ref. [136].

amorphous phase to anatase. The determined particle size by using the Scherrer equation is 5 to 10 nm, which is much smaller than the particle size of 30 to 90 nm determined by AFM in Fig. 13.2 c). The AFM image was recorded on 40 nm annealed TiO_x. The differences may originate from the low intensity of the reflexes and therefore a high error in the particle size determination by XRD or a different degree of crystallization of the two samples, e.g. the annealed ALD sample may indicate anatase particles with an amorphous/crystalline core/shell structure.

8.1.2 SEM of TiO_x

Figure 8.3 shows the SEM picture of as prepared TiO_x and 500 °C post annealed TiO_x. Both surfaces do not show much contrast, which indicates a smooth surface.

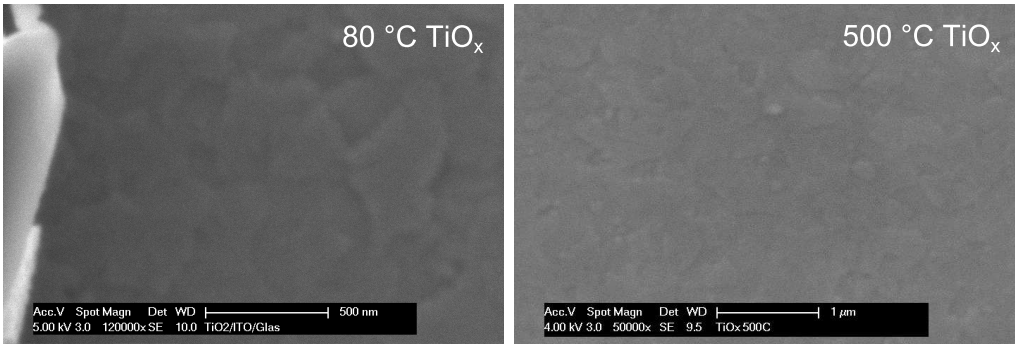

Figure 8.3. – Left: Amorphous ALD TiO_x on ITO/glass. Right: 500 °C annealed ALD TiO_x on ITO/glass.

8.1.3 AFM of TiO_x

In Fig. 8.4 the AFM pictures of as prepared TiO_x d), the 500 °C post annealed TiO_x c), the nanocrystalline anatase b) and the cleaved naturally grown single crystal a) are displayed. Figure 8.4 e) and f) show two different magnifications of the ITO substrate, where the TiO_x films of c) and d) were deposited on. The as prepared TiO_x resembles well the structure of the underlying ITO substrate (Fig. 8.4 e) and f), which displays the same structure. The post annealed TiO_x (Fig. 8.4 c) shows the formation of particles with a particle size distribution in the range of 30 to 90 nm covering the underlying ITO crystallites as observed for the as prepared TiO_x. The nanocrystalline anatase (Fig. 8.4 b) has smaller particle sizes of about 20 to 30 nm, which is in the range of the particle size specified by the supplying company (Solaronix S.A.). Figure 8.4 a) shows the AFM image of the cleaved anatase crystal. It shows terraces with a width of about 3 μm and a height of 8 nm. This indicates an off angle of 0.15° of the cleavage plane. On sputter annealed single crystal TiO_2 (101) surfaces, step edges of atomic height have been observed[82] and Setvín et al. observed trapezoid shaped terraces of single and multistep height on TiO_2 (101).[86] Bondarchuk et al. observed steps of 0.32 nm height on an *in situ* cleaved rutile single crystal (110)[97]. Therefore it can be assumed, that additional step edges exist on the sc-(101) surface, but cannot be resolved in the AFM image shown in Fig. 8.4a).

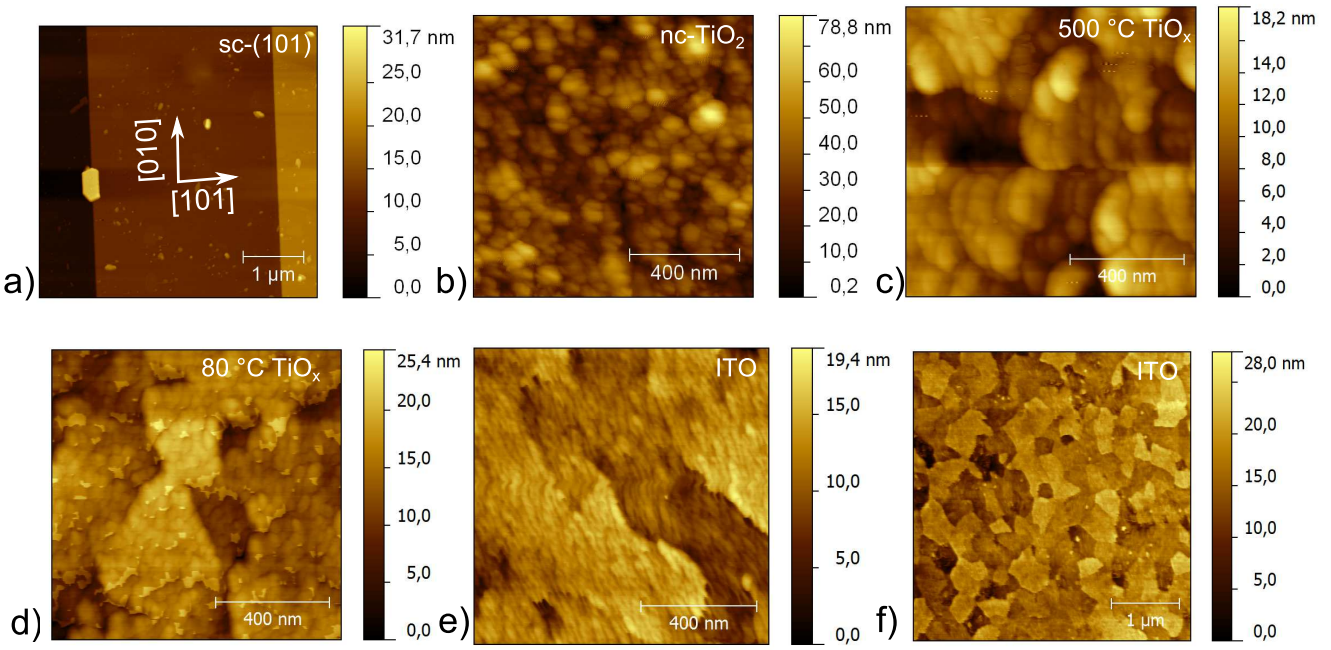

Figure 8.4. – AFM images of a) anatase single crystal (101) surface, b) nc-anatase film, c) ALD titania post annealed, and d) as deposited (80 °C) ALD titania. For comparison the ITO substrate is shown in image e) and f) in different magnifications.

8.1.4 LEED of TiO_2 sc-(101)

Figure 8.5 shows LEED images of an *in situ* cleaved anatase sc-(101 surface) recorded with 61 eV kinetic electron energy (Fig. 8.5 b) and 215 eV electron energy (Fig. 8.5 b). Due to the higher kinetic electron energy the wave length becomes smaller and the Ewald sphere increases (see Section 5.2). Hence more diffraction points are observed. The well-defined diffraction pattern of sharp spots indicates a highly ordered and clean surface. The geometry of the spots indicates a (1 x 1) structure and hence a bulk like terminated surface without reconstruction.[137]

The LEED pattern is in excellent agreement with LEED patterns obtained of an anatase sc-(101) surface grown on $SrTiO_3$ by Herman et al. (Fig. 8.5) c)[138] and Hengerer et al.[137] on crystals grown by chemical transport reaction. Due to time restrictions, investigations of the (100) surfaces are not part of this work.

8.1.5 UV-Vis of TiO_x 80 °C

In Fig. 8.6 a Tauc plot of an ALD TiO_x UV-Vis absorption spectrum is shown. It is unknown if amorphous TiO_x has a direct or indirect energy gap. Anatase has an indirect energy gap, while rutile has a direct energy gap. For the Tauc plot an indirect energy gap (as anatase) of TiO_x is assumed (x=0.5).[15] From the linear extrapolation of absorption onset an energy gap of 3.4 eV is determined. The UV-Vis measurement was performed by Sara Trost from BU Wuppertal.

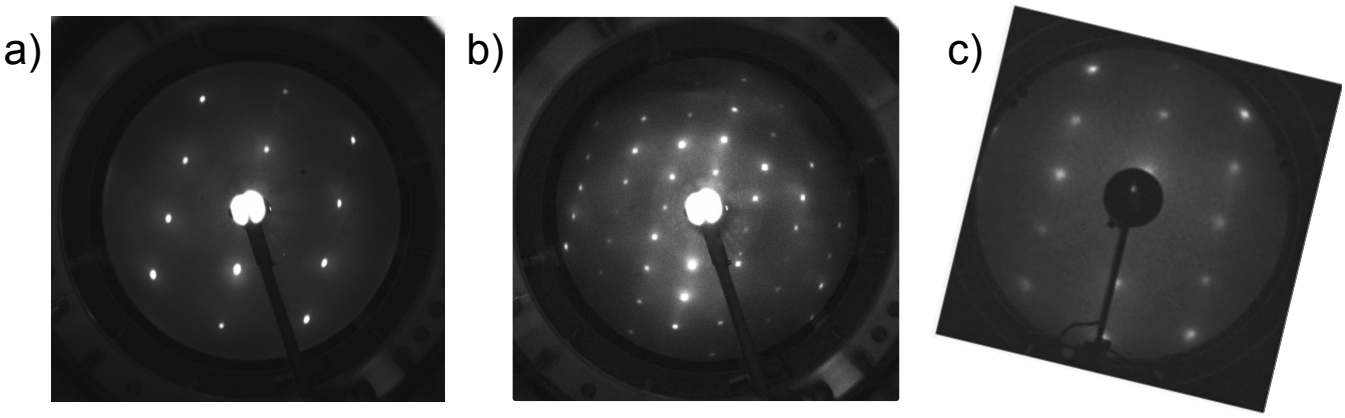

Figure 8.5. – LEED images of the *in situ* cleaved anatase sc-(101) surface. Left: Image recorded at 61 eV electron energy. Middle: Image recorded at 215 eV electron energy. Right: Reference LEED image of an anatase sc-(101) surface grown on $SrTiO_3$ by Herman et al.[138] The LEED images are of good quality (bright and periodic arrangement of the LEED spots) and show a 1 x 1 unreconstructed surface of the (101) anatase surface.

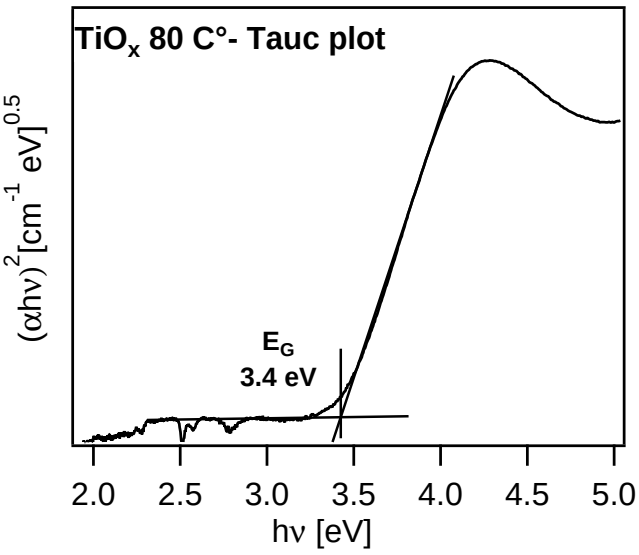

Figure 8.6 – Tauc plot of TiO_x 80 °C for the determination of the optical gap. An indirect band gap is assumed.

8.2 Photoemission spectroscopy on various TiO_x samples

In the following chapter four different titanium dioxides are investigated by photoelectron spectroscopy: Amorphous ALD prepared titania processed at 80 °C, 300 °C and 500 °C and sc-anatase (101) TiO_2. A comparison regarding their composition, e.g. the stoichiometry or existing contaminations and the differences in the energetic position of the energy levels and their relative positions is made.

8.2.1 Photoemission of TiO_x: Fundamentals

Survey spectra of all titania materials

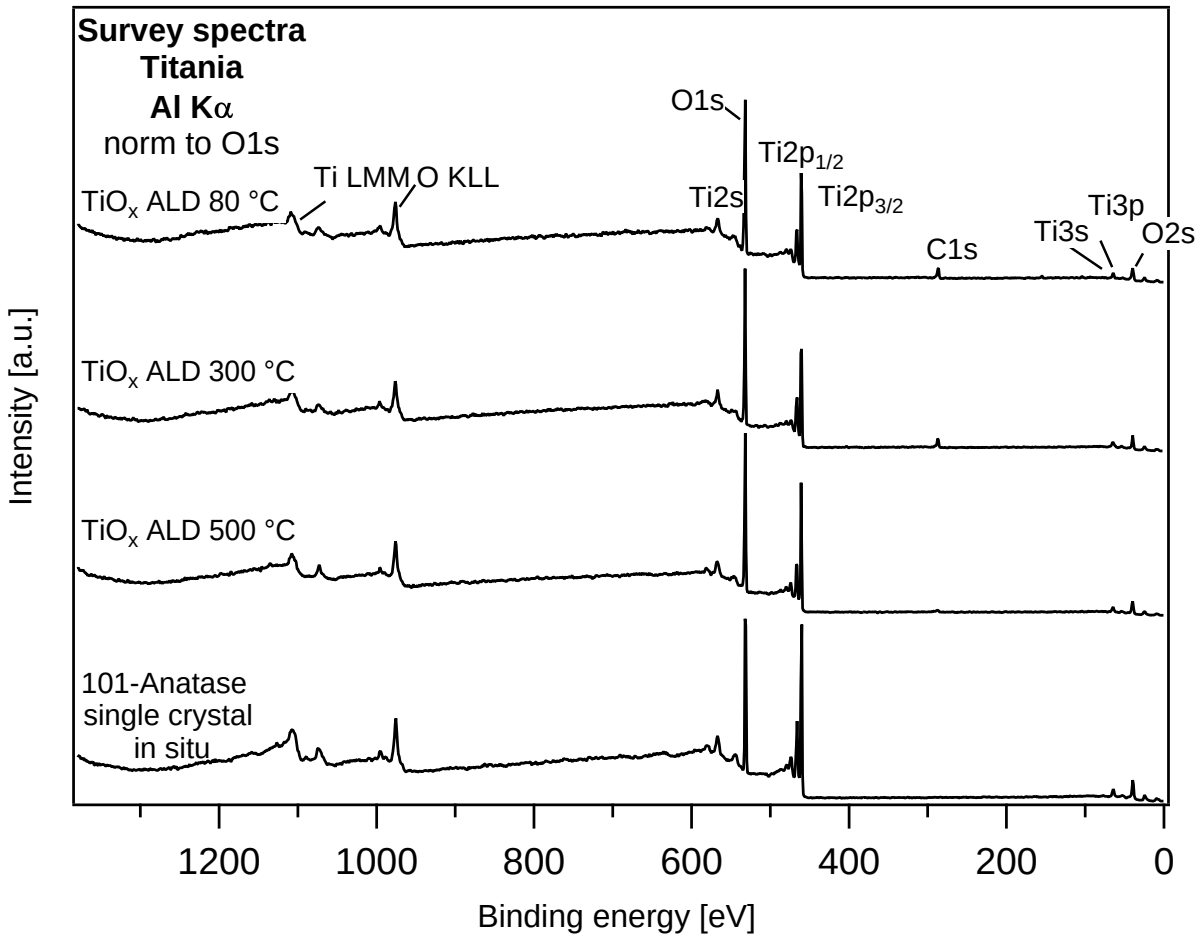

Figure 8.7. – TiO_x survey spectra of all investigated titania: asis TiO_x ALD 80 °C, TiO_x annealed for 60 min at 300 °C, TiO_x annealed for 60 min at 500 °C and *in situ* cleaved 101-anatase single crystal. All spectra show titanium and oxygen core levels and Auger emission lines. The ALD prepared sample shows an additional C 1s emission due to the *ex situ* preparation and/or residues of the precursor due to low temperature manufacturing.

In Fig. 8.7 XPS survey spectra of four differently prepared titania materials are displayed: TiO_x made by ALD with a substrate temperature of 80 °C, TiO_x annealed at 300 °C for 60 min at air, TiO_x annealed at 500 °C for 60 min at air and an *in situ* cleaved naturally grown anatase single crystal. All samples show the expected oxygen and titanium core and Auger electron emissions as indicated in the upper spectrum in Fig. 8.7. The O 1s and O2s are at 531 eV and 23 eV binding energy, respectively and the O KLL Auger

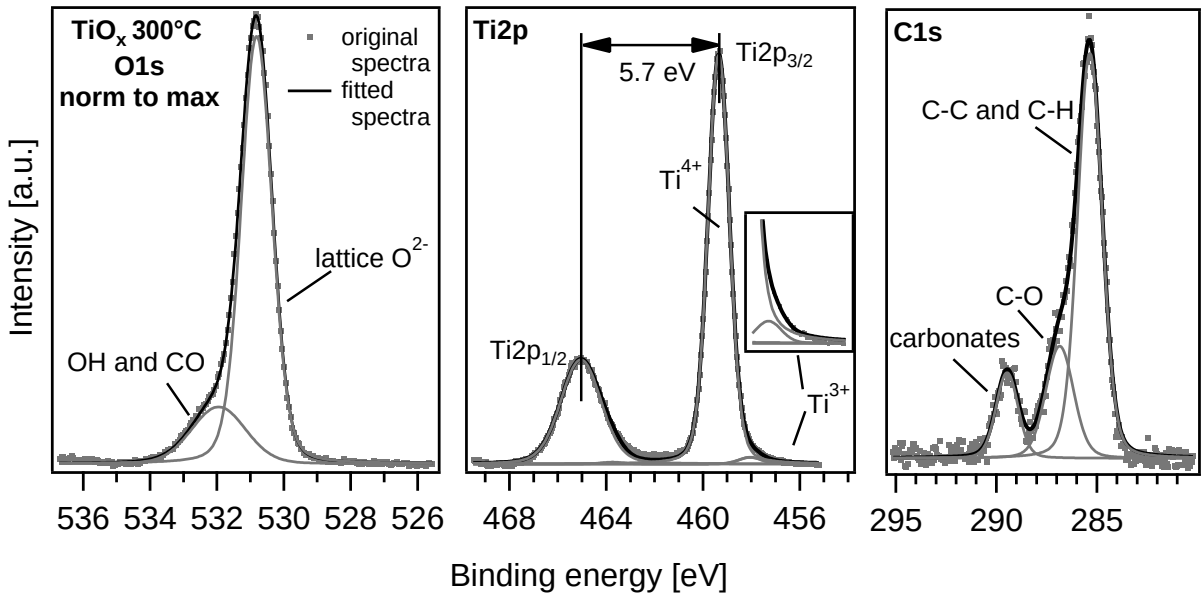

Figure 8.8. – Deconvoluted O 1s, Ti $2p_{3/2}$ and C 1s spectra of 300 °C annealed TiO_x. The O 1s emission consists of lattice oxygen and adsorbed hydroxyl species. The Ti $2p_{3/2}$ emission shows an additional Ti^{3+} emission on the low binding energy side, which is shown in the inset with a magnification of the factor 5. The C 1s emission consist of C-C, C-H, C-O and O-C-O related emissions. The carbon C 1s emission decreases with increasing annealing temperature.

electron emission at around 1013 eV. The core level emission lines of titanium are at 1098 eV (Ti LMM), ~565 eV Ti 2s, ~464 eV (Ti $2p_{1/2}$) ~459 eV (Ti $2p_{3/2}$), ~63 eV (Ti 4s) and ~37 eV (Ti 3p).[110]

All *ex situ*, ALD prepared samples, have an additional emission of carbon around 285 eV. This emission is strongest for the low temperature prepared TiO_x (80 °C) and decreases with increasing annealing temperature. After annealing to 500 °C the C 1s emission is almost not apparent anymore in the survey spectrum. The *in situ* cleaved anatase crystal is free of carbon contaminations. Further typical contaminations of natural anatase crystals like potassium, silicon, or sodium[139] are not detected within the range of the recorded survey spectra and therefore not existent or below the XPS detection level.

Fitting titania XP spectra

For an in depth analysis, detail spectra of the Ti2p, O 1s and C 1s emission were recorded on 300 °C annealed sample and a Shirley background was subtracted from the spectra.[140] The spectra were deconvoluted by the respective emission lines using a set of Gaussian-Lorentzian-Voigt profiles.

The typical core level emission lines are displayed in Fig. 8.8 and it shows O 1s, Ti2p and C 1s core level emissions from a 300 °C annealed TiO_x sample. The O 1s emission consist of the main emission around 531 eV binding energy and a shoulder shifted around 1 eV to higher binding energies. The O 1s main emission is attributed to lattice O^{2-} which is part of the titania itself. The shoulder can be assigned to other oxygen containing species like surface hydroxyls or carbon oxygen bonds. Hydroxyls (adsorbed OH^-) originate probably from water used during the ALD synthesis and from adsorbed water during ex-situ handling (see Section 4.2). CO groups are attributed mainly to residues from the precursor.[141]

The Ti 2p emission is a doublet and consist of the Ti $2p_{3/2}$ at ~459 eV and the Ti $2p_{1/2}$ emission at 465 eV. The doublet is split up by 5.7 eV and their intensity ratio is 2.06 to 1, which in good accordance

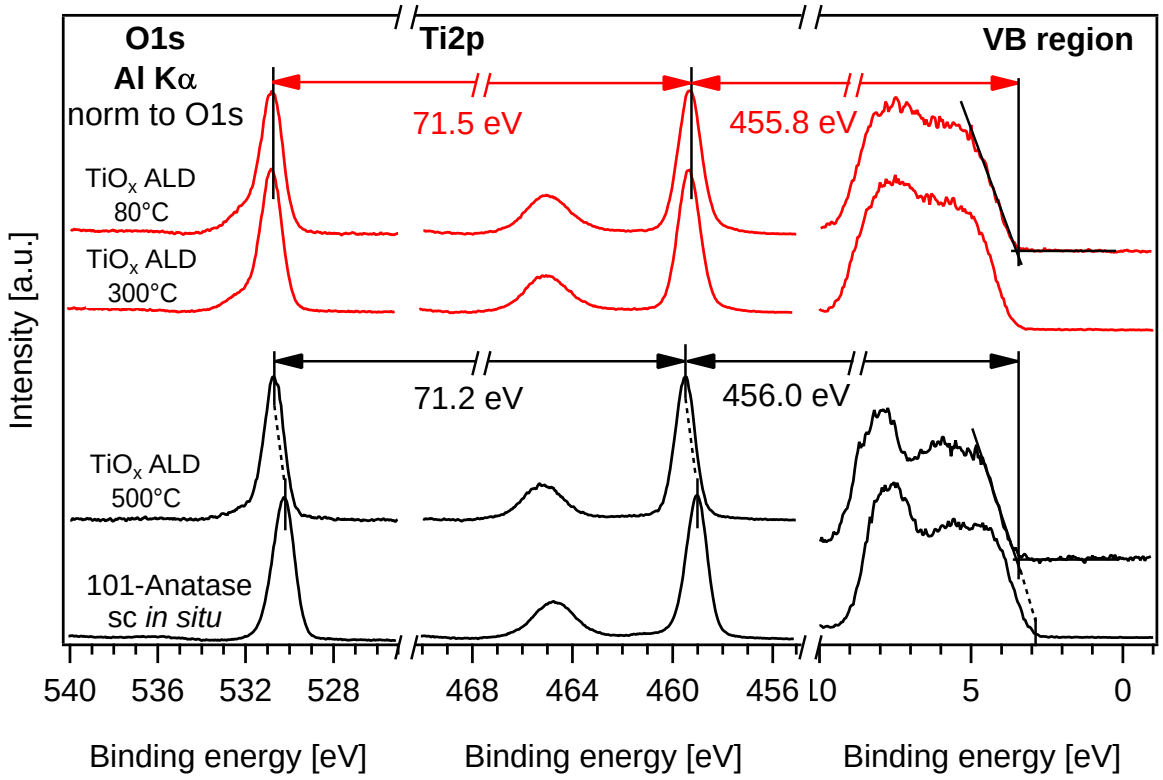

Figure 8.9. – O 1s, Ti $2p_{3/2}$ and VBM distances for *in situ* sc-(101), 80 °C, 300 °C, and 500 °C TiO_x. While the amorphous (80 and 300 °C) have a Ti $2p_{3/2}$-VBM distance of 455.8 eV, the distance for anatase TiO_2 (sc and 500 °C) is 456.0 eV. The O 1s-VBM distance is 527.3 eV for amorphous TiO_x and the distance for anatase TiO_2 (sc and 500 °C) is 527.2 eV

with the formal intensity ratio of 2 to 1. At the low binding energy side of the Ti2p emission a small peak arises (see magnification in Fig. 8.8). This emission is shifted by around 1.3 eV and according to literature is attributed to Ti^{3+} ions.[142][143] Ti^{3+} sites are commonly addressed to oxygen vacancies V_O and are preferentially present at the surface of titania, which was shown by photon energy dependent photoemission measurement on nc-TiO_2 by Schwanitz et al.[81] The presence of Ti^{3+} emission is accompanied with the emission of deep gap states (DGS) around 1 eV binding energy (see Chapter 17).

The third observed element is carbon. The C 1s emission was deconvoluted with three Gaussian-Lorentzian-Voigt profiles. The main component is around 285.3 eV binding energy and is attributed to C-C and C-H bonds. At the high binding energy side is a shoulder, shifted about 1 eV, which can be attributed to C-O bonds and at ~289 eV an additional emission is apparent, which is assigned to carbonates (CO_3^{2-}).[110] The carbon, especially C-C and C-H, stems probably from contaminations due to the *ex situ* handling of the sample. Carbonates and C-O moieties can be residues of the precursor, titanium isopropoxide, particularly if the processing temperature is rather low (80 °C or 300 °C), and indicate that the precursor does not react completely. The *in situ* cleaved sc-TiO_2 shows no C 1s emission.

8.2.2 Influence of temperature and crystallinity

Amorphous and anatase titania: Emission line distances

In Fig. 8.9 the main core level emission lines, O 1s and Ti2p, and the valence band region are displayed of all four titania materials. The core level and valence band emission of the amorphous *ex situ* prepared 80 °C and 300 °C TiO_x have similar binding energies: ~530.80 eV, ~459.35 eV and ~3.55 eV for the O 1s, Ti $2p_{3/2}$ and the valence band maximum (VBM) position, respectively. This data matches reasonable well with data recorded by Ou et al. on amorphous TiO_x prepared by CVD with TTIP as precursor material at 210 °C.[141] The binding energies of the 500 °C annealed anatase are ~530.75 eV (O 1s), ~459.55 eV (Ti $2p_{3/2}$) and 3.55 eV for the VBM, which are similar to values reported by Schwanitz et al. on anatase TiO_2 prepared by CVD at 450 °C with TTIP as precursor material.[143] In contrast all emission lines of the *in situ* cleaved anatase single crystal are shifted by ~0.5 eV to lower binding energies (O 1s: 530.25 eV, Ti $2p_{3/2}$: 459.05 eV, VBM: 3.02 eV). This indicates either a lower n-doping of the single crystal compared to the ALD prepared layer (lower Fermi level) or that the *ex situ* ALD TiO_x layers exhibit a downward band bending at the surface due to the presence of either surface states (such as V_O) or adsorbates on the surface, which cannot be avoided on *ex situ* samples. As the single crystal was cleaved *in situ* and as neither adsorbates nor V_O occur in the photoemission spectrum, a flat band situation at the sc-(101) surface is assumed. Natural n-doping results from intrinsic oxygen vacancies present in TiO_2.[144] By varying the oxygen content during sputtering TiO_{2-x}, the Fermi level position E_F can be tuned from n-type to degenerated n^+-type TiO_x.[145] On crystalline TiO_2, annealing causes formation of V_O at the bridging oxygen rows on the surface.[146] Furthermore V_O can be induced by electron-stimulated desorption,[147] or by Ar-sputtering.[16] Adsorbates can either cause downward band bending (e.g. H_2O) or cause an upward band bending (e.g. O_2).[148]

As XPS is very surface sensitive[2] and band bending at the surface, especially on *ex situ* samples, is likely, a direct comparison of binding energy position of the different *ex situ* samples is not reasonable. Additionally it was found, that $Al_{K\alpha}$ X-ray irradiation influences the binding energy positions (see Sections 11.1 and 11.2). Hence a more appropriate criteria to compare different titania samples among each other is the distance between core level emission lines itself and the VBM. To obtain reliable results, it was taken care, that a possible binding energy shift induced by X-ray was already saturated. Pfeifer et al. showed e.g. that the distance between the O 1s or Ti $2p_{3/2}$ core level and the VBM of rutile is 0.4 eV higher than in anatase, by using photoelectron spectroscopy and electronic structure calculations.[149] The titania samples investigated in this work can be divided into two groups. The amorphous titania samples (80 °C and 300 °C) have an O 1s-Ti $2p_{3/2}$ distance of 71.5 eV whereas the crystalline anatase samples are only separated by 71.2 eV. This is in good accordance with values reported by Ou et al. for amorphous titania[141] and anatase by Pfeifer et al.[149] The decrease of the O 1s-Ti $2p_{3/2}$ distance arises as the Ti $2p_{3/2}$ binding energy increases upon transformation from amorphous to anatase by 0.19 eV from 459.35 eV to 459.54 eV and O 1s binding energies decreases by 0.06 eV from 530.80 eV to 530.74 eV. The O 1s-VBM and Ti $2p_{3/2}$-VBM distance for the amorphous titania is 527.3 eV, respectively 455.8 eV. The O 1s-VBM distance of the anatase samples decreases by ~0.1 eV to 527.2 eV, whereas the Ti $2p_{3/2}$-VBM distance increases by ~0.2 eV to 456.0 eV. The valence band of TiO_2 has contributions of O 2p and Ti 3d

[2] Escape depth of photoelectrons in XPS is about 5-10 nm

Table 8.1. – Energetic positions and distances of the O 1s, the Ti $2p_{3/2}$ and the valence band maximum.

	Energetic positions [eV]			Distances [eV]		
	O 1s	Ti $2p_{3/2}$	VBM	O 1s-VBM	Ti $2p_{3/2}$-VBM	O 1s-Ti $2p_{3/2}$
80 °C	530.80	459.35	3.53	527.27	455.82	71.45
300 °C	530.81	459.34	3.53	527.28	455.81	71.47
500 °C	530.74	459.54	3.55	527.19	455.99	71.20
sc	530.24	459.03	3.02	527.22	456.00	71.21

states, but especially the lowest binding energy region of the VB (i.e. VBM), consist of almost only O 2p states.[83,84] On that account it is reasonable, that the O 1s-VBM distance only decreases by ∼100 meV and the Ti $2p_{3/2}$-VBM distance by ∼200 meV. If the VBM would be completely O 2p derived one would expect no decrease of the O 1s-VBM distance due to initial state effects.

Discussing the observed changes of the O 1s-Ti $2p_{3/2}$ distance as initial state effect, this suggests that the partial charge on the Ti and O atoms changes upon annealing and the transformation from amorphous to anatase. While the O 1s binding energy decreases, the partial charge on the oxygen atoms increases (from amorphous to anatase) and becomes more negative. For titanium the opposite occurs and the electron density in the surroundings decreases and the titanium atoms are charged more positive, leading to an increase of the binding energy of the Ti $2p_{3/2}$ photoelectrons. Another reason for the observed changes of the O 1s-Ti $2p_{3/2}$ distances could be a change of the Madelung constant, which is used to determine the electrostatic potential of a single ion in a crystal. If the Madelung constant changes upon e.g. annealing amorphous TiO_x the binding energy changes as well. The Madelung constant changes e.g. if the structure type of a material changes. Final state effects, like plasmons excitation or electron shake-up processes could also explain the shift of the emissions, but are rather unlikely to be the origin of the observed shifts, as they are lower in intensity.

Valence band maximum determination

The valence band maximum (VBM) was determined after the method of Kraut by using a linear extrapolation of the leading edges to the baselines of the XPS valence band spectra.[150] Due to the low cross section of the valence band electrons at high excitation energies (i.e. $Al_{K\alpha}$ = 1486.6 eV)[114], the signal to noise ratio of the VB region is low. Thus the VB region has to be recorded at minimum 30 times (about 600 s) to get a decent VB spectrum suitable for a VBM determination. It was observed that X-rays and HeI radiation influence the energetic position of the emission lines. This is shown in more detail in Section 9.1 for 80 °C TiO_x and in Appendix A.2 for 500 °C TiO_x. Due to the influence of X-rays and the long time needed to record the VB region, a direct determination of the initial VBM position is not possible by simply measuring the valence band. Instead the fact that the relative energetic positions of a material are considered to be constant is used to determine the VBM.[150] In Section 8.2.1 the Ti $2p_{3/2}$-VBM distances for all investigated TiO_x samples were determined and are 455.80 eV (for 80 °C and 300 °C TiO_x) and 456.00 eV (for 500 °C TiO_x) (see Table 8.1). To determine the initial VBM of the different TiO_x, these binding energies differences are subtracted from the respective Ti $2p_{3/2}$ core level position.

Table 8.2. – VBM positions of all ALD prepared *ex situ* samples and *in situ* cleaved sc-anatase (101). The ALD TiO_x VBM positions are calculated by the determined Ti $2p_{3/2}$-VBM distance and the sc-(101) VBM is determined graphically.

Sample	VBM meas.	Ti $2p_{3/2}$ *initial* [eV]	Ti $2p_{3/2}$-VBM [eV]	VBM calc. [eV]
80 °C	3.51	459.20	455.81	3.39
300 °C	3.59	459.20	455.82	3.38
500 °C	3.53	459.34	456.00	3.34
Anatase sc-(101)	3.05	-	-	-

Figure 8.10 A shows the valence band spectra of all investigated titania samples. In contrast to the anatase single crystal, the energetic position of the VBM is higher and in the range of 3.5 to 3.6 eV. Table 8.2 shows the calculated VBM position of the 80 °C, 300 °C and 500 °C TiO_x. The values for the initial Ti $2p_{3/2}$ position are taken from Figs. 9.4, 11.15 and A.3. For the 80 °C and 300 °C TiO_x the VBM is at about 3.40 eV binding energy. The 500 °C TiO_x VBM is slightly lower and lies around 3.35 eV. In the case of the *in situ* cleaved anatase no X-ray and UV influence on the binding energy positions was observed and the VBM is determined graphically. Figure 8.10 B shows the evolution of the Ti $2p_{3/2}$ core level emission line of a 500 °C TiO_x upon X-ray irradiation (see Appendix A.2 for more details). The first measurement was taken after approx. 25 s. In order to obtain a value for 0 s of irradiation, an exponential fit was performed. The extrapolated value at 0 s is only about 0.02 eV lower, than the binding energy of the initial spectrum after about 25 s X-ray exposure. Hence it is valid to use the initial spectrum to determine the VBM position.

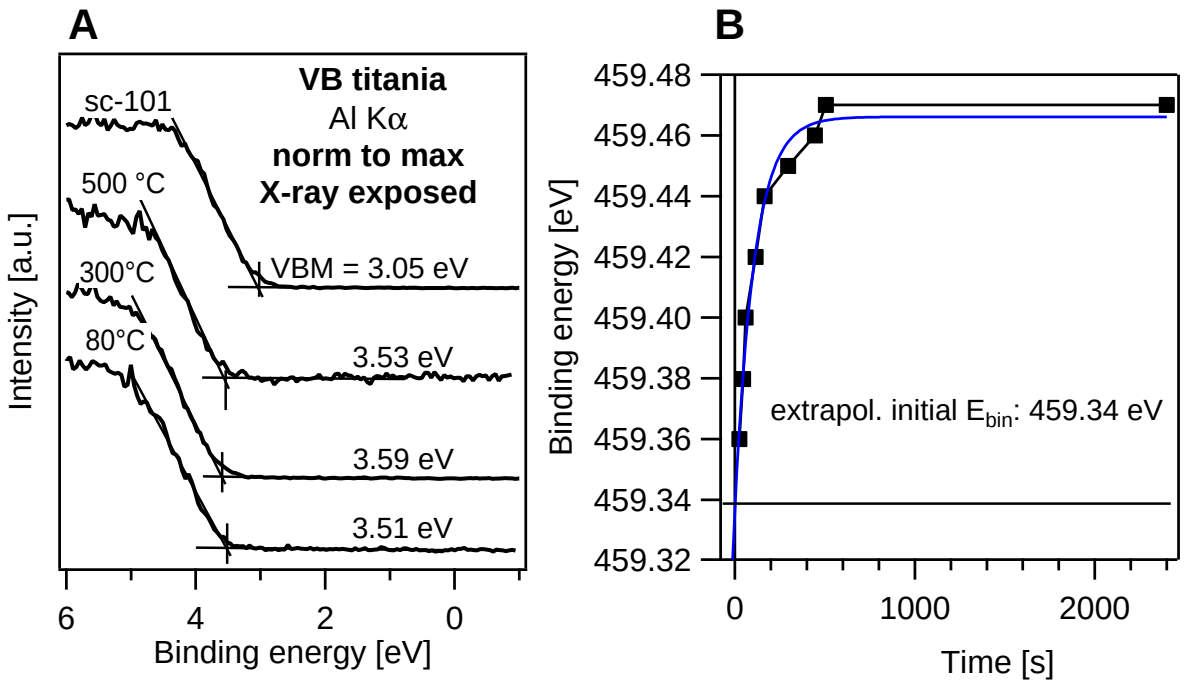

Figure 8.10. – A: Valence band region of *in situ* cleaved sc(101), 500 °C and 300 °C annealed TiO_x and as deposited 80 °C TiO_x. The VBM of the sc-(101) is considerably smaller (~3 eV) than all other *ex situ* samples (~3.5 eV). B: An exponential fit of the Ti $2p_{3/2}$ evolution upon X-rays. The first spectrum recorded represents the extrapolated value for the Ti $2p_{3/2}$ binding energy well.

Amorphous and anatase titania: Line shape and stoichiometry

The different TiO_x materials vary also in the individual line shapes of the emission lines. Fig. 8.11 shows detail spectra of O 1s and the Ti $2p_{3/2}$ emission lines for the differently prepared TiO_x. The amount of Ti^{3+} emission intensity (A), the Ti^{4+} *fwhm* (B), the OH^- to O^{2-} ratio (C) and the stoichiometry (D) are summarized in Fig. 8.12.

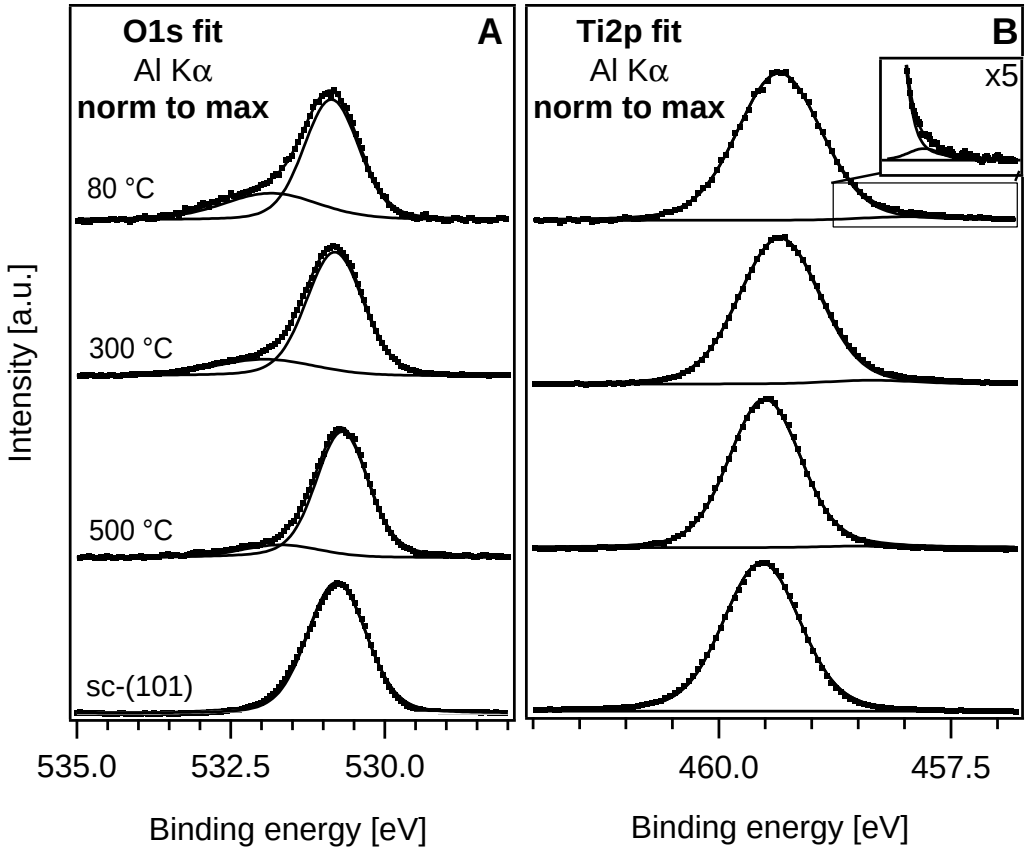

Figure 8.11. – O 1s (A) and Ti $2p_{3/2}$ (B) spectra of the as deposited 80 °C spectra, the annealed 300 °C and 500 °C spectra, and the *in situ* cleaved sc-anatase (101). The O 1s emission lines are deconvoluted with two Gaussian-Lorentzian profiles for the hydroxyl (high binding energy side) and the O^{2-} component (low binding energy side). The Ti $2p_{3/2}$ component is deconvoluted by the Ti^{4+} component (high binding energy side) and the Ti^{3+} component (low binding energy side).

Ti^{4+}/Ti^{3+} ratio and *fwhm* of Ti^{4+}: Fig. 8.12 A shows the evolution of Ti^{3+} amount with increasing annealing temperatures and for the anatase single crystal. Whereas before annealing (80 °C) and after annealing to 300 °C, the Ti^{3+}/Ti^{4+} ratio is rather high (0.4 % and 0.3 %, respectively), it decreases at annealing temperatures of 500 °C to about 0.1 %. The *in situ* cleaved single crystal has no contribution of Ti^{3+} ions or it is below XPS resolution level. The Ti^{3+} content changes with X-ray illumination, which is discussed in more detail in Section 11.2

Besides the shape of the Ti $2p_{3/2}$ emission, also the Ti^{4+} *fwhm* (see Fig. 8.12 B) of the emissions varies for the different titania samples. The low temperature samples (80 °C and 300 °C) have a Ti^{4+} *fwhm* of ∼0.95 eV, whereas the high temperature and crystalline samples (500 °C and single crystal) have a *fwhm* of ∼0.80 eV (see Table 8.1). Considering initial state effects, the crystallinity of anatase (see Section 8.1.1) is the reason of the decrease of *fwhm*. Due to the long-range order the atomic distances

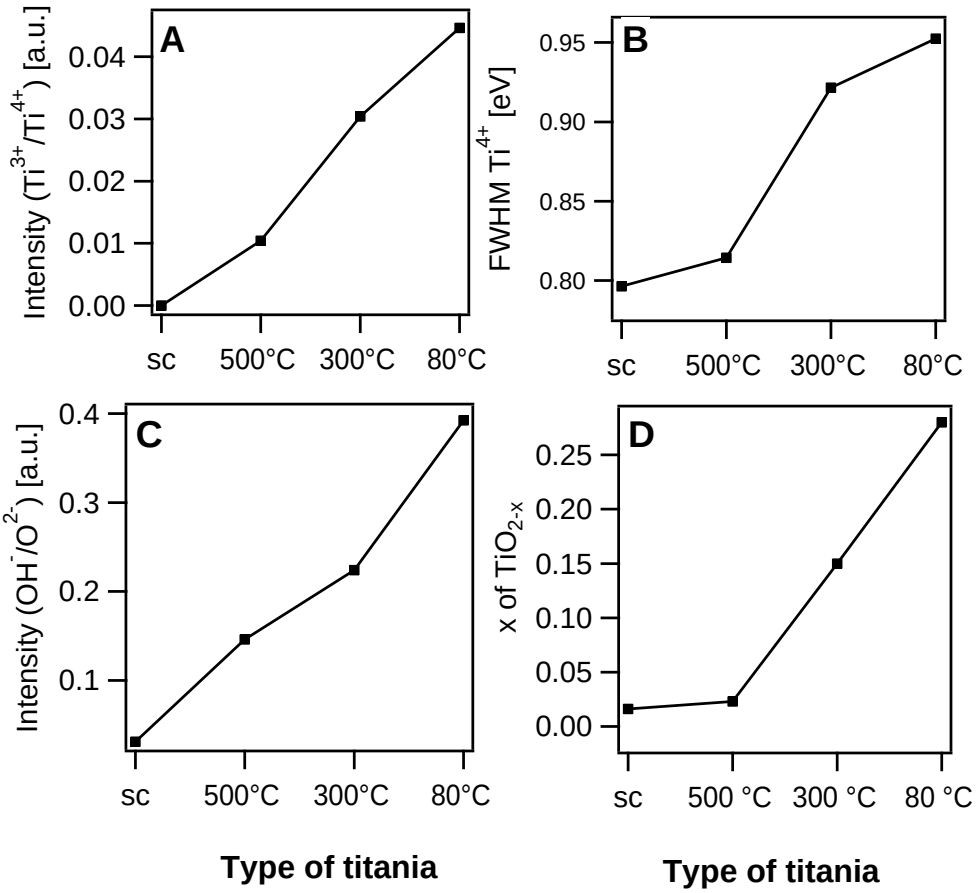

Figure 8.12. – A: Ti^{3+}/Ti^{4+} ratio of the various TiO_x (Note: The values are extracted from spectra which are measured by X-rays. X-rays may influence this ratio. A detailed analysis follows in Section 11.1 and Section 11.2); B: *fwhm* evolution of the Ti^{4+} component; C: OH^-/O^{2-} ratio; D: Stoichiometry of the different TiO_x.

to neighbors are fixed. The partial charge on all Ti atoms is the same and electrons have the same binding energy. Amorphous TiO_x materials are short-range ordered. Due to the missing crystalline order, distances between atoms and type of neighboring atoms varies more and so does the partial charge on the atoms. As a result the binding energy values of the photoelectrons diversify more and Ti^{4+} *fwhm* increases. Additionally final state effects, like photohole screening, may contribute to the variation of the Ti^{4+} *fwhm*.

OH^- to O^{2-} ratio: With increasing annealing temperatures the OH^- and CO component (around 532 eV) decreases. The OH^- component origins from non reacted precursor material (see Section 4.2) and OH^- adsorbates at the titania surface, which can form upon H_2O adsorption on titania (see Fig. 11.9). The CO component origins from precursor residues and adsorbed carbon compounds as well. With increasing annealing temperature of the titania, the precursor material reacts further, adsorbed hydroxyls species desorbs and surface contaminations are burned off. Respectively the OH^- and carbon emissions in the XP spectra diminish. The *in situ* cleaved TiO_2 single crystal shows no OH^-/CO component (Fig. 8.11 C) and no C 1s emission.

Stoichiometry: PES allows the determination of the stoichiometry of materials by comparing the intensity of respective emission lines and considering the respective atomic sensitivity factors (ASF) of the

elements for the specific XPS system (Daisy FUN, see Section 4.5.1). The stoichiometry was calculated by Eq. (1.5). ASF factors for the O 1s and the Ti $2p_{3/2}$ were taken from Ref. [151] and are 3.55 and 6.00 respectively. Figure 8.11 D shows the calculated stoichiometries for the differently prepared titania. The 80 °C titania has the lowest oxygen content and the stoichiometry is $\sim TiO_{1.75}$. Upon annealing the 80 °C titania in air at 300 °C and 500 °C, the stoichiometry changes to $TiO_{1.85}$ and $TiO_{1.98}$ respectively. The *in situ* cleaved anatase single crystal (sc) has a calculated stoichiometry of $TiO_{1.98}$ as well. Therefore it can be assumed, that the accuracy of the determined stoichiometry is reasonable and 500 °C annealed titania is, or almost is, stoichiometric TiO_2. The calculated stoichiometry fits well with the decreasing Ti^{3+}/Ti^{4+} ratio. Only the relatively high Ti^{3+} content of the 500 °C TiO_x and its almost perfect stoichiometry is counter intuitive, but has its origin probably in the accuracy of XPS.

Summary and discussion

In this chapter the influence of annealing temperature on ALD prepared *ex situ* TiO_x was investigated and the results were compared with an *in situ* cleaved anatase single crystal. The *in situ* sc-anatase (101) surface is free of contaminations. Ti^{3+} emission is not visible in the XPS spectra even though results in Section 17.1 indicate the presence of V_O at the very surface.

First the distance between the O 1s and Ti $2p_{3/2}$ emission line among all examples was compared. It could be shown that the distance between the O 1s and the Ti $2p_{3/2}$ line decreases upon the transformation from amorphous to anatase from 71.5 eV to 71.2 eV and Ti $2p_{3/2}$-VBM changes from 455.80 eV to 456.00 eV respectively. For anatase the Ti $2p_{3/2}$-VBM distance was determined experimentally and theoretically by Pfeifer et al. to be 456.00 eV as well.[149] For amorphous TiO_x values of 71.5 eV have been reported e.g. by Ou et al. but literature values are diverse.[141] The change of O 1s-Ti $2p_{3/2}$ distance indicates a change of the partial charge at the oxygen and titanium atoms. Possibly the partial charge of the oxygen atoms increases (becomes more negative) and the partial charge of titanium atoms decreases (becomes more positive) upon annealing to 500 °C. As the oxygen content increases from amorphous to anatase, a higher Ti atom coordination around the O atom can be excluded to be the origin of the partial charge increase of oxygen. As oxygen is more electronegative than titanium a decrease of the interatomic distances between oxygen and titanium could cause the increase of the partial charge of oxygen. The reason for the decrease of the Ti^{4+} *fwhm* is the ordering of the atoms, which occurs along with transformation from amorphous to crystalline. The decrease of the OH^- to lattice O^{2-} ratio upon annealing is that hydrogen or OH^- either reacts further or burns off. The stoichiometry change is due to the annealing process at air. Non-reacted precursor material (TTIP) can react further and oxygen vacancies can be filled in addition with atmospheric oxygen. Further systematic changes in dependence of annealing temperature can be observed for the Ti^{3+} content, but in addition the Ti^{3+} content is strongly influenced by incident X-ray and UV radiation which will be discussed in Section 11.1 and Section 11.2.

8.3 Photoemission spectroscopy of C_{60}

C_{60} is a black powder and can be evaporated without destruction at temperatures of about 400 °C at a base pressure of about $1 \cdot 10^{-9}$ mbar. Such a deposition give polycrystalline grain sizes of 70-100 nm.[152]

To analyze the electronic properties of C_{60} a 150 Å thick C_{60} film was evaporated onto a gold substrate and analyzed with $Al_{K\alpha}$, HeI (red spectra in (Fig. 8.13) and synchrotron radiation (black spectra

in (Fig. 8.13). Prior to the deposition of C_{60}, the gold substrate was Ar-sputtered for 10 min. After sputtering it was free of any adsorbates. After C_{60} deposition the C 1s emission line was observed no gold related emission lines. The SE-edge cutoff (Fig. 8.13 left) is at 4.5 eV and in good accordance with literature values.[153,154] The bottom spectra (red) were recorded with a conventional monochromated $Al_{K\alpha}$ source and the C 1s binding energy is at 284.92 eV. The top spectra were recorded at the synchrotron with an excitation energy of 400 eV and the C 1s binding energy is at 284.86 eV. The C 1s emissions show the typical satellite structure of C_{60} at the high binding energy side of the main emission. The satellites are about 1.9 eV (A'), 3.7 eV (B') and 5.6 eV (C') above the C 1s emission and origin of photoelectrons, which undergo inelastic scattering processes as e.g. excitations of valence band electrons across the energy gap (PES E_G of C_{60} is ~2.3 eV, see at the end of this section and Section 5.1 for shake-ups in PES).[155] On the right the VB range spectra are plotted. Both VB spectra show the typical fingerprint of C_{60} with three emissions at around 2.2 eV (HOMO, A), 3.6 eV (SOMO, B) and 5.8 eV (C). The energetic difference of the VB features and the satellite structure have a good accordance and support that the satellite structure of C 1s origins from shake-up processes from the VB features A, B and C.
The C_{60} VB structure measured with 90 eV excitation energy shows different intensity ratios than the HeI measurement. Whereas the HOMO and the SUMO of the HeI spectra have almost the same intensity, in the 90 eV spectra the SOMO intensity is about twice more intense as the HOMO. The maxima of the HOMO ($HOMO_{max}$) are at 2.17 and 2.27 eV for 90 eV and HeI excitation energy, respectively. This results in a C 1s-$HOMO_{max}$ distance of about 282.7 eV. Literature reports values between 2.0 and 2.5 eV for the $HOMO_{max}$ position. The difference may depend on the deposition method, layer thickness or substrate material.[156–159] The differences in the C 1s-$HOMO_{max}$ distances are in good accordance with former results by Hein et al. (synchrotron induced photoemission)[160] and Reinke et al. (XPS and UPS).[161] The $HOMO_{onset}$ positions are at around 1.8 eV ($h\nu$=HeI) and 1.65 eV ($h\nu$=90 eV). The distance of the $HOMO_{onset}$ to the C 1s core level emission is 283.1 eV ($h\nu$=$Al_{K\alpha}$) and 283.2 eV ($h\nu$=400 eV). After UPS measurement the C 1s core level emission and the secondary electron edge were measured again and show constant values at 284.92 eV E_{Bin} and at 4.5 eV E_{Kin}, respectively.

The CB of C_{60} can be measured by inverse photoemission spectroscopy (IPES) and hence a combination of PES and IPES enables the determination of energy gap E_G. E_G in organic semiconductors is either defined by the $HOMO_{max}$-$LUMO_{max}$ or the $HOMO_{onset}$-$LUMO_{onset}$ distance. According to literature the $HOMO_{max}$-$LUMO_{max}$ distance of C_{60} is around 3.5 eV[162] and the $HOMO_{onset}$-$LUMO_{onset}$ distance is between 2.3 and 2.4 eV.[26,162–164] While the $HOMO_{max}$-$LUMO_{max}$ distance is easier to determine, the $HOMO_{onset}$-$LUMO_{onset}$ distance is of more relevance, as it matches better to the transport gap E_T, which represents the gap between the energy levels, relevant for conduction in organic semiconductors (see Section 2.1.4).[165]

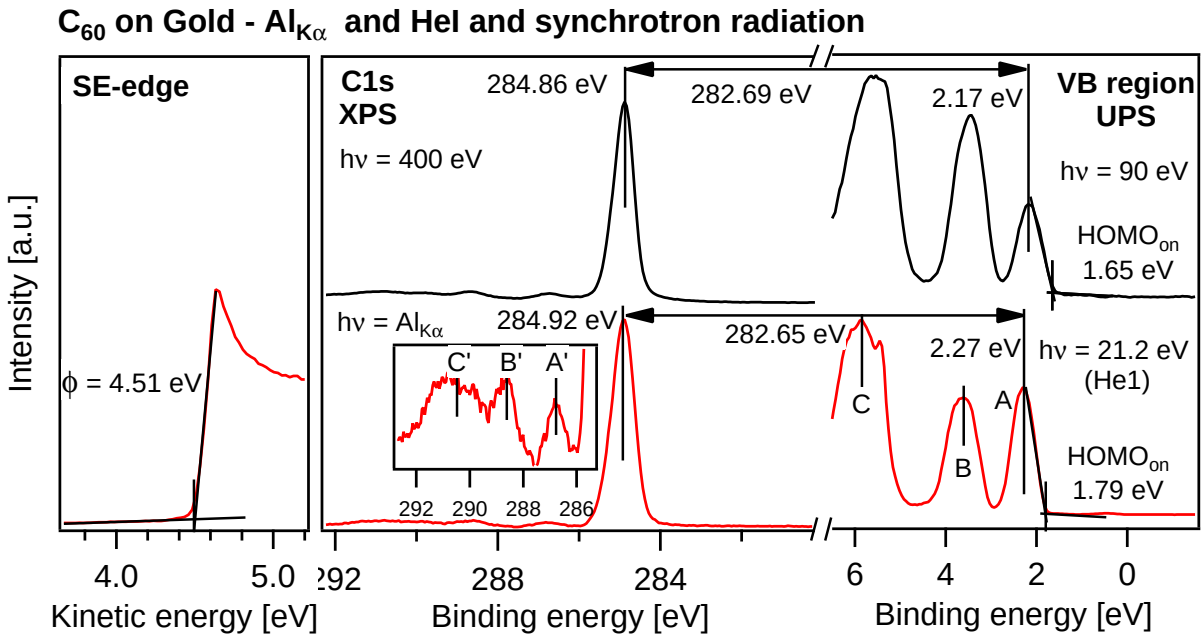

Figure 8.13. – SE-edge (left), C 1s (middle) and valence band spectra (right) of C_{60} on gold. Black spectra (top) were recorded at the synchrotron with an excitation energy at maximum of surface sensitivity. Red spectra were recorded at the Daisy-Fun with $Al_{K\alpha}$ and He1 radiation. The WF of C_{60} is 4.5 eV. The C 1s main emission is at around 284.9 eV and the typical satellites structure (A',B' and C') of C_{60} appears on the high binding energy side. The $HOMO_{max}$ is at 2.2 to 2.3 eV and the $HOMO_{onset}$ at 1.7 to 1.8 eV.

8.3.1 Comparison of the electronic structure of C_{60} and $PC_{61}BM$

In the presented I-V curves of IOSCs in Chapter 7, $PC_{61}BM$ is used as an electron acceptor. As $PC_{61}BM$ cannot be evaporated[95], a thin film deposition of $PC_{61}BM$ on the metal oxide is challenging and the characterization of the metal oxide C_{60} interface is difficult, C_{60} was used as model acceptor material. In Chapter 7 unipolar devices with $PC_{61}BM$ and C_{60} are shown, indicating a good comparability of $PC_{61}BM$ and C_{60} in terms of their electronic behavior.

For comparison a drop-casted $PC_{61}BM$ film on an 80 °C TiO_x substrate has been characterized as well. The $PC_{61}BM$ thickness, calculated from damping of the Ti $2p_{3/2}$ emission, is about 100 Å. Figure 8.14 shows the O 1s, Ti $2p_{3/2}$ and the C 1s emission line after $PC_{61}BM$ deposition. The O 1s emission consists of three peaks at about 534 eV, 532.5 eV and 530.8 eV. The two emissions to the left (high binding energy side) are attributed to $PC_{61}BM$, whereby the emission at 534 eV originates from oxygen in the methoxy group of $PC_{61}BM$ and the emission at 532.5 eV originates from the carbonyl group.[26,166] The low binding side emission still belongs to the O 1s emission of the TiO_x substrate. The Ti $2p_{3/2}$ emission has it maximum at 459.3 eV and the C 1s emission of $PC_{61}BM$ has its maximum at 285.2 eV, which is in good agreement with C_{60} on TiO_x (see Table 9.1).

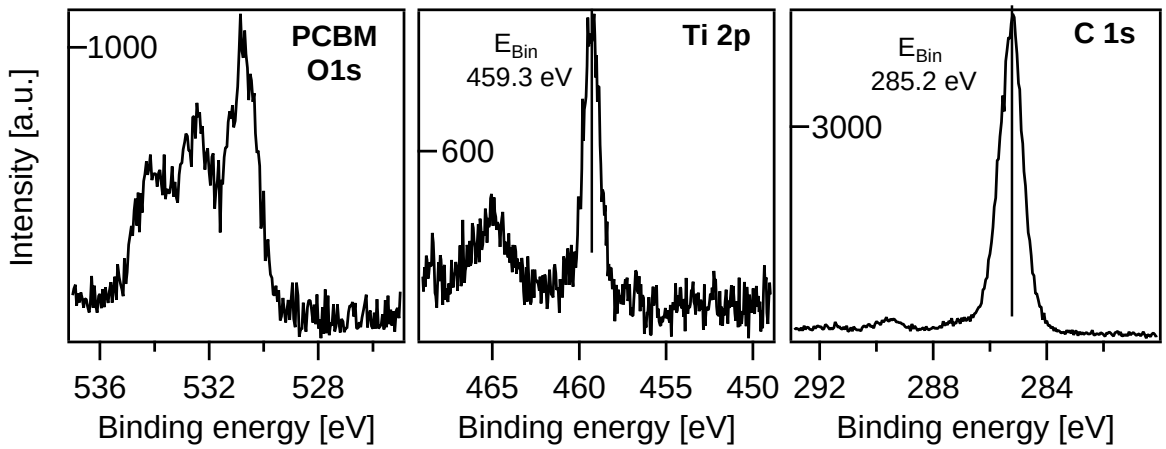

Figure 8.14. – O 1s (left), Ti $2p_{3/2}$ (middle) and C 1s photoemission spectra of drop-casted $PC_{61}BM$ on 80 °C TiO_x.

In Fig. 8.15 the electronic levels of C_{60} and $PC_{61}BM$ are compared. The data for C_{60} is extracted from Table 9.1 (C 1s position) and Fig. 8.13 (C 1s-$HOMO_{onset}$ distance). Data for the C 1s position of $PC_{61}BM$ is taken from Fig. 8.14 and the C 1s-$HOMO_{onset}$ distance was provided by Julia Maibach.[24] The C_{60} energy gap is between 2.3 and 2.4 eV and has been determined by combined inverse photoemission and photoemission measurements.[26,162,163] The $PC_{61}BM$ energy gap has been determined to be between 2.0-2.1 eV by combined inverse photoemission and photoemission experiments, NEXAFS and by electrochemical oxidation and reduction.[26,167,168] As depicted in Fig. 8.15 the LUMO position of C_{60} is similar to the LUMO position of $PC_{61}BM$ evidencing, that C_{60} is a suitable model acceptor material for $PC_{61}BM$ with respect to the electronic alignment to the metal oxide conduction band.

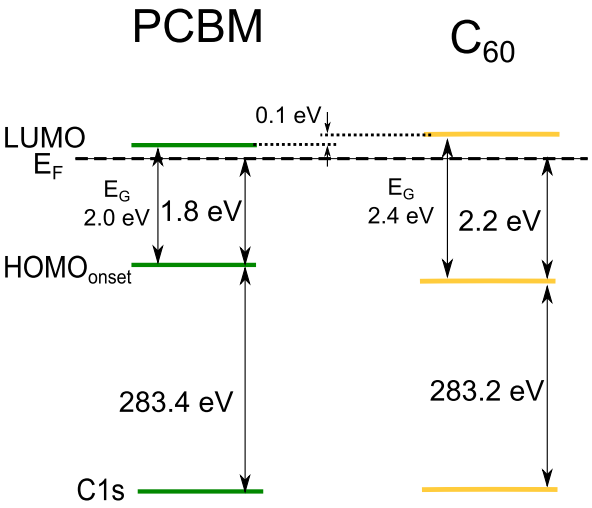

Figure 8.15 – Comparison of the energetic level positions of $PC_{61}BM$ (green, left) and C_{60} (yellow, right). C 1s and $HOMO_{onset}$ positions are directly measured by XPS. The values for the energy gap of $PC_{61}BM$ and C_{60} are extracted from literature.[26] The WF of $PC_{61}BM$ could not be measured due to technical problems and therefore the C_{60} WF was not added as well.

9 Photoemission spectroscopy of the titanium dioxide - C_{60} interface and the effect of UV illumination

Motivated by the removal of S-shaped I-V curves and the increase of the FF upon UV illumination of inverted organic solar cells (IOSCs) with TiO_x as ETL and a P3HT:PC_{61}BM blend as organic absorber (see Fig. 9.1) a detailed investigation of the influence of UV light on IOSC is performed.
While processing IOSC by spin-coating the P3HT:PC_{61}BM blend, a vertical phase separation takes place, which leads to an enrichment of PC_{61}BM at the surface and an abundance of P3HT at the organic/substrate interfaces.[134] In Chapter 7 it was shown that evidence is given that the ETL/organic interface is relevant for UV induced changes of the I-V characteristics and the respective interface is investigated. Instead of PC_{61}BM, C_{60} is used as model acceptor material as PC_{61}BM cannot be evaporated without destruction[95] and a step-by-step deposition, e.g. by drop casting or nebulizing is not possible, as control of the layer thickness is difficult and e.g. nebulizing leads to droplet formation on the substrate.[24] The comparability concerning the TiO_x/C_{60} interface to the TiO_x/PC_{61}BM interface and the similarity with respect to their electronic behavior is shown in Chapter 7 and Section 8.3.1. In this chapter only the influence of UV light on the TiO_x and C_{60} core levels as well as the WF are discussed. The whole energy band diagram of the respective interface is derived in Chapter 15.

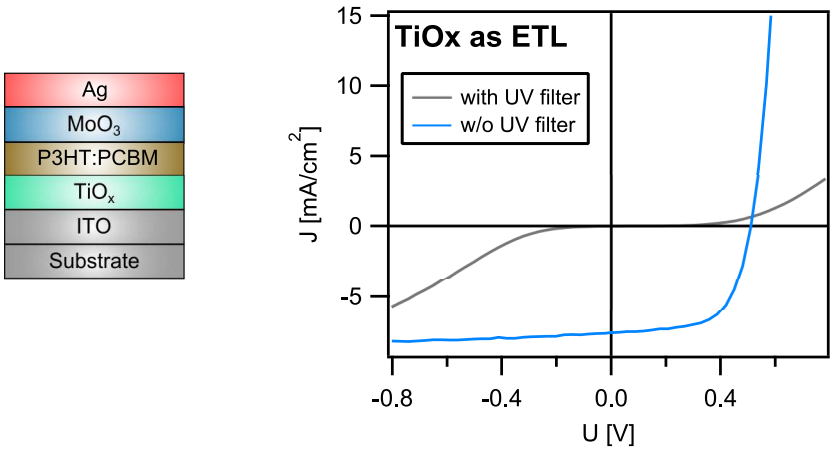

Figure 9.1. – Left: Layer sequence of an IOSC device used for the recorded I-V curves. Right: I-V characteristics of IOSC recorded with UV-filter (gray) and without UV-filter (blue).

9.1 The TiO_x 80 °C/C_{60} interface and influence of UV illumination

In order to investigate the influence of UV on the TiO_x/C_{60} interface, a C_{60} layer was deposited onto 80 °C TiO_x substrate and subsequently measured by photoelectron spectroscopy ($Al_{K\alpha}$ radiation),

irradiated with UV light (365 nm) for 60 min and measured again by photoelectron spectroscopy. This was performed for the TiO_x substrate and for four different C_{60} layer thicknesses on top of the substrate. For each C_{60} layer a new TiO_x substrate was used. By measuring different C_{60} coverages on TiO_x, it is possible to draw an energy diagram before and after UV illumination.

C_{60} was evaporated with a rate of about 0.15 Å/s for 20, 60, 120 and 1200 s onto a TiO_x 80 °C substrate. The nominal layer thicknesses are calculated by the damping of the Ti $2p_{3/2}$ emission and are 3, 10, 26 and 180 Å, respectively. The experiments were performed at the Daisy-Fun (Section 4.5.1), which is equipped with a monochromatic $Al_{K\alpha}$ source. To determine a possible influence by the $Al_{K\alpha}$ radiation, initial, X-ray exposed, only UV and X-ray + UV light exposed spectra were recorded. Initial spectra were measured at first and only one scan, with modified margins, of each spectrum was recorded and hence are minimally influenced by the radiation used for the measurements. The X-ray exposed spectra (indicated only with *X-ray*) were recorded after about 600 s $Al_{K\alpha}$ illumination with an increased number of scans and standard measurement margins. After 60 min *in situ* UV illumination, X-ray spectra were recorded on a new sample spot, which was not irradiated with X-rays before. The only UV spectrum was measured with the same settings as the initial spectrum before UV illumination and minimal X-ray influence. The X-ray + UV spectra were recorded again after about 600 min of $Al_{K\alpha}$ radiation. One exception is the measurement of the TiO_x substrate without C_{60}, in this case no spectrum, which was exposed only to UV light, was recorded.
The position of the secondary electron edge is determined by a linear extrapolation of the intersection with the background. The Ti $2p_{3/2}$ position is determined by a fit of the emission lines with two Gaussian-Lorentzian profiles for the Ti^{4+} and Ti^{3+} components. As binding energy the energetic position of the Ti^{4+} position is used. The O 1s emission is fitted with two Gaussian-Lorentzian profiles as well, one for hydroxides derived species on the high binding energy side of the emission and one for the O^{2-} species derived from lattice oxygen. As O 1s binding energy, the energetic position of the O^{2-} position is used. The C 1s emission was only fitted with one Gaussian-Lorentzian profile.

The TiO_x 80 °C substrate

In Figure Fig. 9.2 three sets of data for TiO_x 80 °C substrate are displayed. On the left the SE-edge, in the middle the O 1s emission line and on the right the Ti $2p_{3/2}$ level are displayed. The lowest spectra were recorded directly after the first exposure to $Al_{K\alpha}$ X-rays, the intermediate spectra after around 600 s of X-ray irradiation and the upper spectra after additional *in situ* irradiation with UV-light (365 nm). The influence of only UV light was not determined for the TiO_x 80 °C substrate, hence a distinction between X-ray and UV influence on the TiO_x is not possible. A distinction of the X-ray and UV influence was performed only on a TiO_x 500 °C substrate and reveals that X-ray and UV light induces the same shifts, but that the influence of UV light is more severe (see Appendix A.2).
On the pristine sample spot, the SE-edge position is at 4.12 eV kinetic energy. Upon illumination with X-rays the SE-edge position shifts to 4.00 eV and after UV illumination further to 3.90 eV. The energetic position of the O 1s emission is also influenced by X-ray and UV radiation. On the non-exposed spot the main O 1s emission is situated at 530.69 eV binding energy and shifts with X-rays to 530.80 eV and after

UV to 530.88 eV. In the course of X-ray irradiation, the Ti $2p_{3/2}$ line shifts from 459.20 eV to 459.35 eV binding energy up to 459.42 eV after UV irradiation.
As core lFspecbvels and the SE-edge shift about the same amount in the same direction, a formation or change of a possible surface dipole is excluded. The observed shifts can be either due to induced downward band bending or removal of an initially given upward band bending of the energy levels at the TiO_x surface.

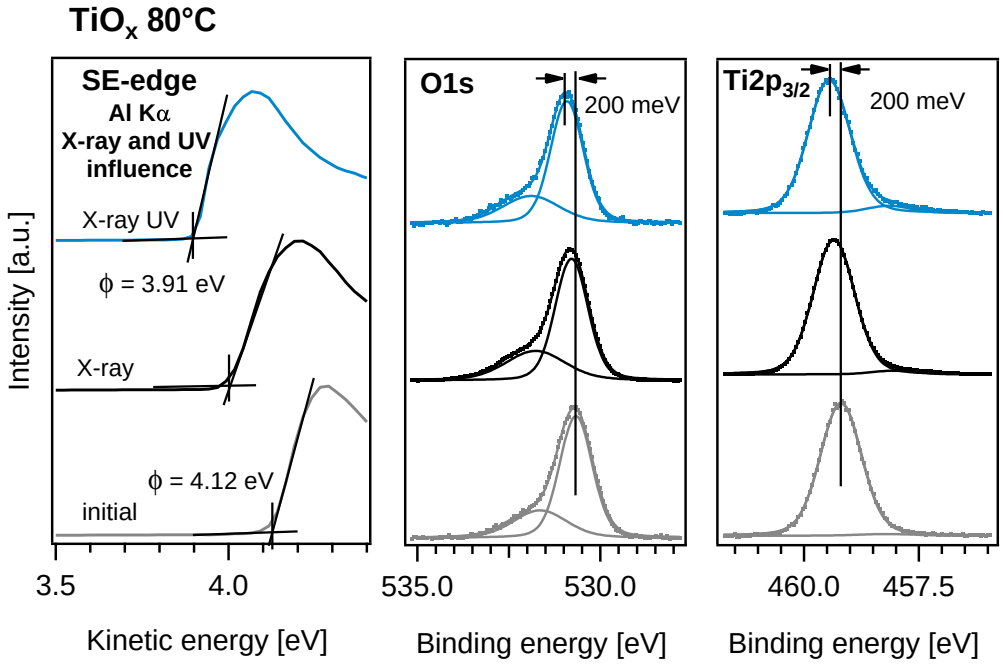

Figure 9.2. – SE-edge (left), O 1s (middle) and Ti $2p_{3/2}$ (right) spectra of the as deposited 80 °C TiO_x sample. Gray spectra (initial) are minimally exposed to X-rays. Black spectra (X-ray) are exposed to X-ray for about 600 s. Blue spectra (UV) were exposed additionally to 60 min UV light.

TiO_x 80 °C + 3 Å C_{60}

Figure 9.3 shows spectra of a TiO_x sample with a nominal coverage of 3 Å C_{60} on top of it. On the left the SE-edge, in the middle the Ti $2p_{3/2}$ and on the right the C 1s level of TiO_x/3 Å C_{60} sample upon X-ray and UV exposure are displayed. The O 1s shifts in parallel to the Ti $2p_{3/2}$ emission and is not displayed. Of each emission the influence of X-rays and UV light was investigated. Gray spectra are initial, black spectra are X-ray exposed, light blue spectra are only UV irradiated and dark blue spectra are UV and X-ray irradiated.

With respect to the initial SE-edge spectrum, the SE-edge spectrum shifts in total by 50 meV to lower kinetic energies after UV and X-ray illumination. This shift already occurs after X-ray illumination. Compared to the SE-edge shift of the pristine substrate in Fig. 9.2, the decrease is 150 meV smaller. The Ti $2p_{3/2}$ emission (middle) shifts first by ~50 meV to higher binding energies upon X-ray irradiation (gray to black). UV illumination increases the shift by ~100 meV (black to dark blue). Comparing the initial Ti $2p_{3/2}$ binding energy (gray) and the binding energy after UV illumination (bright blue) a 100 meV shift is observed as well. In this case X-rays shift the Ti $2p_{3/2}$ emission by 50 meV and UV light

by 100 meV to higher binding energies. In total the Ti $2p_{3/2}$ shift is 50 meV less, than the shift of the pristine TiO_x in Fig. 9.2. About 100 meV of this shift are caused by UV light and 50 meV are caused by X-rays. On the right the C 1s level of C_{60} is displayed. To obtain the binding energy position of the C_{60} C 1s level, the substrate C 1s emission was subtracted from the C 1s spectrum with C_{60}. In total, the C 1s level shifts by 150 meV to lower binding energies upon UV illumination (gray to bright blue spectrum). X-rays already induce a shift of 50 meV (gray to black), but X-rays do not induce a shift after UV illumination (bright blue to dark blue). In contrast to the Ti $2p_{3/2}$ emission, X-ray and UV light have the same effect on the C 1s emission and UV light just has a stronger impact. All energetic positions of the SE-edge, the Ti $2p_{3/2}$ level and the O 1s level are summarized in Table 9.1.

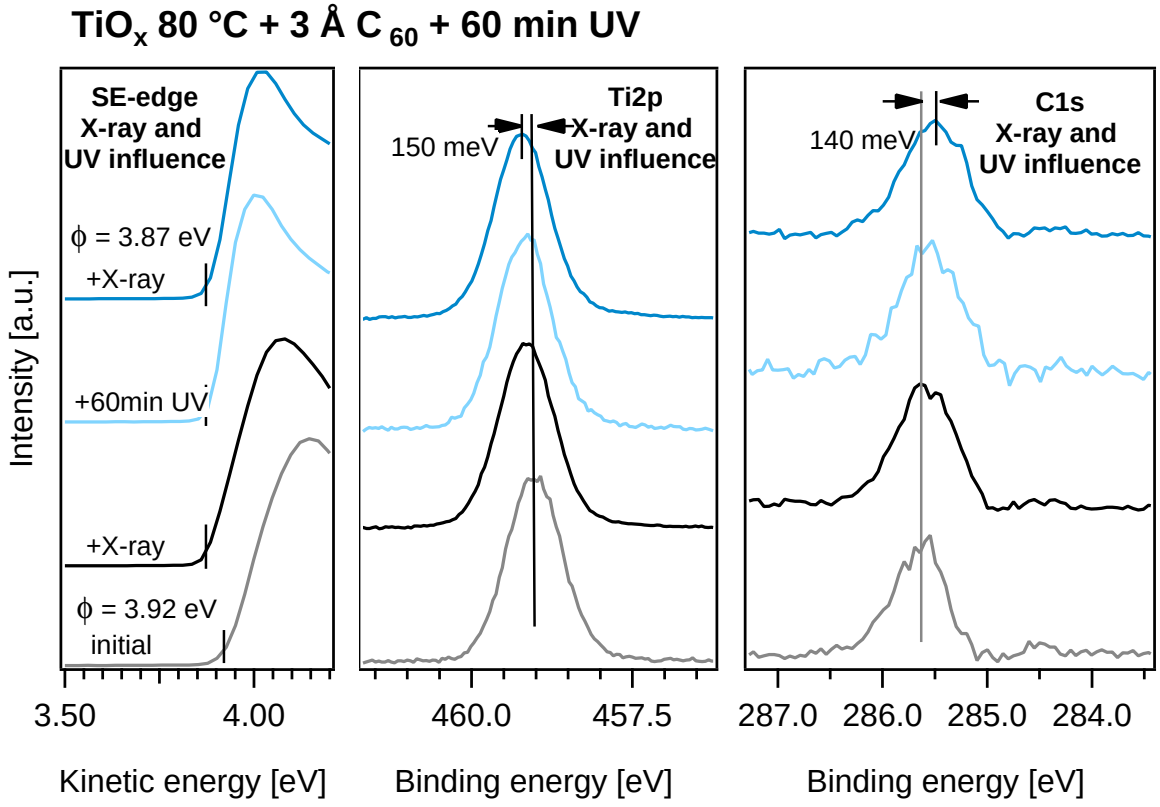

Figure 9.3. – SE-edge (left), Ti $2p_{3/2}$ (middle) and C 1s (right) spectra of the 3 Å C_{60} on TiO_x 80 °C sample. Gray spectra (initial) are minimally exposed to X-rays. Black spectra (X-ray) are exposed to X-ray for about 600 s. Bright blue spectra (UV) are exposed additionally to 60 min UV light and dark blue spectra to UV light and X-rays.

Comparison of energetic positions in dependence of C_{60} layer thickness on TiO_x 80 °C

The influence of UV light was investigated as well for higher C_{60} coverages on TiO_x. Only the initial and the X-ray + UV exposed spectra are considered. The initial and the X-ray + UV influenced spectra are depicted in Fig. 9.4 for the various C_{60} coverages. From bottom to top, the C_{60} coverages increase. Right at the bottom the TiO_x substrate spectra are displayed and are followed by spectra with 3, 10, 26 and 180 Å C_{60} coverage. On the left the SE-edge (left), in the middle the Ti $2p_{3/2}$ emission and on the right the C 1s emission are displayed with increasing C_{60} coverage and in dependence of UV irradiation

(black: before UV, blue: after UV).

As already shown, the SE-edge of the TiO_x substrate without C_{60} coverage shifts by 200 meV from 4.1 eV to 3.9 eV kinetic energy upon UV illumination. After the deposition of the nominal layer thicknesses of 3, 10 and 26 Å C_{60}, the initial SE-edge is situated at ~4 eV kinetic energy. At 3 Å the SE-edge shifts ~50 meV to lower kinetic energies after UV, while at 10 Å C_{60} the SE-edge is almost constant after UV. At 26 Å coverage the SE-edge increases from 4.00 eV to 4.15 eV kinetic energy. The sample with the 180 Å C_{60} coverage has its SE-edge position at 4.2 eV and a small influence of X-rays is observed, but none of UV light (see Table 9.1). Ti $2p_{3/2}$ spectra are displayed in the middle of Fig. 9.4. Before UV light exposure the Ti $2p_{3/2}$ binding energy position is constant at ~459.2 eV with increasing C_{60} coverage (from bottom to top). After UV illumination the binding energy shifts for all investigated C_{60} coverages by 200 meV to 459.4 eV. On the right of Fig. 9.4 the evolution of the C_{60} C 1s level is shown. The bottom spectrum shows the C 1s emission of the TiO_x substrate and is subtracted from all spectra above. No influence on the energetic position and the line shape of the substrate C 1s emission before and after UV illumination is observed. The second C 1s spectrum from below (3 Å C_{60}) is magnified by the factor of three. Before UV illumination, the C 1s level shifts from 285.8 eV to 285.4 eV with increasing C_{60} coverage. While from 3 to 26 Å C_{60} the C 1s shift is about 100 meV to lower binding energies, the binding energy increases by 300 meV from 26 Å to 180 Å. After UV illumination the C 1s level of the 3, 10 and 26 Å C_{60} covered TiO_x substrates, shifts by 150 meV to smaller binding energies. Hence it shifts in the contrary direction of the Ti $2p_{3/2}$ emission line (Ti $2p_{3/2}$ shifts to higher E_{Bin} after UV). At 180 Å C_{60} coverage UV light induces no shifts of C 1s level and it stays constant at 285.4 eV. In total the C 1s level undergoes a shift of 200 meV from 285.6 eV to 285.4 eV with increasing C_{60} coverage after UV illumination. In Fig. 9.5 the course of the Ti $2p_{3/2}$, C 1s (left) and WF (right) energy levels before and after UV illumination are shown.

For all C_{60} coverages the Ti $2p_{3/2}$ level is at 459.2 eV before UV illumination and at 459.4 eV after UV illumination. Before UV illumination the C 1s level shifts by 400 meV to lower binding energies with increasing C_{60} coverage. After UV light illumination the C 1s level shifts by about 150 meV to lower binding energies up to 26 Å C_{60} coverage. At 180 Å C_{60} coverage no shift occurs. The overall shift of the C 1s emission binding energy to lower binding energies is reduced to 200 meV with increasing C_{60} coverage. The SE-edge of the TiO_x substrate shifts to lower E_{Kin} after UV illumination and shows almost no shift at 3 and 10 Å C_{60}. At 26 Å C_{60} the SE-edge shifts to higher E_{Kin} upon UV illumination, while at 180 Å C_{60} UV induces almost no shift of the SE-edge. The energetic values for the various C_{60} coverages are summarized in Table 9.1.

9.2 Energy diagram of the 80 °C TiO_x/C_{60} interface

From the spectra obtained in Fig. 9.4 an energy diagram of the TiO_x 80 °C/C_{60} interface before and after UV exposure is derived and sketched in Fig. 9.6. Depicted are the directly measured Ti $2p_{3/2}$ and C 1s core levels and E_{Vac}. The VBM of TiO_x and the $HOMO_{onset}$ of C_{60} are not included yet, as the UV influence will first be discussed on the basis of the changes of the core levels. The complete energy band line-up including the TiO_x VBM/CB and the C_{60} HOMO/LUMO is discussed in Chapter 15. The energy

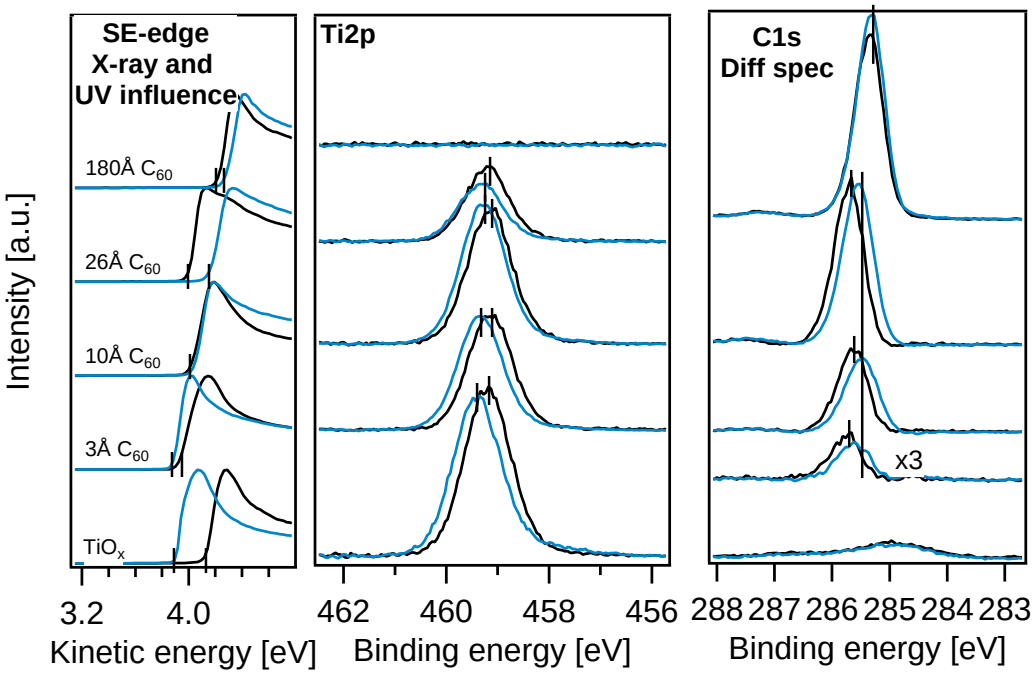

Figure 9.4. – SE-edge (left), Ti $2p_{3/2}$ (middle) and C 1s (right) spectra of the TiO_x/C_{60} interface. Black spectra are initial spectra with lowest possible X-ray exposure. Blue spectra are recorded after 60 min of UV illumination. The bottom spectra are of the TiO_x substrate. Other spectra are covered with 3, 10, 26 and 180 Å C_{60}. After UV illumination the Ti $2p_{3/2}$ levels shift by ~200 meV to higher binding energies. Despite the C_{60} layer of highest coverage, the C_{60} C 1s level shifts by 200 meV to lower binding energies after UV illumination.

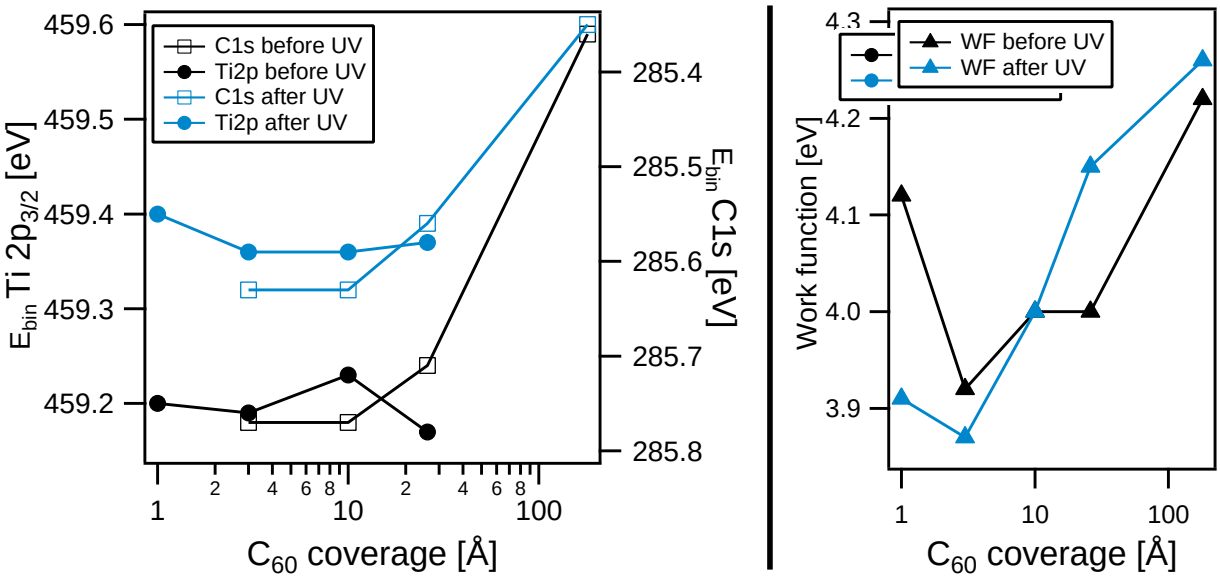

Figure 9.5. – Binding energy (Ti $2p_{3/2}$ and C 1s) and work function evolution for increasing C_{60} coverages on amorphous 80 °C TiO_x. The Ti $2p_{3/2}$ emission is constant independently of the C_{60} coverage, but after UV illumination it increases by 200 meV. The C 1s binding energy decreases with increasing C_{60} coverage as it does after UV illumination (200 meV). The WF evolution has two different trends. At no or low C_{60} coverage the WF decreases, while at higher C_{60} coverages the WF starts to increase after UV illumination.

Table 9.1. – Work function (WF) and Ti $2p_{3/2}$ and C 1s level values of the 60 °C TiO_x samples with different C_{60} coverages.

	C_{60} [Å]	absolute values				with respect to initial			
		initial	X-ray	UV	UV + X-ray	initial	X-ray	UV	UV + X-ray
WF [eV]	0	4.12	4.00	-	3.91	0	0.12	-	0.21
Ti $2p_{3/2}$ [eV]		459.20	459.35	-	459.40	0	-0.15	-	-0.20
C 1s [eV]		-	-	-	-	-	-	-	-
WF [eV]	3	3.92	3.87	3.87	3.87	0	0.05	0.05	0.05
Ti $2p_{3/2}$ [eV]		459.19	459.26	459.30	459.36	0	-0.08	-0.11	-0.17
C 1s [eV]		285.77	285.72	285.68	285.63	0	0.05	0.09	0.14
WF [eV]	10	4.00	4.00	4.00	4.00	0	-0.05	0	-0.05
Ti $2p_{3/2}$ [eV]		459.23	459.29	459.33	459.36	0	-0.06	-0.10	-0.13
C 1s [eV]		285.77	285.72	285.64	285.63	0	0.05	0.13	0.15
WF [eV]	26	4.00	4.05	4.11	4.15	0	-0.05	-0.11	-0.15
Ti $2p_{3/2}$ [eV]		459.17	459.27	459.33	459.37	0	-0.10	-0.16	-0.18
C 1s [eV]		285.71	285.69	285.62	285.56	0	0.02	0.09	0.15
WF [eV]	180	4.22	4.26	4.23	4.26	0	-0.04	-0.01	-0.05
Ti $2p_{3/2}$ [eV]		-	-	-	-	-	-	-	-
C 1s [eV]		285.36	285.38	285.36	285.35	0	-0.02	0	-0.01

levels of the TiO_x are drawn short to indicate that photoelectron escape depth is only about 10 nm. Therefore no statement about any possible band bending towards the bulk of TiO_x can be made.

Before UV illumination the TiO_x shows no shift of the Ti $2p_{3/2}$ core level with increasing C_{60} coverage. Therefore the energy Ti $2p_{3/2}$ is drawn flat towards the interface. The C 1s binding energy changes from 285.4 eV to 285.8 eV and hence C_{60} shows a downward band bending of 0.4 eV towards the interface. The distance of the Ti $2p_{3/2}$ and C 1s level at the surface is 173.4 eV and is directly determined from the XP spectra with 3Å C_{60} coverage. The interface dipole between TiO_x and C_{60} is -0.25 eV and originates from the WF difference of TiO_x (4.1 eV) and C_{60} (4.25 eV) and the 0.4 eV band bending of C_{60} towards the interface.

After UV illumination, the Ti $2p_{3/2}$ level shifts at all C_{60} coverages by 200 meV to ~459.4 eV binding energy and no band bending occurs in the TiO_x. At low C_{60} coverages, the C 1s level of C_{60} decreases in binding energy by about 200 meV after UV irradiation. At 180 Å C_{60} coverage UV induces no changes of the C 1s level. The TiO_x substrate WF after UV is 3.9 eV and the C_{60} WF of highest coverage after UV is 4.25 eV. For the construction of the energy diagram of the TiO_x/C_{60} interface after UV illumination it is assumed that the WF of TiO_x and the Ti $2p_{3/2}$ binding energy at the interface has the value of the pristine substrate after UV (WF: 3.9 eV and Ti $2p_{3/2}$: 459.4 eV). Furthermore it is assumed, that even at the highest C_{60} coverages the C 1s level at the interface behaves as the C 1s level at low coverages. At low C_{60} coverages, UV shifts the C 1s level by 200 meV to lower binding energies the band bending of C_{60} is reduced to 0.2 eV. Due to the decreased WF of TiO_x and the reduced band bending of 0.2 eV, the interface dipole changes direction after UV illumination and its value is -0.15 eV. The total change of the interface dipole is 0.4 eV. The change of the interface dipole is reflected by an increase of the Ti $2p_{3/2}$-

C 1s distance from 173.4 eV to 173.8 eV. The valence and conduction band of the respective materials is not added, this will be done in Chapter 15.

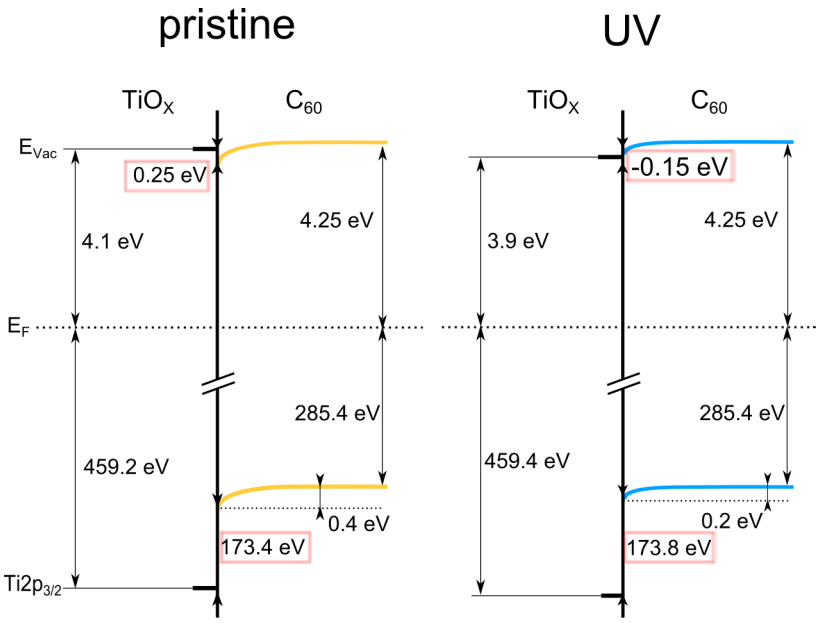

Figure 9.6. – Energy diagram of the TiO_x/C_{60} interface before (left) and after UV illumination (right). The interface dipole before UV illumination is 0.25 eV and the Ti $2p_{3/2}$-C 1s distance is 173.4 eV. After UV illumination the interface dipole changes direction and is -0.15 eV. The Ti $2p_{3/2}$-C 1s distance increases by 0.4 eV to 173.8 eV. The valence and conduction band of the respective materials is not added. This will be done in Chapter 15.

Analysis of the Ti $2p_{3/2}$ and C 1s line shape

In Fig. 9.7 the evolution of the Ti^{3+} content and the C 1s *fwhm* of the previous interface experiment are displayed with respect to the UV influence. Black dots represent values before UV illumination and blue dots after UV illumination. Gray spots represent the Ti^{3+} content of the specific TiO_x substrate before C_{60} deposition. As a measure for Ti^{3+} content the proportion of the Ti^{3+} emission of the whole Ti $2p_{3/2}$ emission is used. The evolution of the Ti^{3+} proportion is of interest as they indicate the concentration of oxygen defects V_O, which act a adsorption sites for e.g. H_2O, OH or O_2 and influence the electrical conductivity of TiO_x.[16,73] UV induced changes of the C 1s *fwhm* are an evidence of an additional component of C_{60} appearing (increase of *fwhm*) or disappearing (decrease of *fwhm*) in the emission. A second component can appear e.g. due to decomposition of C_{60}, a change of the band bending within the photoelectron escape depth, a doping of parts of the C_{60} layer or a change of the partial electron density at the C_{60} molecule due to UV illumination.

All substrate Ti $2p_{3/2}$ emissions have an initial Ti^{3+} content of about 1.5 %. In all cases C_{60} deposition onto TiO_x causes a decrease of the Ti^{3+} percentage (difference gray and black squares). The relative Ti^{3+} decrease after C_{60} deposition reduces with increasing C_{60} coverage. UV illumination causes an increase of the Ti^{3+} emission on all samples, where a Ti $2p_{3/2}$ signal was obtained (difference black and blue squares). While the pristine TiO_x substrate shows an increase to 5 % Ti^{3+}, the C_{60} covered samples show all an increase to about 2.5 % Ti^{3+} after UV illumination. This indicates that the C_{60} adsorption

reduces the UV induced Ti^{3+} formation on TiO_x. The *fwhm* of C 1s level of C_{60} decreases before UV illumination from about 0.58 eV to 0.50 eV with increasing C_{60} coverage. After UV illumination the C 1s *fwhm* increases for small C_{60} coverages (3, 10, and 26 Å), while the increase diminishes with increasing C_{60} coverage. The sample with highest C_{60} coverage shows no increase of the C 1s *fwhm* after UV illumination. This shows that UV induces no changes of the pristine C_{60} layer and only effects the C_{60} at the interface to TiO_x. Thus a UV induced destruction of the C_{60} is unlikely and a doping effect or a change of band bending are more probable to be the origin of the C 1s *fwhm* increase.

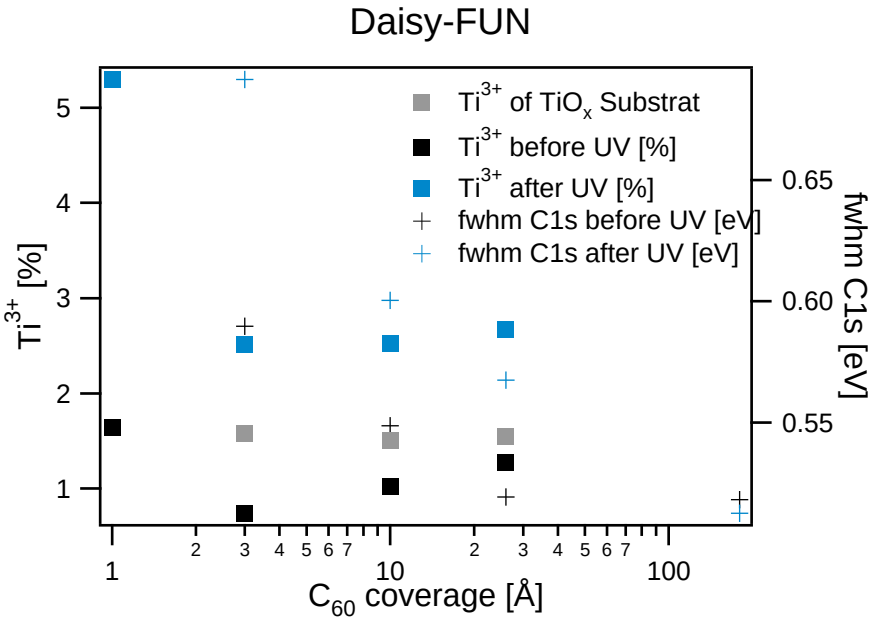

Figure 9.7. – Ti^{3+} proportion of the whole Ti $2p_{3/2}$ emission (squares) and C 1s *fwhm* (crosses) evolution with respect to C_{60} coverage and UV influence. Black squares/crosses represent values of the initial spectra and blue squares/crosses values of UV exposed spectra. The general trend is that the Ti^{3+} percentage and the C 1s *fwhm* increase with UV illumination. The C 1s *fwhm* decreases with increasing C_{60} coverage. The Ti^{3+} percentage is largely independent of the C_{60} coverage.

9.3 Influence of UV light on the TiO_x/C_{60} interface after UV pretreatment of the TiO_x substrate

As UV light induces a shift of the Ti $2p_{3/2}$ and C 1s position at the TiO_x/C_{60} interface, it is investigated how an UV pretreatment of the TiO_x substrate influences the previously observed shifts. Therefore a TiO_x 80 °C substrate was first irradiated for 24 h with UV light before approx. ~10 Å C_{60} were deposited onto the substrate. Subsequently XP spectra were recorded and the sample was irradiated for 60 min with UV light again. The recorded spectra are displayed in Fig. 9.8. The bottom blue spectra are of the TiO_x substrate after 24 h UV illumination. The red spectra are the initial spectra after C_{60} deposition and the top blue spectra are recorded after 60 min illumination of the TiO_x/C_{60} interface.

As expected from the previous measurements, UV illumination shifts the SE-edge of TiO_x to lower kinetic energy. The WF after 24 h UV illumination is at 3.8 eV and about 100 meV lower than after 1 h UV illumination (see Fig. 9.2). The Ti $2p_{3/2}$ binding energy is at 459.4 eV, which is the same value as after 1 h UV. Regarding the SE-edge, the UV induced shift of the TiO_x substrate is not saturated after 1 h

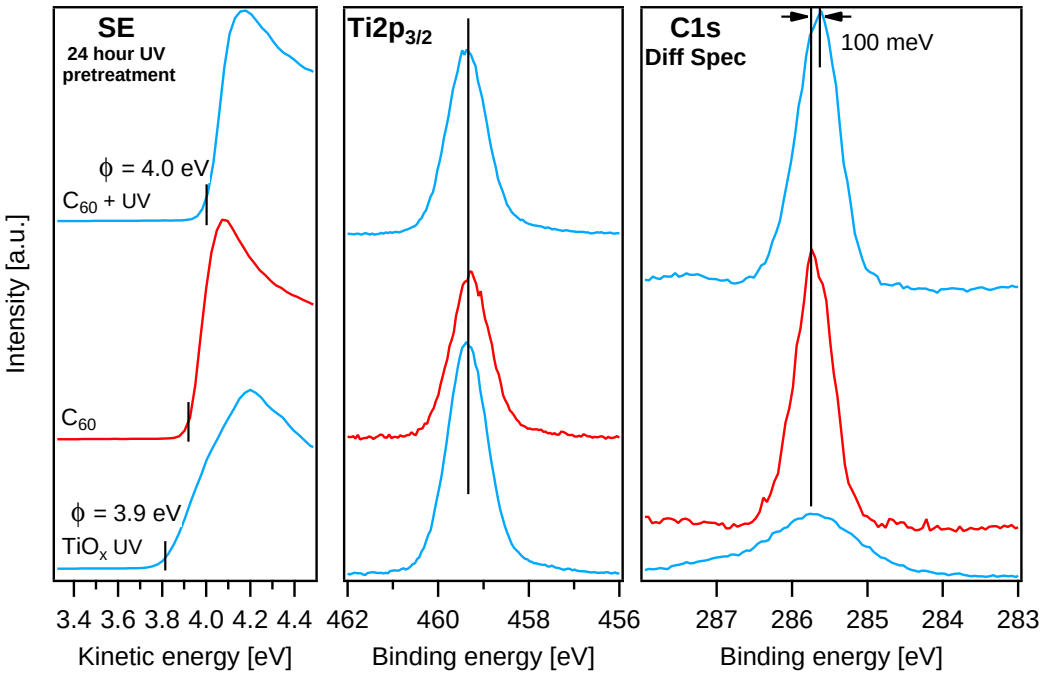

Figure 9.8. – SE-edge (left), Ti $2p_{3/2}$ (right) and C 1s difference spectra (right) of the TiO_x substrate after 24 h of UV irradiation (bottom blue), after 10 Å C_{60} deposition (red) and after 1 h UV irradiation of the TiO_x/C_{60} sample. The WF of the TiO_x is 3.8 eV after UV illumination. After C_{60} deposition the WF increases and the Ti $2p_{3/2}$ level decreases from 459.4 eV to 459.3 eV. After UV illumination the Ti $2p_{3/2}$ level increases by 100 meV again. The C 1s level shift by 50 meV from ~285.7 eV to 285.65 eV. Compared to a non UV pretreated TiO_x/C_{60} interface of similar C_{60} coverage, the UV induced C 1s shift is 100 meV smaller.

of UV, while the Ti $2p_{3/2}$ core level shift is saturated already after 1 h of UV. After deposition of 10 Å C_{60} the SE-edge shifts by ~100 meV to higher kinetic energies (3.9 eV) and after 1 h UV irradiation of the TiO_x/C_{60} interface the SE-edge shifts further to ~4.0 eV. The UV induced changes of the WF have not been observed for the non UV pretreated 10 Å C_{60} sample, where the SE-edge was constant at ~4.0 eV. The Ti $2p_{3/2}$ level decreases by ~100 meV after C_{60} deposition from 459.4 eV to 459.3 eV and increases after UV illumination to the value before C_{60} deposition of ~459.4 eV. The C 1s emission has an initial binding energy of 285.7 eV (after C 1s difference spectrum), which decreases about 50 meV after UV illumination. In comparison to the non UV pretreated sample the initial binding energy of the C_{60} C 1s emission is slightly lower even though the nominal C_{60} coverage is the same. The UV induced shift of the non UV pretreated sample is 150 meV and hence 100 meV higher compared to the sample with UV pretreatment. The results are summarized in an energy band diagram in Fig. 9.9 and in Table 9.2. The energy diagram shows that UV pretreatment causes a decrease of the UV induced Tip-C 1s distance increase (Ti $2p_{3/2}$-C 1s distance w/o UV pretreatment 173.4 eV →173.8 eV, with UV treatment 173.6 eV →173.7 eV).

A comparison of the absolute binding energies of the non-pretreated and pretreated sample may not be reliable as the C_{60} coverages are probably not exactly the same and because the resolution of the XPS system is not good enough. Still the comparison of the UV induced shifts are reliable.

Figure 9.10 shows the influence of UV light on the Ti^{3+} percentage of the Ti $2p_{3/2}$ emission (left) and C 1s *fwhm* (right) of the UV pretreated sample (red squares) and a non UV pretreated sample (black

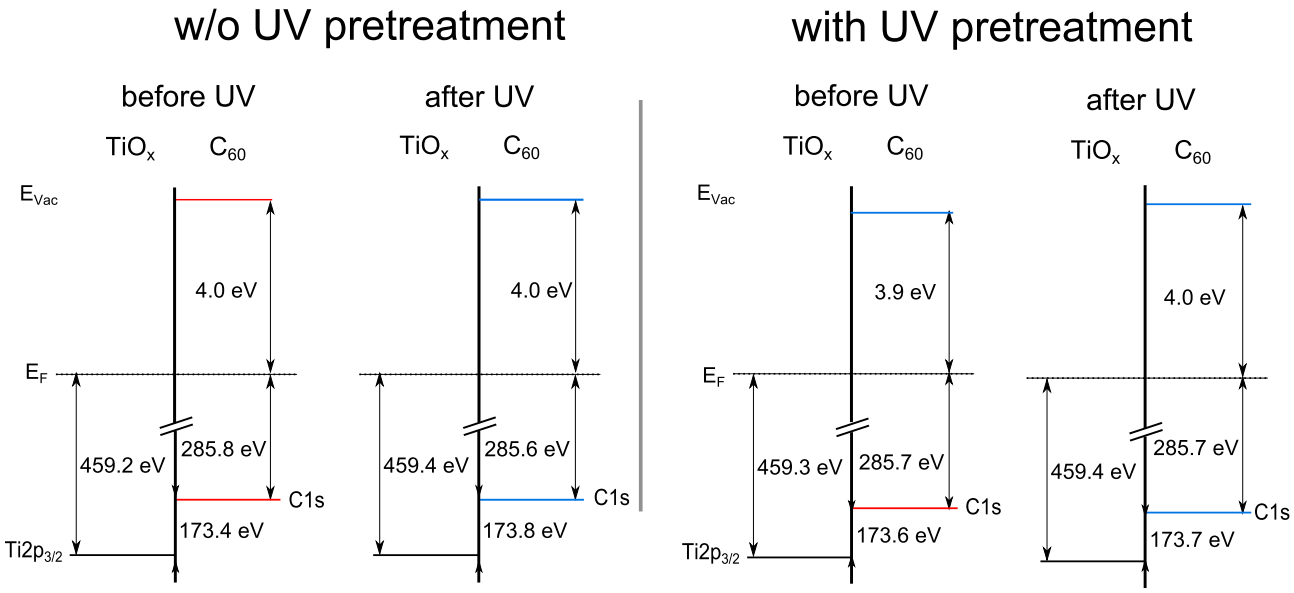

Figure 9.9. – Energy band diagram from the spectra shown in Fig. 9.4 and Fig. 9.8 with TiO_x as substrate and a 10Å C_{60} layer on top. On the left, the TiO_x was not pretreated with UV before C_{60} deposition. UV illumination after C_{60} deposition causes an increase of the Ti $2p_{3/2}$-C 1s distance from 173.4 eV to 173.8 eV. On the right, the TiO_x sample was UV pretreated for 24 h before C_{60} deposition. In the case of the UV pretreated sample, UV illumination after C_{60} deposition causes only a minor increase of the Ti $2p_{3/2}$-C 1s distance from 173.6 eV to 173.7 eV.

Table 9.2. – Work function and binding energy positions of the Ti $2p_{3/2}$ and C 1s core level for UV pretreated and a non UV pretreated TiO_x/C_{60} interface.

10 Å C_{60}	Work function [eV]		Ti $2p_{3/2}$ [eV]		C 1s [eV]	
	initial	UV	initial	UV	initial	UV
with UV pretreatment	3.91	4.00	459.32	459.37	285.72	285.66
w/o UV pretreatment	4.00	4.00	459.23	459.37	285.77	285.62

triangles) with the same nominal layer thickness (about 10 Å). The Ti^{3+} content diminishes in both samples after C_{60} deposition, but less on the UV pretreated sample. After 60 min of UV irradiation the pretreated sample shows only a small increase of Ti^{3+} percentage, while the non-pretreated sample shows an increases from 0.8 % to 2.5 % Ti^{3+} after UV, which is close to the value of the UV pretreated sample. The C 1s *fwhm* evolution of the UV pretreated sample and the non UV pretreated sample shows a similar increase in the course of X-ray and UV irradiation.

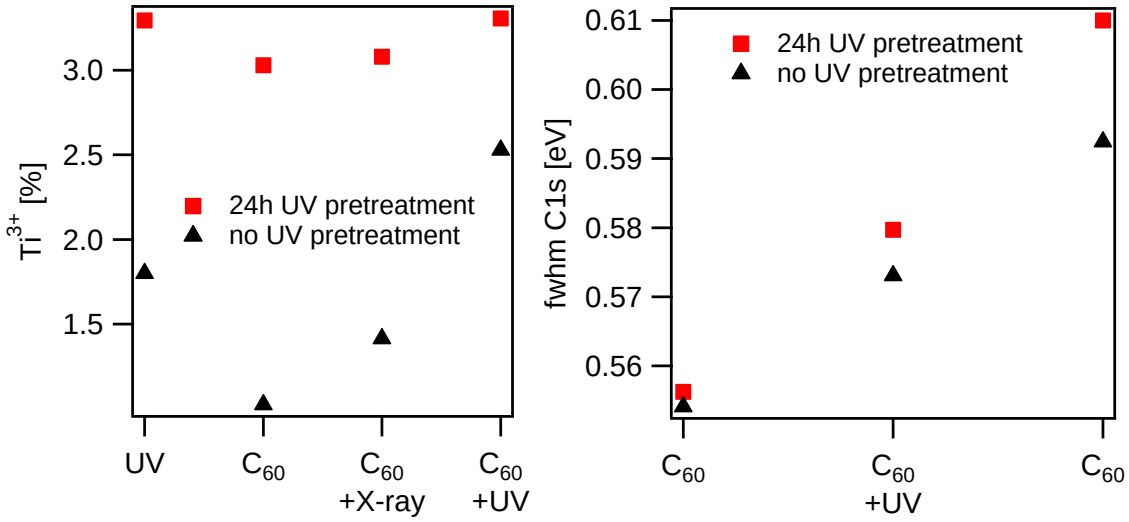

Figure 9.10. – Ti^{3+} percentage of the Ti $2p_{3/2}$ emission (left) and C 1s *fwhm* (right) evolution of the UV pretreated TiO_x/C_{60} interface (red squares) and the non UV pretreated TiO_x/C_{60} interface (black triangles). The Ti^{3+} evolution of the UV pretreated and non-pretreated interface differ and UV pretreatment leads to an almost constant amount of Ti^{3+} states, whereas Ti^{3+} states of the non UV pretreated sample show strong dependence of C_{60} deposition and UV illumination. The C 1s *fwhm* evolution of C_{60} shows the same trend with and w/o UV pretreatment. The pretreated interface shows a stronger increase of the C 1s *fwhm* with X-ray and UV irradiation.

9.4 Summary and discussion: The 80 °C TiO_x/C_{60} interface and the influence of UV illumination

To investigate the interface characteristics of the TiO_x/organic interface varying coverages of C_{60} were evaporated onto TiO_x and the influence of UV light was investigated by XPS. As $PC_{61}BM$ cannot be evaporated[95] and a deposition of thin layers out of solution is difficult, C_{60} was used as a model acceptor material, which proved to have similar electronic properties (see Section 8.3.1).

The irradiation of the TiO_x substrate with UV light showed that the WF is reduced by 200 meV from 4.1 eV to 3.9 eV after UV illumination. The Ti $2p_{3/2}$ level shifts as well by 200 meV from ~459.2 eV to ~459.4 eV. WF and Ti $2p_{3/2}$ level shift in the same direction, which indicates a change of the band bending (position of the Fermi level) at the surface, rather than a change of the surface dipole (see Table 9.1). The WF decrease of ALD titania upon UV illumination was already observed by Kelvin-Probe measurements by Schmidt et al.[169] and by XPS/UPS by Gutmann et al. on nc-TiO_2.[170] The UV induced Ti $2p_{3/2}$ core level shift was not yet observed directly by XPS measurements. Porsgaard et al. showed by ambient pressure photoemission (APXPS) that O_2 induces an upward band bending on rutile,[171]

but did not investigate the influence of UV illumination. The UV induced downward shift of the energy levels at the surface is also supported by the increased conductivity of TiO_2 upon UV illumination, which is attributed to the desorption of oxygen species due the scavenging of photoholes.[73,172,173] Beside the UV induced shifts of the energy levels, the Ti^{3+} component of the TiO_x substrate increases as well after UV irradiation from about 1.5 % to 5 %. The Ti^{3+} state is usually attributed to oxygen vacancies at the surface and the observed increases could be either caused by the removal of adsorbed oxygen species on the surface or removal of oxygen which is incorporated in the TiO_x film at the surface.[174,175]

The investigation of the TiO_x/C_{60} interface showed that even after C_{60} deposition onto the TiO_x substrate, the Ti $2p_{3/2}$ 200 meV core level shift to higher binding energies occurs. The C 1s level shifts at low C_{60} coverages by ~150 meV to lower binding energies. At the highest C_{60} coverage (150 Å) no shift of the C 1s level after UV illumination is observed. Regarding the interface alignment of C_{60} on TiO_x 80 °C before UV illumination, an upward pointing interface dipole of 0.25 eV is formed and the C_{60} energy bands bend downwards by about 0.4 eV towards the interface. After UV illumination the interface dipole switches direction and changes in total by 0.4 eV. C_{60} energy band bending is reduced by ~0.2 eV and the TiO_x energy levels move downwards by about 0.2 eV (see Fig. 9.6). The WF shows a contrary behavior. The TiO_x substrate WF decreases upon UV illumination by 200 meV. At low C_{60} coverages the WF is almost not influenced by UV light. However at 26 Å nominal C_{60} coverage the WF increases upon UV illumination by 150 meV, while at 180 Å C_{60} coverage the WF position stays constant again after UV. The Ti $2p_{3/2}$-C 1s distance changes from 173.4 eV prior UV illumination to 173.8 eV after UV illumination.

As the energy level positions, the Ti^{3+} percentage of the Ti $2p_{3/2}$ emission and the C_{60} C 1s *fwhm* are also influenced by UV light. Upon UV illumination Ti^{3+} content increases at all C_{60} coverages, where the Ti $2p_{3/2}$ emission is still visible. At low C_{60} coverages the C 1s emission is broadened by UV light. The broadening is reduced with increasing nominal C_{60} coverage and at 180 Å C_{60} coverage no C 1s *fwhm* increase is observed anymore.

In Section 9.3 the TiO_x substrate was UV pretreated for 24 h prior the C_{60} deposition. The UV pretreatment resulted in a reduction of the UV induced shifts of the Ti $2p_{3/2}$ and C 1s level (1 h UV illumination after C_{60} deposition). The Ti $2p_{3/2}$ and C 1s line show a reduced shift of ~50 meV to higher binding energy and lower binding energy, respectively (see Table 9.2). The UV induced broadening of the C 1s level is similar to the non UV pretreated TiO_x/C_{60} sample, while the Ti^{3+} emission of the UV pretreated is in total higher, than the Ti^{3+} content of the non UV pretreated sample and stays almost constant in the course of C_{60} deposition and UV illumination. The 24 h UV pretreated sample has an initial Ti $2p_{3/2}$-C 1s distance of 173.6 eV, which changes to 173.7 eV after the UV pretreatment. The non UV pretreated sample with the same nominal layer thickness (~10 Å) has an initial Ti $2p_{3/2}$-C 1s distance of 173.5 eV and increases after UV illumination to 173.8 eV (values taken from Table 9.2).

The following experiments are motivated by the observations made above, with the aim to explain the UV induced changes at the TiO_x/C_{60} interface. In general UV light has an impact on the TiO_x surface (increase of Ti^{3+} emission), the C_{60} close to the interface (increase of C 1s *fwhm* for low C_{60} coverages) or

on adsorbates present on the *ex situ* prepared TiO_x surface (binding energy shift of the Ti $2p_{3/2}$ level). As a model TiO_2 substrate an *in situ* and *ex situ* cleaved anatase (101) surface is used, C_{60} is deposited on it and the influence of UV light is investigated on it (Chapter 10). Additionally the effect of oxygen exposure and UV light illumination on (101) anatase and amorphous TiO_x surfaces is investigated (Chapter 11).

10 Anatase (101)/C_{60} interface experiments

In this section C_{60} is deposited onto *in situ* and *ex situ* cleaved anatase sc-(101) surfaces. Both interfaces are investigated with respect to a possible UV influence on the energetic positions of TiO_2 and C_{60} energy levels. By cleaving the anatase crystal *in situ*, it is possible to obtain an adsorbate free surface. This permits the determination of the influence of adsorbates on the TiO_2/C_{60} interface. Processes like sputter annealing cannot exclude the presence of e.g. subsurface defects or molecular adsorbed oxygen at the surface.[135] The following two interface experiments were performed at the synchrotron Bessy II in Berlin at the beamline U49/2-PGM-2. Due to the adjustable excitation energy at a synchrotron, measurements with higher surface sensitivity are possible. The UV light influence on *ex situ* and *in situ* cleaved anatase C_{60} interfaces is investigated with the Daisy-Fun setup.

10.1 TiO_2 anatase *in situ*/C_{60} interface

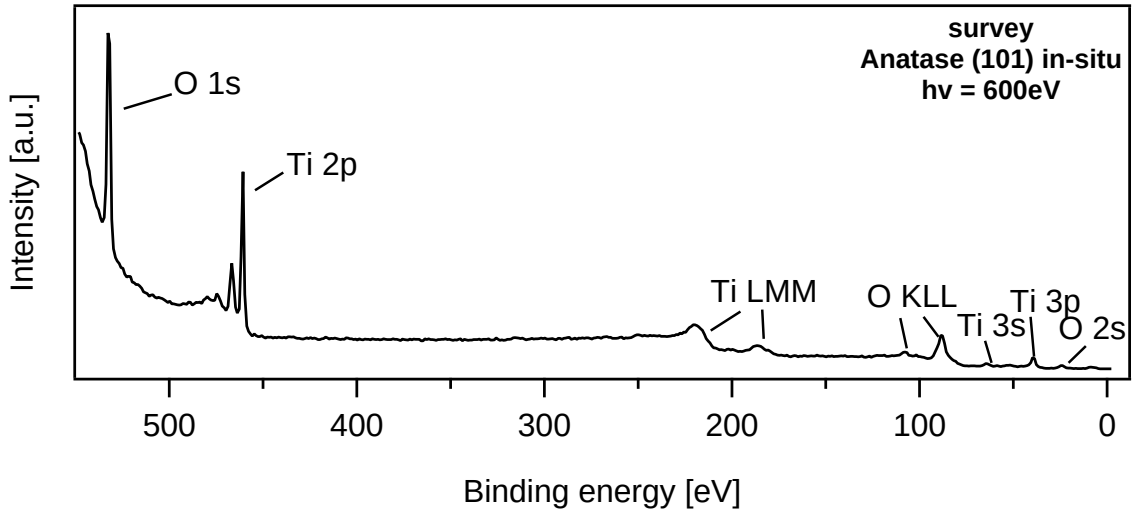

Figure 10.1. – Survey spectrum of the *in situ* cleaved (101) surface plane prior C_{60} deposition. Only oxygen and titanium photoelectron and Auger emissions are observed. Especially no carbon emission is detected within the XPS detection level.

To investigate the interface of an adsorbate free TiO_2 with C_{60}, TiO_2 anatase was cleaved *in situ*. Figure 10.1 shows the resulting survey spectrum of the *in situ* cleaved anatase (101) surface. In the measured binding energy range no carbon or any other contamination is visible. On top of the sc-(101) surface, C_{60} was evaporated with a rate of about 0.1 Å/ s. Evaporation times were 5, 10, 20, 40, 80, 200 and 600 s. The nominal C_{60} coverages, calculated by the damping of the Ti $2p_{3/2}$ line, are 0.5, 1, 2, 4, 8, 40 and 120 Å. The SE-edge, Ti $2p_{3/2}$, C 1s and valence band spectra of the interface experiment are displayed in Fig. 10.2. The Ti^{3+} contribution and the C 1s *fwhm* evolution are discussed in Section 10.3.

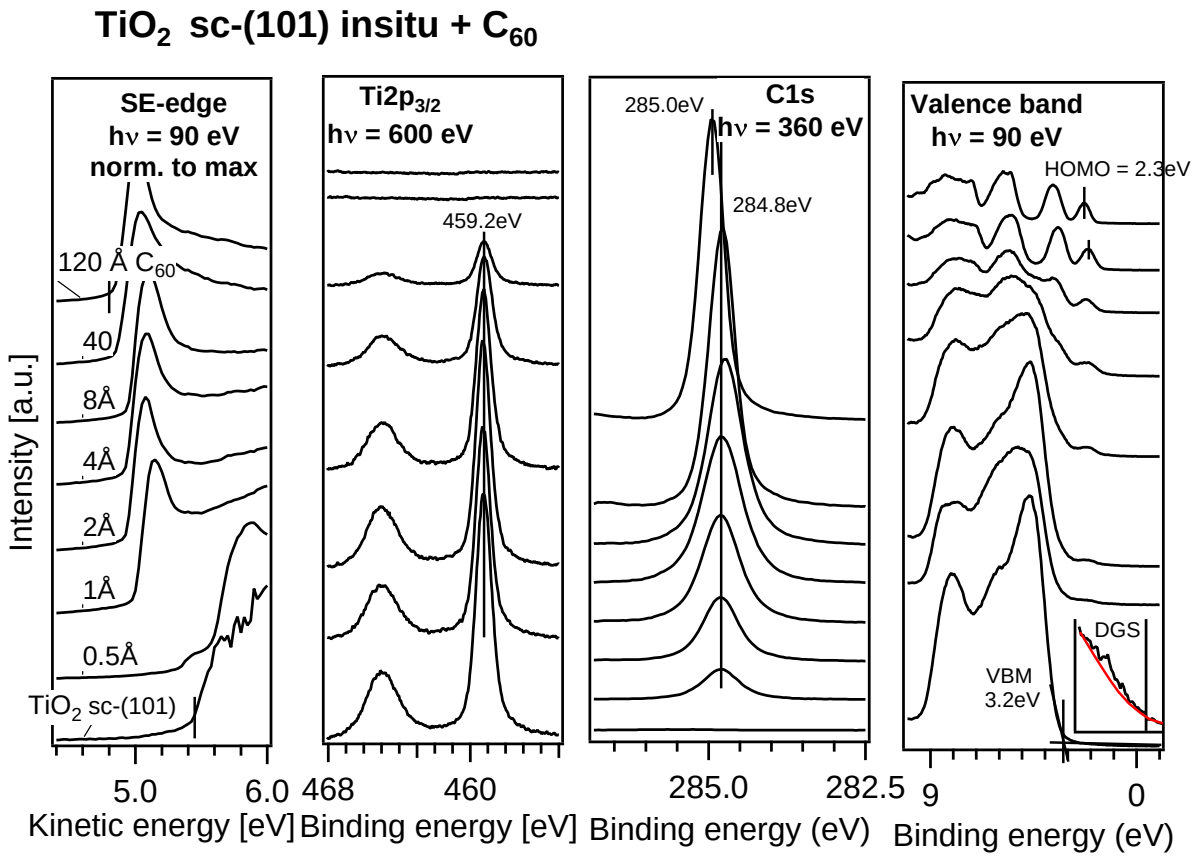

Figure 10.2. – Anatase *in situ* cleaved C_{60} interface experiment. Left: SE-edge of the anatase TiO_2 (101) surface. The WF of the freshly cleaved sc-(101) surface plane is 5.5 eV. In the course of C_{60} deposition it decreases to 4.9 eV. The Ti $2p_{3/2}$ emission (second from left) is at 459.2 eV and stays constant during C_{60} deposition. No Ti^{3+} emission is observed. The C_{60} C 1s emission is at 284.8 eV and E_{Bin} does not change for the first six C_{60} depositions. After the last C_{60} deposition the C 1s emission shifts by 100 meV to higher binding energies. The VBM of the TiO_2 is at 3.2 eV. Already after the first C_{60} deposition step, the C_{60} HOMO is visible. The C_{60} $HOMO_{max}$ after the last deposition is at 2.3 eV. The VB spectrum of the freshly cleaved surface shows almost no band gap emissions, indicating the mostly absence of oxygen vacancies on the (101) surface. The inset shows the DGS emission of the *in situ* cleaved anatase. The red curve is the polynomial background.

The freshly *in situ* cleaved anatase crystal has a WF of ~5.5 eV, which is about 1 eV higher, than for *ex situ* cleaved sc-(101) TiO_2 or badly (meaning not clean) cleaved sc-(101) TiO_2 (see Fig. 10.5). In the course of C_{60} deposition, the WF decreases to a value of 4.9 eV. The doublet Ti2p emission is damped with increasing C_{60} coverage. The sc-(101) Ti $2p_{3/2}$ emission is situated at a binding energy of 459.2 eV and does not shift with increasing C_{60} coverage. The C_{60} C 1s emission is constant till 40 Å coverage and then shifts from 284.8 eV to 285.0 eV binding energy. The bottom C 1s spectrum shows, that no carbon contaminations are present on the surface after cleavage. The $HOMO_{max}$ of the thickest C_{60} layer is at 2.3 eV and its distance to the C 1s emission is 282.7 eV, which is in good agreement with the value obtained in Section 8.3 for a 150 Å C_{60} layer on gold. The VBM of the *in situ* cleaved anatase crystal is at 3.2 eV binding energy and the distance to the Ti $2p_{3/2}$ level is 456.0 eV, which is in agreement with the previously observed distance of sc and nc anatase (see Fig. 8.9). The Ti $2p_{3/2}$ emission shows no Ti^{3+} component. In the band gap region, a small emission at 1 eV is observed, which indicates only a small

amount of V_O at the surface. The O 1s emission is shown in the appendix in Fig. A.1 and compared to the O 1s emission of an *ex situ* cleaved sc-(101). No O 1s emission of hydroxyls occurs on the *in situ* cleaved sc-(101).

10.1.1 TiO_2 anatase *in situ*/C_{60} interface - influence of UV light

To investigate the influence of UV light on the *in situ* cleaved sc-(101)/C_{60} interface, a thin C_{60} layer (approx. 10 Å) was deposited on to the *in situ* cleaved TiO_2-(101) and subsequently irradiated with UV light for 60 min. Figure 10.3 shows the secondary electron edge, the Ti $2p_{3/2}$, the O 1s and the C 1s core level emission of an *in situ* cleaved anatase single crystal (red) plus 9 Å C_{60} layer directly after the C_{60} deposition (gray), upon the exposure of X-rays (black) and after 60 min UV illumination (top, blue). No initial spectra were recorded of the Ti $2p_{3/2}$ emission.

Compared to the *in situ* cleaved crystal of the previous interface experiment, the WF of this *in situ* cleaved crystal is about 1 eV smaller at 4.0 eV E_{Kin}. A possible reason for the WF difference could be a small contamination of the surface with carbon species (see magnified red C 1s spectrum on the right of Fig. 10.3). The O 1s emission is at 530.5 eV and its shape is symmetric. On the high binding energy side no emission is observed, which indicates a hydroxyl free surface. The Ti $2p_{3/2}$ level is at 459.3 eV. No contribution of Ti^{3+} states is observed in the Ti $2p_{3/2}$ emission. After C_{60} deposition the WF value remains at about 4.0 eV. The Ti $2p_{3/2}$ and O 1s emissions are damped, while the C 1s emission increases. After C_{60} deposition and UV illumination no change of the O 1s and Ti $2p_{3/2}$ shape and binding energy position is observed. The C 1s core level emission exhibits almost no change as well, while the work function decreases by ~100 meV upon UV. The *fwhm* of the C 1s is constant too. In comparison to the previous *in situ* sc-(101) interface experiment the C_{60} C 1s binding energy position is 300 meV lower at about 285.1 eV. All energy values are summarized in Table 10.1.

10.2 TiO_2 anatase *ex situ*/C_{60} interface

The photoemission spectra of the O 1s, Ti $2p_{3/2}$, C 1s and VB region of the *ex situ* sc-(101)/C_{60} interface are displayed in Fig. 10.4. C_{60} was evaporated with a rate of 0.1 Å/ s on the *ex situ* cleaved anatase. The evaporation times were 5, 10, 40, 80, and 200 s and the calculated nominal C_{60} coverages are 0.5, 1, 7, 16 and 64 Å. Due to technical problems no SE-edges could be recorded. The Ti^{3+} percentage of the Ti $2p_{3/2}$ emission and the C 1s *fwhm* evolution are discussed in Section 10.3.

The bottom spectra show the photoemission of the TiO_2 substrate. The O 1s emission shows two components, where the main emission (at ~530.6 eV E_{Bin}) is attributed to lattice oxygen of the anatase crystal and the emission at 532.5 eV to hydroxyls caused by *ex situ* cleavage and subsequent H_2O adsorption. The Ti $2p_{3/2}$ emission is located at 459.4 eV E_{Bin} and shows no indication of Ti^{3+} states on the low energy side of the main emission. The C 1s spectrum of the substrate prior C_{60} deposition, shows already a C 1s emission due to *ex situ* handling. The valence band emission resembles well the shape of the *in situ* cleaved VB (see Fig. 10.2) and shows little emission at ~1 eV E_{Bin} as indicative of the presence of oxygen

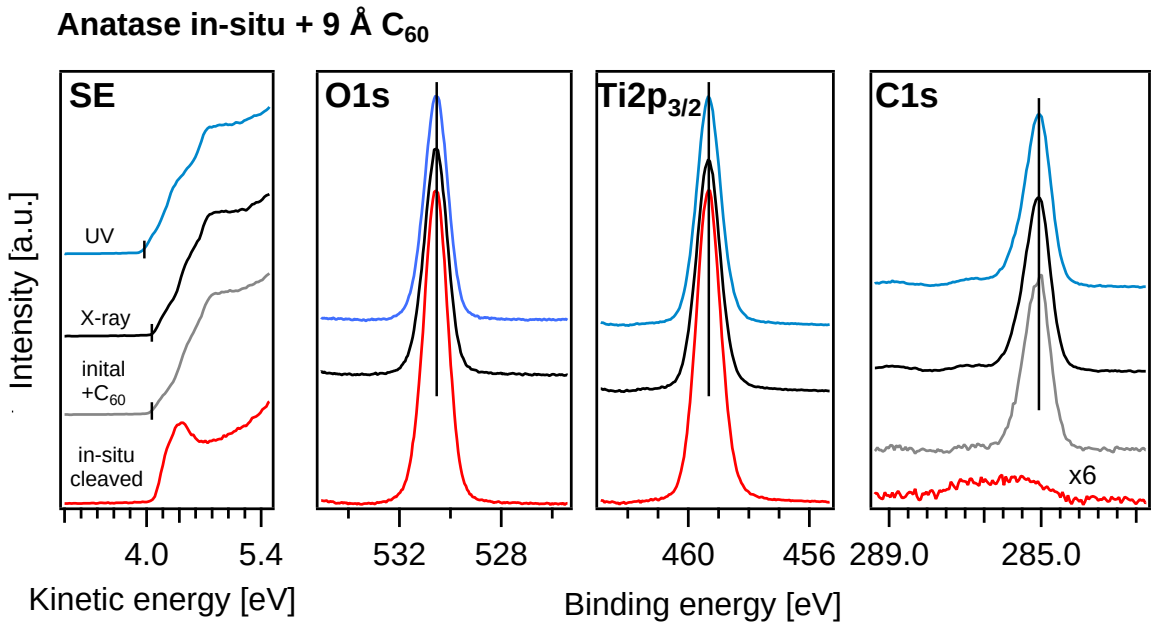

Figure 10.3. – Influence of UV light on the *in situ* cleaved anatase (101)/C_{60} interface. Depicted are the SE-edge, O 1s, Ti $2p_{3/2}$ and C 1s spectra. The bottom spectra (red) are of the *in situ* cleaved anatase prior C_{60} deposition. It is almost free of any carbon contamination. No indication of hydroxyls in the O 1s spectrum and of Ti^{3+} states in Ti $2p_{3/2}$ spectrum is given. Gray and black spectra are recorded after 9Å C_{60} deposition. Beside a damping, the O 1s and Ti $2p_{3/2}$ emission do not show any change in shape or binding energy. Blue spectra are recorded after 60 min of UV illumination. Neither the O 1s and Ti $2p_{3/2}$, nor the C 1s of C_{60} shows any change in shape or binding energy after UV illumination.

vacancies. The VBM of TiO_2 substrate is at 3.4 eV and the Ti $2p_{3/2}$-C 1s distance is 456.0 eV. With increasing C_{60} coverage the Ti $2p_{3/2}$ and O 1s signals are damped, while the C 1s emission increases. As for the *in situ* cleaved anatase crystal the O 1s and Ti $2p_{3/2}$ emissions do not shift with increasing C_{60} coverage. The C 1s spectrum after C_{60} deposition are all corrected by the initial C 1s emission. With increasing C_{60} coverage the C 1s emission shifts by 200 meV from 285.3 eV to 285.1 eV. A C_{60} emission and the C_{60} shift can also be seen in the VB spectrum starting with the first deposition step. The $HOMO_{max}$ of C_{60} at highest C_{60} coverage is at 2.4 eV, which results in a C 1s-$HOMO_{max}$ distance of 282.7 eV as observed for the *in situ*/C_{60} interface and results obtained in Section 8.3.

10.2.1 TiO_2 anatase *ex situ*/C_{60} interface - influence of UV light

In this experiment a 7 Å thick C_{60} layer was deposited on an *ex situ* cleaved anatase single crystal. Figure 10.5 shows the SE-edge, O 1s, Ti $2p_{3/2}$ and C 1s emission lines of the *ex situ* sc-(101) crystal core level lines before (red) and after C_{60} deposition (gray). The blue spectra are recorded after subsequent UV illumination of 1 h.

Prior to C_{60} deposition the SE-edge, the O 1s emission and the Ti $2p_{3/2}$ emission are at 3.9 eV E_{Kin}, 530.7 eV E_{Bin}, and 459.5 eV E_{Bin}, respectively. At 532.5 eV binding energy, the O 1s spectrum shows a small emission, which is attributed to hydroxyls. The C 1s spectrum shows a carbon emission from contaminations. After the deposition of the C_{60} layer, the Ti $2p_{3/2}$ and the O 1s emissions are damped

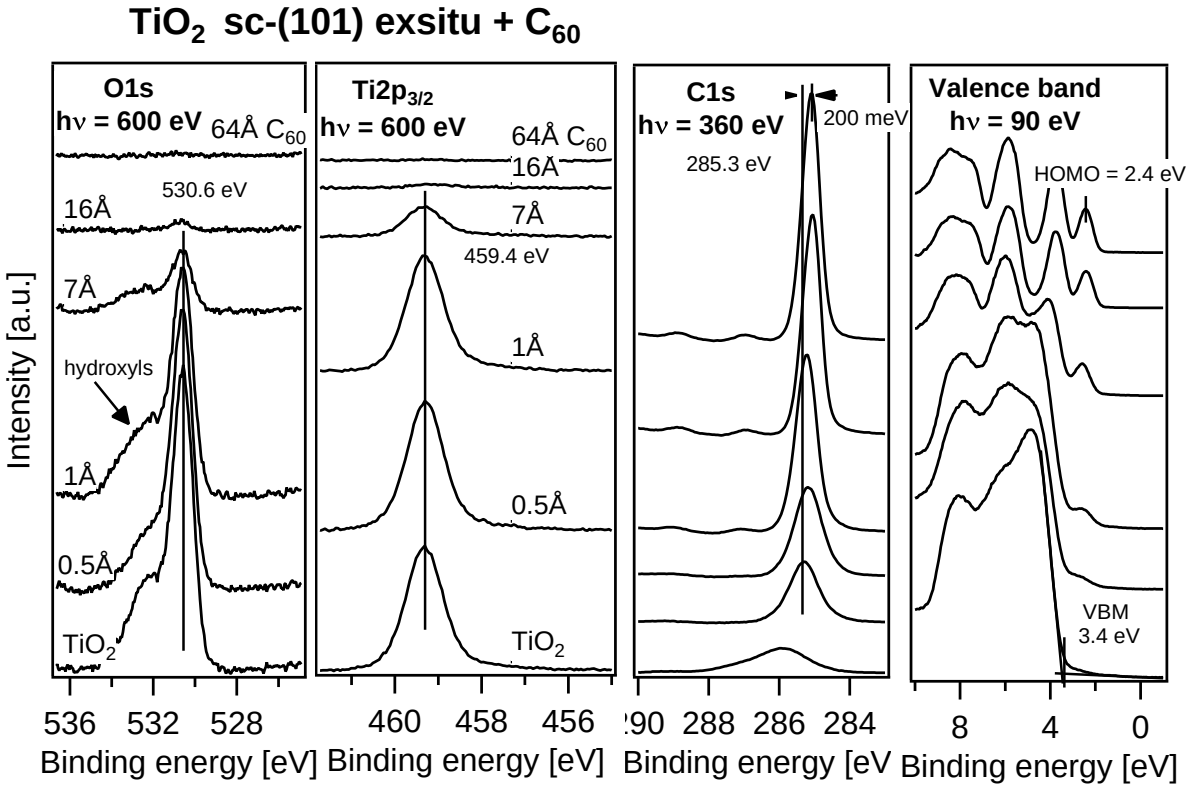

Figure 10.4. – Anatase *ex situ* cleaved/ C_{60} interface experiment. On the left the O 1s emission of the anatase TiO_2 (101) surface is shown. Besides its main emission at 530.6 eV, it shows a component at 532.5 eV, indicating hydroxyl species present on the surface. The Ti $2p_{3/2}$ emission is at 459.4 eV and stays constant during C_{60} deposition. No Ti^{3+} emission is observed. The C_{60} C 1s emission is at 285.1 eV and shifts by 200 meV to lower binding energies in the course of C_{60} deposition. The VBM of the TiO_2 is at 3.4 eV. Already after the first C_{60} deposition the C_{60} HOMO is visible. The C_{60} $HOMO_{max}$ after the last deposition is at 2.4 eV. The VB spectrum of the cleaved surface shows almost no band gap emission, indicating a low concentration of oxygen vacancies on the (101) surface.

and their binding energies remain unchanged, while the SE-edge shifts from 3.9 eV to ~4.0 eV E_{Kin}. The C_{60} C 1s emission has been corrected by subtracting the C 1s substrate emission and is at 285.8 eV after C_{60} deposition. After UV irradiation the SE-edge shifts back by 100 meV to 3.9 eV E_{Kin}. The Ti $2p_{3/2}$ and the O 1s core level stay both at the same binding energy position. The C 1s level shifts 300 meV to lower binding energies after UV illumination. Additionally the C 1s spectrum shows a broadening after UV illumination and its *fwhm* increases from 0.58 eV to 0.69 eV (see Section 10.3). The absolute values and relative shifts are summarized in Table 10.1.

10.3 Analysis of the Ti $2p_{3/2}$ and C 1s line shape of synchrotron experiments

In Fig. 10.6 the evolution of Ti^{3+} and the *fwhm* of the C 1s emission with increasing C_{60} coverage on *in situ* and *ex situ* cleaved TiO_2 are compared. Considered are the two interface experiments conducted at Bessy II. The Ti^{3+} content is extracted from Gaussian-Lorentzian fits with two components for the Ti^{4+} and Ti^{3+} emission and the C 1s *fwhm* of a fit of the C 1s emission with only one component.

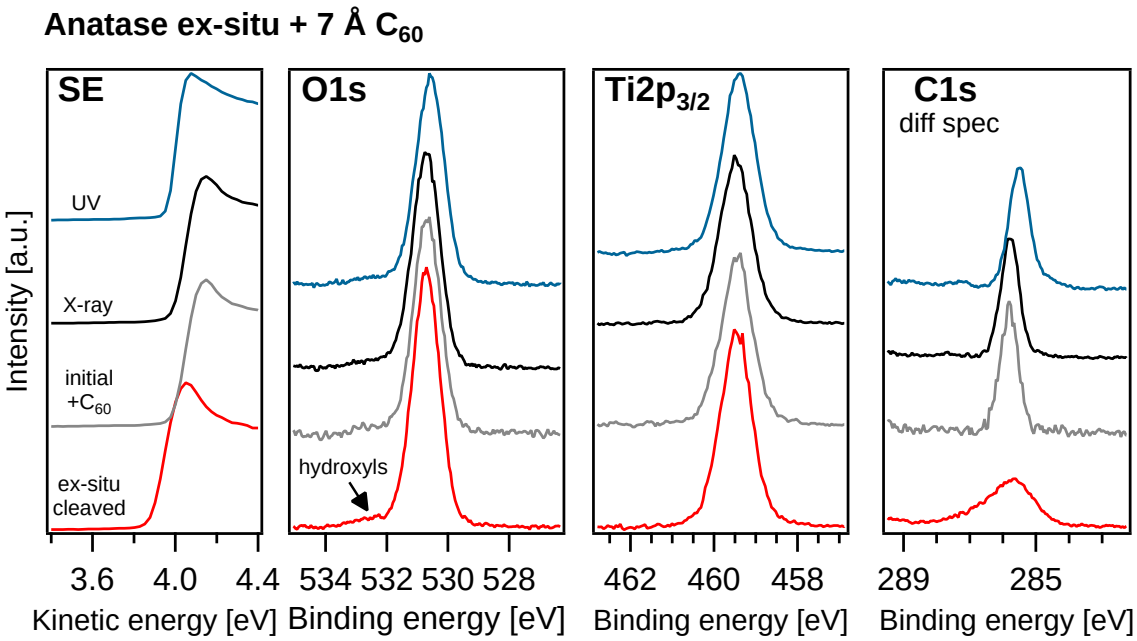

Figure 10.5. – Influence of UV light on the *ex situ* cleaved anatase (101)/C_{60} interface. Depicted are the SE-edge, O 1s, Ti $2p_{3/2}$ and C 1s spectra. The bottom spectra (red) are of the *ex situ* cleaved anatase prior C_{60} deposition. A carbon emission is observed. The O 1s emission shows a small emission at the high binding energy side, indicating the presence of hydroxyls on the surface. The Ti $2p_{3/2}$ emission gives no indication of Ti^{3+} states at the low energy side of the spectrum. Gray and black spectra are recorded after 7Å C_{60} deposition. Besides a damping, the O 1s and Ti $2p_{3/2}$ emission do not show any change in shape or binding energy. Blue spectra are recorded after 60 min of UV illumination. The O 1s and Ti $2p_{3/2}$ emission do not show any change in shape or binding energy after UV illumination. The C 1s level shifts 300 meV to lower binding energies after C_{60} deposition. Furthermore the C 1s *fwhm* increases from 0.6 eV to 0.7 eV.

The percentage of the Ti^{3+} emission of the Ti $2p_{3/2}$ overall emission of the *in situ* cleaved (101) sample is first around 9 % till it starts to increase at nominal coverages above 2 Å. At 16 Å coverage the percentage of the Ti^{3+} emission of the Ti $2p_{3/2}$ emission is ∼14 %. The *ex situ* cleaved sc-(101) displays a similar behavior and shows an increase of the Ti^{3+} emission at a C_{60} coverage of 1 Å. The C 1s *fwhm* of C_{60} on *in situ* sc-(101) is at low coverage about 0.65 eV and decrease for the 110 Å thick C_{60} layer to 0.40 eV. On the *ex situ* sc-(101) the C 1s *fwhm* was determined after subtraction of the C 1s emission of the TiO_2 substrate. The C 1s *fwhm* decreases progressively with increasing C_{60} from around 0.7 eV to 0.4 eV. Between 16 and 64 Å C_{60} no change of the C 1s *fwhm* occurs. Note that both interface experiments were recorded at different beamtimes and that the resolution, given by the width of Fermi edge of a clean silver foil, was for the *in situ* experiment 0.2 eV and for the *ex situ* experiments 0.3 eV. To facilitate the comparison of the *in situ* and the *ex situ* TiO_2-(101)/C_{60} interface experiment, the C 1s *fwhm* value of the *ex situ* TiO_2-(101)/C_{60} interface was corrected by subtracting 100 meV (due to the experimentally caused broadening).

The UV experiments of the TiO_2 *ex situ* and *in situ* C_{60} interface showed that UV light causes no change of the C_{60} C 1s *fwhm* if it is deposited onto an *in situ* prepared sc-(101) surface. In contrast the C_{60} C 1s *fwhm* on an *ex situ* prepared sc-(101) surface increases from 0.58 eV to 0.69 eV (see Table 10.1).

Table 10.1. – SE-edge, Ti $2p_{3/2}$, C 1s energy emission values and *fwhm* of C 1s, obtained from the *in situ*/C_{60} + UV light and the *ex situ*/C_{60} + UV light experiment.

sc-(101)		absolute values				with respect to initial		
		substrate	initial	X-ray	UV	initial	X-ray	UV
in situ + 9 Å C_{60}	WF [eV]	4.05	4.06	4.06	3.97	0	0	0.09
	Ti $2p_{3/2}$ [eV]	459.33	-	459.27	459.28	-	0	-0.01
	C 1s [eV]	-	285.11	285.11	285.10	0	0	0.01
	fwhm C 1s [eV]	-	0.72	0.72	0.73	-	-	-
ex situ + 7 Å C_{60}	WF [eV]	3.86	3.99	3.99	3.94	0	0	0.05
	Ti $2p_{3/2}$ [eV]	459.48	459.46	459.46	459.48	0	-0.00	-0.02
	C 1s [eV]	-	285.81	285.78	285.50	0	0.03	0.31
	fwhm C 1s [eV]	-	0.58	0.59	0.69	-	-	-

10.4 Anatase/C_{60} interface diagrams determined from synchrotron experiments

Figure 10.7 left shows the energy diagrams derived from the *in situ* (left) and *ex situ* (right) anatase-(101)/C_{60} interface experiments. The VBM of *in situ* TiO_2 is at 3.2 eV E_{Bin} and the distance to the Ti $2p_{3/2}$ level is 456.0 eV as measured in Section 8.2.2. The *in situ* sc-(101)/C_{60} energy diagram shows no shift of the Ti $2p_{3/2}$ level upon increasing C_{60} coverage. As no adsorbates are present on the TiO_2 sc-(101) surface a flat band situation is assumed from the bulk to the surface, even though the presence of oxygen vacancies might leads to the formation of an accumulation layer at the surface of TiO_2.[16] The C 1s level of C_{60} exhibits an upward band bending of 200 meV towards the interface. The $HOMO_{max}$ position of the 110 Å C_{60} layer is at 2.3 eV and its distance to the C 1s level is 282.7 eV, which is in agreement with the values obtained in Section 8.3. The difference in WF of 0.65 eV of both materials is adjusted by the formation of an interface dipole of 0.45 eV and a 200 meV upward band bending of the C 1s level. This results in a VBM/$HOMO_{max}$ offset of 1.1 eV and Ti $2p_{3/2}$/C 1s distance of 174.4 eV.

The *ex situ* sc-(101)/C_{60} interface is depicted in the middle of Fig. 10.7. As for the *in situ* case, the TiO_2 shows no band bending, but as adsorbates are present on the surface, a band bending towards the surface is likely and the measured Ti $2p_{3/2}$ binding energy values are only representative for the surface and not for the bulk. The VBM of TiO_2 is at 3.4 eV and its distance to the Ti $2p_{3/2}$ level is 456.0 eV. The C_{60} C 1s level shows a downward band bending of 200 meV towards the interface. For highest C_{60} coverage the C_{60} $HOMO_{max}$ is at 2.5 eV and the C 1s level at 285.3 eV. The C 1s/$HOMO_{max}$ distance is 282.7 eV and again in good agreement with the values obtained for C_{60} on gold (see Section 8.3). Compared to the *in situ* sc-(101)/C_{60} interface the VBM/$HOMO_{max}$ offset decreases by 0.4 eV to 0.7 eV and the Ti $2p_{3/2}$/C 1s distance to 174.0 eV.

UV influence on *in situ* and *ex situ*/C_{60} interface

On the *in situ* sc-(101) surface, the Ti $2p_{3/2}$ level and C_{60} C 1s core level are not influenced by UV light and the binding energy stays constant at 459.3 eV and 285.1 eV, respectively. This results in a Ti $2p_{3/2}$/C 1s distance of 174.2 eV before and after UV. In contrast to the Ti $2p_{3/2}$/C 1s distance, the Ti $2p_{3/2}$ and the C_{60} C 1s level on the *ex situ* cleaved crystal are influenced by UV light. The Ti $2p_{3/2}$ level

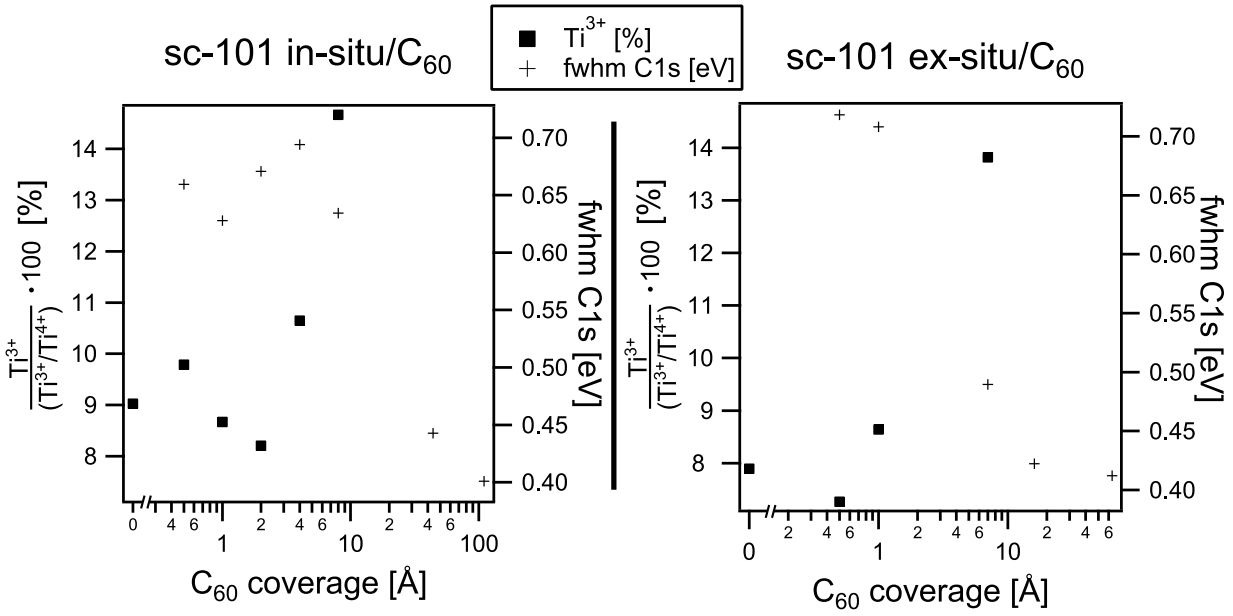

Figure 10.6. – On the left, the evolution of Ti^{3+} emission (black squares) and C_{60} C 1s *fwhm* (black plus signs) in the course of the C_{60} deposition onto an *in situ* cleaved sc-(101) surface is depicted. For the first two depositions, the Ti^{3+} diminishes (till 2 Å) and then starts to increase. The C 1s *fwhm* is at first constant at around 0.65 eV and starts decreasing at 40 and 110 Å C_{60} to 0.45 and 0.40 eV respectively. On the right, the evolution of Ti^{3+} (black squares) and C_{60} C 1s *fwhm* (black plus signs) of the sc-(101) *ex situ*/C_{60} interface is depicted. The Ti^{3+} content at the beginning is around 8 % and starts to increase at a C_{60} coverage of 8 Å. The C 1s *fwhm* is first at around 0.7 eV and then decreases at a coverage of 7 Å. At 16 Å and higher C_{60} coverage the C 1s *fwhm* is ∼0.4 eV.

moves upwards by 100 meV to 459.4 eV and the C 1s core level binding energy decreases by ∼300 meV from 285.8 eV to 285.5 eV upon UV illumination. The resulting Ti $2p_{3/2}$/C 1s distances are 173.7 eV before UV illumination and 173.9 eV after UV illumination.

10.5 Discussion anatase/C_{60} interfaces

In this section the TiO_2/C_{60} interface formation of *in situ* and *ex situ* cleaved sc-(101) TiO_2 surface was investigated. Figure 10.7 shows the energy diagrams of the TiO_2 sc-*in situ*, sc-*ex situ* and the amorphous TiO_x/C_{60} interface. In all cases the Ti $2p_{3/2}$ level does not shift upon increasing C_{60} coverage. But while C_{60} energy levels bend upwards towards the interface on *in situ* TiO_2, C_{60} energy levels bend downwards towards the interface on *ex situ* cleaved TiO_2 and the amorphous TiO_x. This indicates an electron transfer from C_{60} to TiO_2 at the *in situ*/C_{60} interface, while at the *ex situ*/C_{60} interfaces the charge transfer is from TiO_2 to C_{60}. The difference in the C_{60} band bending towards the interface is reflected by a change of the Ti $2p_{3/2}$-C 1s distance which is 174.4 eV for the *in situ*/C_{60} interface, 174.1 eV for the *ex situ*/C_{60} interface and 173.4 eV for the amorphous TiO_x/C_{60} interface. The Ti^{3+} evolution in Fig. 10.6 shows an initial decrease of Ti^{3+} states, followed by an increase at higher C_{60} coverages. This could be caused by

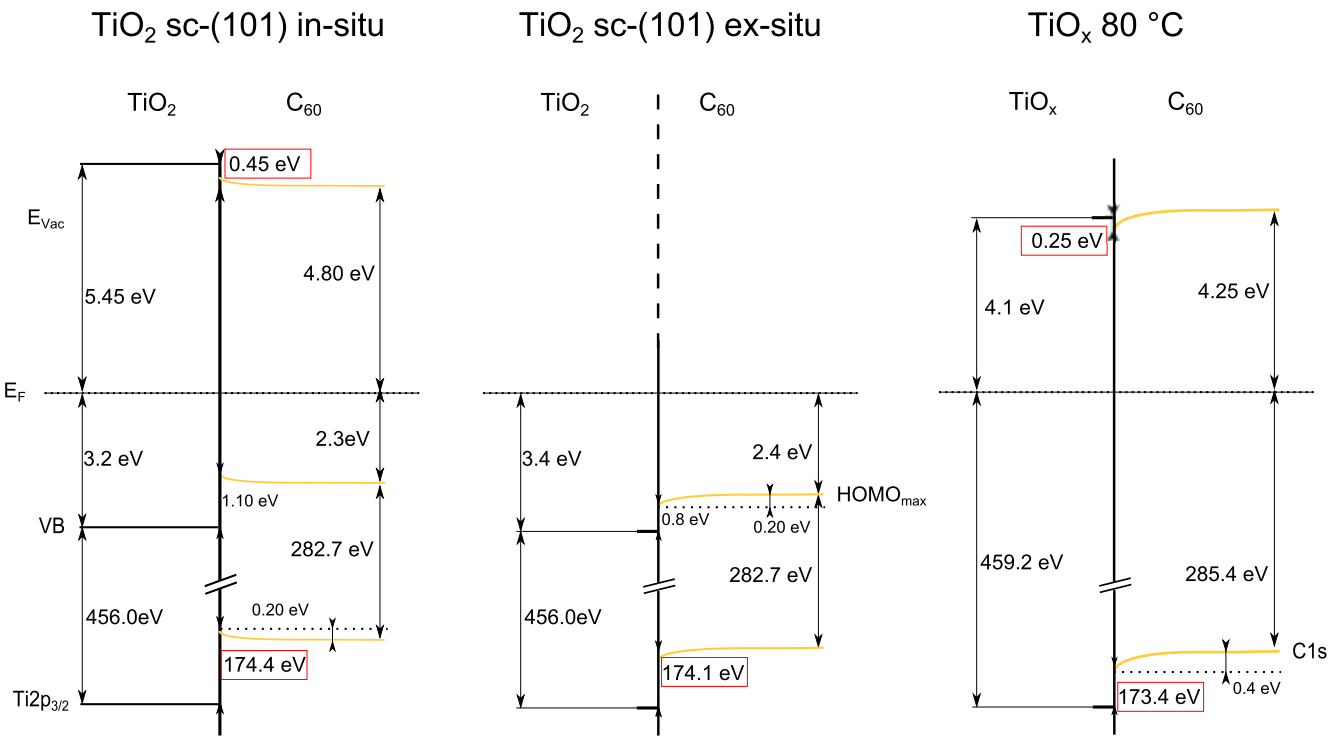

Figure 10.7. – Energy diagrams of the *in situ* TiO_2/C_{60} interface (left), the *ex situ* TiO_2/C_{60} interface (middle) and the TiO_x 80 °C/C_{60} interface (right). For the *in situ* case a flat band situation in the TiO_2 is assumed. The VB and the Ti $2p_{3/2}$ level do not show any band bending. C_{60} shows an upward band bending of 0.2 eV towards the interface. At the interface the VBM/$HOMO_{max}$ distance is 1.1 eV and the Ti $2p_{3/2}$/C 1s distance is 174.4 eV. In the *ex situ* case the Ti $2p_{3/2}$ level shifts neither upon C_{60} deposition, but adsorbates on the TiO_2 surface might induce a band bending at the TiO_2 surface. C_{60} shows a downward band bending of 0.2 eV towards the interface. At the interface the VBM/$HOMO_{max}$ distance is 0.8 eV and the Ti $2p_{3/2}$/C 1s distance is 174.1 eV. For the amorphous *ex situ* C_{60} interface, the C 1s level bends 0.4 meV downwards and the Ti $2p_{3/2}$/C 1s distance is 173.4 eV at the interface. Both *ex situ* interfaces show the trend to a reduction of the Ti $2p_{3/2}$-C 1s distance compared to the *in situ* interface, while the amorphous TiO_x interface displays a stronger decrease of the Ti $2p_{3/2}$/C 1s distance.

a reordering of C_{60} molecules from oxygen vacancies to defect free areas of the surface at increasing C_{60} coverage and/or increased levels of synchrotron induced Ti^{3+} states. At both C_{60} interfaces, with *ex situ* and *in situ* TiO_2, the initial C 1s *fwhm* is at around 0.65 eV and decreases for high C_{60} coverages to ~0.4 eV.[1] While the C_{60} C 1s *fwhm* on *in situ* TiO_2 is constant till 8 Å C_{60} coverage and shows a strong decrease at 40 Å, the C_{60} C 1s *fwhm* on *ex situ* TiO_2 shows already a decrease at 7 Å C_{60}. At 16 Å C_{60} the C 1s *fwhm* decrease is saturated to 0.4 eV. The C 1s *fwhm* is of interest as a change can be an indication for a different adsorption configuration of C_{60} on the TiO_2 or a different energetic alignment at the interface. If e.g. a *fwhm* increase is observed, this could be either due to band bending of the C_{60} within the escape depth of the photoelectrons, doping of parts of the C_{60} layer or a change of the molecular structure of the molecule.

By depositing C_{60} onto an *in situ* and *ex situ* cleaved sc-(101) surface and the subsequent illumination with UV light, it was shown, the UV induced changes of the Ti $2p_{3/2}$-C 1s distance can be clearly

[1] The C 1s *fwhm* values of the *ex situ* interface experiment are corrected by subtracting 0.1 eV, as the resolution of the measurement of the *ex situ* experiment was lower compared to the *in situ* experiment. The resolution was determined by the width of the Fermi edge of a clean silver sample.

attributed to adsorbates on *ex situ* TiO_2. Typical adsorbates on TiO_2 are water and oxygen[175] and both are known to undergo UV triggered reactions.[176–179] Furthermore the C 1s *fwhm* of a thin C_{60} layer on *in situ* cleaved sc-(101) is constant after UV illumination, but increases on an *ex situ* cleaved sc-(101) surface after UV illumination.

Table 10.2 shows all Ti $2p_{3/2}$-C 1s distances determined so far. The Ti $2p_{3/2}$-C 1s distances on the *in situ* samples are 174.4 eV and 174.2 eV. On the *ex situ* sample (sc-(101) and 80 °C TiO_x) the distance is smaller and ranges from 173.4 eV (80 °C TiO_x before UV) to 174.0 eV (sc-(101) at Bessy). UV light causes an increase of the Ti $2p_{3/2}$-C 1s distance at both interfaces, *ex situ* sc-(101) and 80 °C TiO_x. The increase after UV is towards the value of Ti $2p_{3/2}$-C 1s distance of the *in situ* interface (174.4 eV and 174.2 eV).

Table 10.2. – Ti $2p_{3/2}$-C 1s distance of the differently prepared TiO_2/C_{60} interfaces and the influence of UV light.

Ti $2p_{3/2}$-C 1s distance [eV]	Bessy	Daisy-Fun before UV	Daisy-Fun after UV
TiO_2 *in situ*/C_{60}	174.4	174.2	174.2
TiO_2 *ex situ*/C_{60}	174.1	173.7	174.0
TiO_x 80 °C/C_{60}	-	173.4	173.8

10.6 Summary anatase/C_{60} interfaces

In Chapters 9 and 10, titania/C_{60} interfaces and the influence of UV light were investigated by means of photoelectron spectroscopy. The C 1s level at low C_{60} coverages on *in situ* prepared titania samples has a lower binding energy than on *ex situ* surfaces (E_{Bin} (C 1s) on *in situ* = 284.8 eV; on *ex situ* = 285.3 eV). UV induces an upward shift (to lower binding energies) of the C_{60} C 1s energy level at *ex situ* titania/C_{60} interfaces, while no shift is observed at *in situ* titania/C_{60} interfaces. From the performed experiments, it is evident that adsorbates directly adsorbed on the TiO_2 are a prerequisite for UV induced shifts. Furthermore UV induced shifts at the *ex situ* titania/C_{60} interface cause a C_{60} C 1s shift to lower binding energies and therefore towards the C 1s binding energy of the *in situ* TiO_2/C_{60} interface.

Origins of the C 1s shift could be an UV induced charge transfer between TiO_2 and C_{60}. Kamat et al. observed an electron charge transfer from TiO_2 colloids in ethanol to C_{60} upon UV irradiation (C_{60} reduction)[180] as well as a C_{60} oxidation upon illumination with light in the range of 400 to 700 nm in the presence of TiO_2 nanoparticles.[181] As the *in situ*/C_{60} interface does not show any change after UV influence a C_{60} reduction or oxidation is excluded in this case. Concerning adsorbates like water or oxygen on the titania surfaces, C_{60} might react with each of them. Lee et al. reported that C_{60} is stable in water and no reaction occurs.[182] Upon UV illumination Lee et al. demonstrated by XPS that C_{60} dissolved in water degrades and observed a drastic change of the C 1s emission.[183] Such a change of the C_{60} C 1s emission was not observed in the present results and therefore a degradation of the C_{60} is unlikely. Concerning the interaction of C_{60} with oxygen, electron transfer from C_{60} to oxygen is reported by Tanaka et al. They performed UPS measurements and observed an upward shifts of C_{60} energy

states upon oxygen exposure, which they attributed to the partial positive charge forming at the C_{60} molecule ($\overset{\delta+}{C}_{61}$).[184,185] Ng at al. observed similar results by UPS.[153] Yang et al. reported a decrease of the electrical conductivity of C_{60} upon O_2 exposure and attributed this decrease to the formation of an O_2^+–C_{60}^- dipole moment, which acts an acceptor to attract free electron carriers.[186,187] A degradation of C_{60} by UV[188] itself can be excluded as no influence of UV exposure on the C 1s shape at the *in situ* TiO_2/C_{60} interface was observed in our study. This was confirmed by UV illumination of a C_{60} layer on gold, where no UV influence is observed (see appendix Fig. A.2).

The results obtained in this section clearly indicate that adsorbates are responsible for UV induced alignment changes at the TiO_x/C_{60} interface. In the next chapter the influence of UV light and adsorbates on different titania surfaces is investigated.

11 The titania / air interface and the influence of UV light

The interface experiments with *in situ* and *ex situ* cleaved anatase single crystals strongly suggest that adsorbates are responsible for the observed energy shifts upon UV illumination. Therefore the influence of adsorbates and UV illumination on the specific substrates is investigated in more detail in this chapter. The focus is on the influence of adsorbates on the TiO_2 surface and the impact on the specific surfaces. In Sections 11.1.1 and 11.1.2 the influence of *in situ* and *ex situ* cleavage as well as the UV influence on the anatase sc-(101) surface is investigated. Additionally the influence of oxygen on an *in situ* cleaved anatase sc-(101) surface is investigated (Section 11.1.4). Differently prepared TiO_2 sc-(101) surface are compared with respect to the energy level positions and shifts. Possibly the shifts are induced by adsorbates or UV light, but it must be considered that these can also originate from a different natural doping of different naturally grown crystals.

11.1 Anatase single crystal: Influence of air and UV light

11.1.1 Anatase single crystal *in situ*: Influence of air exposure and UV illumination

In Fig. 11.1 XP spectra are shown of an *in situ* cleaved TiO_2 sc-(101) surface (red), the same crystal exposed to air (gray/black) and subsequent irradiation with UV light for 60 min (blue). On the left are the O 1s spectra, in the middle the Ti $2p_{3/2}$ and on the right the C 1s spectra. The O 1s emission is at E_{Bin} = 530.50 eV after *in situ* cleavage. After exposure to air, the O 1s level shifts to 530.60 eV and after UV irradiation to 530.65 eV. The Ti $2p_{3/2}$ emission of the *in situ* cleaved sc-(101) surface is at 459.25 eV binding energy and shifts after air exposure to 459.35 eV. UV light leads to a further shift of the Ti $2p_{3/2}$ emission to 459.45 eV. The O 1s and Ti $2p_{3/2}$ core emission lines shift in parallel and their difference is 71.2 eV, which is in good accordance with results obtained in Section 8.2.2. As can been seen on the right of Fig. 11.1, there is still some carbon on the cleaved surface. After exposure to air the C 1s emission clearly increases. The O 1s emission shows an additional emission at 532.5 eV, which is attributed to hydroxyls. Due to technical problems, no SE-edge spectra could be recorded.

The results are summarized in a surface potential diagram in Fig. 11.2. For the *in situ* case (left), flat band conditions are assumed. After exposure to air (middle) the Ti $2p_{3/2}$ binding energy increases by 100 meV which is reflected by a downward band bending at the surface. After UV illumination (right) the Ti $2p_{3/2}$ binding energy increase further by 100 meV, which is reflected by an overall 200 meV downward band bending at the surface.

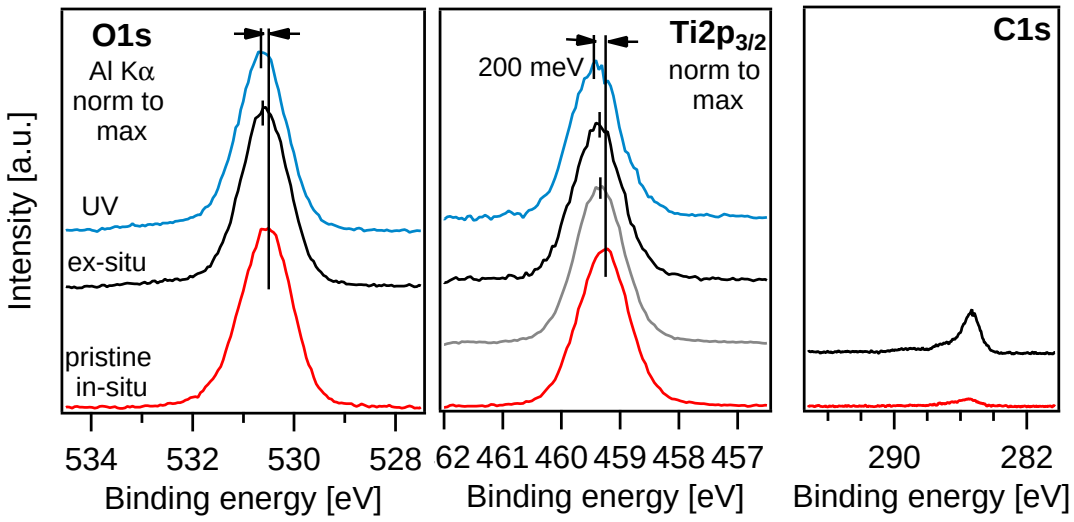

Figure 11.1. – Influence of air exposure and subsequent UV illumination on an *in situ* cleaved (101) surface. On the left and in the middle the O 1s and Ti $2p_{3/2}$ level emissions are displayed. Both shift 100 meV in parallel to higher binding energies upon exposure to air (red→black). After UV illumination the O 1s and the Ti $2p_{3/2}$ emission shift by additional 100 meV to higher binding energies (black→blue). On the right the C 1s emission is shown after cleavage (red) and after subsequent air exposure (black).

Figure 11.2 – Surface potential energy diagram of the *in situ* cleaved anatase (101) surface (left) upon exposure to air (middle) and subsequent UV irradiation (right). For the *in situ* case a flat band situation is assumed at the surface. Air exposure induces a downward band bending at the surface of 100 meV, which increases to 200 meV after UV irradiation.

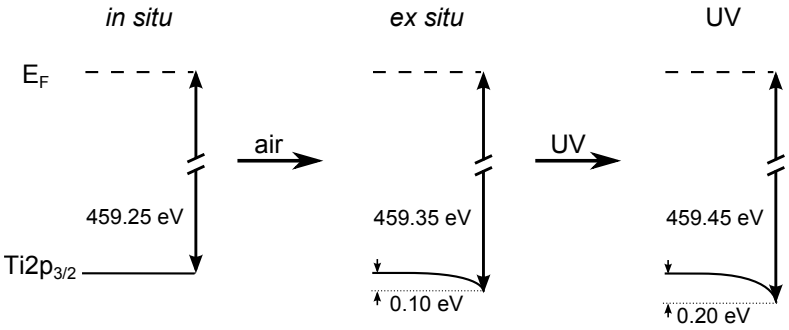

11.1.2 Anatase single crystal: Influence of UV illumination on *in situ* and *ex situ* cleaved anatase

Figure 11.3 shows the SE edge, the O 1s and the Ti $2p_{3/2}$ emission line of an *in situ* cleaved crystal (red), the same crystal after 60 min UV illumination (blue), an *ex situ* cleaved crystal (gray) and the *ex situ* crystal after about 600 s X-ray (black) and 60 min UV exposure (blue). Compared to the previous *in situ* cleaved crystal the surface contamination with carbon was much smaller (see Fig. 11.4).

The WF of the clean *in situ* cleaved crystal is 4.93 eV and diminishes after 60 min UV by 100 meV to 4.83 eV. The *ex situ* cleaved crystal has an initial WF value of 4.05 eV (about 120 s X-ray exposure). Additional 600 s X-ray irradiation decreases the WF further to 3.95 eV. Again the sample was exposed to 60 min UV, which decreased the WF to 3.82 eV. The core emission lines, O 1s and Ti $2p_{3/2}$, show comparable results. After UV illumination of the *in situ* cleaved sample neither the O 1s and Ti $2p_{3/2}$ nor the VBM show any change. The O 1s binding energy of the *ex situ* cleaved sample is 530.50 eV and is 250 meV higher compared to the *ex situ* cleaved surface. UV illumination shifts the O 1s binding energy ~200 meV further to higher binding energies (530.70 eV). The Ti $2p_{3/2}$ emission behaves the same as the O 1s emission and is initially 250 meV higher compared to the *in situ* cleaved sample (459.00 eV and 459.25 eV respectively) and then UV light induces a further shift by 250 meV to higher binding energies

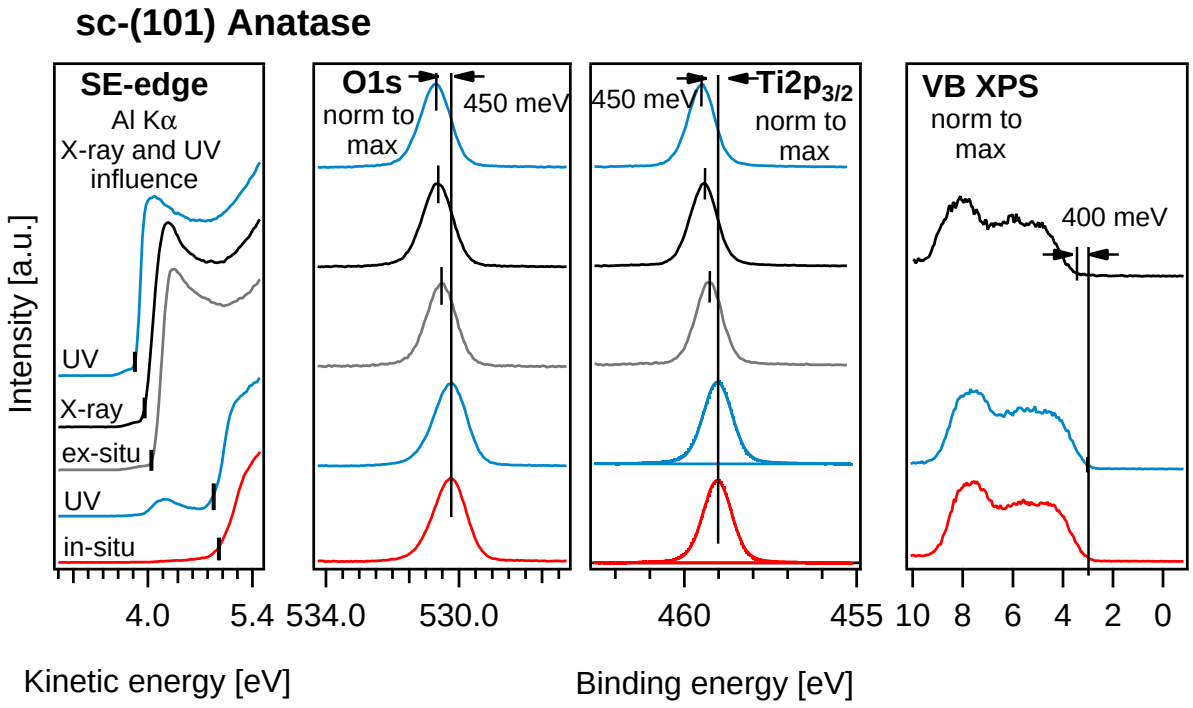

Figure 11.3. – SE-edge, O 1s, Ti $2p_{3/2}$ and valence band spectra of an *in situ* and *ex situ* cleaved anatase crystal. The lowest two spectra show the *in situ* cleaved sc-anatase before (red) and after UV (blue) illumination. The gray spectrum shows the *ex situ* cleaved anatase upon minimal X-ray exposure. The black spectrum is recorded after about 600 s X-ray exposure and the top blue spectrum after additional 60 min UV illumination.

(459.49 eV *ex situ* + UV). Accordingly, the VBM shifts in parallel too and increases from initially 3.03 eV to 3.43 eV after X-ray exposure.

While the line shape of the Ti $2p_{3/2}$ emission of the *ex situ* and *in situ* cleaved sample is very similar, the O 1s line shape of the *ex situ* cleaved sample is slightly different. At the high binding energy side a small additional component is visible (see Fig. 11.4A). The emission is around 532.5 eV and is attributed to H_2O or OH^- adsorption. The same emission in the O 1s spectrum appears as well in Fig. 11.1. UV light does not induce any change of the line shape, neither at the O 1s nor at the Ti $2p_{3/2}$ emission, thus a formation of Ti^{3+} states can be excluded or is below XPS detection level (see Fig. 11.4B). As the crystal is cleaved and no further treatment of the crystal is performed, only a small or no surface defect concentration is expected. The data from synchrotron induced photoemission measurements on an *in situ* cleaved anatase single crystal (see Chapter 17) indicate the occurrence of small fraction of V_O. The C 1s emission is higher on the *ex situ* cleaved (101) surface (see Fig. 11.4C) and contains three emissions. The emissions are attributed to C-C bonds (~285.0 eV), C-O (~286 eV) and O-C-O (~289 eV) moieties (see Section 8.2.1).[110]

11.1.3 Discussion of energy level positions of *in situ* and *ex situ* cleaved TiO_2 samples

Compared to the *in situ* cleaved TiO_2 (101) surface in Fig. 11.3, the O 1s and Ti $2p_{3/2}$ emissions of the *in situ* cleaved sc-(101) in Fig. 11.1 are shifted by 250 meV to higher binding energies. The difference in binding energy position can either be a bulk property and be caused by a different doping due to

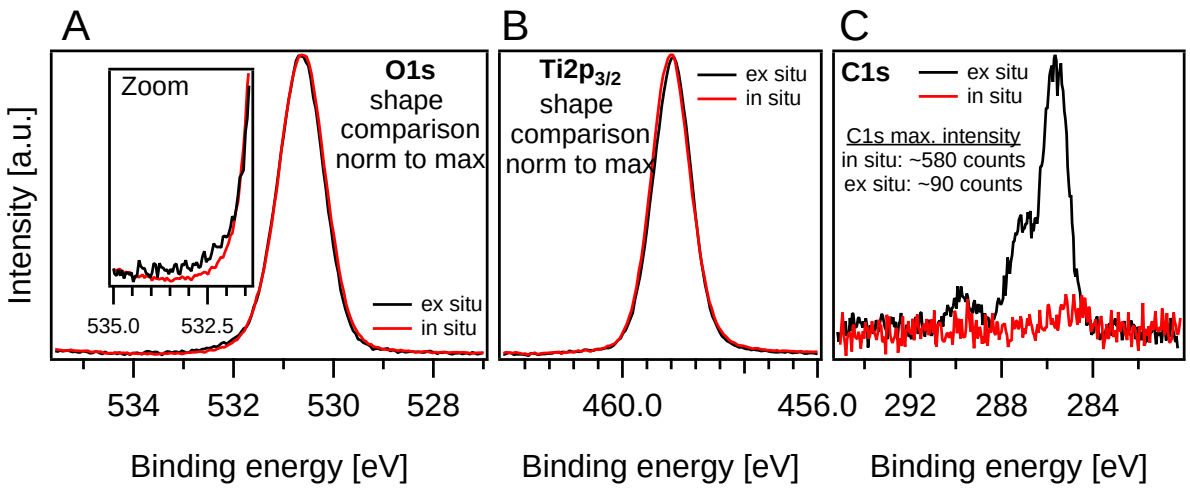

Figure 11.4. – Detail spectra of the O 1s (A), the Ti $2p_{3/2}$ (B), and the C 1s (C) emission lines for the *in situ* (red) and *ex situ* (black) cleaved single crystal. The O 1s emission and the Ti $2p_{3/2}$ emission are normalized to the same maximum intensity to compare the line shape. While no change of the line shape is observed for the Ti $2p_{3/2}$ core level, the O 1s line shows a small shoulder at the high binding energy site. The C 1s core level is not normalized and shows that the C 1s emission of the *ex situ* cleaved sample is about 6 times higher, than the C 1s intensity of the *ex situ* cleaved anatase.

Table 11.1. – Work function, binding energy and valence band maximum position of the *in situ* and *ex situ* sc-anatase (101), in dependence of X-ray and UV illumination. *Calculated by the Ti $2p_{3/2}$ core level minus 456.00 eV (see Section 8.2.1).

	in situ	*in situ* + UV	*ex situ*	*ex situ* + X-ray	*ex situ* + UV
O 1s [eV]	530.23	530.23	530.52	530.62	530.68
Ti $2p_{3/2}$ [eV]	459.02	459.02	459.25	459.39	459.49
VBM [eV]	3.03	3.05	3.25 (calc.)*	3.40	3.49 (calc.)*
WF [eV]	4.93	4.83	4.05	3.95	3.82

impurity atoms, or it is due to adsorbates, which may induce depletion or accumulation layers at the surface. Comparing *in situ* cleaved samples with respect to contaminations on the surface, no O 1s emission from hydroxyls is observed, but different amounts of carbon contaminations. The carbon contaminations probably arises from the scissor blades of the pliers, which can scratch over the surface during the cleavage process. The *in situ* cleaved sc-(101) surface shown in Fig. 11.3 was by far the cleavage with the lowest carbon contamination (C 1s/Ti $2p_{3/2}$ ratio = 0.001). All other presented *in situ* cleavages have about the same carbon contamination (C 1s/Ti $2p_{3/2}$ ratio = ~0.01).

Experiments in Section 11.1.2 indicate that air exposure of the (101) surface leads to a decrease of the WF and an increase of the Ti $2p_{3/2}$ binding energy. The binding energy shift after air exposure is confirmed by the air exposure of an *in situ* crystal in Section 11.1. Assuming flat band conditions of the anatase crystal after UHV cleavage, the increase of the Ti $2p_{3/2}$ binding energy is attributed with the formation of an accumulation layer at the surface of the anatase crystal. Regarding the influence of UV illumination on the TiO_2 (101) surface, it is shown, that UV light induces no core level shift on *in situ* cleaved anatase and a 100 meV decrease of the WF. On *ex situ* samples, either cleaved *ex situ* or *in situ* cleaved and exposed to air, UV light induces a shift of the core levels of 100-200 meV to higher binding energies. The increase in binding energy is equivalent to a further increase of the accumulation layer already present at the sc-anatase (101) surfaces.

From the obtained XP spectra a schematic energy diagram showing the influence of air and UV light on an anatase sc-(101) surface is derived and depicted in Fig. 11.5. As the *in situ* cleaved anatase crystal in Section 11.1.2 has the lowest carbon contamination, this is assumed as the pristine case of an *in situ* cleaved anatase (101) surface. As there is no indication of surface states as well, a flat band situation for the *in situ* cleaved anatase (101) surface is assumed (*in situ*). After *in situ* UV illumination a downward surface dipole potential of 0.1 eV is induced. The Ti $2p_{3/2}$ core level does not shift (*in situ* + UV). The exposure to air results in a core level shift of about 200 meV to higher binding energies, which corresponds to a downward band bending at the surface (*ex situ* initial). UV light increases the downward band bending at the surface by approx. 200 meV (*ex situ* + UV). The WF decreases almost by 1 eV upon air exposure and an additional surface dipole pointing downward is induced. After UV exposure, the SE-edge shifts in parallel to the core levels, which shows that the surface dipole does not change with UV illumination. All binding energies and work functions are summarized in Table 11.1.

11.1.4 Influence of O_2 plasma on anatase

In a second experiment a soft oxygen plasma was applied to an *in situ* cleaved sc-anatase (101) to investigate the effect of activated O_2 on TiO_2 surfaces. A soft oxygen plasma means that the shutter was kept in front of the plasma source, reducing the amount of charged oxygen species directly impinging onto the TiO_2 surface. This was done to reduce the possibility of oxygen plasma induced surface modifications. After the oxygen plasma treatment the influence of X-ray and UV irradiation was investigated.

Fig. 11.6 shows the progression of the work function and the O 1s/Ti2p core level after UV illumination, subsequent oxygen plasma and repeated UV irradiation. As already shown above, the work function of the anatase crystal changes upon UV irradiation, whereas the core levels do not show any shift or a formation of Ti^{3+} states. After the oxygen plasma the SE-edge increases by about 200 meV from 4.8 eV

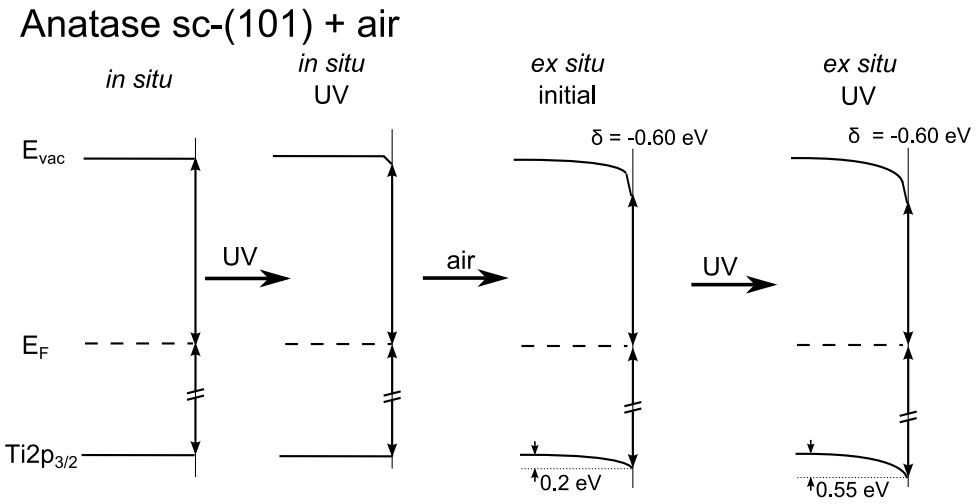

Figure 11.5. – Schematic surface potential diagrams for the *in situ* and *ex situ* cleaved sc-anatase. UV induces a small surface dipole on the *in situ* cleaved crystal. Air induces an accumulation layer and a negative surface dipole at the surface. With UV irradiation the band bending increases, while the surface dipole stays constant.

Table 11.2. – Work function and binding energy (O 1s and Ti $2p_{3/2}$) of the *in situ* and O_2 plasma treated sc-anatase (101) in dependence of X-ray and UV illumination.

	X-ray	X-ray + UV	O_2 (1)	O_2 (2)	O_2 (3)	UV
O 1s [eV]	530.28	530.28	530.14	530.21	530.34	530.58
Ti $2p_{3/2}$ [eV]	459.04	459.04	458.87	458.96	459.11	459.35
WF [eV]	4.9	4.82	5.06	4.99	4.81	4.47

to 5.0 eV kinetic energy and the core levels shift by about 150 meV to lower binding energies. The difference of about 50 meV arises probably from the fact that the SE-edge spectrum was recorded first and the Ti2p/O 1s level about 120 s later. While repeating the measurement (see O_2 (2) and O_2 (3)), the core levels and SE-edge shift further to higher binding energies and to lower kinetic energies, respectively. After about 600 s exposure to X-rays, core levels and WF are shifted back to the initial values after cleavage. After 60 min of UV illumination the anatase crystal work function and O 1s/Ti2p core level binding energies decrease by 300-400 meV below the starting point (see Fig. 11.7). While the shape of the Ti $2p_{3/2}$ emission does not change significantly (i.e. no Ti^{3+} emission is detected), the O 1s emission exhibits a small shoulder after oxygen plasma treatment at the high binding energy side of the O 1s emission, which is attributed to hydroxyls.[189]

The resulting surface potential diagrams for the O_2 plasma treatment is depicted in Fig. 11.8. After O_2 plasma treatment an upward band bending (eV_{bb}) of 200 meV at the surface occurs. This diminishes upon continuous X-ray exposure and flat band conditions are almost restored (eV_{bb} = -0.05 eV). Upon UV light irradiation a downward band bending of 300 meV is apparent and a surface dipole of -100 meV forms. Thus an accumulation layer forms again at the surface.

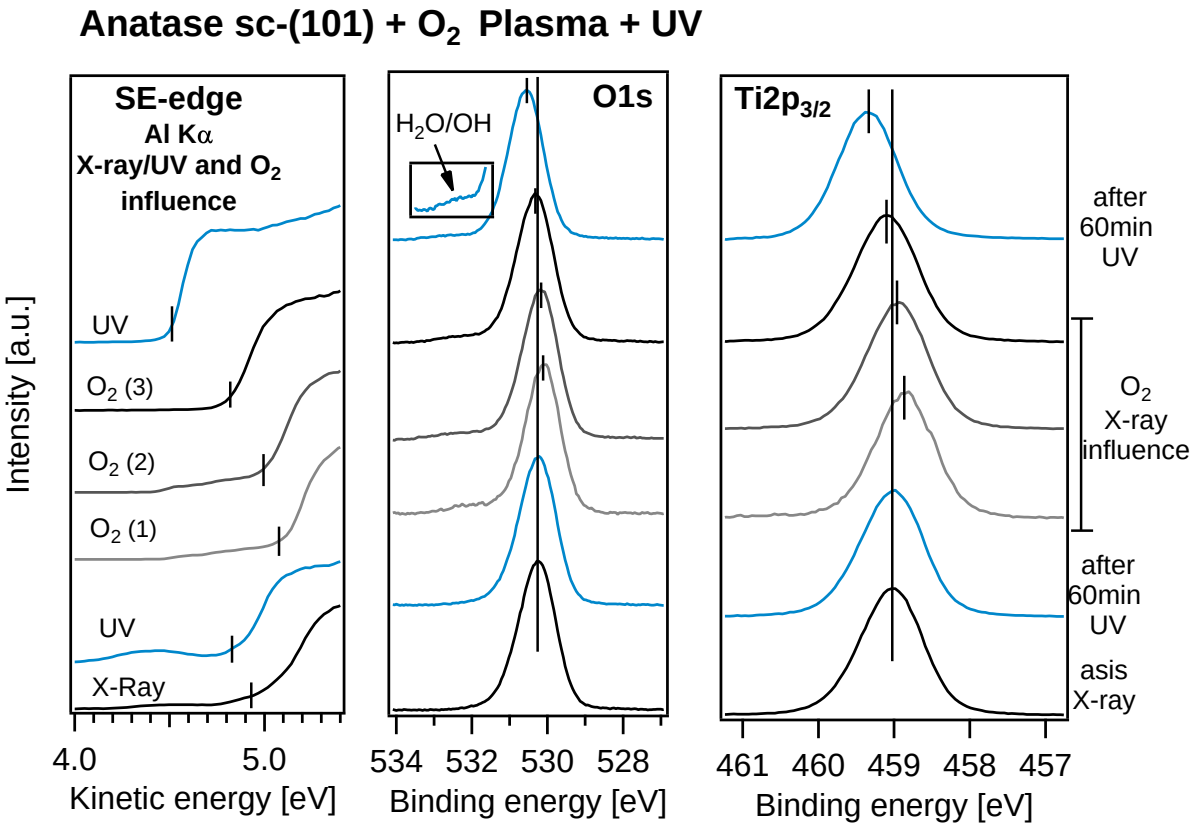

Figure 11.6. – SE-edge (left), O 1s core level (middle), and Ti $2p_{3/2}$ core level (right) of the oxygen plasma treated *in situ* cleaved TiO_2 sc-(101) surface. Oxygen plasma increases the WF and decreases the core level emission (O_2 (1)). Upon X-ray illumination the WF and the core levels shift back to the initial values (O_2 (2) and O_2 (3)) and UV illumination shifts the emission lines about 400 meV above the initial values (upper blue spectrum). The inset of the upper blue spectrum shows a magnification of the H_2O/OH binding energy range.

11.1.5 Discussion anatase single crystal: Air and UV influence

UV influence *in situ* cleavage

UV illumination of the *in situ* cleaved sc-anatase has only an impact on the WF of TiO_2. The reason for the WF reduction may be UV induced formation of V_O defects at the surface. Although the Ti $2p_{3/2}$ emission does not show any formation of Ti^{3+} states after UV, Ti^{3+} formation cannot be excluded as XPS is not surface sensitive enough.

V_O certainly can be induced by electromagnetic radiation, e.g. by synchrotron radiation in a range of about 90 eV on sc-anatase (101).[86,136,190] In Chapter 17 this is discussed in more detail for an *in situ* cleaved sc-(101) crystal and compared to amorphous TiO_x. Shultz et al. reported Ti^{3+} formation on rutile (110) upon irradiation with a mercury lamp (about $500\frac{W}{m^2}$) by second harmonic generation and XP spectroscopy, but could not certainly determine, whether the loss of bridging oxygen on the surface or O_2^- species chemisorbed on oxygen vacancy sites, is responsible for the Ti^{3+} appearance.[191] STM measurement by Mezhenny et al.[174] revealed that UV light with a power density of $9000\frac{W}{m^2}$ and an average photon flux of $10^{22}\frac{1}{m^2 \cdot s}$ creates 0.1 ML V_O within 300 h of illumination on rutile (110). For the synchrotron radiation used in Section 17.1, a power density of about 200000 $\frac{W}{m^2}$ at 90 eV binding energy can be assumed, which corresponds to a photon flux of $\sim 10^{22}\frac{1}{m^2 \cdot s}$.[106] (Note: The cross section

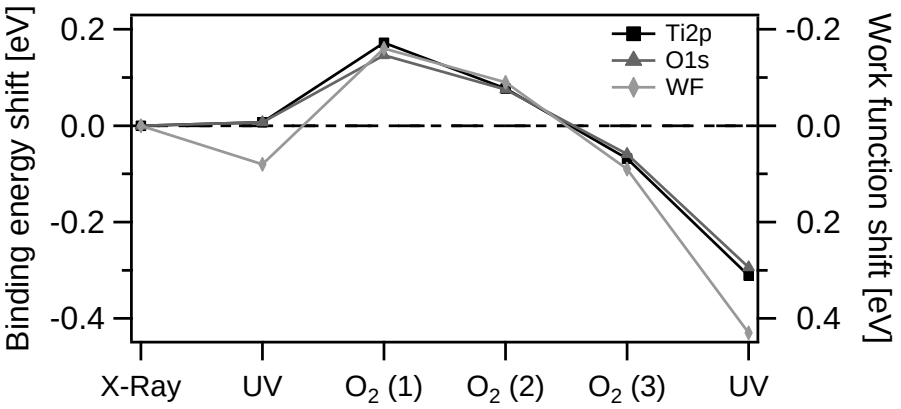

Figure 11.7. – Binding energy and work function shifts upon O_2 plasma and subsequent X-ray/UV treatment. Binding energy and work function shift in parallel, indicating no formation of a surface dipole.

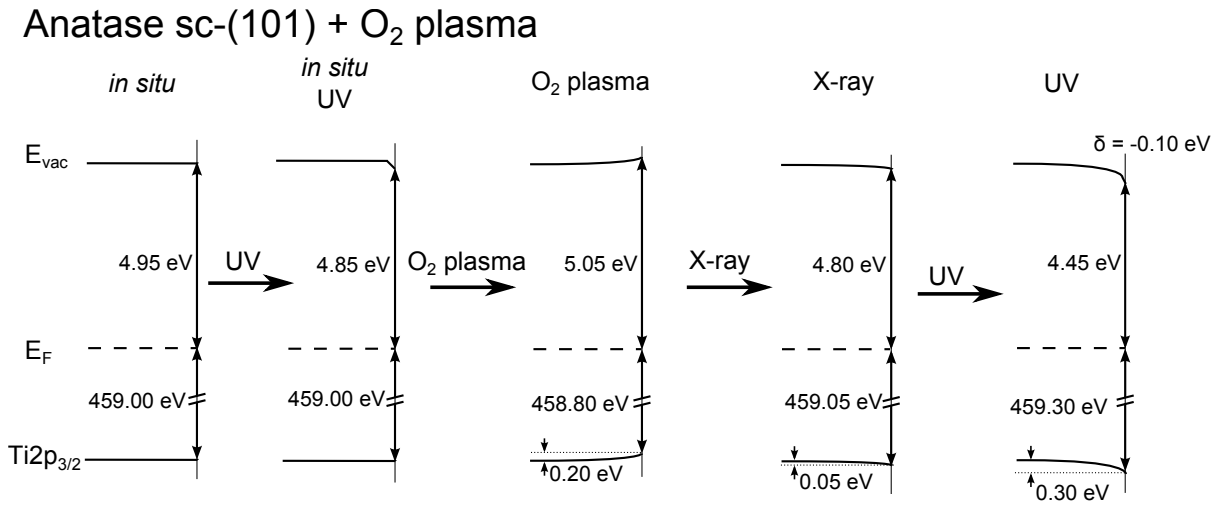

Figure 11.8. – Schematic surface potential diagrams for the *in situ* sc-(101) surface exposed to a soft oxygen plasma. UV induces a small surface dipole on the *in situ* cleaved crystal. O_2 plasma induces a depletion layer. With X-rays, bands bend downward till flat band situation is restored. UV increases downward band bending, which results in a band diagram similar to the air exposed sample.

of electrons for 90 eV and 3.4 eV photon energy is different, what makes a direct comparison, concerning V_O formation upon UV light with an energy of 3.4 eV difficult.) The power density of the used UV lamp on the sample surface was determined by a Bolometer and is $\sim 100 \frac{W}{m^2}$. Assuming a photon energy of 3.4 eV (as specified by the manufacturer[105]) this corresponds to a photon flux density of $\sim 10^{20} \frac{1}{m^2 \cdot s}$. Power density and photon flux of the mercury lamp used by Mezhenny et al. and the synchrotron radiation used are both much higher than of the UV lamp used in the experiments here. As Mezhenny et al. did not observe any V_O formation with a much higher power density and photon flux on rutile (110)[174] it is unlikely, that a significant amount of V_O forms upon UV illumination in this experiment. Borodin at al. reported a WF decrease of 300 meV on rutile (110) with V_O formation compared to a quasi a stoichiometric surface, but observed no VBM shift.[192] Therefore it may be concluded, that UV irradiation of the specific lamp induces little V_O density on the sc-anatase (101) surface, which results in only a small decrease of 0.1 eV of the WF. As the cleaved surface is quiet inhomogeneous, a different measurement spot might be responsible for the different WF values as well (even though this was tried to be avoided).

The formation of Ti^{3+} surface states could also induce a surface band bending due to charge transfer between the bulk and surface states. As a possible Ti^{3+} formation on cleaved anatase (101) is below XPS detection level, this will not be further discussed in this section. In Section 11.2.1 the influence of Ti^{3+} surface states on surface band bending at a different titania sample is discussed in more detail.

Air and UV influence on the *ex situ* cleaved sc-(101)

Air contains mainly nitrogen, oxygen and carbon dioxide. While N_2 is an inert gas, the other main components, O_2 and CO_2 can in principle adsorb onto TiO_2 surfaces. Ambient air is also humid to some degree and water (H_2O) or other hydroxyls are further components which may adsorb to TiO_2. The spectra in Fig. 11.4 show, that hydroxyls (Fig. 11.4 A), C-O and carbonates adsorb onto the surface of the *ex situ* cleaved sample (Fig. 11.4 C).

PES experiments by Herman et al. showed that water adsorbs molecularly on a homoepitaxial grown defect free (101)-anatase surface,[193] while it dissociates on a (001) anatase surface.[194] XPS results by Walle et al. showed molecular and dissociative adsorption of water on a sputter-annealed natural anatase crystal (101) surface.[195] From the obtained spectra in this chapter (see Fig. 11.1) no evidence is given, if molecular or dissociative water adsorption on the *in situ* cleaved anatase (101) surface occurs, but the results presented in Section 17.3 indicate molecular adsorption of water at liquid nitrogen (LN) temperature on an almost defect free anatase-(101) surface. Nevertheless dissociative water adsorption after *ex situ* handling of the crystal cannot be excluded as the O 1s spectra in Fig. 11.1 are not accurate enough.

In Fig. 11.5 it is shown that air induces a downward band bending on the TiO_2 surface and a surface dipole pointing downward. Anpo et al. deduced from photoluminescence measurements of TiO_2 in the presence of water that water causes a downward band bending at the surface of TiO_2.[148] Hugenschmidt observed a water induced downward band bending of 0.1 eV on the almost perfectly stoichiometric rutile (110) surface, which they attributed to a charge transfer from the water to the substrate. The O 1s emission in this experiment indicated molecular adsorption of the water on the rutile (110)

surface.[196] Hugenschmidt and many other authors observed a WF decrease upon hydroxylation of TiO_2 surfaces.[170,192,197,198] While Hugenschmidt attributed the WF decrease to molecular water, Marques et al. assigned the WF change to dissociated OH^-, existing on a reduced rutile (110) surface.[197] Onda et al. attributed the decrease to both, H_2O and OH^-, on a reduced rutile (110) surface.[198] The observed downward band bending in the work of about 100-200 eV upon air exposure of the *in situ* cleaved crystal (Figs. 11.2 and 11.5 agrees well with the data presented by Hugenschmidt et al. The same accounts for the observed decrease of the WF upon air exposure of the *in situ* cleaved anatase crystal, which is in the same range as observed by e.g. Marques and Onda upon hydroxylation of TiO_2.[196–198]

The probable mechanism that causes the electron donating character of water and the downward band bending at the TiO_2 surface is shown in Eq. (1.1). On V_O defect sites H_2O dissociates and forms Ti-OH,[199] where the oxygen occupies the V_O and the hydrogen points perpendicular to the surface.[197] The resulting free electron then causes the accumulation layer at the titania surface. As shown, oxygen vacancies are necessary for this process and the Ti $2p_{3/2}$ emission spectrum of the *in situ* cleaved anatase (101) surface recorded in Fig. 11.1 does not give any indication of existing Ti^{3+} species and hence V_O. However data obtained from highly surface sensitive synchrotron measurements in Section 17.1 evidences that V_O are present on the *in situ* cleaved anatase (101) surface as well. Therefore it is assumed that oxygen vacancies are certainly present on the *in situ* cleaved anatase sc-(101) surface.

$$Ti^{3+} + 1/2V_O + H_2O \longrightarrow Ti - OH + H^+ + e^- \tag{1.1}$$

For a direct electron transfer from the HOMO of water or hydroxyls to the TiO_2 surface, the H_2O (or OH) HOMO position should be above the occupied states of TiO_2 (either E_{VB} or E_{V_O}). Evidence of the V_O at the titania surface is given by the titania gap state at 1.3 eV binding energy. As shown in literature (Ref. [200]) and in Section 17.3 the HOMO's of H_2O and OH ($1b_1$(OH): ~6 eV eV and $1b_1$(H_2O): ~7.5 eV) are all below the titania gap states at 1.3 eV and therefore a direct electron transfer is not possible. Mayer et al. investigated water adsorption on WSe_2 and observed an electron donating character of H_2O as well. As the measured position of the H_2O HOMO is far below E_F of WSe_2 a direct electron transfer was excluded in this case. Mayer et al. explained the electron transfer from H_2O to WSe_2 by developing a model, where a donor state is derived by linear combination of atomic orbitals (LCAO) from the occupied W(d_z^2) valence band states, which interact with the occupied lone pair orbitals of adsorbed H_2O.[201] A corresponding model is shown in Fig. 11.9, where the donor state is derived from a LCAO from V_O derived gap state just below E_F and the occupied water orbitals. By an electron transfer from the donor state to the TiO_2, an accumulation layer forms at the TiO_2 surface.

Upon X-ray and UV radiation the air exposed sample shows an increase of the downward band bending, while the surface dipole stays constant. Gutmann et al. observed a WF decrease and presumed that $Al_{K\alpha}$ and HeI radiation creates oxygen vacancies in nanocrystalline anatase (see Eq. (1.2)).[170] Such an increase of V_O could enhance the reaction proposed in Eq. (1.1) and thus lead to the observed increase

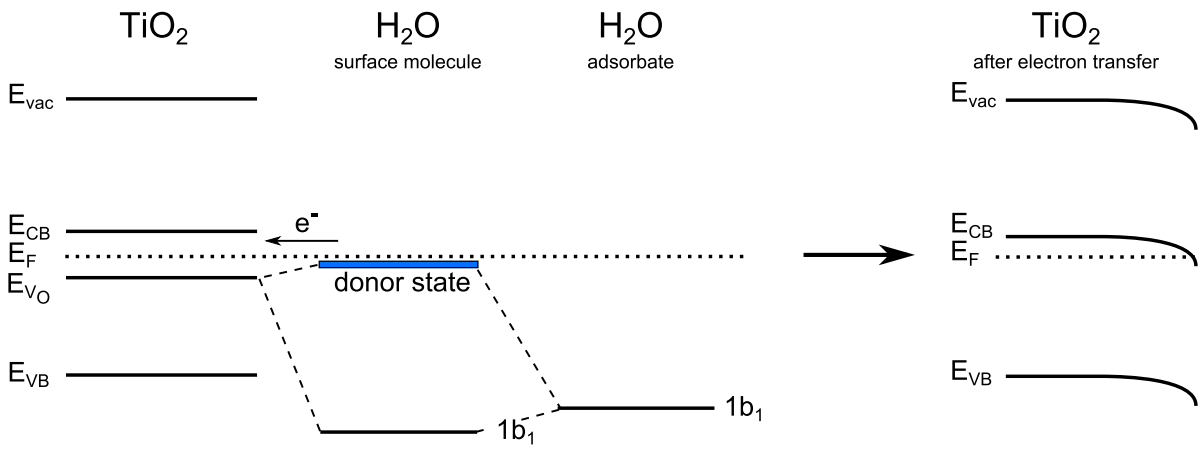

Figure 11.9. – Model for the accumulation layer formation on TiO_2 surfaces. As the HOMO of H_2O and water is below the occupied states right at the Fermi level a direct transfer from the HOMO of H_2O/OH to the TiO_2 gap state (E_{VD}) can be excluded. By linear combination of atomic orbitals of TiO_2 and the H_2O adsorbate, an extrinsic donor surface state forms, which allows the transfer of electrons from water to the TiO_2 surface. Adapted from Ref. [201].

of the downward band bending upon irradiation with $Al_{K\alpha}$ and HeI radiation on nanocrystalline TiO_x *ex situ* samples.[170]

$$2TiO_2 \xrightarrow[\text{radiation}]{\text{heat or}} 2Ti^{3+} + 3V_O^{2-} + 2O_2 \tag{1.2}$$

However the Ti $2p_{3/2}$ spectra in Fig. 11.5 do not give any evidence of the formation of Ti^{3+} upon $Al_{K\alpha}$ or UV irradiation. As discussed above V_O can be induced by synchrotron radiation,[86,136,190] but a formation upon the used UV light source is unlikely.[174] There is no report concerning X-ray induced V_O, but the probability of V_O formation upon $Al_{K\alpha}$ radiation certainly is less than for the used UV source. From the experiments performed in comparison to results from literature a significant V_O formation upon X-ray and UV irradiation on sc-anatase (101) seems unlikely.

Summarizing, it is most likely that H_2O or OH^- adsorbs on the anatase-(101) surface inducing a downward pointing surface dipole and the formation of an accumulation layer. Water dissociation and OH^- formation on UV induced V_O is doubtful and is ruled out as possible reason for the observed downward band bending. An exact identification of the adsorbed species and a statement about possible V_O at the surface is not possible as the surface sensitivity of XPS is not high enough.

O_2 influence and UV influence on the *in situ* cleaved sc-(101)

In contrast to hydroxyls, O_2 can adsorb on TiO_2 by scavenging electrons from the surface and inducing a depletion layer at the surface. Oxygen adsorbs as O_2^- by scavenging an electron and desorbs by scavenging a hole (h^+) (see Eqs. (1.3) and (1.4)).[171] The resulting effect on the energy diagram is depicted in Fig. 11.10. Upon adsorption of oxygen and scavenging of an electron, a depletion layer and a surface dipole forms at the TiO_2 surface (Fig. 11.10a). The negatively charged oxygen may

desorbs again molecularly by scavenging a hole, which e.g. is formed upon UV irradiation of TiO_2 (Fig. 11.10b).[171,178,202,203]

$$O_2 + e^-(TiO_2) \longrightarrow O_2^-(ads) \tag{1.3}$$

$$O_2^-(ads) + h^+(TiO_2) \longrightarrow O_2 \uparrow \tag{1.4}$$

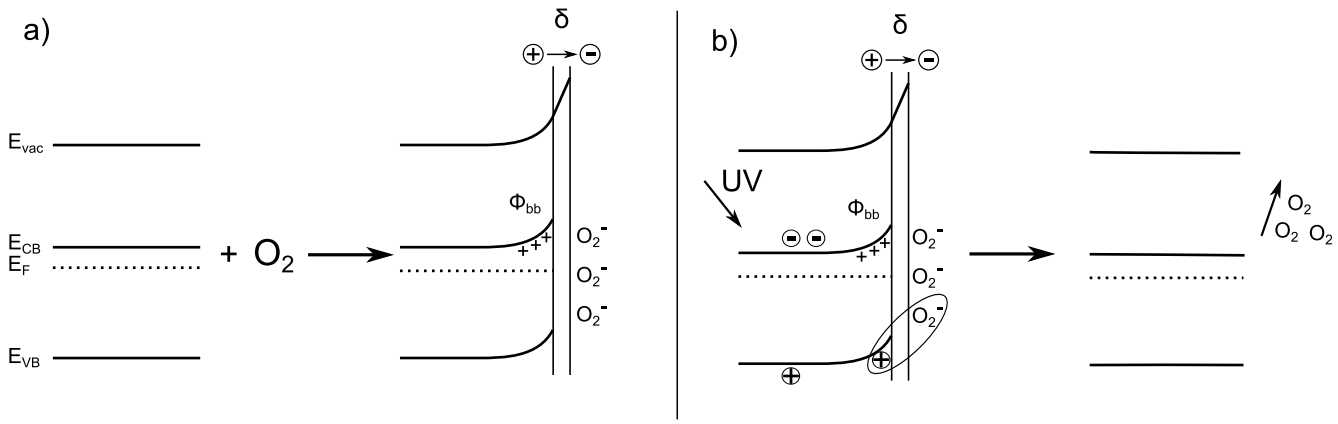

Figure 11.10. – a) Oxygen adsorbs as O_2^- at the TiO_2 surface inducing a depletion layer at the surface and a surface dipole. b) Upon irradiation with UV light, electrons are excited above the energy gap and O_2^- desorbs as O_2 by scavenging a hole.

Setvín et al. showed by STM measurements that O_2 adsorbs on the anatase (101) surface at oxygen subsurface vacancies as O_2^-.[204,205] Furthermore it is known that O_2 can adsorb on defective rutile (110) below temperatures of 410 K.[206,207] Setvín et al. showed as well that step edges on anatase (101) surface (4-fold coordinated Ti atoms) are donors and preferential adsorptions sites for acceptor molecules.[86] Furthermore adsorption of oxygen (or another electronegative element) at fivefold coordinated Ti sites does not violate the rules for creating a stable surface.[16] For instance, oxygen atoms can occupy fivefold coordinated Ru atoms of RuO_2 (110) under certain conditions. RuO_2 (110) has the same rutile structure as TiO_2.[16,208]

Regarding the influence of oxygen on the energy level positions of TiO_2, Porsgaard et al.[171] performed ambient pressure XPS (APXPS) of the rutile (110) surface and exposed it to 1.3 mbar O_2, which is the partial pressure of O_2 in air. They reported a shift of the Ti $2p_{3/2}$ and O 1s photoemission line of 0.4 eV to lower binding energies upon the exposure to 1.3 mbar O_2 compared to UHV conditions. Assuming a similar behavior of the investigated cleaved anatase (101) surface, this implies that O_2 at the TiO_2 surface causes a binding energy shift of 0.4 eV to lower binding energies, which is removed upon insertion of the sample into UHV.

The observed results of the O_2 plasma treated sc-anatase (see Section 11.1.4) are in good agreement with literature and upon exposure of TiO_2 to oxygen a depletion layer forms at the anatase (101) surface (see Fig. 11.8). Nevertheless no upward pointing surface dipole is observed in our experiments after oxygen exposure. The reason for this might be that some oxygen already desorbs after introduction of the sample into UHV, what is indicated by the experiment of Porsgaard et al. Already X-ray irradiation causes a shift of the binding energy values to its initial values. After UV illumination binding energies increase

(WF decrease) even further and an accumulation forms at the surface. A possible reason for this maybe the formation of hydroxyls during plasma treatment (see O 1s spectrum in Fig. 11.6) and therefore a hydroxyl induced formation of an accumulation layer at the TiO_2 surface (see discussion above). During plasma reactive oxygen species are formed, which may react with always present hydrogen[1] and form hydroxyls at the surface. Another reason for the observed downward band bending could be a surface modification due to the oxygen plasma. A formation of Ti^{3+} states, which would be an indication for such a surface modification, is not observed after oxygen plasma treatment.

11.1.6 Conclusion and summary: Anatase and adsorbates

From the conducted experiments surface potential diagrams of the *in situ* cleaved anatase crystal and the impact of air, oxygen and of X-ray/UV induced changes were derived. The surface potential diagrams are shown in Fig. 11.5 and Fig. 11.8. It is apparent that air induces a downward band bending and the formation of a surface dipole pointing in downward direction. UV illumination enhances downward band bending by about 200 meV, while the surface dipole stays constant. Assuming a complete oxygen desorption during UV illumination, O_2 adsorbed at air and remaining adsorbed in UHV, induces an upward band bending of 0.2 eV. This is in good agreement with data obtained on reduced rutile (110) surface, where $200L$ O_2 were exposed to the surface at room temperature and 200-300 meV upward band bending was observed.[16] It is presumed that oxygen weakly bounds at the (101) surface and is stronger bound at the donor like step edges present at the surface.[86] Porsgaard et al.[171] observed an upward band bending of 0.4 eV upon exposure of a rutile (110) surface to 1.3 mbar oxygen compared to UHV. Therefore an even higher, oxygen caused upward band bending at air, can be expected. Moreover it is presumed that water or hydroxyls induce a downward band bending and a surface dipole pointing downward. Band bending is probably caused by dissociative adsorption of water as OH^-, while the dipole is caused by molecular adsorbed water.[80,197]

A formation of Ti^{3+} surface states, respectively V_O, could not be detected by XPS. However the surface sensitivity of XPS might not be good enough to resolve Ti^{3+} states on the very surface. By taking the energy density of the used UV source into account and comparing it with experiments performed on rutile (110) by Mezhenny et al.[174] it seems unlikely that V_O are induced by UV irradiation on the anatase (101) surface. Thus a photochemical reaction of H_2O at additional UV induced V_O sites forming OH^-, suggested by Gutmann et al.,[170] is unlikely.

From the conducted experiment a model for air adsorption on sc-anatase (101) is derived (see Fig. 11.11). Air, specifically the water present in air induces an accumulation layer at the sc-(101) surface and bands bend downward. H_2O and OH^- adsorbs at oxygen vacancies (V_O) and on 5-fold coordinated Ti (belonging to the stoichiometric surface). O_2^- adsorption takes place simultaneously at certainly present step edges, which causes an electron depletion layer at the TiO_2 surface. The *in situ* cleaved anatase (101) surface is adsorbate free and displays V_O and step edges along the cleavage plane. At the surface flat band conditions are assumed (Fig. 11.11 top). On the bottom left oxygen adsorption is displayed. Oxygen adsorbs on step edges, V_O and on the defect free surface as O_2^-, inducing a depletion

[1] Hydrogen is diffusive even through solid steel and is expected to be the most prevalent contaminant in an UHV chamber.[117]

layer at the surface. Upon air adsorption (bottom middle), water and oxygen adsorb simultaneously. While oxygen induces an upward band bending, water and hydroxides induce a downward band bending and a downward pointing surface dipole. In total the electron donating character of water and hydroxides dominates the electron scavenging character of oxygen and a net downward band bending is observed. After UV illumination oxygen is desorbed and the downward band bending increases (bottom right).

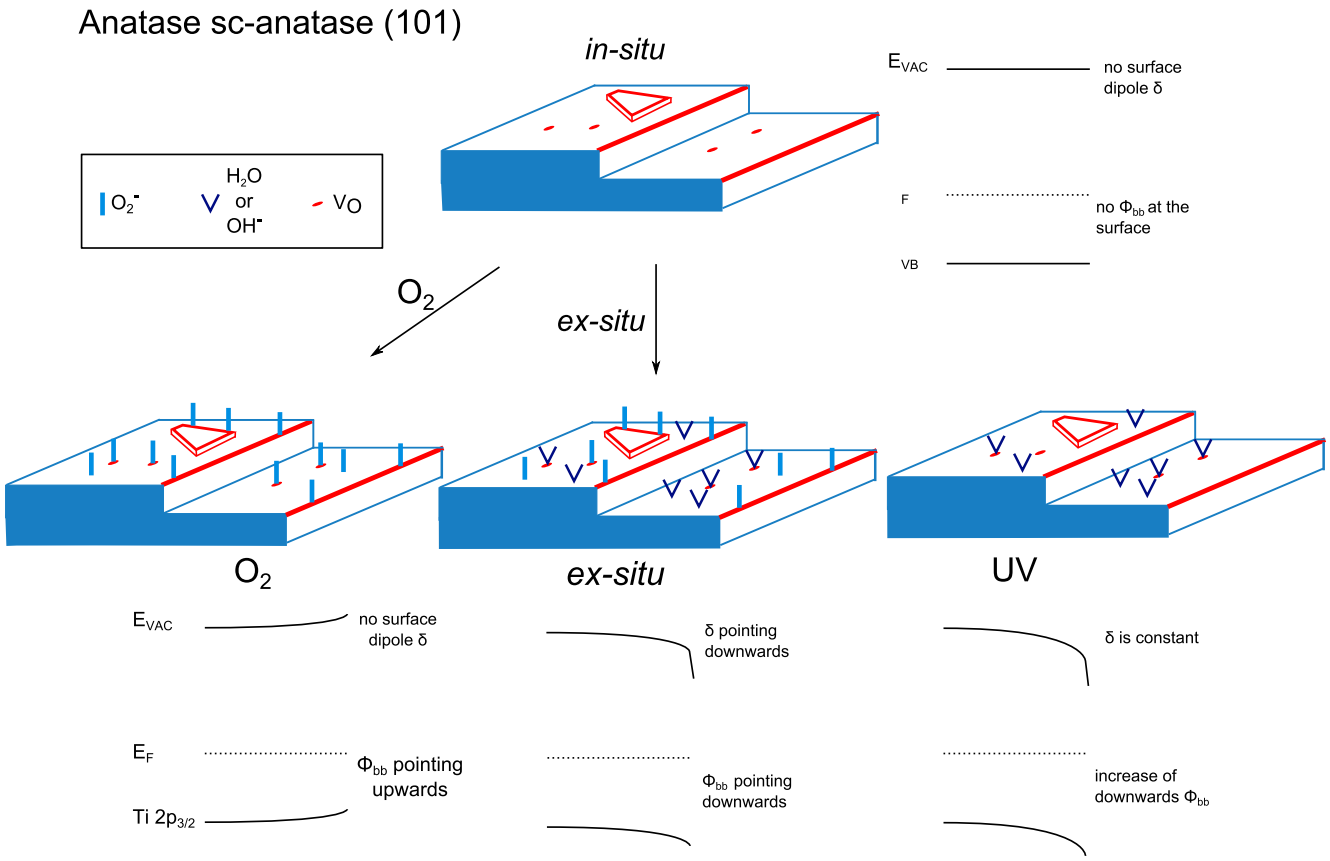

Figure 11.11. – Model of H_2O and O_2 adsorption/desorption on a defect free sc-anatase (101) surface and the respective band diagrams. At the top, the almost defect free, clean *in situ* cleaved anatase crystal is depicted. For the energy diagram flat band situation is assumed. At the bottom left the case for O_2^- adsorption is illustrated. O_2^- causes an upward band bending. After air adsorption (*ex situ*), H_2O and O_2^- are adsorbed on the surface. Bands bend downwards due to H_2O adsorption, which is damped by the electron scavenging character of O_2^-. Additionally a surface dipole is induced (bottom middle). UV illumination causes O_2 desorption, which results in an increase of the downward band bending (bottom right).

An unambiguous origin of the UV induced downward band bending could not be derived in this chapter. A reasonable model to explain the observations made are the simultaneous adsorption of water and oxygen, where the electron donating nature of water dominates (total net downward band bending). Due to UV radiation O_2 desorbs and downward bending increases. A formation of OH^- upon X-ray and UV irradiation, due to V_O formation is not probable as $Al_{K\alpha}$ and UV light do not induce V_O. To gather a better picture, further investigations on the effect of a water exposed anatase surface and its interactions with UV light are needed. Additionally experiments with molecular oxygen should be performed as well.

11.2 ALD prepared *ex situ* TiO_x: Influence of air and UV light

In Fig. 11.12 the UV induced transition of the energy levels of TiO_x 80 °C is shown in an energy diagram (derived from Fig. 9.2). Included is the VBM position calculated from the Ti $2p_{3/2}$-VBM distance (455.8 eV, see Table 8.1) and the CBM position, calculated with the energy gap E_G of 3.4 eV of TiO_x 80 °C determined by UV/Vis spectroscopy in Section 8.1.5. On the left, the energy diagram deduced from the initial (minimal X-ray exposure) spectra is depicted and E_F is right at E_{CB}. After UV irradiation E_F at the surface is 0.2 eV above E_{CB}.

From the previous experiments and results it is strongly suggested, that air induces an accumulation layer at the surface of sc-anatase (101) TiO_2 (see Section 11.1). Furthermore, X-ray and UV radiation induce a downward shift of the energy levels on *ex situ* sc-(101) and TiO_x 80 °C as shown in Figs. 9.2 and 11.3. While on anatase the UV induced changes are most probable due to an increase of the downward band bending, this maybe not the case for the *ex situ* TiO_x annealed at 80 °C. For TiO_x 80 °C the only definite statement, which can be made is that the energy levels move in downward direction upon X-ray and UV illumination. It is unknown, if the observed energy level shift of the *ex situ* samples is related to a decrease of upward band bending or an increase of downward band bending at the surface, as the starting situation is unknown. Taking the results of the *in situ* and *ex situ* cleaved sc-anatase (101) into account, it may be assumed, that air causes an accumulation layer on the other ALD prepared TiO_x as well and hence UV induces an increase of downward band bending due to oxygen desorption. Oxygen and water can originate from *ex situ* handling and the ALD deposition process itself, which involves the usage of water (see Section 4.2).

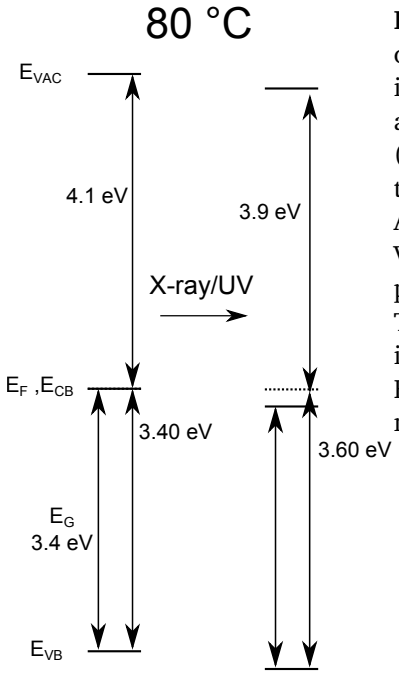

Figure 11.12 – Energy diagram of TiO_x 80 °C as measured after introduction into UHV (left) and after 60 min UV illumination (right). Before UV illumination the E_{CB} is right at the Fermi level. After UV E_{CB} is below E_F. The VBM is derived from the Ti $2p_{3/2}$ position in Fig. 9.2 and the Ti $2p_{3/2}$-VBM distance determined in Section 8.2.1. The energy gap E_G was measured by UV/Vis measurements.

Evidence that a downward and not an upward band bending is present at the surface is given by the evolution of the Ti^{4+} *fwhm*, in dependence of X-ray and UV irradiation shown in Fig. 11.13. All

ex situ samples show an increase of the Ti^{4+} *fwhm* upon the irradiation with X-ray and UV photons, while the *in situ* sc-anatase (101) does not exhibit a broadening. As photoelectrons in XPS have an escape depth of about 10 nm, a possible band bending occurring within this 10 nm influences the *fwhm* of the measured emission lines. Downward and upward band bending at the surface increase the Ti^{4+} *fwhm*. In the conducted experiments, X-ray/UV irradiation increases the binding energy, which is equivalent to an increase of a downward band bending or a decrease of an upward band bending. For the Ti^{4+} *fwhm*, a decrease of an upward band bending is equivalent to a reduction of the Ti^{4+} *fwhm*. Hence the broadening of the *fwhm* indicates that downward band bending is present at the surface and supports the assumption made above.

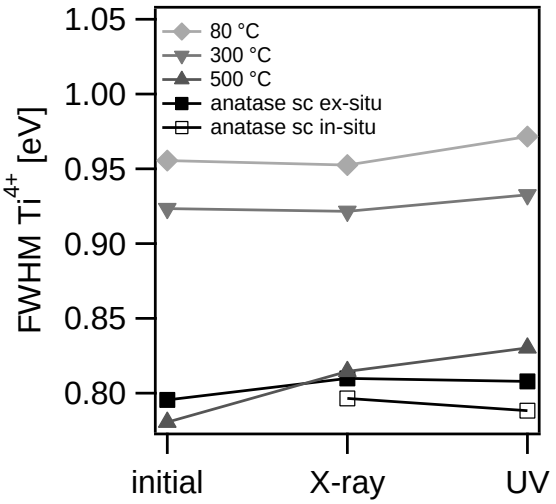

Figure 11.13 – Ti^{4+} *fwhm* evolution of all *ex situ* samples and the *in situ* cleaved sc-(101) upon X-ray and UV illumination. All *ex situ* samples show an increase of the Ti^{4+} *fwhm* upon X-ray/UV illumination, while the *in situ* cleaved sc-(101) does not. This supports the assumed increase of downward band bending at the surface upon UV illumination of *ex situ* TiO_2 samples.

11.2.1 Origins of surface band bending upon X-ray/UV illumination

In Sections 11.1 and 11.2 X-ray and UV induced shifts of the energy levels at the surface were observed on amorphous and crystalline *ex situ* cleaved titania surfaces. Surface band bending can be caused by intrinsic and extrinsic mechanisms. Intrinsic surface band bending happens due to a charge transfer between bulk and surface states,[209] while extrinsic band bending originates from charge transfer between the surface and external adsorbates.[117] Results obtained in Section 11.1 suggest that extrinsic mechanism like O_2 or H_2O ad- and desorption are responsible for band bending on the anatase (101) surface.

In Fig. 9.2 an increase of Ti^{3+} states upon X-ray and UV irradiation is observed. This could be an indication of intrinsic surface band bending. In this section the impact of X-ray and UV radiation on the formation of Ti^{3+} states and the influence of O_2 adsorption is analyzed in more detail to obtain more information about the origin of surface band bending.

UV caused Ti^{3+} states formation on 80, 300, and 500 °C ALD TiO_x films

Figure 11.14 shows the evolution of the Ti^{3+} emission of all ALD prepared *ex situ* samples upon irradiation with X-ray and UV light. All samples show an increase of the Ti^{3+} component with X-ray and

UV illumination. The 80 °C TiO_x sample has an initial Ti^{3+} concentration ratio of the Ti $2p_{3/2}$ emission of ~1.5 %. The Ti^{3+} concentration increases after X-rays to 3 % and after extended UV illumination to 5.5 %. The 300 °C sample has an initial Ti^{3+} content of below 1 %. X-ray and UV radiation increase it to 2 % (X-ray) and ~3 % (UV). The initial Ti^{3+} concentration of the 500 °C post annealed TiO_x is below 1 % as well and increases only after UV illumination to about 1.5 %. The intensity of Ti^{3+} is extracted from the fits used in Figs. 9.2, 11.15 and A.3.

In summary Fig. 11.14 shows that with increasing annealing temperature the initial Ti^{3+} content and the sensitivity to X-ray and UV irradiation is reduced. The Ti^{3+} states origin mainly from oxygen vacancies at the surface, but can be part of the bulk as well.[16] V_O can either be an intrinsic property of the respective TiO_x layer dependent on synthesis conditions or may be induced by X-ray or UV irradiation.[175] In the former case, this would mean that e.g. adsorbed O_2^- desorbs as O_2 in the course of UV irradiation and as a result the intrinsic Ti^{3+} emissions appears (extrinsically caused band bending). In the latter case, this means that lattice oxygen[2] O^{2-} is removed upon irradiation (intrinsically caused band bending).

For ALD prepared *ex situ* samples as well as for the *ex situ* cleaved sc-anatase (101) (see Sections 11.1.1 and 11.2) it was shown that bands bend downwards upon X-ray and UV illumination. This can be explained with intrinsic and extrinsic band bending mechanisms. In general V_O are donor like surface states, as desorbed molecular oxygen leaves two extra electrons behind, which occupy the lowest orbital of the conduction band, the Ti 3d states.[83] This causes a downward band bending towards the surface. In the case of extrinsic band bending, adsorbed oxygen scavenges electrons from existent Ti^{3+} states and bands bend upwards. In Section 11.1 no evidence by XPS was given that the used UV source induces V_O on an *in situ* cleaved sc-anatase (101) surfaces. On the other hand, amorphous 80 °C deposited TiO_x was shown to be much more affected by synchrotron radiation than anatase (see Section 17.1).[136] Hence, amorphous TiO_x could be more affected with respect to V_O formation by UV radiation than anatase, as well.

Oxygen influence on 300 °C ALD TiO_x films

As the Ti^{3+} states are usually attributed to oxygen vacancies, the effect of O_2 exposure on amorphous TiO_x sample is investigated. For this purpose a 300 °C deposited ALD TiO_x film was used. TiO_x 300 °C shows similar properties as the TiO_x 80 °C and only the initial Ti^{3+} content is smaller. The sample was *in situ* exposed to 0.030 mbar O_2, subsequently measured with XPS and at last irradiated with UV light and measured again.

Figure 11.15 shows the evolution of the SE-edge, the O1s and the Ti2p core level emissions upon UV illumination, O_2 exposure and subsequent UV illumination of the sample. After UV illumination the work function and the core level emissions show a shift in the same direction of about 150 meV (see Fig. 11.15A). In the next step, the sample was exposed to 0.030 mbar O_2 for 30 min and transferred back to the XPS chamber. As X-ray exposure influences the energetic position strongly, first the secondary electron edge, followed by the Ti $2p_{3/2}$ and O1s core level were recorded. Within the next 10 min further spectra were recorded, to determine the influence of X-rays. The first recorded spectra after O_2 exposure

[2] The term "lattice" is usually referred only to crystalline materials. Here it is used for atoms belonging to the material itself, meaning non-adsorbed atoms.

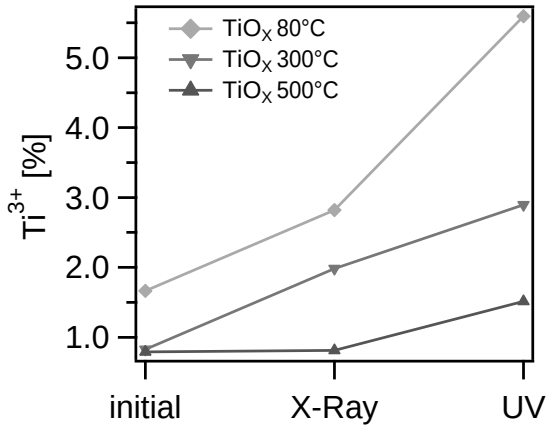

Figure 11.14. – X-ray and UV induced Ti^{3+} emission of as deposited 80 °C, and 300 °C and 500 °C post annealed TiO_x. With increasing annealing temperatures the influence of irradiation gets smaller.

show all a shift about 150 meV to lower binding energies/higher kinetic energy. Upon increase of the radiation time the core emission lines shift back to the initial position, whereas the secondary electron edge even shifts back to the level of the previous UV illumination. The repetition of UV illumination shifts the core level spectra back to the same position as after first UV illumination, whereas no further change of the work function is observed. Figure 11.16A summarizes the shifts of the secondary electron edge and the core level emissions upon sequential UV and O_2 exposure. The WF and the core levels shift in parallel, hence no dipole forms and band bending is just switching back and forth. After the final UV illumination, the energy levels shift almost to the initial post UV values. The slight difference of about 20 meV may indicates that some oxygen is not removed and e.g. dissociated on the surface. Figure 11.16B shows the course of the Ti^{3+} content upon O_2 and UV exposure on the 300 °C sample. As shown before (see Fig. 11.14), the Ti^{3+} content increases after UV exposure. After the exposure to O_2 the Ti^{3+} content diminishes strongly and is even lower than in the initial Ti $2p_{3/2}$ spectrum. Further X-ray exposure only increases the Ti^{3+} content to the value of the initial spectrum. The second UV exposure increases the Ti^{3+} content again, but to a lower level compared to the first illumination (2.8 % compared to 2.1 %). As for the binding energy, this may indicates remaining oxygen. Comparing the shifts of the core levels (Fig. 11.16A) and the intensity of Ti^{3+} emission in dependence of UV illumination and O_2 exposure, a parallel behavior is observed. Upon UV light illumination the Ti^{3+} intensity rises and with O_2 exposure Ti^{3+} intensity diminishes again, to almost zero intensity. This confirms that the formation of Ti^{3+} due to UV light is relevant for the downward shift of the energy levels. Ti^{3+} states can either occur due to desorption of adsorbed hydroxyls or oxygen on V_O, or due to UV induced removal of lattice oxygen at the surface.

The exposure of the 300 °C TiO_x to O_2 leads to a quenching of the Ti^{3+} surface state emission and to an upward band bending (see Fig. 11.16). The obtained O_2 induced shift of about 150 meV is in good agreement with a reported upward shift by about 0.2 eV to 0.3 eV upon 200 *L* O_2 exposure at *RT* by Diebold et al.[16] Quenching of the Ti^{3+} states is attributed to the ionosorption of O_2 at V_O (see Eq. (1.3)).[205] As the experiment was performed at room temperature it is unlikely, that oxygen is incorporated in the TiO_x

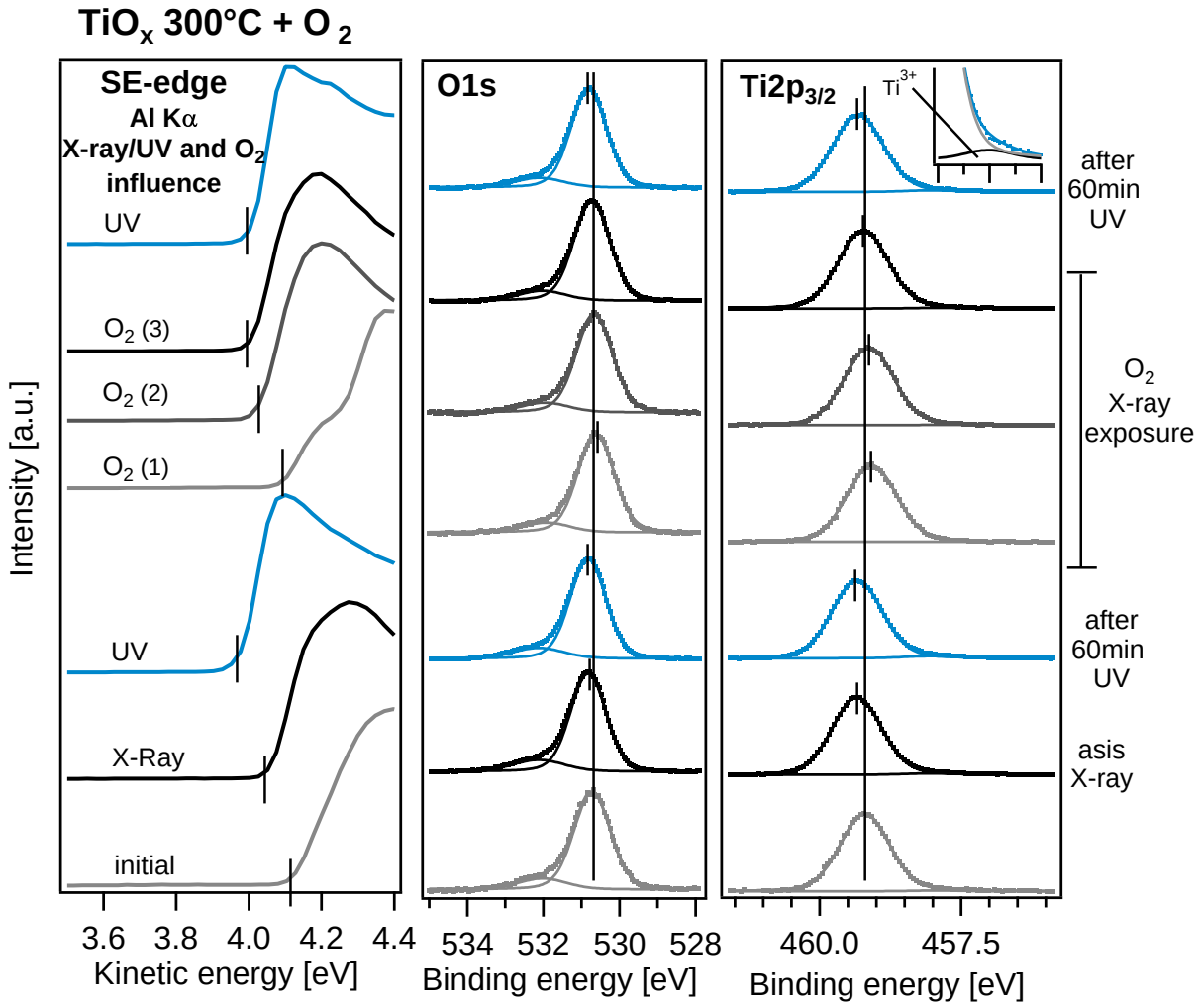

Figure 11.15. – Evolution of the SE-edge, the O1s emission and the Ti $2p_{3/2}$ emission upon X-ray and UV irradiation, subsequent O_2 treatment and a last UV illumination. O_2 (1) is the first measurement after O_2 exposure and O_2 (3) the last measurement after O_2 exposure. At the top right a magnification of the Ti $2p_{3/2}$ emission between 457 and 459 eV E_{Bin} is added. The black curve shows the fit of the Ti^{3+} emission, the gray curve the fit of the Ti^{4+} emission and the blue curve the sum of both. Similar fits were performed for all other Ti $2p_{3/2}$ spectra, but are not displayed.

lattice (chemisorption).[16,210] The ionosorbed O_2^- desorbs with UV irradiation (Eq. (1.4)) as O_2.[211] The remaining electrons occupy Ti 3d states (as for the lattice oxygen) and downward band bending occurs at the surface.

After the second UV illumination the energy level shifts are smaller (~20 meV reduced shift) and the Ti^{3+} content is decreased (2.8 % to 2.1 %). The smaller energy level shift could be due to a reduced desorption of O_2, which would correlate with the higher occupation of Ti^{3+} surface states. Another reason for the energy shifts could be a UV caused formation of additional hydroxylated species on the surface, as OH^- is a stronger electron donor than H_2O.[170,197] However, it was shown by Henderson and Wendt that dissociative adsorption of water leads only to small attenuation of Ti^{3+} states,[189,212] which makes a hydroxyl caused decrease of the Ti^{3+} surface state density unlikely.

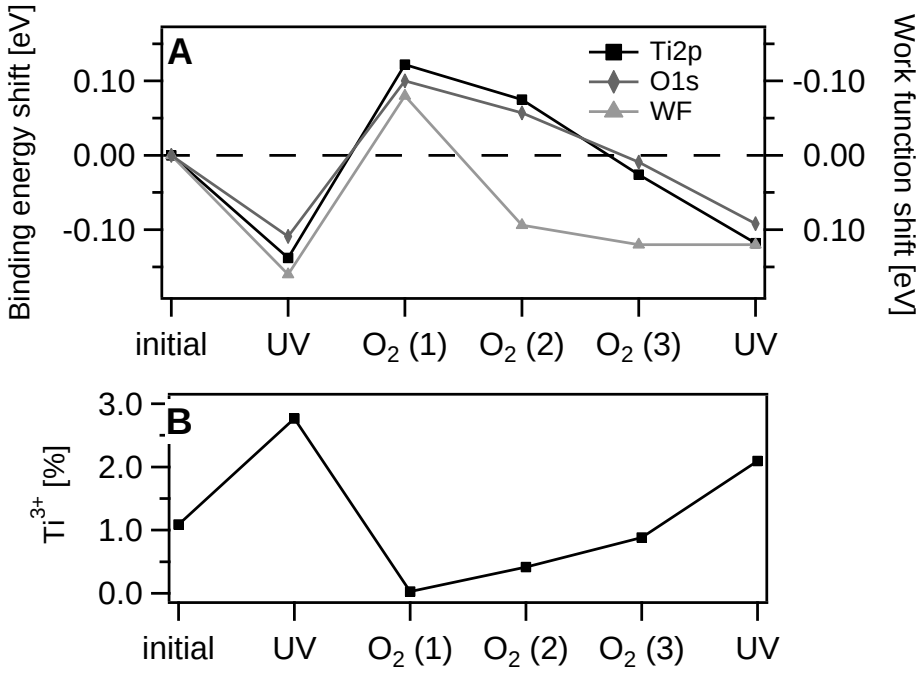

Figure 11.16. – **A**: Progression of the SE-edge, the O1s emission and the Ti $2p_{3/2}$ emission upon O_2/UV treatment. **B**: Progression of the Ti^{3+} states upon O_2/UV treatment. Binding energy, work function and Ti^{3+} states run in parallel, as Ti^{3+} states decrease goes along with a decrease of the binding energy and receptively an increases of the work function. An example for the fit of the Ti $2p_{3/2}$ emission is given in Fig. 11.15 top right.

Table 11.3. – Work function, binding energy (O1s,Ti $2p_{3/2}$) and Ti^{3+} states evolution upon X-ray, UV and O_2 exposure on 300 °C TiO_x.

	initial	X-ray + UV	O_2 (initial)	O_2 (X-ray 1)	O_2 (X-ray 2)	X-ray + UV
O1s [eV]	530.72	530.83	530.62	530.66	530.73	530.81
Ti $2p_{3/2}$ [eV]	459.20	459.34	459.08	459.13	459.23	459.32
WF [eV]	4.12	3.96	4.2	4.03	4	4
Ti^{3+} [%]	1.1	2.8	0.0	0.47	0.9	2.1

Gedankenexperiment on the space charge layer effect

Figure 11.17 visualizes the effects of surface states on a semiconductor surface. As an example a n-doped semiconductor is assumed. A degenerated n-type semiconductor as evidenced by the XPS measurements (see Fig. 11.12 right) would behave in principle the same. Two cases can be distinguished: a) filled surface states above E_F are added and b) empty surface states below E_F are added at the surface. Empty surface states above E_F and filled ones below E_F do not effect surface band bending and are not depicted in Fig. 11.17 and discussed further.

Figure 11.17a) illustrates the case, where occupied surface states are induced above E_F. Occupied surface states above E_F lead to the formation of an accumulation layer. To reach the thermodynamical equilibrium, electrons flow from the surface states to the TiO_x bulk. The maximal magnitude of band bending is limited by the position of the charge neutrality level (E_{CNL}). An increase of the surface states

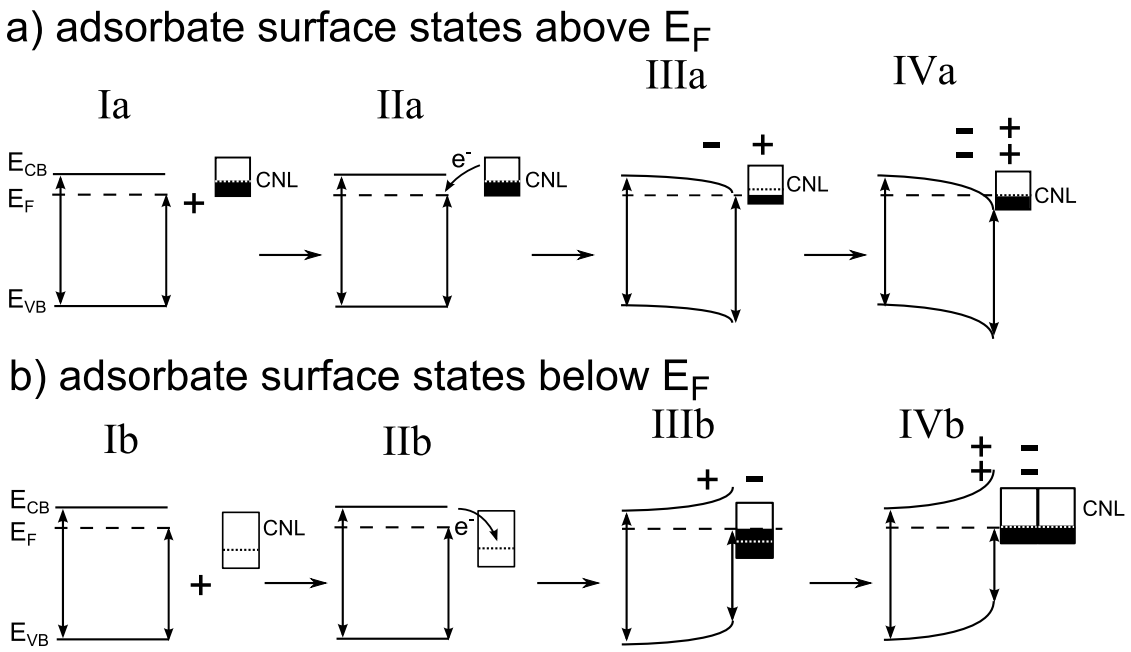

Figure 11.17. – Effect of surface states on a n-type semiconductor: a) Inducing filled surface states above E_F (IIa) results in a formation of an accumulation layer at the surface (IIIa). An increase of the density of states increases band bending and the width of space charge layer (IVa). b) Inducing empty surface states below E_F (IIb) results in a formation of a depletion layer at the surface (IIIb). An increase of states may increases band bending, i.e. the width of the space charge layer (IVb).

DOS increases the band bending till E_F and E_{CNL} are on the same level. In Fig. 11.17b) empty surface states below E_F are added to n-type TiO_x without pristine surface states. As they are below E_F, electrons flow from TiO_x to the surface states and a depletion layer at the surface is formed. They are acceptor like surface states. As soon as E_F and the E_{CNL} are in equilibrium (IVb), the surface state induced band bending is at its maximum and E_F is pinned to the charge neutrality level. The desorption process of O_2^- can be described as a removal of surface states below E_F, while the adsorption of O_2 describes a process, where surface states below E_F are induced (IIb). A detailed explanation of Fermi level pinning is given in Section 2.2.4.

Concerning the UV and O_2 induced band bending this implies that UV light, as it causes a downward shift of the energy bands, removes surface states below E_F, which could be due to oxygen desorption. Vice versa, O_2 adsorption is equivalent to an implementation of empty surface states below E_F (see Fig. 11.17c) IIIb). The formation of Ti^{3+} states due to UV light leaves electrons in the TiO_x behind. This is equivalent to case IIa→IIIa and induces a downward band bending as well. The quenching of Ti^{3+} states leads to an upward band bending (IIIb). Hence desorption of oxygen, either ionosorbed one, or oxygen belonging to the lattice (chemisorbed), has same effect on band bending. As water is electron donating, adsorption of water leads to a formation of an accumulation layer (case IIIa). As UV light increases the downward band bending, a water desorption upon light can be excluded.

11.2.2 Conclusion and summary: ALD prepared TiO_x

In this section the influence of X-rays and UV radiation and oxygen on ALD prepared titania was analyzed. As shown in Section 9.1 for 80 °C TiO_x and in Appendix A.2 for 500 °C TiO_x UV light induces a

decrease of the TiO_x WF and an increase of the Ti $2p_{3/2}$ binding energy by about 200 meV independent of the annealing temperature of the ALD titania sample. The Ti^{3+} content increases in all ALD titania samples upon irradiation with X-ray and UV light, but the Ti^{3+} increase is reduced with increasing annealing temperature. Furthermore it was shown that exposure of 300 °C TiO_x to oxygen quenches Ti^{3+} states and induces an upward band bending (as does the oxygen plasma at the anatase (101) surface, see Section 11.1). Both, the band bending and the Ti^{3+} quenching are almost completely reversible upon the illumination with X-rays and UV light. The reversibility of band bending upon illumination excludes the formation of OH^- species as this would increase the downward band bending and is an irreversible process. A direct assignment, if O_2^- or lattice O^{2-} is removed from the surface upon UV illumination is not possible, but both mechanism result in downward band bending (see *Gedankenexperiment on the space charge layer effect*).

While on the sc-anatase (101) surface UV induced lattice oxygen desorption (V_O formation) is rather unlikely (see Section 11.1),[174] this may be different for amorphous TiO_x (see Section 17.1).[136] But both, the apparently more radiation resistive sc-anatase (101) surface and the amorphous samples show UV induced shifts of the same magnitude. Thus the shifts of the energetic positions and intensity changes of the Ti^{3+} emissions are attributed to ad- and desorption of oxygen on the TiO_x surface and not to the removal of lattice oxygen. A model of the UV induced oxygen desorption on 80 °C TiO_x is depicted in Fig. 11.18 bottom right. Additionally a model for an air free amorphous titania surface is depicted on the left of Fig. 11.18 and has only oxygen vacancies and no water or oxygen adsorbed at the surface. Due to the oxygen vacancies a small band bending at the surface is assumed at the surface.[16] The *ex situ* surface (top middle) has water on V_O sites and on the stoichiometric surface.[213] Taking literature into account it is assumed that oxygen adsorbs at V_O sites as O_2^- [204,206] and also on the stoichiometric surface as O_2^-.[16] In total the adsorbates induce a further downward band bending and a surface dipole formation (pointing downward) at the surface. UV illumination (right) causes a desorption of molecular oxygen. Therefore the amount of oxygen vacancies increases as does the downward band bending.

11.3 Summary of air exposed titania interfaces

In this chapter different titania samples (mainly 80 °C and *ex situ/in situ* cleaved anatase (101)) were compared with respect to the influence of adsorbates and UV irradiation on the energetic positions of the energy levels. For the anatase single crystal it was shown, that air induces an accumulation layer at the surface and that oxygen induces a depletion layer. Upon UV illumination of the air exposed samples the energy bands shift downwards, which was attributed to the desorption of oxygen. Upon illumination with UV light with an energy above the band gap (3.4 eV for amorphous titania and 3.2 eV for anatase) electrons are excited above the band gap and holes recombine with the O_2^- and O_2 desorbs neutrally (see Fig. 11.10).[178,203] On the contrary, dissociated water is an electron donor and induces an accumulation layer at the surface of TiO_2 and bands bend downwards (see Fig. 11.9).[80,148] The formation of oxygen vacancies, e.g. by UV light, can favor the photochemical reaction of H_2O to OH^- at the surfaceEq. (1.1).[170] For the *in situ* cleaved anatase (101) surface no UV induced V_O formation was observed and therefore a UV induced OH^- formation is excluded as the origin for UV induced downward

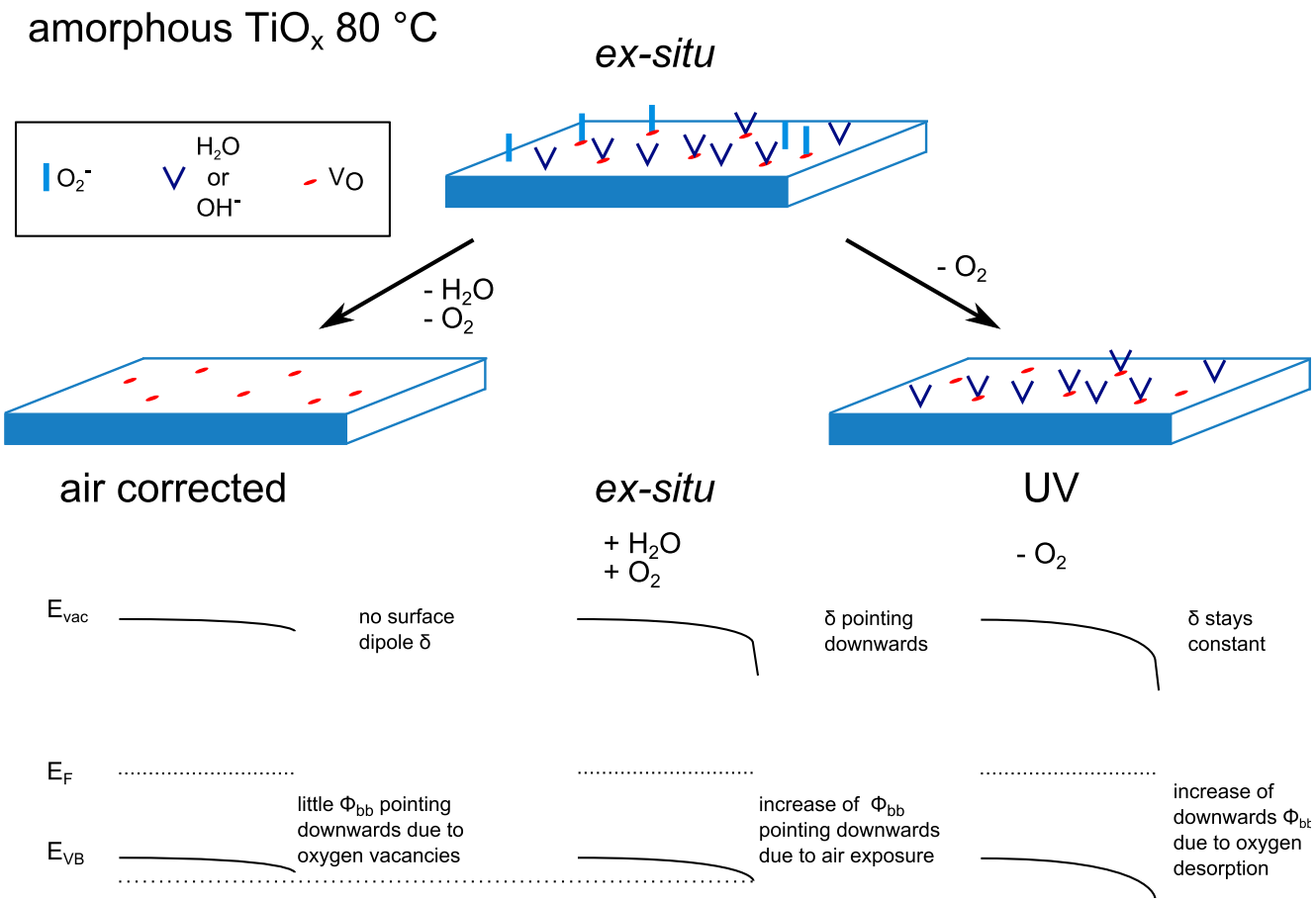

Figure 11.18. – Model of *ex situ* amorphous ALD prepared samples upon UV illumination. On the left an air corrected band diagram is shown. This means that adsorbates are theoretically removed of the surface and oxygen vacancies V_O are present on the surface. The V_O cause a downward band bending of the *air free* surface. In the middle is the *ex situ* prepared titania as measured. Adsorbates at the surface cause a downward band bending and a dipole formation at the surface. O_2^- and H_2O adsorbs on V_O on the defect free surface. Upon UV illumination oxygen desorbs and an increase of the downward band bending occurs. Water remains at the surface.

band bending on anatase and on the amorphous TiO_x surface. Therefore O_2 desorption seems to be the most probable origin of UV light induced downward band bending at the titania surface.

12 Mechanistics for UV light induced changes at the TiO_x/C_{60} interface

In Chapter 9 it was shown that UV light changes the electronic line-up at the 80 °C TiO_x/C_{60} interface. It is observed that the Ti $2p_{3/2}$-C 1s distance increases after UV illumination and that the interface dipole changes its direction. In Chapter 11 the anatase sc-(101) surface and the TiO_x 80 °C film were investigated with respect to adsorbates and UV illumination induced changes. From the gained results in Chapters 9 and 11 a mechanistic model is derived to explain the observed, UV induced shifts at the TiO_x/C_{60} interface. Two different models are taken under consideration. In both models UV induced oxygen desorption from the TiO_x surface is assumed to be the origin for the observed changes. While in the first model (see Fig. 12.1) oxygen desorption causes only changes of the line-up between C_{60} and TiO_x, the second model assumes an additional UV induced charge transfer from the TiO_x to C_{60}.

12.1 Summary of previous results

1. Results from TiO_2/C_{60} interface experiments derived in **Chapter 9** are:
   a) Adsorbates on the TiO_2 surface are responsible for the UV induced shifts of the Ti $2p_{3/2}$ and C 1s level of TiO_2 and C_{60}, respectively.
      - UV light induces shifts of the Ti $2p_{3/2}$ and C 1s level on *ex situ* cleaved sc-(101)/C_{60} samples (see Fig. 10.5).
      - UV light induces **no** shifts on *in situ* cleaved sc-(101)/C_{60} samples (see Fig. 10.3).

   b) The C 1s energy level of C_{60} at the interface to TiO_x moves upwards relative to the Ti $2p_{3/2}$ level of TiO_2 after UV illumination, meaning that their energy difference becomes larger. Additionally the interface dipole changes its direction.

   c) The C 1s emission broadens after UV irradiation, if C_{60} is deposited on *ex situ* samples (amorphous TiO_x or anatase). No change of the *fwhm* is observed, if it is deposited on *in situ* cleaved anatase (see Table 10.1).

   d) A 24 h UV pretreatment of a 80 °C TiO_x substrate diminishes the UV induced energetic shift of the C_{60} C 1s level after UV illumination of the TiO_x/C_{60} interface (see Fig. 9.9).

   e) The C 1s binding energy is lower on the *in situ* cleaved sc-(101), than on the *ex situ* cleaved anatase samples (see Table 10.2).

   f) Interface experiments of *in situ* cleaved anatase and C_{60} showed that the C 1s *fwhm* is constant (about 0.7 eV) till a nominal C_{60} coverage of about 10 Å and decreases to 0.4 eV at high C_{60} coverages. On the *ex situ* cleaved anatase (101) surface, the C 1s *fwhm* decreases already at lower C_{60} coverages to a value of 0.4 eV (see Fig. 10.6).

g) UV dependent measurements on the *in situ* anatase surface showed, that C_{60} has a high, UV independent *fwhm* of ~0.7 eV. In contrast, C_{60} on *ex situ* anatase has a smaller *fwhm* of ~0.6 eV, which increases after UV illumination to ~0.7 eV (see Table 10.1).

2. In **Chapter 11** the anatase sc-(101) surface and the TiO_x 80 °C ALD film were investigated with respect to adsorbate and UV light induced changes. The results are the following:

   a) Adsorbates from air cause the formation of an accumulation layer at the surface of TiO_x and TiO_2. It is proposed that water or hydroxide adsorbates cause the downward band bending at the surface of TiO_2 or TiO_x (see Figs. 11.11 and 11.18).

   b) O_2 adsorption at the TiO_x causes the formation of a depletion layer at the surface of TiO_2 and TiO_x surface. The formation of an upward pointing surface dipole was not observed, but maybe is apparent at ambient pressure (see Fig. 11.10).

   c) It is concluded that the oxygen induced upward band bending is smaller, than the water induced downward band bending. Therefore a net downward band bending at the surface is observed (see Figs. 11.11 and 11.18).

   d) UV illumination leads to an increase of the downward band bending at the surface. The increase of the downward band bending originates from UV induced desorption of oxygen and maybe from the formation of additional UV induced V_O, which increases the amount of free excess electrons causing the formation of an accumulation layer (Fig. 11.18).

12.2 Deriving a mechanistic model to explain changes of theTiO_x/C_{60} interface

12.2.1 Model I: UV induced oxygen desorption at the TiO_x surface - No further interactions between the TiO_x surface and C_{60}

The probable origin of the UV induced shifts at the TiO_x/C_{60} interface is a UV induced desorption of oxygen. Figure 12.1 shows the mechanism how UV influences the energy level line-up at the TiO_x/C_{60} interface. Oxygen at the TiO_x surface causes the formation of a depletion layer and a surface dipole pointing upward (Fig. 12.1 Ic). After C_{60} deposition the depletion layer and the surface dipole still exist at the interface to C_{60}. In Fig. 12.1 IIb) the C_{60} E_{Vac} and HOMO are added to the TiO_x surface. At the interface exists now an interface dipole between the vacuum levels E_{Vac} and a certain distance between the E_{VB} (TiO_x) and HOMO (C_{60}). Upon UV illumination oxygen desorbs and the surface dipole plus the depletion layer disappear (Fig. 12.1 Id) as O_2^- recombines with holes induced by the UV irradiation (see Fig. 11.10) and O_2 desorbs molecularly. In Fig. 12.1 IIc) this removal of the band bending and the surface dipole is subdivided into two steps. On the left side of Fig. 12.1 IIc), only the depletion layer is removed and the surface dipole on the TiO_x still exists. When the depletion layer is removed, the C_{60} energy levels move the same amount downwards. This causes no change of the interface dipole between TiO_x and C_{60} and no change of the distance between E_{VB} of TiO_x and the HOMO of C_{60}. On the right of Fig. 12.1 IIc) the surface dipole on the TiO_x is removed as well. The leads again to a shift of the C_{60} energy levels. While the interface dipole remains unchanged, the C_{60} HOMO moves downwards relative to the E_{VB} of TiO_x.

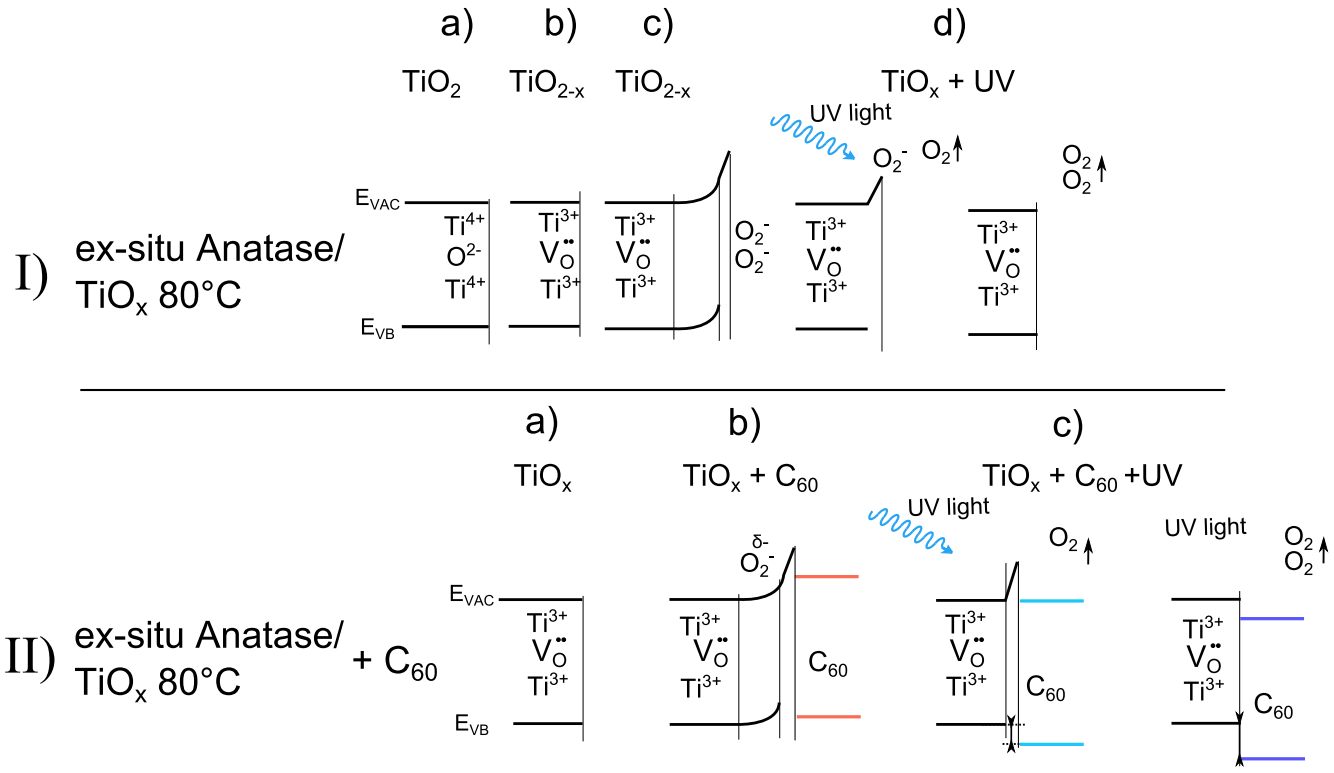

Figure 12.1. – Model I of the UV influence on the TiO_2/C_{60} interface. I) shows the band diagram of a stoichiometric TiO_2 (Ia), a reduced TiO_x (Ib) and a reduced TiO_x with adsorbed O_2^-, which induces an accumulation layer and an upward pointing surface dipole on the TiO_x surface (Ic). Id) shows the UV light induced removal of, first the accumulation layer and second the surface dipole on the TiO_2 surface. II) shows the model for C_{60} deposition and UV illumination onto an *ex situ* prepared titania sample. C_{60} attaches on the oxygen covered TiO_x surface (IIb). Upon UV illumination oxygen partially desorbs and the accumulation layer disappears. The line-up at the interface between the vacuum levels and E_{VB} remains unchanged. With increasing UV illumination more oxygen desorbs and the surface dipole disappears as well. This causes a downward shift of the C_{60} energy levels and the distance between E_{VB} of TiO_x and the HOMO of C_{60} increases.

12.2.2 Model II: UV induced oxygen desorption at the TiO_x surface - Assuming interactions between the TiO_x surface and C_{60}

In the second mechanistic model again oxygen induced desorption is assumed, but additionally an interaction between the TiO_x surface and C_{60} is assumed. In Fig. 12.2 I), the *ex situ* cases (anatase (101) surface and TiO_x 80 °C) are displayed. Depicted are E_{Vac} and E_{VB}, which is in parallel to the core levels. Oxygen adsorbs as O_2^- at the titania surface by scavenging one electron and induces an upward band bending at the surface (Ic). In contrast to the model in Fig. 12.1 no surface dipole is assumed at the TiO_x surface. This in an agreement with the results upon oxygen adsorption on TiO_2 and TiO_x in Chapter 11 measured under UHV conditions.

In the *in situ* case (d) flat band conditions are assumed at the surface. In Fig. 12.2 II) the situation after C_{60} deposition on an 80 °C annealed *ex situ* titania surface and subsequent UV irradiation is depicted. First C_{60} binds (at least partly) on the adsorbed O_2^- (IIb). As O_2^- is negatively charged, C_{60} becomes partially positively charged. This is reflected by an upward dipole of the C_{60} at the interface. At high C_{60} coverages an upward band bending of the C_{60} energy levels is observed (illustrated by a step). Upon UV illumination, oxygen desorbs molecularly and C_{60} becomes negatively charged C_{60}^- (IIc). By this it induces a strong dipole in the contrary direction, which induces an upward shift of the C_{60} energy levels at the interface. In Fig. 12.2 III) the model for C_{60} deposition on the *in situ* cleaved, adsorbate free, sc-(101) surface is depicted. In the adsorbate free case C_{60} adsorbs directly as C_{60}^- on the surface (IIIb), which immediately induces an upward shift of the C_{60} energy levels. UV illumination induces no changes in this case.

12.3 Comparison and discussion of both mechanistic models

According to model I in Fig. 12.1 the C_{60} energy levels move downwards after UV. This explains the interface dipole change after UV illumination, but contradicts with the observation that the C 1s level of C_{60} right at the interface moves upwards after UV illumination (2b) in Section 12.1). Furthermore no surface dipole upon oxygen adsorption on the titania surfaces is observed in experiments under UHV conditions in Chapter 11.

In the second model not only oxygen desorption is assumed, but also a charge transfer from the TiO_x surface to C_{60}. In the case of the *in situ* cleaved anatase (101) surface the charge from TiO_2 to C_{60} takes place immediately after C_{60} adsorption and C_{60} attaches as C_{60}^-. Upon evaporation of the C_{60} onto the *ex situ* ALD prepared TiO_x/TiO_2 the charge transfer occurs after UV induced oxygen desorption. Additionally the upward band bending at the TiO_x surface disappears upon UV illumination. Because of the charge transfer to C_{60} and the formation of C_{60}^-, the second model in Fig. 12.2 can explain the change of the interface dipole and the upward movement of the C 1s level of C_{60}. Furthermore this model explains, why the C 1s attaches with a lower binding energy at the *in situ* titania surface, than on *ex situ* titania surface, as C_{60} attaches as C_{60}^- on the *in situ* anatase ((2e) in Section 12.1)). The formation of the C_{60}^-, can also explain the increase of the *fwhm* of the C 1s emission, as the coexistence with C_{60} causes a broadening of the overall *fwhm* of the C 1s emission.

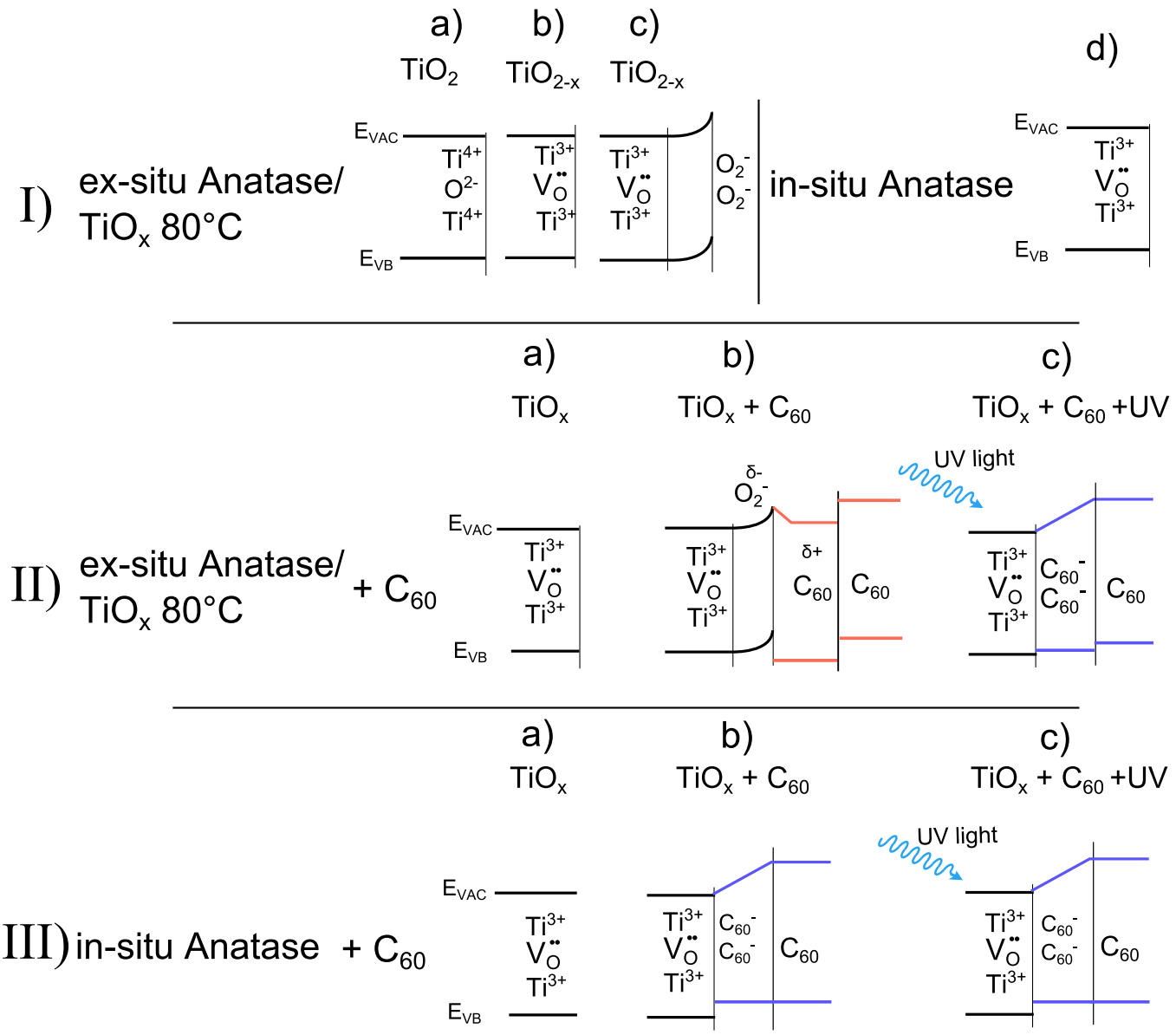

Figure 12.2. – Model II of the UV influence on the TiO_2/C_{60} interface. I) shows the band diagram of a stoichiometric TiO_2 (Ia), a reduced TiO_x (Ib), a reduced TiO_x with adsorbed O_2^- (Ic) and *in situ* prepared TiO_2 with oxygen vacancies. II) shows the model for C_{60} deposition and UV illumination onto an *ex situ* prepared titania sample. First C_{60} attaches partially positively charged on the oxygen covered TiO_x surface. This induces a dipole pointing downward at the interface. With increasing C_{60} coverage an upward shift of the C_{60} energy levels occurs. After UV illumination (IIc) oxygen desorbs and C_{60}^- forms at the interface. C_{60}^- induces a strong dipole pointing upward, which causes an upward shift of the C_{60} energy levels. With increasing C_{60} coverage the upward shift of the C_{60} energy levels becomes smaller. III) shows the model of C_{60} deposition and UV illumination onto an *in situ* prepared titania sample. C_{60} attaches immediately as C_{60}^-. UV light induces no change at the interface.

As the second model explains the observed observations better, it is the favored model to describe the observed UV influence on the TiO_x/C_{60} interface. The model does not claim to be completely correct, but gives good explanation for the observations made. One weaknesses, e.g. is that the assumed C_{60}^- component is not clearly visible in the C 1s photoemission spectra of the interface experiments in Fig. 9.4 or Fig. 10.4 and the only evidence is given from the C 1s *fwhm* changes of the C 1s emission in dependence of C_{60} layer thickness and UV light influence.

13 Inverted organic solar cells without S-shaped I-V characteristics

Not all inverted organic solar cells show S-shaped I-V characteristics prior to UV irradiation. Our project partner from BU Wuppertal, in person of Sara Trost, showed that IOSC with ALD prepared aluminum doped ZnO (AZO) layers do not show S-shaped I-V characteristics before illumination with UV light (see Fig. 13.1 left).[15] Furthermore Kuwabara et al. showed that I-V curves of IOSC with amorphous TiO_x ETL (annealing temperature 150 °C) show S-shaped I-V characteristics, while annealing of the amorphous TiO_x layer to 450 °C leads to IOSC devices, which showed no S-shaped I-V characteristic before UV illumination (see Fig. 13.1 right). The 450 °C annealed TiO_x layers of Kuwabara et al. showed a partial transformation from amorphous TiO_x to anatase.[71]
In this chapter the AZO/C_{60} interface before and after UV illumination is investigated and the morphology and optical properties of AZO are discussed. The 500 °C TiO_x/C_{60} was investigated as well and the results are in the appendix.

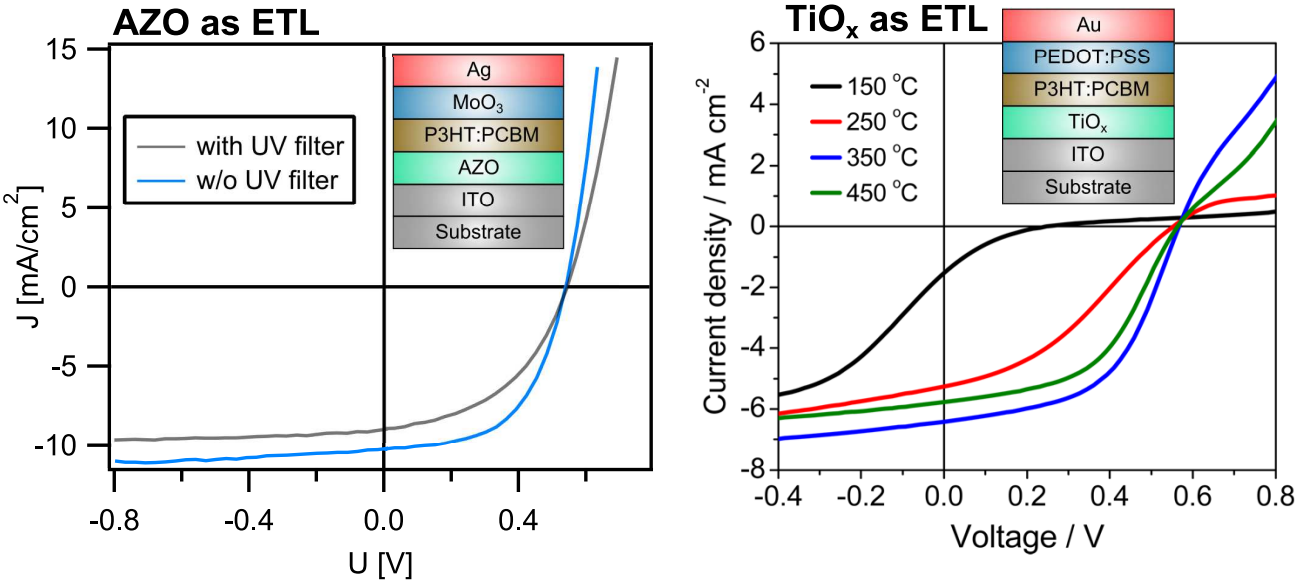

Figure 13.1. – Left: I-V characteristic from IOSC with AZO as ETL. The I-V curves with or w/o UV filter show no S-shaped I-V characteristics (adapted from Ref. [15]). Right: I-V characteristic of IOSC with different TiO_x layers of different annealing treatments. With increasing annealing temperature the S-shaped I-V curve transforms into a diode like I-V curve (adapted from Ref. [71]).

13.1 Al:ZnO substrates - structure and morphology

All ALD ZnO and Al:ZnO (AZO) layers were prepared by our project partner of the BU Wuppertal in person of Sara Trost. ZnO was prepared by using diethylzinc and water as precursors. AZO layers were

prepared by alternating deposition of 50 cycles of ZnO and 2 cycles of Al_2O_3. Such a sequence is about 9 nm thick. Al_2O_3 was deposited by using trimethylaluminium (TMA) and water.[214] The investigated ZnO and AZO films were about 40 nm thick. For the preparation of IOSC with AZO layers with 80 nm thickness were used.

13.1.1 SEM and AFM of ZnO and AZO

In Fig. 13.2 SEM images of ALD prepared ZnO (a) (substrate temperature 150 °C) and ALD prepared AZO (b) are displayed. As the ALD prepared TiO_x films, the ALD prepared ZnO and AZO films appear very smooth in SEM and AFM images in Fig. 13.2 c) shows a structure which resembles well structure of the ITO crystals of the underlying substrate (as for ALD prepared TiO_x, see Fig. 8.4 e).

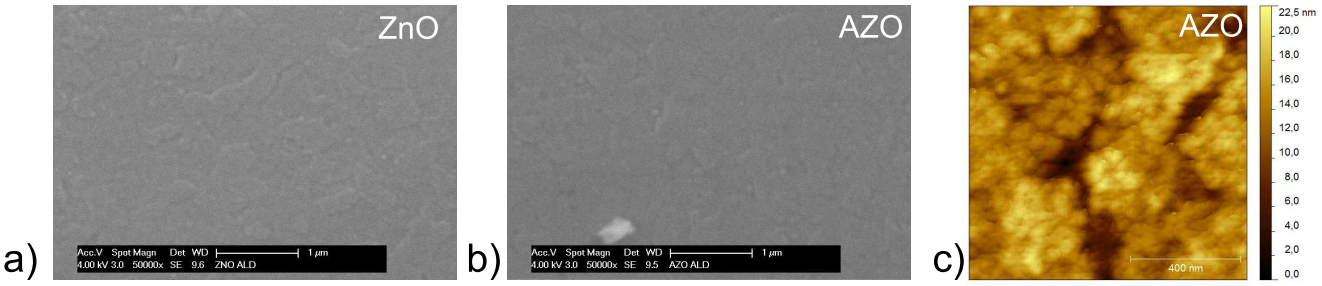

Figure 13.2. – In a) and b) SEM images of 80 nm ALD ZnO and AZO layers on ITO are shown. The ZnO and AZO layer appear both smooth and show slight structures of the underlying ITO substrate. In c) an AFM image is displayed. It shows a uniform coverage of the underlying ITO crystals.

13.1.2 XRD of ZnO and AZO

Figure 13.3 left shows XRD patterns of the ITO substrate (bottom), ZnO on ITO (middle) and AZO on ITO (right). ITO shows most intense reflexes at 21, 31, 35, 50 and 60° which are associated with the (211), (222), (400), (440) and (622) crystal plane of In_2O_3 respectively.[215] As the ZnO and AZO films are only about 40 nm thick, the substrate reflexes are still very strong in the ZnO and AZO XRD data, but still additional reflexes can be observed in both figures. The ZnO shows a weak reflex at 34°. It originates from the (002) plane of ZnO. The (101) plane is usually observed at about 37° and is not observed, but may be hidden by the ITO substrate reflex at same position.[216] Lim et al. found that ALD prepared ZnO at 130 °C substrate temperature showed a 1:1 ratio of the (002)/(101) reflexes, while at 170 °C substrate temperature the ratio changed strongly in favor of the (002) orientation.[216] Besides the ITO reflexes, the AZO XRD pattern (Fig. 13.3 top) shows a reflex at 32°, but no reflex at 34° anymore. As the ZnO to Al_2O_3 ratio is 25:1 one would expect the occurrence of an (002) reflex of ZnO. Apparently the Al_2O_3 leads to a texturing of the ZnO into the (100) orientation. Banerjee et al. suggested that the preferential growth of the (100) orientation, is caused by Al^{3+} ions, which disturb the charge neutrality of the (100) plane and by this reduce the surface energy of the (100) plane causing the observed preferential growth orientation.[89]

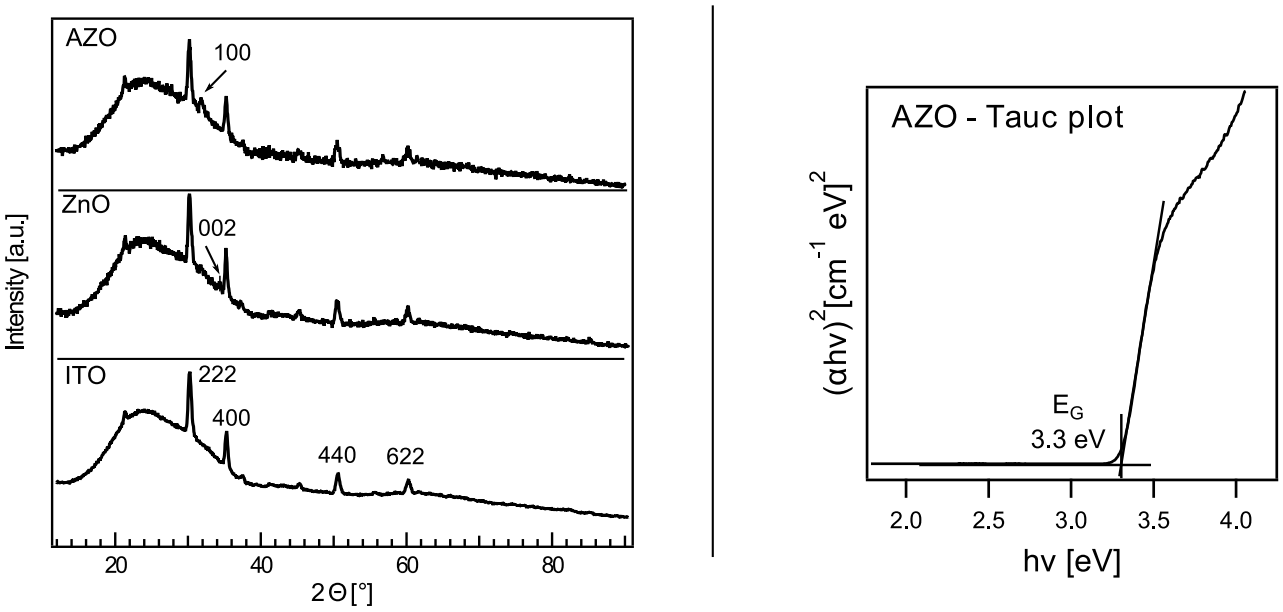

Figure 13.3. – Left: XRD spectra of ITO, ITO/ZnO and ITO/AZO (from bottom to top). Right: Tauc plot of ALD prepared AZO. The determined energy gap E_G is 3.3 eV. For the determination a direct band gap is assumed.

13.1.3 UV-Vis of AZO

On the right of Fig. 13.3 a Tauc plot of an ALD AZO UV-Vis absorption spectrum is shown. For the Tauc plot a direct energy gap of AZO is assumed (x=2). From the linear extrapolation of the absorption onset an energy gap of 3.3 eV is determined. The UV-Vis measurement was performed by Sara Trost from BU Wuppertal.

13.2 Photoemission of AZO and its interface to C_{60}

Figure 13.4 shows the XP spectra of an ALD prepared aluminum doped zinc-oxide (AZO) sample. At the top the survey spectrum is shown. Besides emissions of zinc and oxygen, a C 1s emission is apparent as well. The carbon origins probably from non-reacted precursor material and carbon contamination due to the *ex situ* handling of the sample. At the bottom of Fig. 13.4, detail spectra of the SE-edge, Zn $2p_{3/2}$, O 1s, C 1s and valence band emission are displayed. The Zn $2p_{3/2}$ emission is at 1022.6 eV. The O 1s is composed of two emissions, the main emission at around 531.0 eV and a component at around 532.5 eV. Both, the Zn $2p_{3/2}$ and main O 1s emission binding energies are in good agreement with literature values.[87] The high binding energy component of the O 1s is mostly attributed to adsorbed species including water, hydroxides, physisorbed or chemisorbed oxygen, and CO_x species.[217] Even sputter deposited ZnO films can exhibit a hydroxide component in the O 1s emission.[217] The C 1s component consists of three emission at ~285.5 eV, ~286.5 eV and 289 eV (not shown), which are assigned to C-C/C-H, C-O and to carbonates (CO_3^{2-}), respectively. On the right the VB emission, including the Zn 3d emission is shown. The Zn 3d emission is at 11.0 eV binding energy and the VBM is at 3.5 eV binding energy. The SE-edge is at 4.05 eV kinetic energy. The difference between the Zn $2p_{3/2}$ emission and VBM is 1019.1 eV.

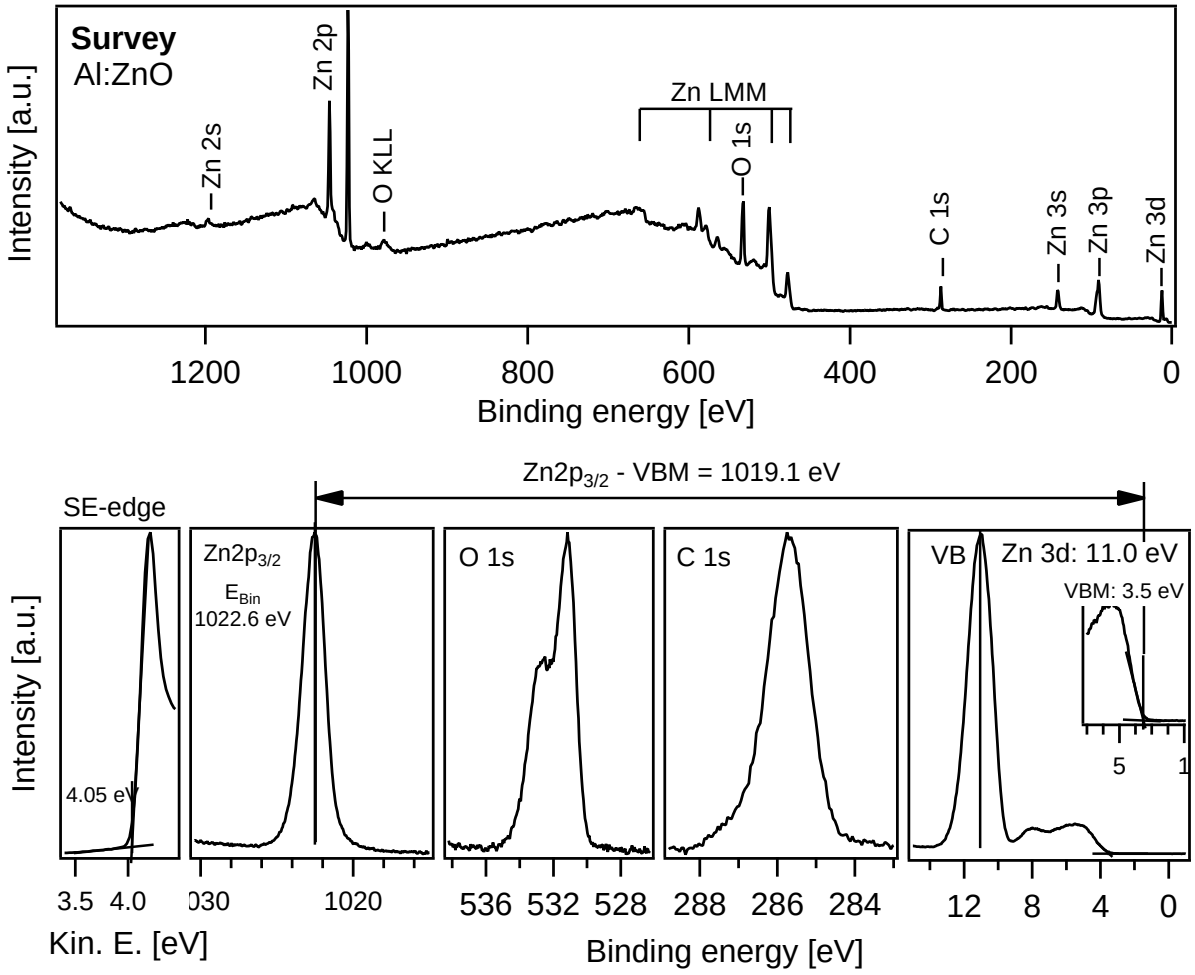

Figure 13.4. – Top: Survey spectrum of Al:ZnO (AZO). Bottom: Detail spectra of the SE-edge, the Zn $2p_{3/2}$, O 1s, C 1s and VB emission. The Zn $2p_{3/2}$-VBM distance is 1019.1 eV. The excitation energy is $Al_{K\alpha}$ radiation.

13.2.1 UV influence on the AZO substrate and the AZO /C_{60} interface

The bottom spectra in Fig. 13.5 show the SE-edge the Zn $2p_{3/2}$ level and the C 1s level of the ALD AZO film. The black bottom spectra are measured with the lowest possible X-ray exposure and the blue spectra after 60 min of UV illumination. The SE-edge shifts from 4.05 eV to 3.8 eV upon UV illumination. The Zn $2p_{3/2}$ core emission shows only a shift of 100 meV from 1022.50 eV to 1022.60 eV after UV illumination. As the SE-edge and the core level do not shift in parallel, there is a surface dipole change of 150 meV and a band bending change of 100 meV at the surface.

As for TiO_x, the AZO/C_{60} interface was also investigated with respect to UV illumination effects. Therefore three different C_{60} layer thicknesses were evaporated with a rate of 0.1 Å/ s onto an ALD prepared AZO sample. The nominal C_{60} coverages were calculated from the damping of the Zn $2p_{3/2}$ emission lines and are 3, 15, and 150 Å. As before, all samples were first measured with low X-ray exposure and then again after 60 min of *in situ* UV irradiation.

Figure 13.5 shows the SE-edge (left), Zn $2p_{3/2}$ (middle) and C 1s (right) photoemission spectra of the pristine sample (black) and the UV illuminated sample (blue). The SE-edge of the pure AZO sample shifts by 250 meV to lower binding energy upon UV illumination. With increasing C_{60} coverage, the UV induced shift is reduced, till it is reversed at a C_{60} coverage of 15 Å. At 150 Å C_{60} coverage no UV induced shift of the SE-edge is observed anymore. The Zn $2p_{3/2}$ spectra are damped with increasing C_{60} coverage. No energetic shift of the Zn $2p_{3/2}$ level occurs with increasing C_{60} coverage. After UV illumination the Zn $2p_{3/2}$ emission shifts about 100 meV to higher binding energies for all C_{60} coverages, where the Zn $2p_{3/2}$ emission is still visible. The C_{60} C 1s spectra are depicted on the right of Fig. 13.5. The bottom spectra shows the C 1s emission of the AZO ALD sample, which originates from leftovers of the precursors or adsorbates due to *ex situ* handling of the sample. All other C 1s spectra were corrected by subtracting the C 1s emission of the substrate. The C 1s emission of the substrate shows no shift upon UV illumination. For 3 and 15 Å C_{60} coverage, the C 1s level shifts 200 meV to lower binding energies after UV illumination. At highest C_{60} coverage, the C 1s level shows no UV induced shift and stays at the same binding energy as before UV illumination.

Figure 13.6 shows the evolution of the C 1s *fwhm* of C_{60} with increasing C_{60} coverage before (black plus signs) and after UV illumination (blue plus signs). With increasing C_{60} coverage the C 1s *fwhm* is reduced from ~0.9 eV before UV to 0.5 eV after UV. After UV light illumination the C 1s *fwhm* increases for 3 and 15 Å C_{60} coverage, while the increase is higher at 3 Å C_{60}. At 150 Å C_{60} coverage UV induces no C 1s *fwhm* increase.

13.2.2 Energy diagram of the AZO/C_{60} interface

From the experiments in Section 13.2.1 an energy diagram of the AZO/C_{60} interface before and after UV illumination is deduced (see Fig. 13.7). Before UV illumination (left) AZO shows no band bending towards the interface. The Zn $2p_{3/2}$ level is around 1022.5 eV below E_F and E_{Vac} is 4.0 eV above E_F. C_{60} shows no band bending towards the interface and the C 1s level is at ~285.3 eV E_{Bin} at all C_{60}

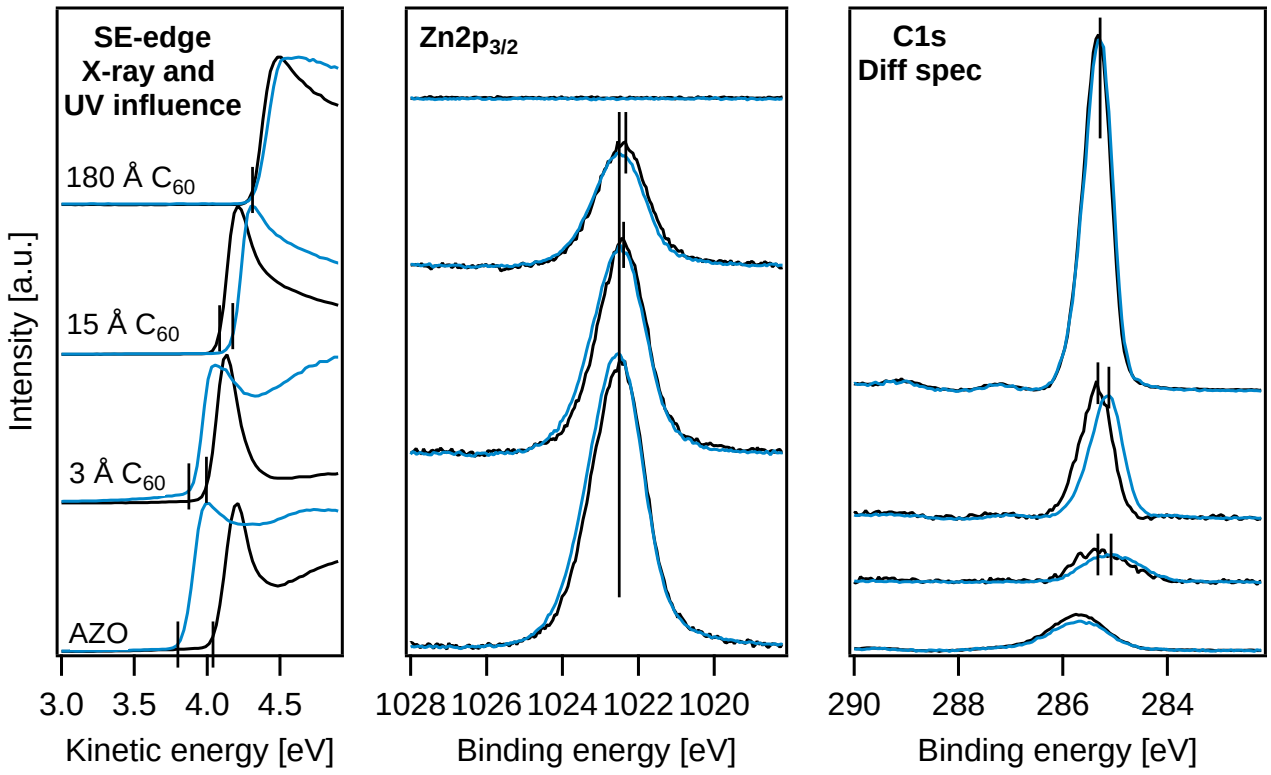

Figure 13.5. – Photoemission spectra of the AZO substrate and the AZO/C_{60} interface before (black) and after UV illumination (blue). On the left is the SE-edge of the pristine AZO with increasing C_{60} layer thickness. The SE-edge of the substrate shifts in the course of X-ray and UV irradiation 250 meV to lower kinetic energies, while the Zn $2p_{3/2}$ level only shifts 100 meV to higher binding energies upon UV illumination. After C_{60} deposition UV induces a lowering of the WF at the pristine AZO at low C_{60} coverages (3 Å C_{60}), the WF of the 15 Å C_{60} sample increases after UV illumination. At higher C_{60} coverages no WF shift occurs upon UV. In the middle, the evolution of the Zn $2p_{3/2}$ emission is shown with increasing C_{60} coverage and UV irradiation. The Zn $2p_{3/2}$ emission does not shift upon increasing C_{60} coverage, but 100 meV upon UV illumination. On the right, the C 1s emission is depicted. The bottom spectra shows the carbon contamination of the AZO sample and is subtracted, from all other C 1s spectra. UV light induces a shift of the C 1s energy level of ~200 meV to lower binding energies. At highest C_{60} coverage no UV induced shift is observed.

Figure 13.6 – Evolution of the C_{60} C 1s *fwhm* with increasing C_{60} coverage before UV illumination (black plus signs) and after UV illumination (blue plus signs). With increasing C_{60} coverage the *fwhm* is reduced. At low C_{60} coverages, UV light increases (blue plus sign) the *fwhm* of the C 1s emission.

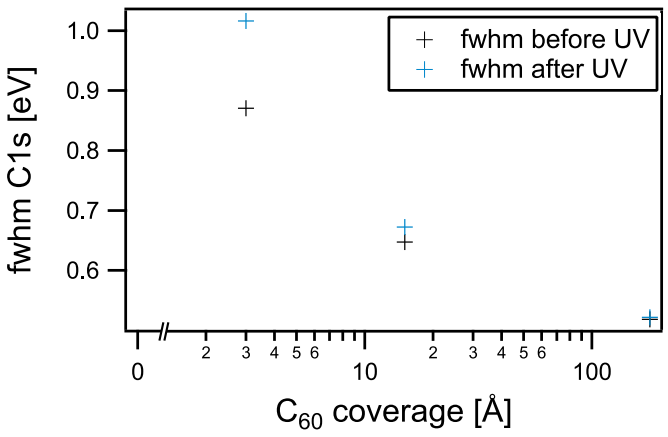

Table 13.1. – Work function (WF) and Zn $2p_{3/2}$ and C 1s level values of the ALD AZO samples with different C_{60} coverages.

	C_{60} [Å]	absolute values initial	X-ray	UV	with respect to initial initial	X-ray	UV
WF [eV]	0	4.05	4.00	3.80	0	0.05	0.25
Zn $2p_{3/2}$ [eV]		1022.51	1022.56	1022.59	0	-0.03	-0.08
C 1s [eV]		-	-	-	-	-	-
WF [eV]	3	4.00	3.95	3.90	0	0.05	0.10
Zn $2p_{3/2}$ [eV]		1022.47	1022.52	1022.57	0	-0.05	-0.10
C 1s [eV]		285.29	285.23	285.07	0	0.08	0.19
WF [eV]	15	4.08	4.12	4.17	0	-0.04	-0.09
Zn $2p_{3/2}$ [eV]		1022.47	1022.48	1022.56	0	-0.01	-0.09
C 1s [eV]		285.30	285.28	285.15	0	0.02	0.2
WF [eV]	180	4.33	4.32	4.34	0	0.01	-0.01
Zn $2p_{3/2}$ [eV]		-	-	-	-	-	-
C 1s [eV]		285.33	285.32	285.30	0	0.01	0.03

coverages. E_{Vac} of C_{60} is 4.3 eV above E_F. At the interface the Zn $2p_{3/2}$-C 1s distance is 737.2 eV and the interface dipole is -0.7 eV. On the right the energy diagram after UV illumination is illustrated. The energy diagram after UV illumination is determined as for TiO_x in Section 9.1 and only directly measured core levels are shown. It is assumed that the UV induced changes of the AZO substrate and of samples with low C_{60} coverage also occur at the AZO/C_{60} interface with the highest C_{60} coverage, where the substrate emission lines do not appear anymore and the C 1s emission of C_{60} shows no shift. As before UV illumination, AZO shows no band bending towards the interface after UV illumination. The Zn $2p_{3/2}$ level shifts to 1022.6 eV below E_F and E_{Vac} is only 3.8 eV above E_F. C_{60} shows an upward band bending of 200 meV towards the interface after UV illumination. At the interface the C 1s level is ~285.1 eV and at high C_{60} coverages at 285.3 eV below E_F. E_{Vac} of C_{60} is 4.3 eV above E_F and bends 200 meV towards the interface as well. The energetic changes result in a Zn $2p_{3/2}$-C 1s distance of 737.5 eV at the interface and an increase of the interface dipole to -0.7 eV.

13.3 Summary: AZO/C_{60} interface and the UV influence

Summarizing the results, it is observed that the UV induced shifts at the AZO/C_{60} interface are similar to the ones observed at the TiO_x 80 °C/C_{60} interface in Section 9.1. The model for the UV induced changes at the 80 °C TiO_x/C_{60} interface derived in Chapter 12 is also applicable for the AZO/C_{60} interfaces.
At the AZO/C_{60} interface, the C 1s binding energy at the interface decreases after UV illumination by 200 meV as it does on a TiO_x 80 °C/C_{60} interface. Together with the increase of the Zn $2p_{3/2}$ binding energy this leads to an increase of Zn $2p_{3/2}$-C 1s distance from 737.2 eV to 737.5 eV. The interface dipole changes by 400 meV. Furthermore the C 1s *fwhm* increases after UV illumination at low C_{60} coverages.
In Appendix A.2 results of a 500 °C annealed TiO_x substrate, its interface to C_{60} and the influence of UV illumination on them are shown. The results of the 500 °C TiO_x/C_{60} interface show basically the same

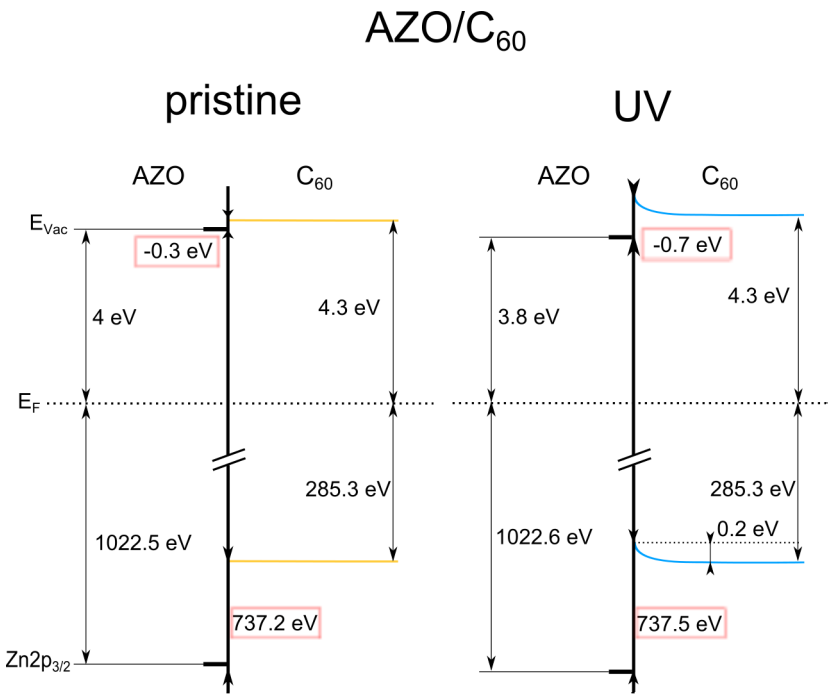

Figure 13.7. – Energy diagram of the AZO/C_{60} interface before UV illumination (left) and after UV illumination (right). Before UV illumination the Zn $2p_{3/2}$-C 1s distance is 737.2 eV and after UV illumination it is 737.5 eV. The interface dipole increases from -0.3 eV before UV to -0.7 eV after UV illumination.

trends as the 80 °C TiO_x/C_{60} and AZO/C_{60} interfaces.

Table 13.2 shows the Ti $2p_{3/2}$-C 1s and Zn $2p_{3/2}$-C 1s distances of all so far prepared metal oxide C_{60} interfaces. Also the AZO/C_{60} and 500 °C TiO_x/C_{60} interfaces show an UV induced increases of the Ti $2p_{3/2}$/Zn $2p_{3/2}$-C 1s distances at the respective interfaces. The 500 °C TiO_x/C_{60} distance is similar to the *ex situ* anatase (101) Ti $2p_{3/2}$-C 1s distance.

Table 13.2. – Ti $2p_{3/2}$-C 1s and Zn $2p_{3/2}$-C 1s distances of the differently prepared TiO_2/C_{60} and AZO/C_{60} interfaces and influence of UV light.

Ti $2p_{3/2}$-C 1s distance [eV]	Bessy	Daisy-Fun before UV	Daisy-Fun after UV
TiO_2 *in situ*/C_{60}	174.4	174.2	174.2
TiO_2 *ex situ*/C_{60}	174.1	173.7	174.0
TiO_x 80 °C/C_{60}	-	173.4	173.8
TiO_x 500 °C/C_{60}	-	173.8	174.2
AZO/C_{60}	-	737.2	737.5

14 TiO_x/C_{60} and AZO/C_{60} interface obtained at synchrotron Bessy II

The TiO_x/C_{60} and AZO/C_{60} interface was also investigated at the beamline U49-2/PGM-2 at Bessy II in Berlin. The synchrotron enables PE measurements with a high surface sensitivity (as $h\nu$ can be adjusted) and high intensity (due to a high photon flux and a high cross section at the respective photon energies). By this it allows the direct recording of the core levels and the valence band. C_{60} was used as acceptor material of the hetero interface and evaporated *in situ* onto TiO_x and AZO. After each deposition step photoelectron spectra of the secondary electron edge, the C 1s, Ti $2p_{3/2}$ or Zn $2p_{3/2}$ core level and the VB region were recorded. As synchrotron radiation can cause beam induced damages of the sample, as for example a reduction of the metal-oxide or a decomposition of the organic component, the undulator beamline was detuned on the cost of signal-to-noise ratio and energy resolution, and each sample position was only used for recording a single spectrum only. The shown results were already published in an article '*Overcoming the "Light-Soaking" Issue in Inverted Organic Solar Cells by the Use of Al:ZnO Electron Extraction Layers*' by Sara Trost, Kirill Zilberberg, Andreas Behrendt, Andreas Polywka, Patrick Görrn, Philip Reckers, Julia Maibach, Thomas Mayer and Thomas Riedl.[15]

TiO_x/C_{60} interfaces

C_{60} was evaporated with rate of 0.1 Å/s on the TiO_x substrate. The development of the spectra of the TiO_x/C_{60} interface experiment with increasing C_{60} deposition are displayed in Fig. 14.1 for the secondary electron onset (a), the Ti $2p_{3/2}$ (b) and C 1s core emissions (c) and the valence band region(d), respectively. The binding energy positions of the Ti $2p_{3/2}$ and C 1s levels are extracted from a fit with Lorentz-Gaussian components. To determine the formal C_{60} layer thickness, the damping of the Ti $2p_{3/2}$ core level was used and the coverages are 0.6, 2, 4, 8 and 20 Å as indicated. The pristine Ti $2p_{3/2}$ doublet emission shows a main Ti $2p_{3/2}$ emission at 459.5 eV and a component with a chemically shift of 1.3 eV (Fig. 14.1b). The shifted component is assigned to a reduced Ti^{3+} component due to oxygen surface defects. With increasing C_{60} deposition, the Ti $2p_{3/2}$ binding energy stays constant at 459.5 eV indicating that E_F is pinned at the surface of TiO_x. The Ti^{3+}/Ti^{4+} ration does not change either. Figure 14.1 c) displays the evolution of the C 1s emission upon C_{60} deposition. As can be seen at the C 1s bottom spectrum the pristine TiO_x indicates remnants of the precursor and carbon contamination due to *ex situ* handling of the substrates. In the consecutive C 1s spectra the substrate C 1s emission is subtracted. The C_{60} C 1s emission is at 0.6 Å coverage at 285.5 eV and shifts by 0.2 eV to lower binding energies in the course of C_{60} deposition.

Valence band onset spectra measured in the course of increasing C_{60}-deposition (excitation energy 90 eV) are displayed in Fig. 14.1 d). The valence band maximum is determined by two different ways. Once by a linear extrapolation of the valence band emission onset and the intersection to the background intensity (VBM 2) and once by aligning a tangent at the emission onset and the intersection to the

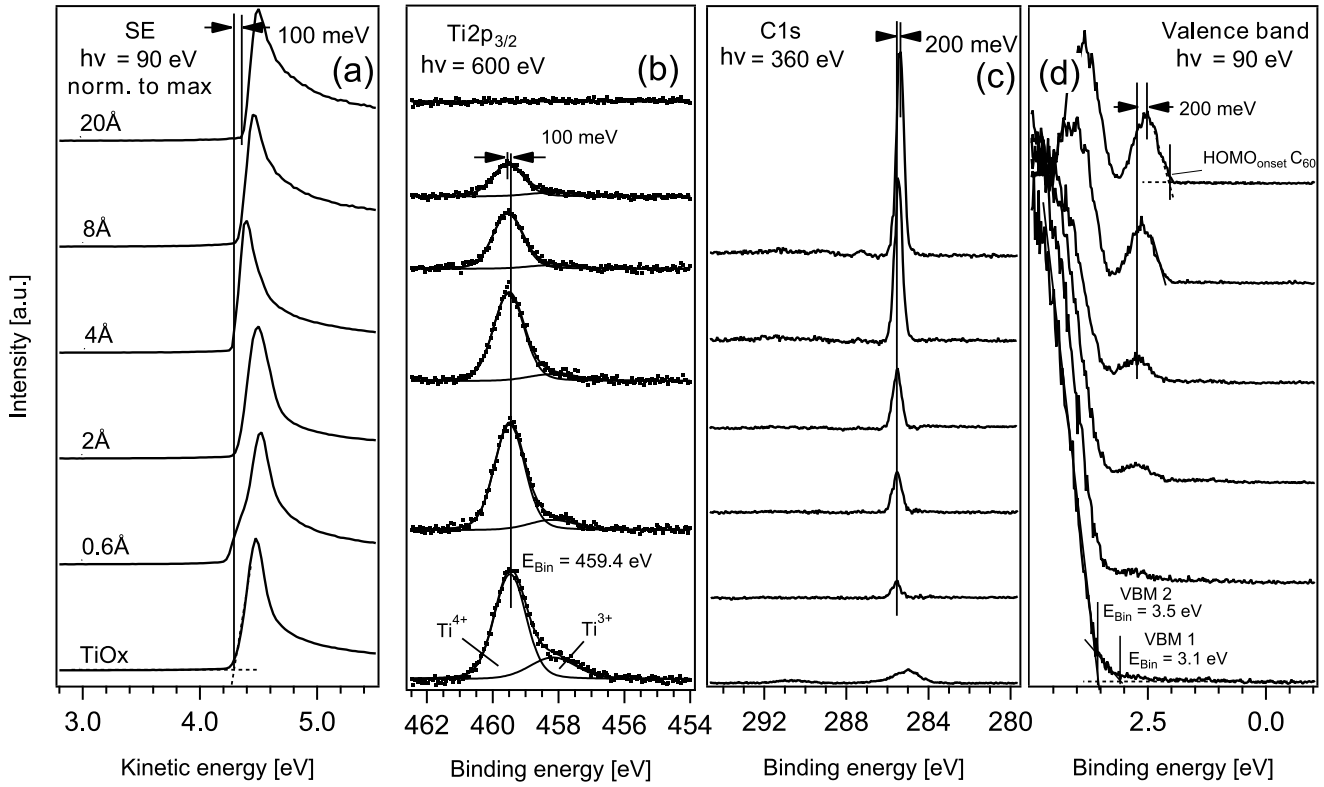

Figure 14.1. – The secondary electron emission edge (a), Ti $2p_{3/2}$ core level emission (b), C 1s core level emission (c) and valence band spectra (d) in the course of TiO_x/C_{60} interface formation. The Ti $2p_{3/2}$ and VB binding energies stay constant, while the C 1s and HOMO binding energies shifts 200 meV to lower binding energies with increasing C_{60} coverage.

background intensity (VBM 1). The VBM 2 is at 3.5 eV while VBM 1 is at 3.1 eV. For the energy diagram (see Fig. 14.3) the VBM 1 position is used as the relevant valence band onset. The VBM 1 position as valence band onset was used before for low photon energies by Pekkola and Kumarasinghe.[25,218] Pekkola proposed that minor valence band emissions on the low energy side of the VB spectrum tend to be underestimated for small photon energies compared to high photon energies and attributed this to different cross section of the O 2p orbital.[25] As the Ti $2p_{3/2}$ emission shows rather high Ti^{3+} content, an emission at ~1.3 eV is actually expected as this emissions usually show up together. A reason for the occurrence of the Ti^{3+} emission in the Ti $2p_{3/2}$ emission and the absence of the VB emission at 1.3 eV, could be that the sample spot, where the Ti $2p_{3/2}$ emission was measured was already beam damaged by synchrotron radiation, while the sample spot of the VB emission was not damaged by synchrotron radiation. A detailed analysis of the effects of synchrotron exposure on different titania surfaces is given in Section 17.1.1. The C_{60} HOMO emission can be identified already for the first deposition step. For increasing layer thickness, the HOMO binding energy decreases continuously by a total of 0.2 eV to the final position of the $HOMO_{onset}$. The WF is directly given by the kinetic energy of the secondary electron emission edges as measured at 90 eV (Fig. 14.1a). The pristine TiO_x WF is 4.3 eV and in agreement with the Kelvin Probe results recorded by Trost et al.[15] With C_{60} deposition the WF increases to 4.4 eV, which is the value of unintentionally n-doped pristine C_{60}. Values for the C 1s emission, the position of the C_{60} $HOMO_{onset}$ and the WF are in good agreement with former results.[160]

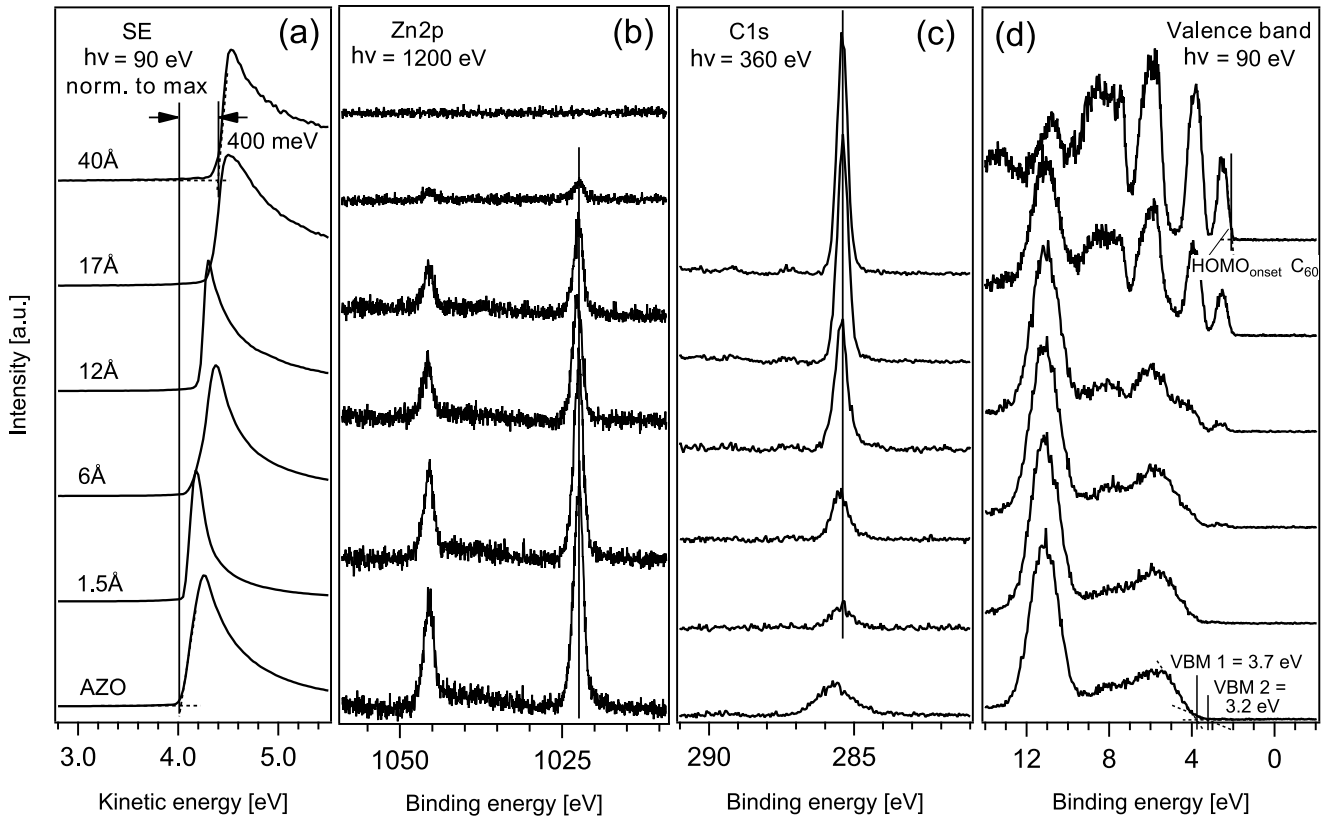

Figure 14.2. – The secondary electron emission edge (a), Zn $2p_{3/2}$ core level emission (b), C 1s core level emission spectra (c) and valence band spectra (d) in the course of AZO/C_{60} interface formation. The Zn $2p_{3/2}$, C 1s and VB/HOMO binding energies stay constant, indicating that no band bending occurs at the interface.

AZO/C_{60} interfaces

The corresponding spectra of the AZO/C_{60} interface formation are displayed in Fig. 14.2. C_{60} was deposited with a rate of 0.2 Å/s. The respective C_{60} layer thicknesses were calculated from the damping of Zn $2p_{3/2}$ emission and are 1.5 Å, 6 Å, 12 Å, 17 Å and 40 Å. The Zn $2p_{3/2}$ emission (Fig. 14.2 b) shows a constant binding energy of 1022.5 eV, with increasing layer thickness. The binding energy is similar to published pristine ALD AZO values.[87] For the determination of the C_{60} C 1s binding energy position, the substrate C 1s emission has been subtracted. The C 1s binding energy is constant at 285.3 eV for all C_{60} layer thicknesses. The VBM position was determined according to the determination of VBM 1 of TiO_x and yields a VBM at 3.2 eV. The C_{60} $HOMO_{onset}$ is at 2.1 eV (Fig. 14.2 d). As the C_{60} C 1s core level, the $HOMO_{onset}$ does not shift and is constant with increasing C_{60} deposition. The secondary electron edge shifts from 4.0 eV kinetic energy for AZO to 4.4 eV kinetic energy of unintentionally n-doped pristine C_{60}.

The TiO_x/C_{60} and AZO/C_{60} energy diagram

In Fig. 14.3 interface diagrams of the TiO_x/C_{60} and AZO/C_{60} interfaces are illustrated. All energetic values are directly measured in photoemission. On the left is the TiO_x/C_{60} interface. The VBM of TiO_x is below the $HOMO_{onset}$ of C_{60} and its distance is 0.8 eV. Furthermore an interface dipole of 0.1 eV exists. The Ti $2p_{3/2}$-C 1s distance is 173.9 eV. On the right is the AZO/C_{60} interface. Due to the 0.3 eV smaller WF of AZO, an interface dipole in the opposite direction (compared to TiO_x/C_{60}) of -0.4 eV is induced.

The VBM of AZO is 1.1 eV below the C_{60} $HOMO_{onset}$ and the Zn $2p_{3/2}$-C 1s distance is 737.1 eV. A further difference is that the C_{60} bends downwards by 0.2 eV towards the TiO_x interface, which is not present at the AZO/C_{60} interface. The Ti $2p_{3/2}$-C 1s distance before UV exposure of 173.9 eV is 0.5 eV larger than determined at the Daisy Fun (see Table 13.2). The differences arise from the different determination of the VBM position. The Zn $2p_{3/2}$-C 1s distance determined at Bessy (737.1 eV) is similar to the distance determined at the Daisy Fun (737.2 eV).

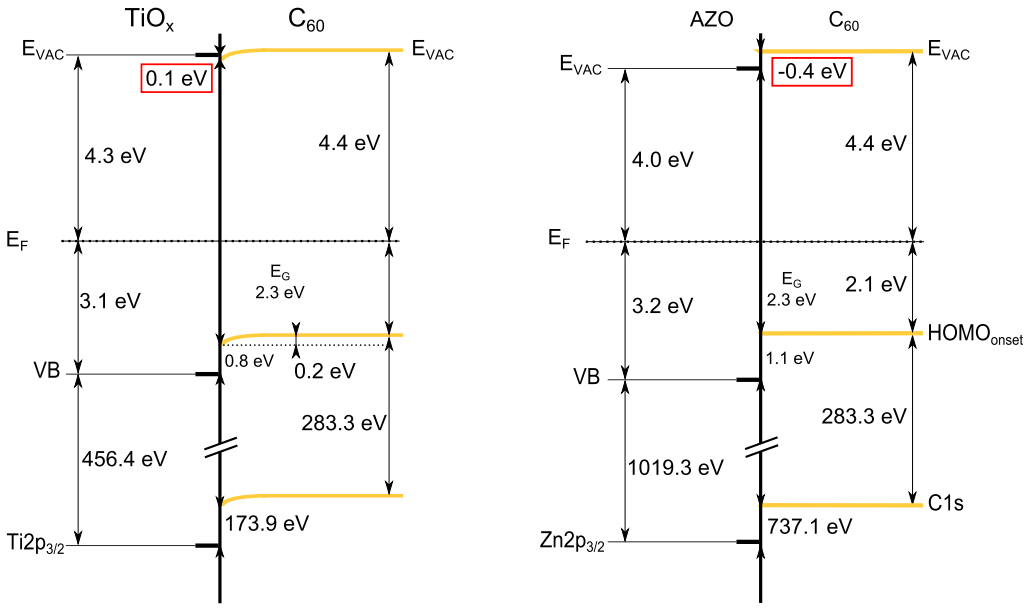

Figure 14.3. – Energy diagrams directly derived from the photoemission measurements. The TiO_x VBM -C_{60} $HOMO_{onset}$ distance is 0.8 eV and the AZO VBM - C_{60} $HOMO_{onset}$ is 1.1 eV. The interface dipole is 0.1 eV at the TiO_x C_{60} interface and -0.4 eV at the AZO/C_{60} interface.

15 Comparing energy band diagrams and I-V characteristics

15.1 Comparison and discussion of I-V curves and derived energy band diagrams

The main goal of this study is to correlate I-V characteristics of inverted organic solar cells with the energy level line up of solar cells. The alignment of the respective charge transport levels at the interface is crucial for the functionality of solar cells.[28,219–221] In this work the focus is on the ETL/organic interface in dependence of the ETL materials and UV illumination. The ETL was varied (TiO_x and AZO) and C_{60} was used as organic acceptor material. Figure 15.1 shows I-V characteristics in dependence of the ETL and UV illumination recorded by Trost et al. and Kuwabara et al. I-V curves on the left by Trost el al. show that IOSC with TiO_x as ETL show only good diode like I-V characteristics after the illumination with UV light. IOSC with AZO as ETL show diode like I-V characteristic before and after illumination with UV light. The I-V curves on the right by Kuwabara et al. show that the shape of the I-V curves with TiO_x as ETL changes from a S-shape to diode like I-V characteristics with increasing annealing temperature of the TiO_x. Along with the increasing annealing temperature goes a change of the phase from amorphous to anatase.[15,71]

So far the interface band diagrams were only derived for the directly measured energetic levels of the specific material. For the case of the ETL/organic interface electrons are the relevant charge carriers and hence the E_{CB}-$LUMO_{onset}$ offset is critical, and for the HTL[1]/organic interface the E_{VB}-$HOMO_{onset}$ offset is important. The value of E_{VB} and $HOMO_{onset}$ is accessible by using photoelectron spectroscopy. As in our study the electron extraction side of a solar cell is considered, E_{CB} and the $LUMO_{onset}$ have to be accessed to allow a statement about the electron extraction behavior. The E_{CB} and $LUMO_{onset}$ position can be accessed by determining the energy gap of the respective material. The electronic energy gap (E_G) for the metal oxides was determined by UV-Vis spectroscopy in Sections 8.1.5 and 13.1.3 and are 3.4 and 3.3 eV, for the ALD prepared 80 °C TiO_x and AZO respectively. For the 500 °C post annealed TiO_x, the fundamental band gap of anatase, which 3.2 eV, is assumed.[16] As the dielectric constant of organic semiconductors is low, excitons form upon the excitation of electrons (see Section 2.1.3) and the energy gap determinations cannot be performed by UV-Vis spectroscopy.[22] Instead inverse photoemission spectroscopy (IPES) is used to determine the photoemission gap of organic semiconductors. For C_{60} the $HOMO_{onset}$-$LUMO_{onset}$ energy gap (determined with IPES) was reported to be between 2.3 and 2.4 eV.[26,162,163] The photoemission energy gap gives good evidence of the transport gap,[222] which is discussed to be 100-200 eV smaller than the photoemission gap.[21] The determined energy gaps are added to the VBM or $HOMO_{onset}$ position of the respective material. The VBM and

[1] **H**ole **T**ransport **L**ayer

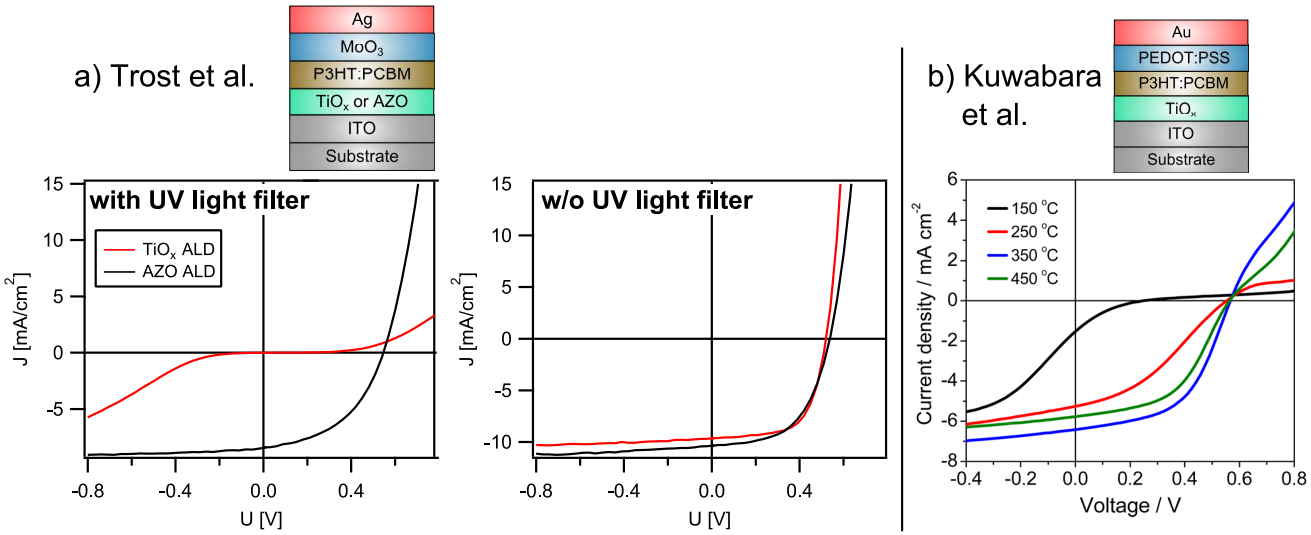

Figure 15.1. – I-V characteristic of different inverted organic solar cells. a) Shows IOSC with TiO_x (red) and AZO (black) as ETL. While the AZO containing IOSC shows good diode like I-V characteristic with and w/o UV illumination, IOSC containing TiO_x show only good diode like I-V characteristics after illumination with UV light. The I-V curves were recorded be Sara Trost from BU Wuppertal.[15] b) shows I-V curves of IOSC with TiO_x ETL annealed at different temperatures. At low annealing temperatures I-V curves show a S-shape, which disappears with increasing annealing temperatures. At the same time TiO_x transforms from amorphous to anatase. The I-V curves are adapted from Kuwabara et al.[71]

$HOMO_{onset}$ positions of the respective metal oxide and C_{60} are determined from the respective core level distances determined in Table 8.2 (TiO_x 80 and 500 °C), Fig. 13.4 (AZO) and Fig. 8.13 (C_{60}). For C_{60} the C 1s-$HOMO_{onset}$ is 283.3 eV for Bessy experiments and 283.2 eV for experiments at the Daisy-Fun.

The resulting band diagrams are discussed in terms of the correlation between I-V curves and energy diagrams. In Chapter 7 it was concluded that the derived TiO_x/C_{60} interface is suitable to be compared with I-V characteristics obtained for inverted organic solar cells containing the $TiO_x/PC_{61}BM$ interface. Furthermore in Section 8.3.1 E_{CB} of TiO_x and the C_{60} LUMO were added to the energy diagram and the similarity of the energetic LUMO position of C_{60} and $PC_{61}BM$ on TiO_x was shown.

15.1.1 IOSC with 80 °C TiO_x

In Fig. 15.2 the TiO_x/C_{60} energy line-ups, before UV illumination derived from experiments at Bessy and at Daisy-Fun are depicted (left and middle). Included is the E_{VB} and E_{CB} of TiO_x and the HOMO/LUMO position of C_{60}. Before UV illumination the IOSC with TiO_x as ETL showed S-shaped I-V characteristic with a reduced fill factor FF (see Fig. 7.2). The energy band line-up derived at Bessy displays that the E_{CB} of TiO_x is 0.3 eV above E_F and 0.2 eV above the $LUMO_{onset}$ of C_{60}. This offset displays a barrier for electrons and is an electron extraction barrier. The energy line-up derived from the interface experiment at the Daisy-Fun in Darmstadt shows a different situation. While the E_{CB}-$LUMO_{onset}$ distance is 0.2 eV as well, the relative position of E_{CB} of TiO_x and the $LUMO_{onset}$ of C_{60} are lower compared to E_F. E_{CB} of TiO_x is right at E_F and the C_{60} $LUMO_{onset}$ at the interface is 0.2 eV below E_F. In contrast to the Bessy derived line-up, the energetic line-up concluded from Daisy-Fun experiments before UV, does not show an electron extraction barrier for electrons. Furthermore E_F of TiO_x is on the same level as E_{CB}, which

is evidencing a good conductivity of TiO_x.
The differences in both line-ups (Bessy and Daisy-Fun before UV) origin probably mostly from the different method of VBM determination. While the VBM of TiO_x at the Daisy-Fun experiments were determined after the method of Kraut by using a linear extrapolation of the leading edges to the baselines of the XPS spectra,[150] the VBM of TiO_x measured with 90 eV photon energy at Bessy, were derived as proposed by Pekkola and Kumarasinghe for small photon energies using the emission onset.[25,218] The differences in the VBM determination methods result in differences of 0.4-0.5 eV in the position of the VBM (see Fig. 14.1). After UV illumination an energy level line-up was only derived at the Daisy-Fun (see Fig. 15.2 right). The Ti $2p_{3/2}$-C 1s distance increases from 173.4 eV to 173.8 eV. As a result also the E_{CB}-$LUMO_{onset}$ changes and the $LUMO_{onset}$ of C_{60} rises above (0.1 eV) E_{CB} of TiO_x. This line-up indicates good electron extraction behavior at the interface as well.

The comparison of the experiments performed at Bessy and the Daisy-Fun make it evident how crucial the VBM position determination is, to derive a proper energy level line-up. As a result two similar experiments derived with different photon energies lead to two different energetic line-ups of the TiO_x/C_{60} interface. While the line-up derived at Bessy gives rise to an electron extraction barrier at the interface and low conductivity of TiO_x, the line-up obtained at the Daisy-Fun does not explain S-shaped I-V characteristics before UV illumination as neither an extraction barrier for electrons is observed nor is a low conductivity of the TiO_x (see Section 2.5).[54] In the following paragraphs influences of adsorbates on the energy level line-up on the basis of the Daisy-Fun experiments are discussed.

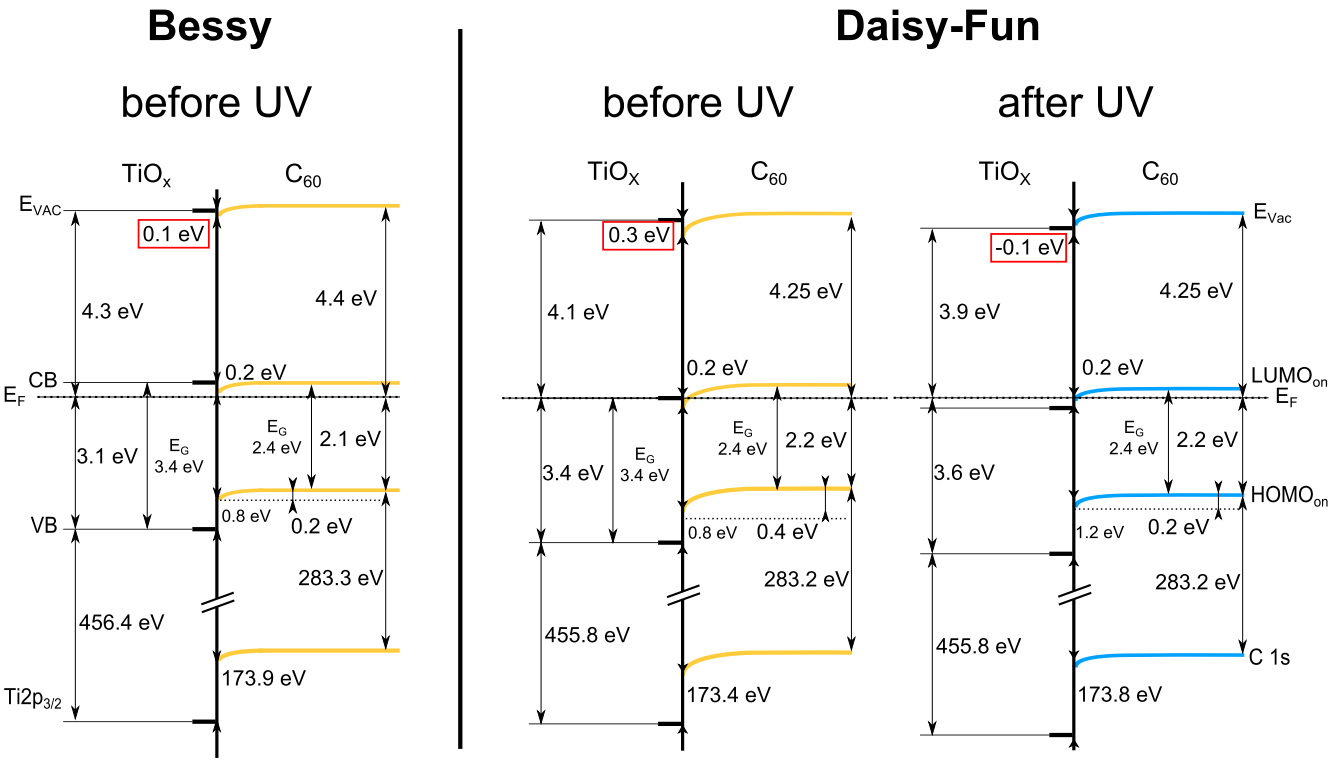

Figure 15.2. – Energy band diagrams of 80 °C TiO_x/C_{60} interface derived at Bessy before UV (left), derived at Daisy-Fun before UV (middle) and derived at the Daisy-Fun after UV (right).

Air influence: The results in Section 11.1 indicate that air exposure causes adsorbates at the surface inducing a downward band bending at sc-(101) anatase surface of 100-200 meV. Therefore the energy levels in the bulk of the TiO_x may are at different positions, than determined at the surface (as XPS is surface sensitive). As the bulk properties of the ALD prepared sample are not accessible by XPS, it is assumed that air induces a similar surface band bending on TiO_x as on the sc-(101) anatase surface (see Section 11.1). Such a situation is depicted in Fig. 15.3. In the energy diagram it is assumed, that air induces a downward band bending of 200 meV from the bulk of TiO_x towards the surface. The line-up at the interface does not change compared to Fig. 15.2. In the bulk of TiO_x the CBM is now above E_F indicating a reduced conductivity of the TiO_x. After UV illumination the band bending towards the interface increases to 400 meV and the TiO_x CBM at the surface is below E_F.

As many others Ecker et al. observed S-shaped I-V characteristics of IOSC with TiO_x ETL's before UV illumination and diode like I-V characteristics after UV illumination. Ecker et al. performed impedance measurements and attributed the S-shape to a reduced conductivity of TiO_x, which improves after illumination with UV light.[54] The derived energy diagram in Fig. 15.3 with the air induced downward band bending towards the surface supports the model, that a reduced conductivity of the TiO_x before UV illumination is existent. However XPS only allows a statement about the CBM at the surface and no statement about a possible change of CBM position in the bulk after UV illumination can be made. In this context Pomoni et al. reported an increased conductivity of nc-TiO_2 after UV irradiation.[73] Concluding, the line up shown in Fig. 15.3 could support the assumption that an increased conductivity of TiO_x after UV is responsible for the improved I-V characteristics of the IOSC with TiO_x as ETL.

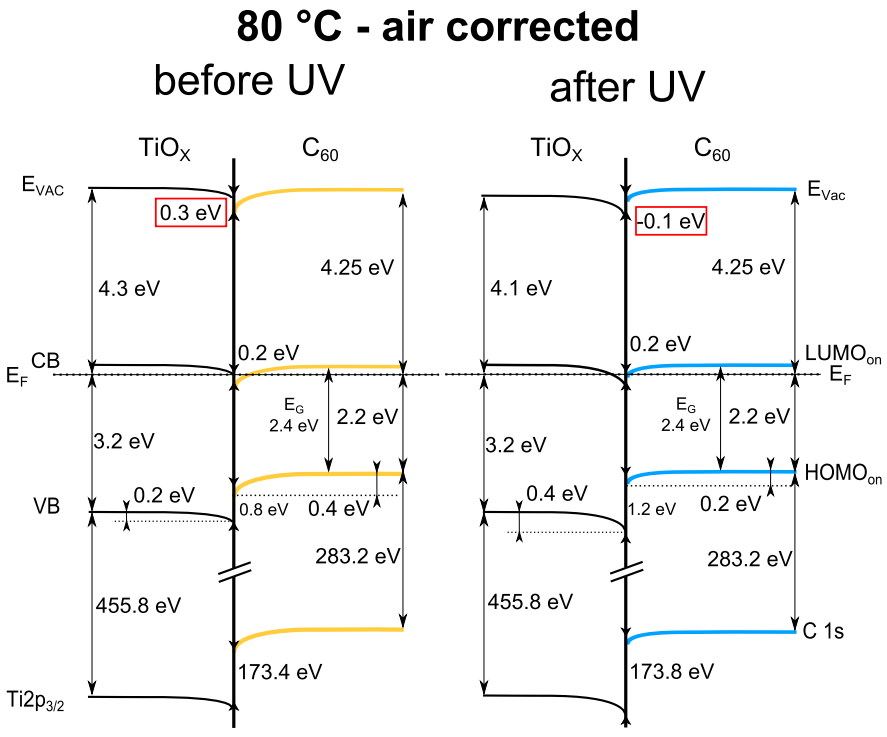

Figure 15.3 – Energy diagram with an assumed accumulation layer at the TiO_x surface due to the adsorption of hydroxyls and oxygen at the surface. It is assumed that oxygen causes an accumulation layer at the surface.

In Fig. 15.4 dark current voltage curves measured on IOSC with TiO_x as ETL are displayed on a logarithmic scale. The red and blue curve represent dark I-V characteristics before and after UV

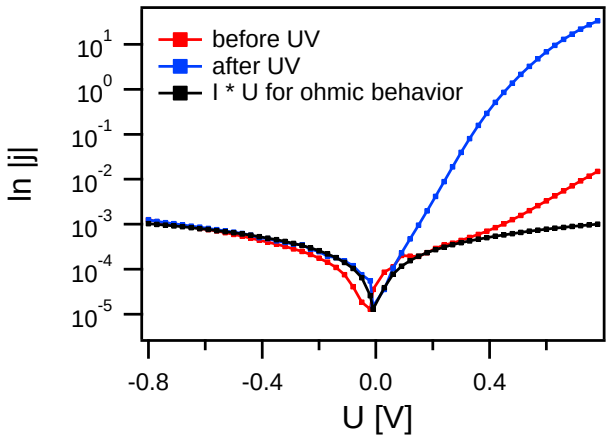

Figure 15.4 – Logarithmic plot of the dark I-V curves of IOSC with TiO_x as ETL. They correspond to the I-V curves shown in Fig. 7.2. The red curve is before UV and the blue curve after UV illumination. The black curve follows an ohmic behavior.

illumination. The black curve represents the ohmic behavior of a resistor. The blue and black curve are in good accordance in negative bias direction, while the red curve is different to the black, ohmic, curve. In an ideal solar cell all contacts/interfaces, besides the absorbing p-n contact, should be ohmic contacts. At negative voltages the diode is in reverse direction and only the dark current flows, while the I-V curve is mainly determined by the contacts. The good accordance of the blue and the black curve shows, that at negative voltages (in reverse direction) the I-V characteristics are ohmic, indicating a good blocking behavior of the p-n diode and ohmic contacts. The difference of the red I-V curve before UV and the black I-V curve indicates an additional non ohmic contact within the solar cell. This could be an evidence for the existence of a diode in reverse direction to the photo diode (counter diode) as it is described in Section 2.4. The origin of such a counter diode could be the $TiO_x/PC_{61}BM$ interface, if the $HOMO_{onset}$ of the organic material is above E_{CB} of the ETL. As the S-shape disappears with AZO as ETL it is unlikely that any other interface, than the ETL/organic interface, occurring in the IOSC device is responsible for the S-shape.

O_2 influence: A third option is that the energy diagram observed under UHV condition does not represent the actual line-up, which occurs under ambient pressure conditions. Porsgaard et al. reported, that molecular oxygen with a partial pressure of 1.3 mbar induces an upward band bending of 0.4 eV on a rutile (110) surface, compared to UHV conditions.[171] Hence there might be a significant upward band bending at the surface of TiO_x at atmosphere, which is not observed in XPS due to desorption of O_2 under UHV conditions. Therefore an upward band bending of 0.4 eV towards the interface is added in the line-up depicted in Fig. 15.5. This is reflected by an upward shift of all TiO_x energy levels at the surface by 0.4 eV. Now E_{CB} is 0.4 eV above E_F. The TiO_x energy level are drawn short, as the band positions within the bulk are not discussed. Compared to line-up in Fig. 15.2 this changes the line-up at the interface significantly. Before UV illumination, an extractions barrier occurs, as now E_{CB} of TiO_x at the surface is 0.4 eV above E_F. An offset of the TiO_x E_{CB} and the C_{60} LUMO of 0.6 eV is apparent at the surface. This leads to an electron extraction barrier of 0.4 eV (as the C_{60} LUMO at the interface is 0.2 eV below E_F). Assuming oxygen species adsorption at the surface, the E_{CB} position suits well to the observed low conductivities of amorphous TiO_x.[223] After UV illumination the line-up is the same as in Fig. 15.2 right and no electron extraction barrier is observed.

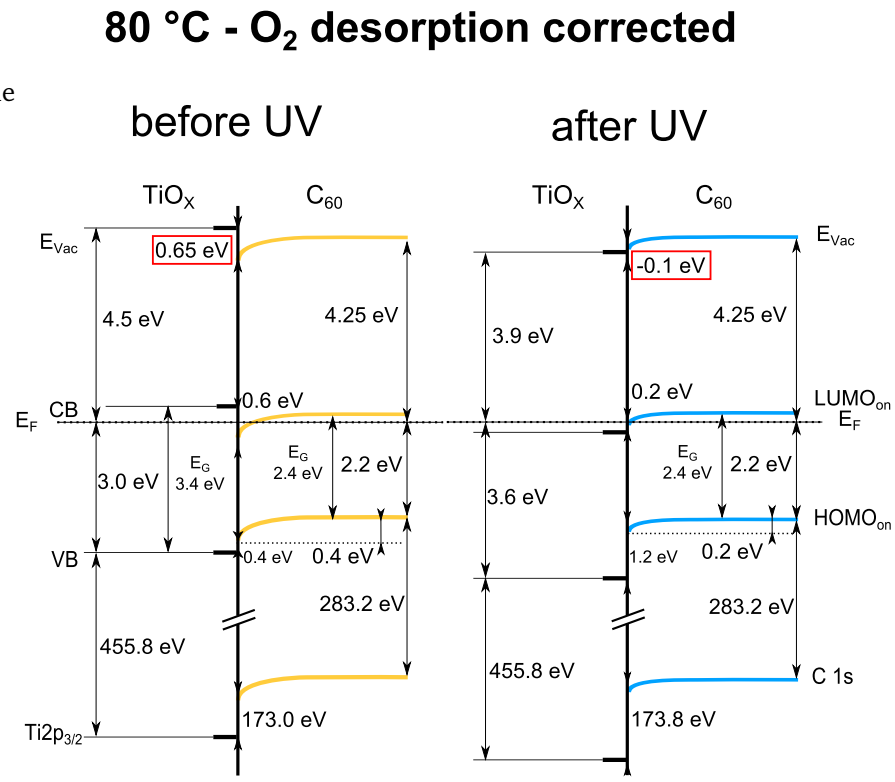

Figure 15.5 – TiO_x/C_{60} energy diagram with an assumed upward shift of the energy levels by 0.4 eV due to adsorbed oxygen species. The oxygen species desorbs under UHV conditions.

15.1.2 Complete AZO/C_{60} energy band line-up

On the left of Fig. 15.6 the energy diagram from the AZO/Co interface experiment derived at Bessy is shown. The LUMO is 0.2 eV above E_{CB} of AZO indicating no extraction barrier for electrons. Compared to results formerly published by Sara Trost and us,[15] the LUMO position is 0.1 eV higher as a C_{60} energy gap of 2.4 eV instead of 2.3 eV is assumed. The surface dipole at the interface is -0.4 eV. Figure 15.6 right shows the AZO/C_{60} energy line-up before and after UV illumination. Included is the Zn $2p_{3/2}$-VBM distance of 1019.1 eV determined in Section 13.2 and the electronic band gap of 3.3 eV determined in Section 13.1.3. In contrast to the TiO_x/C_{60} interface, the C_{60} shows an upward band bending towards the interface instead of a downward band bending. This indicates a charge transfer from the C_{60} to AZO at the interface. The barrier at the AZO/C_{60} interface before UV is -0.5 eV (similar to the Bessy experiment) and -0.8 eV after UV, whereby no electron extraction barrier is observed and in both cases the barrier favors electron extraction. Even the existence of an oxygen caused depletion layer at the surface at ambient pressure of e.g. 0.4 eV (as assumed before), would still not result in an electron extraction barrier before UV illumination. Comparing the interface energy diagrams without UV illumination derived at Bessy and the Daisy-Fun both display an interface dipole of about the same height and no electron extraction barrier. The observed electron extraction favoring nature of the electronic alignment is in good agreement with the I-V characteristics observed for IOSC with AZO as ETL (see Fig. 15.1), where the solar cell devices showed diode like device characteristics before and after UV illumination.

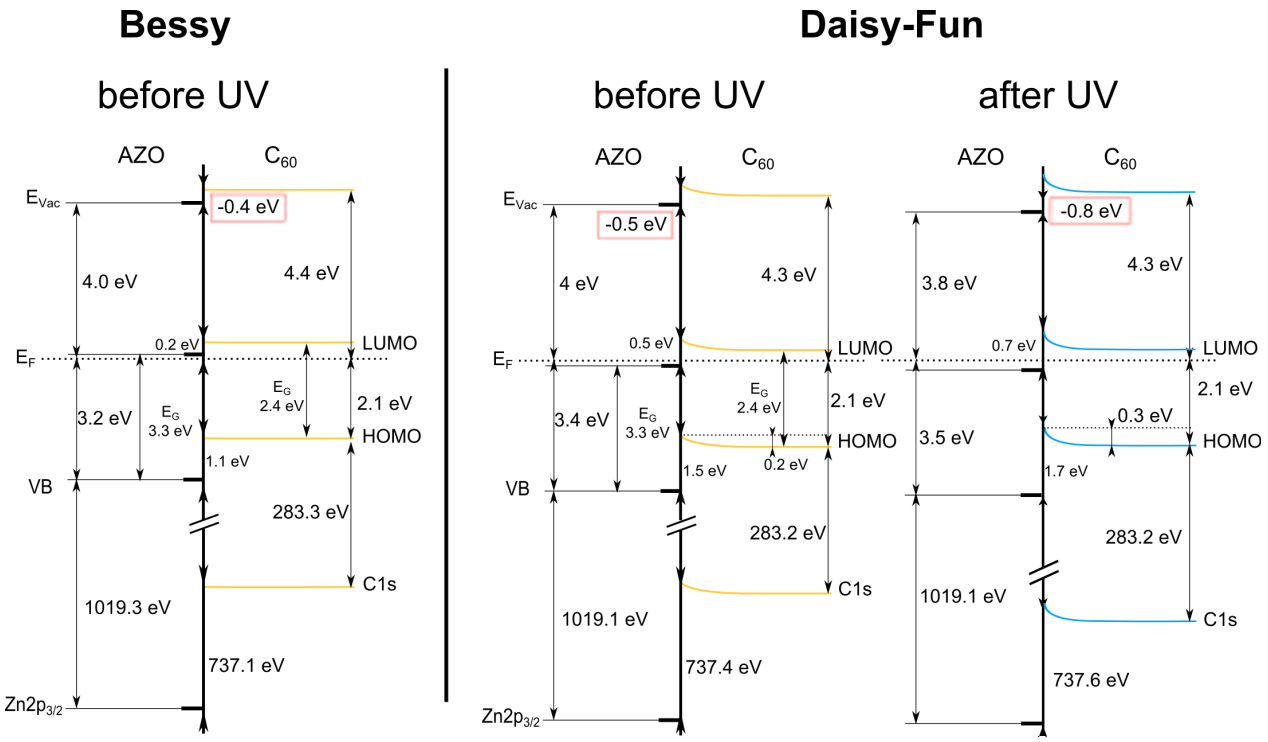

Figure 15.6. – Left: Energy diagram of the ALD AZO/C_{60} interface derived at Bessy without UV illumination. Right: As measured energy diagram of the AZO/C_{60} interface derived from Daisy-Fun experiments. Neither before nor after UV illumination an electron extraction barrier for electrons is observed. Both times the $HOMO_{onset}$ of the C_{60} is above the CB of AZO. Included is the AZO energy gap of 3.3 eV.

16 Summary and Outlook of UV influence on interfaces in organic solar cells

Inverted organic solar cells (IOSCs) are superior compared to conventional organic solar cells in the way that they allow to use more stable electrode and therefore help to improve the stability of organic solar cells against moisture and heat. One drawback of IOSCs is that some cells exhibit only good device characteristics after illumination with UV light, which can damage the organic absorber material. Trost et al. found that the UV dependence of I-V characteristics of IOSC depends on the electron transfer layer (ETL) used in the device stack and that the organic acceptor/ETL interface is most likely to be the origin of S-shaped I-V characteristics. IOSC devices are typically manufactured with $PC_{61}BM$ as organic absorber (which forms the interface to the ETL). $PC_{61}BM$ cannot be evaporated without destruction and therefore is not suitable for interface investigations. Therefore C_{60} was used as model acceptor and it was shown that both, the electronic alignment and the electrical characteristics of C_{60} and $PC_{61}BM$ are comparable. As ETL materials, amorphous ALD prepared TiO_x, crystalline ALD prepared TiO_x, single crystalline anatase and ALD prepared AZO were used. While IOSC devices with TiO_x show a S-shape before UV illumination, devices with AZO or crystalline TiO_x do show good, diode like I-V characteristics before and after UV illumination.

First the 80 °C TiO_x/C_{60} interface was analyzed by performing a XPS interface experiment. Additionally the UV influence on the interface is investigated. Inverted organic solar cells with TiO_x as ETL show S-shaped I-V characteristics before UV irradiation and good diode like I-V characteristics after UV irradiation. At the 80 °C TiO_x/C_{60} interface UV light causes a downward shift of the TiO_x Ti $2p_{3/2}$ core level and an upward shift of the C_{60} C 1s level.

By performing experiments with *in situ* cleaved anatase crystals, the origin of the UV induced change in the energy line-up was measured. While UV light has no influence on the *in situ* anatase/C_{60} interface, the energy levels of the *ex situ* anatase/C_{60} interface show the same tendency of the energetic shifts as UV light on the 80 °C TiO_x/C_{60} interfaces. Furthermore the Ti $2p_{3/2}$-C 1s distance at the *in situ* anatase/C_{60} interface is in the region of the 80 °C TiO_x/C_{60} interface after UV light and the Ti $2p_{3/2}$-C 1s distance at the *ex situ* anatase/C_{60} interface is in the region of the 80 °C TiO_x/C_{60} interface before UV irradiation. That indicates that adsorbates on the titania are responsible for the interface line-up to C_{60}.

Experiments on the anatase (101) surface regarding the influence of UV light and adsorbates show that UV light has no influence on the *in situ* cleaved surface. Exposing the *in situ* cleaved surface to air or cleaving an anatase single crystal *ex situ*, results in downward band bending at the surface of the anatase (101) surface. The irradiation with UV light of the air exposed and *ex situ* cleaved anatase in vacuum increases the band bending at the surface. Exposing an *in situ* cleaved anatase crystal to oxygen

plasma results in an upward band bending of the energy levels at the surface. Experiments on *ex situ* prepared ALD TiO_x samples show corresponding results to the anatase crystal. While UV light induces a downward shift of the energy levels at the surface, exposure to oxygen leads to an upward shift of the energy levels at the surface of TiO_x. From the obtained results a model is derived to explain the UV induced shifts at the TiO_x/C_{60} interface. Oxygen, which is adsorbed as O_2^- at the surface of TiO_x, induces an upward shift of the energy bands at the surface of the TiO_x. Upon irradiation with UV light, oxygen desorbs and the negative charge is transferred to the C_{60} resulting in C_{60}^- at the interface. C_{60}^- induces an interface dipole, which causes an upward shift of the C_{60} energy levels.

In the second part the AZO/C_{60} interface with respect to UV irradiation is investigated. IOSC with AZO show good diode like I-V characteristics even without prior UV illumination. The energy levels at the AZO/C_{60} interface experiences a similar UV influence as the energy levels at the 80 °C TiO_x/C_{60} interface and the C 1s C_{60} energy level undergoes a reduction of the binding energy. Furthermore the AZO Zn $2p_{3/2}$ energy level undergoes a decrease in binding energy. A corresponding interface experiment was also made with the 500 °C TiO_x/C_{60} and shows similar results (see Appendix A.2).

In the last chapter the valence and conduction bands are added to the earlier derived energy diagrams of the 80 °C TiO_x/C_{60} (Section 9.2) interface and the AZO/C_{60} interface (Section 13.2.2). The complete energy diagram of 80 °C TiO_x/C_{60} does not show an electron extraction barrier at the interface before and after UV. Furthermore the position of E_{CB} (right at respectively below E_F) indicates a good conductivity of the 80 °C TiO_x. Therefore the energy diagram cannot explain the S-shape of IOSC with TiO_x as ETL before UV and the removal of the S-shape after UV illumination (see Fig. 15.2). As the IOSC are not prepared in vacuum (preparation takes place in a glove box), oxygen is most likely adsorbed on the TiO_x surface during preparation. This oxygen probably (partly) desorbs in UHV. Assuming that this oxygen is present during the IOSC preparation, an extraction barrier at the TiO_x/C_{60} interface would exist, which is in accordance with the I-V characteristics observed before UV illumination. Then, assuming UV induced oxygen desorption also explains the improvement of I-V characteristics with TiO_x as ETL (see Fig. 15.5). In contrast to the energy diagram derived at the Daisy-Fun, the TiO_x/C_{60} energy diagram derived at Bessy shows an electron extraction even before UV. This is probably due to the different VBM determination. The AZO/C_{60} energy diagram shows no electron extraction barrier for electrons, even if taking the oxygen caused upward band bending at the AZO surface into account and therefore suits well to the observed I-V characteristics, which did not show S-shaped behavior before UV illumination (see Fig. 15.6). In case of the Bessy derived AZO/C_{60} energy diagram, no extraction before UV is observed as well. For the 500 °C TiO_x the energy diagram does not depict an electro extraction barrier, as well, even if oxygen desorption in the vacuum is taken into account (see Fig. A.9). This also agrees with I-V characteristics of IOSC obtained by Kuwabara et al., which show no S-shape with (partly) crystalline TiO_x as ETL.[71]

The interface experiments performed in this work clearly show that UV light induces an energy level line-up shift at the ETL/organic interface to such an extent, that an existing extraction barrier for electrons can be reduced or removed. Still the determination of the energy level line-up at the interface bears some uncertainties. First the energy diagrams were accessed by experiments performed under

UHV conditions, while the relevant interfaces of the respective IOSC devices are prepared under ambient pressure conditions. The interfaces prepared in vacuum do not necessarily represent the interfaces resulting at ambient pressure preparation as for example oxygen desorption from the TiO_x or AZO surface in the vacuum has to be taken into account.[171] Furthermore the dark current voltage curves shown in Fig. 15.4 give indication of an existing counter diode, which could be the reason for the S-shape before UV, as well. Additionally the determination of energy gap of organic semiconductors is difficult as well and especially the position of the transport level of electrons. This results in an uncertainty about the position of the energy level, where electrons are transported (hence about the relevant LUMO position).

In summary this work gives strong evidence that the UV induced removal of an extraction barrier for electrons is causing the removal of the S-shape in the obtained I-V curves, nevertheless the occurrence of a counter diode as reason for the S-shape cannot be excluded. What can be excluded is that an UV induced increased conductivity of TiO_x is the reason for the removal of the S-shape as the TiO_x/AZO bilayer structure in Fig. 7.1 does not show a S-shape.

16.1 Outlook

With their superior properties in many fields organic solar cells enable new applications, which are difficult to access or not accessible with classic inorganic solar cells. Due to their lightness they can be easily used on exterior walls (of a house), their semi transparency in different colors enables the use as coating for windows and as design element for architects and their flexibility permits the use e.g. implemented in tents. As solar cells are used outdoors, this puts high requirements at the stability against humidity and sun. IOSC are superior against humidity compared to conventional OSC, as they allow the use of more stable electrodes. Unfortunately some IOSC exhibit only good I-V characteristics, if they are irradiated with UV light, which degrades the organic absorber. Therefore further research on IOSC and what determines their electronic device characteristics is necessary.

In this work it was shown that UV light induces a shift of the energy levels at the metal oxide/organic interface, if the metal oxide is prepared *ex situ*. As the inverted solar cells are manufactured in the glove box under nitrogen atmosphere and C_{60} is deposited in vacuum, the adsorbates on the metal oxide during deposition of the organic material are different. In order to improve the comparability, the preparation methods and materials can be adjusted. Instead of C_{60}, $PC_{61}BM$ could be deposited in a nitrogen purged glass cell. As deposition methods drop casting or nebulizing could be used. While drop casting does not allow a step by step deposition of $PC_{61}BM$, Julia Maibach showed in her PhD thesis, that nebulizing is a promising method for a step by step deposition of organic materials out of solution, but has still to be developed further.[24]

In regards to the origin of the UV induced shifts, further experiments with varying adsorbates and metal oxides are necessary. In this work *in situ* TiO_2 was exposed to air and oxygen. Further exposure to other adsorbates like water or CO_2 could be performed and the influence regarding C_{60} deposition and UV illumination could be investigated. A variation of the metal oxide, e.g. by using *in situ* cleaved ZnO single crystals, could give further evidences what influences I-V characteristics. As the C_{60} is deposited on the metal oxide is in contact with the adsorbates on the metal oxides, exposure of C_{60}

to various adsorbates would help to understand the origin of interface formation between *ex situ* metal oxides and C_{60}. Furthermore the use of an ambient pressure XPS (APXPS) with different atmospheres would allow to measure directly the influence of adsorbates on the substrate and the interface.

Manufacturing IOSC devices with different metal oxides like e.g. SnO_2 and other fullerenes like e.g. C_{70} and comparing the resulting I-V characteristics with the results of interface experiments, would further help to understand the influence of the energetic interface alignment on the device performance.

By XPS, only the energetic position of occupied states is accessible and hence the conduction band of the metal oxide and the LUMO of the organic acceptor are not directly accessible. Using inverse photoelectron spectroscopy allows to access directly the energetic positions of the unoccupied conduction band of the metal oxide and the LUMO of the organic acceptor.

Part III.

Results and discussion II: Investigation of gap states in TiO_2

17 Synchrotron induced study of gap states in TiO_2

Fs The results of the following chapter Section 17.1 have already been partly published by Philip Reckers, Mariel Dimamay, Joachim Klett, Sara Trost, Kirill Zilberberg, Thomas Riedl, Bruce A. Parkinson, Joachim Brötz, Wolfram Jaegermann, and Thomas Mayer in the Journal of Physical Chemistry C (2015).[136]

The role of electronic states in the TiO_2 energy gap concerning charge transport and catalytic activity e.g. in water dissociation, their energetic, and geometric distribution and their chemical nature is under much discussion.[15,224,225] In nanoporous anatase TiO_2 films the electron mobility is much smaller than in single crystalline anatase TiO_2,[226,227] which has been attributed to electrons spending a large part of their transit time in traps.[228,229] On the other hand gap states have been suggested to promote the transport of photo generated holes from the Si valence band through the amorphous ALD titania protection layer for water oxidation.[230] Various methods have been used for the determination of the chemical nature, the energetic distribution, and the location of gap states in anatase as well as in rutile or amorphous TiO_2. Bisquert and many others focused on electrochemical methods as cyclic-voltammetry, impedance spectroscopy, and voltage decay charge extraction.[231,232] There is clear evidence from STM,[16] theory,[144,233] and photoemission,[84,234] that deep gap states (DGS) in anatase and rutile form at the surface, due to occupied Ti^{3+} states between bridging oxygen vacancies. In both polymorphs, DGS due to oxygen vacancies are found around 1 eV below the conduction band edge.[16,84,85,235] Some evidence was given that interstitial Ti atoms on rutile (110) may induce gap states in this energy region as well.[212] In contrast to the Gaussian distribution of DGS separated from the conduction band by 1 eV usually an exponential tail of states below the conduction band is used for modeling charge transport.[231,232] On nanocrystalline anatase additional shallow gap states (SGS) were observed by UPS starting at around 0.5 eV binding energy and reaching up to the Fermi level ($E_{Bin} = 0$).[143,224] Due to usually strong non-intentional n-doping in TiO_2 the Fermi level is near the conduction band. So far the origin of SGS in nc-TiO_2 remained unclear. One interpretation was that a Ti_2O_3 layer has formed at the surface,[236] which at room temperature shows a Mott transition to metallic conductivity.[237] In addition it was shown that the solvent acetonitrile, which is used in dye-sensitized solar cells (DSSC) and gives highest energy conversion efficiency, strongly quenches deep gap states while SGS are little affected. It was suggested that DGS play a detrimental role in recombination and that the SGS have a beneficial role in charge injection in DSSC.[143,236] Using quantum mechanical calculations it has been shown that the density of states inherently induced by under coordinated Ti sites at intersections of the anatase (101) surfaces of the 3D crystallites extend below the conduction band into the energy gap.[78]

17.1 Identification of gap states in different titania samples

In Section 8.1 and Section 8.2 different titania samples were characterized by AFM, XRD/Laue diffraction and XPS. In this section the valence band and band gap region has been studied in detail, focusing on the appearance of gap states in amorphous ALD prepared TiO_x (substrate temperature 80 °C), at 500 °C at air post annealed ALD prepared TiO_x, nanocrystalline TiO_2 and cleaved anatase sc-(101) surface. Up to this work PES results were only published of surfaces prepared by sputter anneal cycling. The preparation of clean anatase single crystal surfaces under UHV conditions by sputter anneal cycling is e.g. facing the problem of iron segregation at the surface or a roughening of the TiO_2 surface.[238] Therefore a new method for *in situ* anatase preparation was developed in this work. The natural grown single crystal was cleaved *in situ* with pliers and by this a clean anatase surface was obtained under UHV conditions without any post treatment like sputtering and annealing. For details of the preparation process see Section 4.1.

Figure 17.1 shows various valence band (left) and band gap spectra (right) of *in situ* and *ex situ* anatase sc-(101) surfaces (spectra 1-14), nanocrystalline TiO_2 out of slurry (15), ALD prepared 500 °C annealed TiO_x (16) and as deposited 80 °C ALD TiO_x (17). Some cleavage surfaces had residues of carbon on the surfaces. The structure of the valence band varies at the different cleavage surfaces. In the band gap region two different band gap emission are observed, deep gap states (DGS) at around 1.2 eV and shallow gap states (SGS) arising just below E_F and extending to about 0.6 eV binding energy. Sample 1 displays only SGS (see Fig. 17.8 spectrum B), while sample 17 displays only DGS (see Fig. 17.2 spectrum D). All other samples display DGS and SGS emissions.

17.1.1 Valence band and gap state analysis of different titania samples

In Fig. 17.2 VB spectra of an *in situ* cleaved anatase sc-(101) (A), a nanocrystalline anatase film (B), an ALD film prepared at 80 °C substrate temperature (C) and post annealed film at 500 °C are displayed (D). All spectra were recorded with an excitation energy of 90 eV.

The VB spectrum of the *in situ* cleaved sc-(101) surface has a width of 5 eV and extends from about 4 eV to 9 eV binding energy. Both shape and width of the mostly O 2p derived valence band states are in good agreement with spectra recorded on a (1x1) reconstructed surface cleaned by sputter anneal cycles.[85] The (1x1) structure of the cleaved single crystal was also measured on a different crystal, cleaved in the same way (see Section 8.1). The onset of the main valence band emission (VBM) is found at 3.4 eV, which is larger than the optical energy gap of 3.2 eV.[239] Due to the *in situ* cleavage of the single crystal, adsorbate induced band bending at the surface is not expected as the reason for the observed VBM position. René Pekkola showed in his PhD thesis, that the relative intensity of the small onset emission above the main onset becomes more pronounced when photons of several hundred eV are used.[25] Therefore this onset is defined as the main VBM position intersecting with the background intensity at 3.0 eV binding energy. A similar method of VBM determination of clean anatase (101) at 47 eV excitation energy was already used by Kumarasinghe et al.[218] The corresponding CBM is still close to the Fermi level position, which can be caused by n-doping of the natural crystal due to an oxygen deficiency and contaminations like sodium, silicon or potassium, which are typically found in

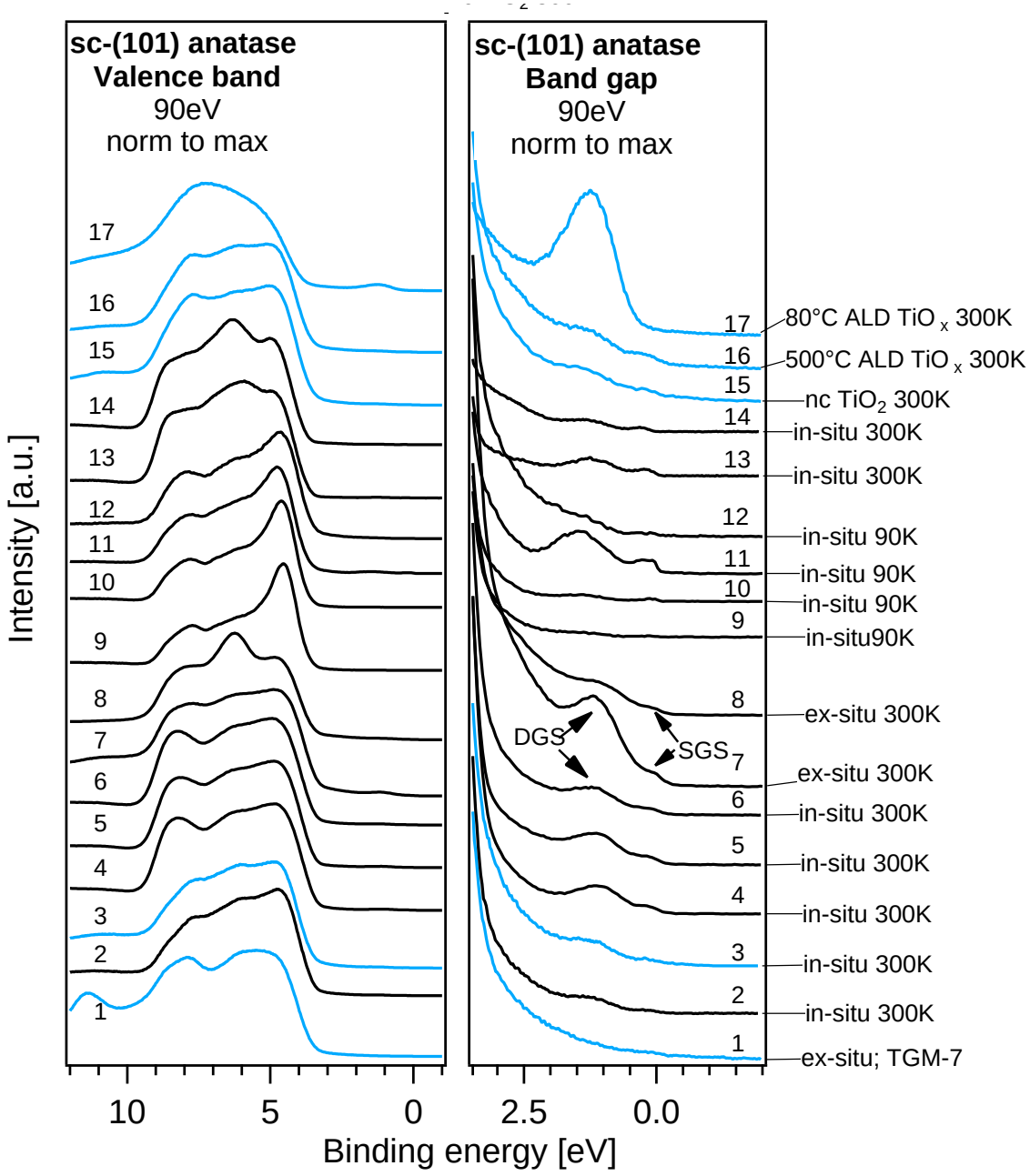

Figure 17.1. – Different valence band (left) and band gap (right) spectra of *in situ* and *ex situ* cleaved anatase sc-(101) surfaces compared to thin film TiO_2 prepared under different conditions. Spectrum **1** was recorded at the beamline TGM-7. All other spectra were recorded at the beamline U49-2/PGM-2. Spectrum **15** is nanocrystalline TiO_2 out of a slurry, **16** is ALD prepared at 80 °C and **17** is ALD prepared and annealed to 500 °C. Spectra were taken at 300 K and 90 K as indicated. All blue spectra are discussed later in more detail.

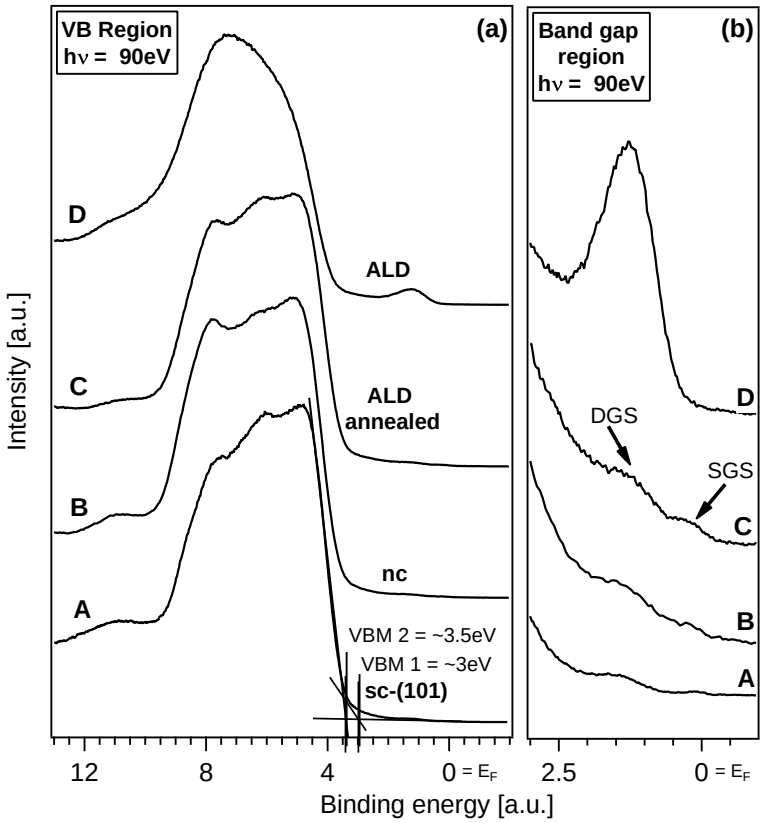

Figure 17.2. – Valence band region (a) and band gap (b) spectra of D: ALD prepared amorphous TiO_x; C: 500 °C post annealed ALD TiO_x; B: nanocrystalline anatase out of a slurry and A: *in situ* cleaved anatase sc-(101) surface. Depending on the method of the VBM determination, the VBM is between 3 and 3.5 eV. Amorphous ALD TiO_x shows only DGS emission. All other titania show DGS and SGS emission.

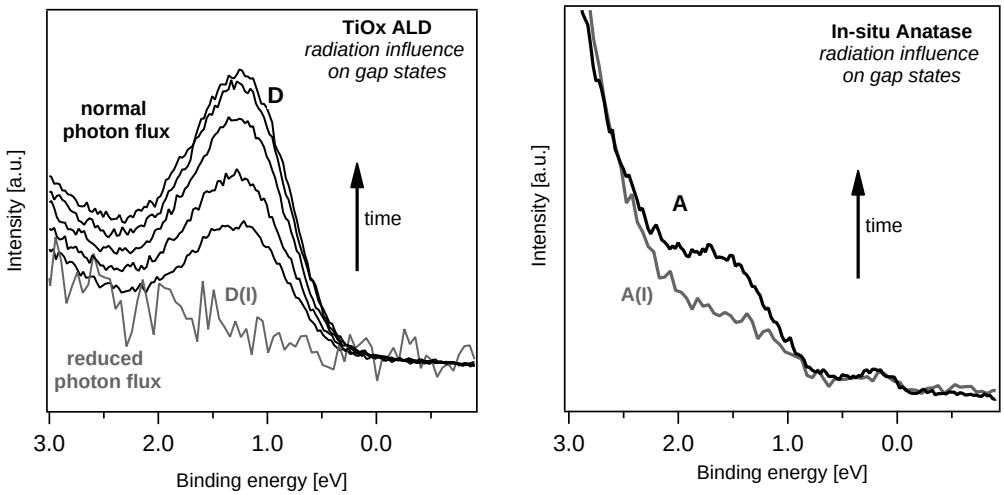

Figure 17.3. – Left: Amorphous ALD TiO_x spectra affected by synchrotron radiation. The gray spectra (D(I)) is recorded with a reduced photon flux and increased step width. Black spectra (D) are recorded with standard source conditions. Initially no DGS are observed and they increase drastically with synchrotron irradiation. Right: Influence on the *in situ* cleaved sc-(101) surface. DGS increase with synchrotron irradiation time, while SGS seem not to increase.

naturally grown anatase single crystals.[139] A survey scan of the single crystal ranging from 550 eV to -2 eV did not reveal any emission of species besides Ti and O and hence contaminations are not existent or below the detection level of PES (which is in the range of 1 vol %). In Fig. 17.2 B and C the valence band spectra of the nanocrystalline and post annealed ALD TiO_x are displayed. Both are very similar to the single crystal anatase spectra, which suggest a complete transformation of the amorphous, 40 nm thick, ALD film to anatase after annealing. This is in contrast to the partial transformation evidenced by XRD on a 150 nm thick film. The reason could be a complete transformation of the 40 nm film or the presence of an amorphous phase deeper in the layer of the 150 nm film, which cannot be detected by the surface sensitive method of photoemission.

In Fig. 17.2b) a magnification of the band gap region of the four titania samples is displayed. The amorphous as prepared ALD TiO_x sample (D) shows a strong emission from deep gap states (DGS) around 1.2 eV binding. The in air annealed ALD TiO_x shows much smaller DGS emission, but additionally an emission of shallow gap states (SGS), which arises just below E_F and extends to about 0.6 eV binding energy. The nanocrystalline sample (B) and the anatase single crystal (A) show similar gap state emissions of DGS and SGS as the post annealed ALD sample. On all *ex situ* samples (80 °C ALD, 500 °C ALD and nc-anatase) the increase of the O 2p derived valence band is less compared to the *in situ* cleaved anatase crystal.

All PES spectra of the four investigated titania samples show an increase of the DGS emission with exposure time to synchrotron radiation as shown for non-annealed ALD titania (Fig. 17.3 left) and the sc-(101) cleavage plane (Fig. 17.3 right). In contrast the SGS emission of the sc-(101) surface is not or only slightly increasing upon synchrotron irradiation (see Fig. 17.3 right). Apparently the origin of the DGS emission does increase with synchrotron exposure, while the origin of SGS does not. The light gray spectra in Fig. 17.3 D(1) and A(1) represent initial spectra, where the influence of synchrotron irradiation was kept to a minimum. D(I) (Fig. 17.3 left) has been taken at the TGM-7 beamline with increased step

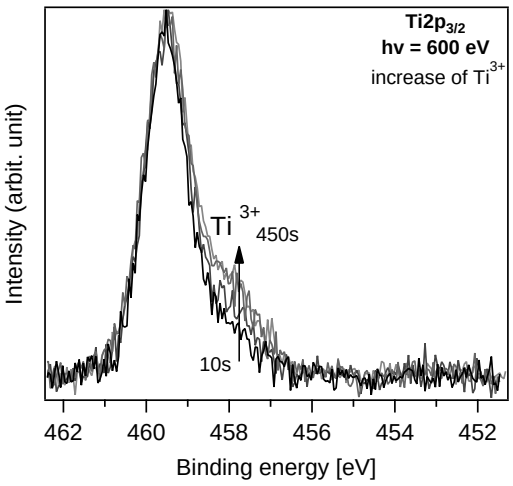

Figure 17.4. – Ti^{3+} increase of an as deposited ALD prepared TiO_x sample upon synchrotron irradiation. All spectra were recorded under same source conditions. First spectrum (black) was recorded after about 10 s irradiation time. The measurement was performed on a different sample, than displayed in Fig. 17.3 left.

width and reduced photon flux, while the other, exposure time dependent spectra, have then been taken with a smaller step width and the standard photon flux. With exposure to synchrotron light the DGS emission first grows fast till its intensity saturates after 3000 s of synchrotron radiation (spectrum D). Along with the DGS emission, the Ti^{3+} emission of the Ti $2p_{3/2}$ core level line increases as well (Fig. 17.4). Hence the DGS emission of the amorphous ALD titania layer can be assigned to occupied Ti 3d orbitals of TiO_x due to missing oxygen as shown for crystalline anatase.[85] The results are in contrast to the interpretation of the results in Section 11.2, where it was assumed that oxygen vacancies are always present at the surface and not induced by electromagnetic radiation. One interpretation of the results in this chapter and Section 11.2 is that oxygen vacancies at the surface of ALD prepared TiO_x are present, but adsorbed oxygen from the atmosphere is disguising the vacancies. Synchrotron radiation then causes the desorption of the attached oxygen. At 0 eV ($=E_F$) and up to 0.5 eV below no emission is observed and no SGS are observed.

The *in situ* cleaved sc-(101) surface shows initially already a SGS emission, while the DGS emission is comparably low (see Fig. 17.3). The first spectrum in Fig. 17.3 right, A(I), was recorded with standard exposure conditions. To reach the binding energy region of the gap state region, the crystal was exposed to synchrotron radiation for about 30 s. After an additional synchrotron exposure time of 30 s the DGS intensity is strongly increased (see spectrum A). Thus the DGS emission in the initial spectrum A(I) is already influenced by the measurement and the initial DGS density of the cleaved sc-(101) surface may be zero or close to zero before the exposure to synchrotron radiation. The DGS emission of the sc-(101) surface is also very low compared to surfaces prepared by sputter anneal cycling.[85] STM measurements on sputter annealed sc-(101) surface did not show V_O at the surface.[240,241] *In situ* cleavage also avoids additional pitfalls of clean surface preparation, as e.g. surface segregation of contaminations present in natural crystals.[238] The increase of DGS on sc and nc anatase is generally attributed to oxygen vacancies caused by beam damage due to the synchrotron radiation.[86] Summarizing it is observed that SGS emission of the sc-(101) surface is not or only slightly increasing with synchrotron irradiation time, while DGS are strongly influenced by synchrotron light on amorphous and crystalline TiO_2. SGS

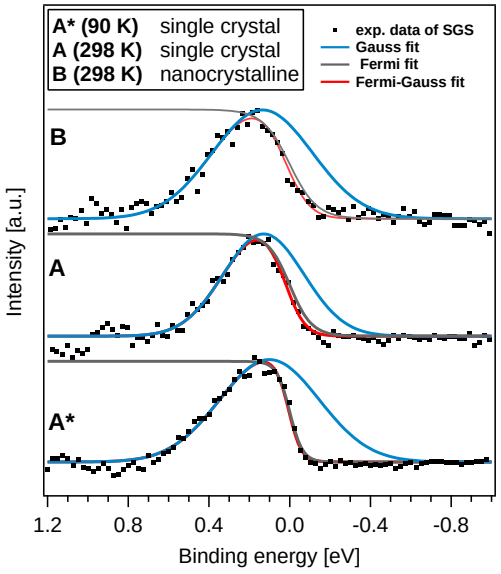

Figure 17.5 – Fit of the SGS emission (black dots) of the *in situ* cleaved sc-(101) surface at 90 K sample temperature (A*), at 298 K (A) and a nc-TiO_2 at 298 K. Spectra were subtracted by a polynomial background and a Gaussian fit of the DGS (see Fig. 17.6). The Fermi-Gauss fit (red) is composed of a Gaussian fit (blue) of the SGS emission and Fermi fit (gray) of the Fermi-edge. The $fwhm_F$ of the Gaussian like derivative of the Fermi part in the fits are 0.18, 0.23 and 0.27 eV for A*, A and B spectra.

are present only on crystalline anatase, be it the single crystal (101) cleavage plane or nanocrystalline anatase (also 500 °C post annealed anatase), while SGS occur not on amorphous ALD titania and cannot be induced by the photoemission light source.

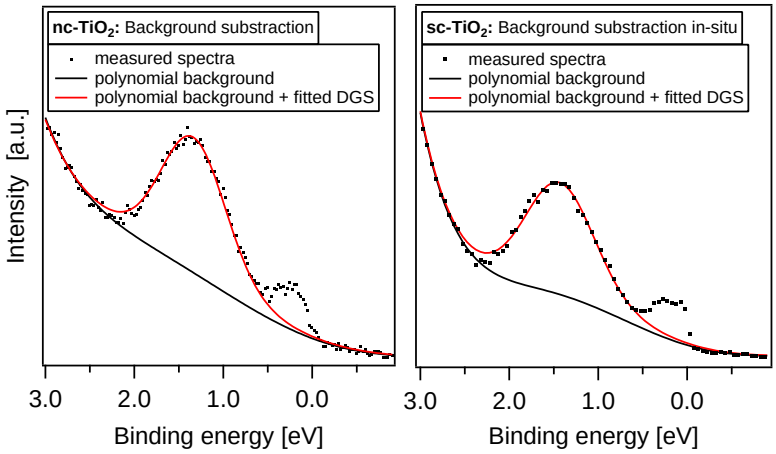

Figure 17.6. – Background treatment of the nc-TiO_2 (left) and the sc-(101) anatase band gap region (right). Background was subtracted by a polynomial fit. DGS were subtracted by a Gaussian-Lorentzian fit.

In addition to the performed experiments at room temperature, the *in situ* cleaved sc-(101) surface was also measured at 90 K temperature. In Fig. 17.5 the SGS emissions of sc-(101) taken at 90 K (A*) and at room temperature (RT) (A), and for nc anatase at RT (B) are displayed for further analysis. To facilitate a comparison of the SGS emission of the three measurements, DGS emission and secondary electron background have been subtracted from the experimental spectra by a Gaussian peak and a polynomial base line, respectively, thus the SGS emission is only left. The respective spectra of the background removal are shown in Fig. 17.6. The SGS emission is fitted using a Gaussian peak line multiplied by the Fermi distribution of state occupation. The maximum of the Gaussian is at around 0.13 eV binding energy and its $fwhm_G$ is 0.47 eV and 0.58 eV for the single crystal and nanocrystalline film respectively. The $fwhm_F$ of the Gaussian like derivative of the Fermi edge fit broadens for the single

crystal from 0.17 eV at 90 K to 0.23 eV at 300 K. This $fwhm_F$ is composed (square root of sum of squares) of thermal broadening and overall photoemission resolution of around 0.1 eV. The mathematical fitting treatment and the fit parameters are given in the appendix in equation Eq. (1.3) and table Table B.1. The temperature dependence of the low energy onset clearly demonstrates that the occupied SGS DOS and thus its appearance in the spectra is limited by a Fermi edge. The Gaussian part in the SGS fit is weakened as only the occupied part of the DOS appears in photoemission and the signal to noise ratio is low. Therefore it is not claimed that the fitted Gaussian distribution is the actual DOS of the SGS states, but merely is an approximation in accord to our measurements. The high binding energy part was modeled using an exponential tail as a trial function as well, but the resulting fit had less compliance, than the modeled Gaussian distribution.

17.1.2 Discussion: Gap states of different titania samples

As the SGS emission appears on the cleaved anatase (101) surface, it is excluded that another titania phase can be the cause for SGS. Furthermore SGS are not present on amorphous titania and neither can be induced on it. As they only appear on crystalline anatase, it appears reasonable to conclude that crystallinity is a precondition for the appearance of SGS emission. While on the sputter annealed anatase (001), occupied states just below the conduction band were assigned to small polaron formation,[190] Setvín et al. showed by DFT calculations, that this is not favorable in a perfect anatase lattice, neither in the bulk nor on the (101) surface plane.[86] Furthermore Setvín et al. showed that Nb dopants can induce the formation of excess electrons at shallow donor states.[86] In photoemission the cleaved surface appears clean. Hence certainly present dopants in the natural crystal can be excluded as the cause for SGS emission with a high certainty. A scanning tunneling spectroscopy (STS) study on a sputter annealed anatase (101) surface by Setvín el al. found occupied states just below E_F. They attributed the excess electrons to step edges at the trapezoidal shaped terraces of the surfaces.[86] Nunzi et al. performed DFT calculations of anatase nanocrystals and showed a Gaussian like distribution extending below the conduction band, which is formed by 4 folded Ti edge sites at the intersection of the (101) planes of nc-TiO_2. As the cleavage plane is non-ideal, terrace edges on the (101) cleavage plane in AFM are observed (see Fig. 8.4). Probably there are additional edges of smaller height and possibly step edges below the resolution of the used AFM. The step edges on anatase (101) are autocompensated as is the (101) surface, meaning that for each Ti-O bond a O-Ti bond is broken during cleavage of the crystal.[80] Ti atoms at step edges on the anatase (101) surface are 4 fold coordinated[82] similar to Ti atoms at the intersections of the (101) planes in anatase (nano)crystals, where they form a density of states with a maximum in the conduction band and a tail extending into the energy gap.[78] As the anatase crystals naturally are strongly n-doped the Fermi level in the samples is close to the conduction band minimum. In thermodynamic equilibrium with the n-doped bulk, the part of the DOS-tail at under-coordinated Ti edge sites below the Fermi level becomes occupied. Thus it is assumed that the charge in the Ti 3d shallow gap states observed in PES stems from trapped electrons from the n-doped bulk and not from missing oxygen as in the case of oxygen vacancies on the terraces. The trapped charges at step edges are clearly shown by STM/STS measurements by Setvín et al.[86]

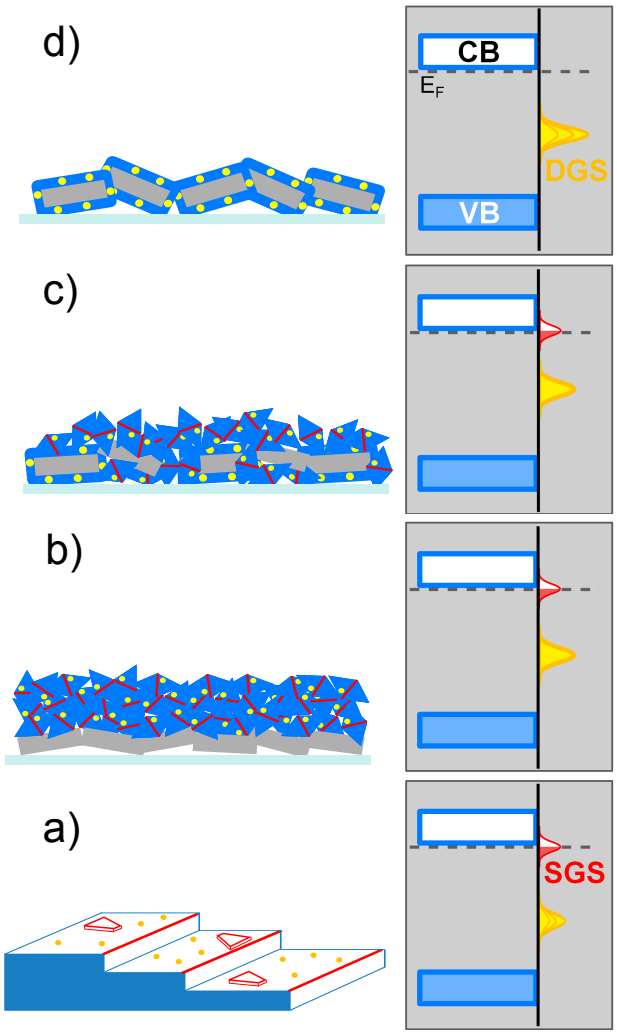

Figure 17.7 – Model of band gap emissions and morphology of the investigated titania samples. a) *in situ* cleaved sc-(101) anatase has one dimensional structures of edge sites (red) at possibly present step edges of trapezoid shaped terraces (red) and oxygen vacancies (point defect) induced by synchrotron radiation. Edge site are mirrored by SGS photoemission right at E_F (SGS) and oxygen vacancies by DGS emission (yellow). b) Nanocrystalline anatase (blue) on crystalline ITO substrate (gray). The intersection of the (101) planes are red and oxygen vacancies (DGS) on the (101) planes are yellow. c) Nanocrystals formed from a low temperature ALD film by annealing. It has similar edge composition and gap state emission as the nc-film b). d) Amorphous ALD film conformal covering ITO crystallites. It shows only DGS emission, which is induced by the irradiation used for photoemission.

17.1.3 Summary and conclusion: Gap states of different titania samples

The UHV cleaved anatase single crystals (101) surface, nanocrystalline sintered slurry, low temperature ALD titania, and annealed ALD films have been investigated with X-ray Diffraction (XRD), atomic force microscopy (AFM), and synchrotron induced photoelectron spectroscopy (PES). No further preparation treatment as e.g. sputter anneal cycling, generally used in anatase (101) surface preparation for photoemission, was applied. Laue diffraction clearly identifies the (101) orientation of the cleavage plane. The ALD films are amorphous before and crystallized to the anatase structure after annealing (XRD and AFM). The cleavage plane shows terraces of typically 8 nm height, but smaller steps and additional step edges cannot be excluded. The (101) surface is the most probable face exposed on nc films.[242] On nano- and single crystalline samples two PES gap state emissions are found. Deep gap state emission (DGS) is situated at around 1.2 eV and shallow gap state emission (SGS) just below (about 0.6 eV) and up to the Fermi level. On the cleavage plane the DGS emission initially is very low but increases with exposure time to synchrotron radiation and may be zero before exposure. Amorphous ALD films initially show very low DGS emission intensity and it may be zero before exposure to synchrotron

radiation. As presumed in Section 11.2, oxygen vacancies and therefore DGS, are most likely present in the bulk and on the surface of the ALD prepared amorphous TiO_x. Hence this is in contradiction with those results and the absence of the DGS emission on the ALD sample could be due to a passivation of the surface defects with adsorbates at ambient pressure. The adsorbates may desorb under the influence of synchrotron and XPS radiation. DGS formation due to hydroxyls[213] on the anatase (101) surface can be excluded at least for the anatase single crystal cleaved *in situ*, therefore no water, which could possibly be dissociated by the synchrotron radiation, is present on the anatase (101) cleavage plane. For the *ex situ* prepared nc-anatase and the amorphous ALD titania the presence of water cannot be excluded. But the correlation of DGS emission and oxygen defect density in literature is strong.[86,243–245] SGS emission is found on the single crystal cleavage plane and on nanocrystalline samples with stable intensity with respect to synchrotron light exposure. No SGS emission is found on the amorphous layer and it cannot be induced by exposure to synchrotron radiation. The valence band spectra of annealed ALD titania appear very similar to the spectra of sintered nanocrystalline anatase slurry. Also the gap state spectra are similar as both show DGS and SGS emission. The line shape of the SGS emission can be modeled by a Gaussian emission peak (with a maximum at around 0.13 eV binding energy and about 0.6 eV *fwhm*) multiplied by the Fermi distribution of temperature dependent width. As only the occupied part of the DOS is available to PES and the signal to noise ratio is low, there is some ambiguity concerning intensity and position of the Gaussian part in the fit. The low energy onset of the SGS emission is clearly dominated by the Fermi distribution, indicating that the SGS emission represents the occupied part of a DOS peak spreading across the Fermi edge. Such a DOS could also explain the scanning tunneling spectroscopy (STS) extraction current on step edges in this energy range and the additional step edge STS injection current observed in Ref. [86]. Figure 17.7 displays in a simple picture the experimental results. We assumed that the SGS emission results from one dimensional structures of under coordinated Ti sites at edges and the DGS emission is due to point like oxygen defects. In Fig. 17.7a) the anatase (101) cleavage plane (white) is sketched with edge sites (red) at terraces due to off angle cleavage and possibly present trapezoid shaped terraces with step edges related to SGS emission (red). Point like oxygen defects (yellow) related to DGS emission (yellow) are induced by exposure time dependent radiation. In Fig. 17.7b) the nanocrystalline anatase (blue) film formed from sintered slurry is sketched on the ITO (gray) substrate with intersections of crystallite surfaces (red) and oxygen point defects (yellow) related to SGS emission (red). In Fig. 17.7d) the amorphous ALD film conformal covering the ITO substrate crystallites is displayed with oxygen point defects induced by exposure to synchrotron light giving rise to DGS emission. In Fig. 17.7c) the post annealed ALD film is sketched with anatase particles covering the ITO substrate crystallites and oxygen point defects (yellow) and edges at crystallite surface intersections (red) giving rise to DGS (yellow) and SGS (red) emission.

17.2 Resonant photoemission of titania gap states

In the previous section, as prepared ALD TiO_x, post annealed TiO_x, nc-TiO_2 and sc-(101) surfaces were investigated by photoemission and the existence of SGS in some crystalline anatase materials was shown. A powerful method to investigate valence band structures and gap states is resonant photoemission. In RESPES (an introduction is given in Section 5.1.6), the photon energy is scanned over a photon absorption edge and the intensity of the photoelectron emission is measured in dependence of the photon

energy. By this, the relative emission intensity of valence band features de- or increases. In the case of titania, two different transitions can be excited: The Ti 3p→Ti 3d/4 sp transition is excited by photon energies above the binding energy of the Ti 3p level, which is ∼36 eV E_{Bin} (see Fig. 3.4 for the molecular orbital diagram of anatase).[84] The second transition is the Ti 2p→Ti 3d/4sp transition. As the Ti $2p_{3/2}$ binding energy is ∼460 eV, photon energies have to be above 460 eV to excite the Ti 2p→Ti 3d/4sp transition. Due to the spin orbit coupling, a second resonance due to the Ti $2p_{1/2}$ emission is expected at around 466 eV binding energy (Ti $2p_{3/2}$-Ti $2p_{1/2}$ distance is 5.7 eV).[246] As the hybridization of oxygen and titanium in TiO_2 is strong, not only 3d related orbitals resonate, but also the O 2p core level and the O 2p derived valence band.[84,235]

Several articles involving RESPES of the different TiO_2 polymorphs and surface planes have been published so far, but mainly focused on surfaces prepared with sputter and annealing steps. RESPES on rutile (110), anatase (101) and anatase (001) showed a clear Ti 3p→3d resonance of DGS states.[84,85] Thus the occupied deep gap states are clearly of Ti 3d orbital nature. As the DGS emission, the SGS emission has been shown to resonate with the Ti 3p→3d transition evidencing the Ti 3d orbital nature of the SGS also.[143]

In this chapter *ex situ* and *in situ* cleaved sc-(101) surfaces, and nanocrystalline and amorphous TiO_x are compared. A special focus is put on the resonant behavior of SGS. Investigations of the Ti 3p→Ti 3d/4 sp transition have been performed at the TGM-7 beamline at BESSY II, which is a source for photon energies between 30 and 120 eV. The Ti 2p→Ti 3d/4 sp transition was investigated at the U49/2-PGM-2 beamline, which provides photons between 90 and 1600 eV. In Fig. 17.8 the band gap region of amorphous ALD TiO_x (D), nc-TiO_2 (C), an *ex situ* cleaved sc-(101) surface and an *in situ* cleaved sc-(101) surface are displayed. On the left are spectra measured at 90 eV excitation energy and on the right are spectra measured *in resonance*. The upper three spectra are probed by the Ti 3p→Ti 3d/Ti4 sp resonance and the lowest spectra by the Ti 2p→Ti 3d/Ti 4sp resonance, which is indicated by the excitation energies of 45.5 eV (Ti 3p→Ti 3d/Ti 4sp) and 467 eV (Ti 2p→Ti 3d/Ti 4sp). As already shown in Section 17.1, the amorphous TiO_x (D) shows only DGS emission. In resonance, this DGS emission is strongly enhanced. The nc-TiO_2 (C) shows DGS and SGS emission at 90 eV photon energy. In resonance both emissions become more pronounced. The *ex situ* cleaved sc-(101) (B) surface shows no emission, neither DGS nor SGS, in the band gap region at 90 eV excitation energy. In resonance an emission of SGS is observed right at E_F. The absence of DGS in spectrum B could by due to the *ex situ* cleavage and adsorbates on the surface which are quenching the DGS emission, or because DGS on the *in situ* cleaved crystal are synchrotron induced as already indicated in Fig. 17.3. The *ex situ* cleaved crystal (spectrum B) was recorded at the beamline TGM-7, while all other sc-(101) surfaces (including spectrum A and the spectra in Fig. 17.3) were measured at the beamline U49-2/PGM-2. The photon flux at the U49-2/PGM-2 can be approximated as a data sheet is available.[106] As discussed in Section 17.1 and shown in Fig. 17.3 synchrotron induced V_O formation takes place. No information about the photon flux density at the TGM-7 is available, hence a comparison of both photon fluxes is not possible. In general is can be assumed that the photon flux density at a dipole beamline is lower, than on an undulator beamline (as the U49-2/PGM-2). The *in situ* cleaved anatase sc-(101) surface (A) shows DGS and SGS at 90 eV photon energy. The resonance spectrum was recorded at 467 eV (Ti 2p→Ti 3d/Ti 4sp transition) and shows strong emission of SGS and if at all, only a weak emission of DGS. The low intensity of the DGS emission

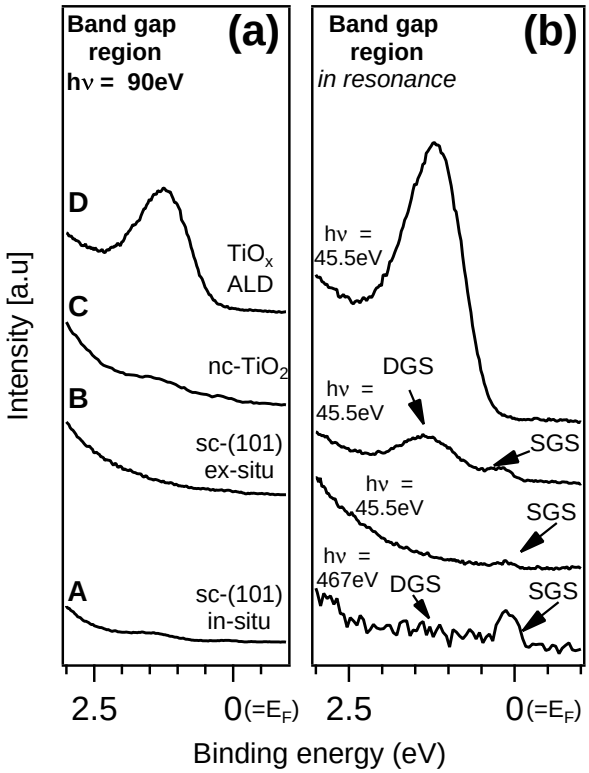

Figure 17.8 – Band gap region of ALD prepared TiO_x (D), nanocrystalline TiO_2 (C), *ex situ* cleaved sc-(101) surface (B) and the *in situ* cleaved sc-(101) surface (A). On the left (a) spectra are recorded at 90 eV. TiO_x ALD shows only DGS, nc-TiO_2 and *in situ* sc-(101) show DGS and SGS and *ex situ* TiO_2 shows no band gap emission. On the right, spectra measured *in resonance* are shown. DGS emission of ALD TiO_x and DGS and SGS of nc-TiO_2 are strongly enhanced in intensity. The *ex situ* cleaved surface shows SGS now. The *in situ* cleaved (101) surface shows strong emission from SGS and only a small emission of DGS at 467 eV photon energy (Ti 2p→3d transition).

for the specified excitation energy is related to the fact that DGS and SGS do not resonate at the same excitation energy. While the amplification of the SGS is high at 467 eV, the DGS amplitude is attenuated at 467 eV photon energy. The different resonant behavior of DGS and SGS is shown and discussed in Section 17.2.3.

The post annealed ALD TiO_x showed a similar behavior as the nc-TiO_2 (see appendix Fig. B.1) and is not further discussed.

17.2.1 Results and discussion: RESPES on amorphous TiO_x, nc-TiO_2 and sc-(101) surfaces

RESPES of amorphous TiO_x ALD 80 °C

Figure 17.9 left shows Ti 3p→Ti 3d/Ti 4sp resonance of the valence band region of amorphous as prepared ALD titania. The excitation energy was varied between 40 and 70 eV. For the sake of clarity, not all measured spectra are displayed in Fig. 17.9 left. On the right of Fig. 17.9 constant initial state (CIS) spectra derived from the valence band spectra at different binding energy positions are displayed. For the CIS profiles all available data points are used (even if not displayed as photoemission spectrum). For the DGS CIS spectrum a fitted Fano profile (red) is added. w describes the line width of the resonant energy and q the asymmetry of the Fano profile.

The VB region spectra on the left of Fig. 17.9 clearly show strong DGS emission at around 1 eV E_{Bin}. The CIS spectra of the DGS emission (black squares in Fig. 17.9 right) show the photon energy dependent intensity of DGS emission. To determine the DGS intensity a polynomial background (see Fig. 17.6) is subtracted from the band gap region of the original spectrum and the area of the DGS emission is integrated. The CIS spectrum of the DGS emission is highest at ~45 eV. Between 50 and 60 eV a little bump is apparent. As shown before, the O 2p derived VB of the amorphous TiO_x has not such clear

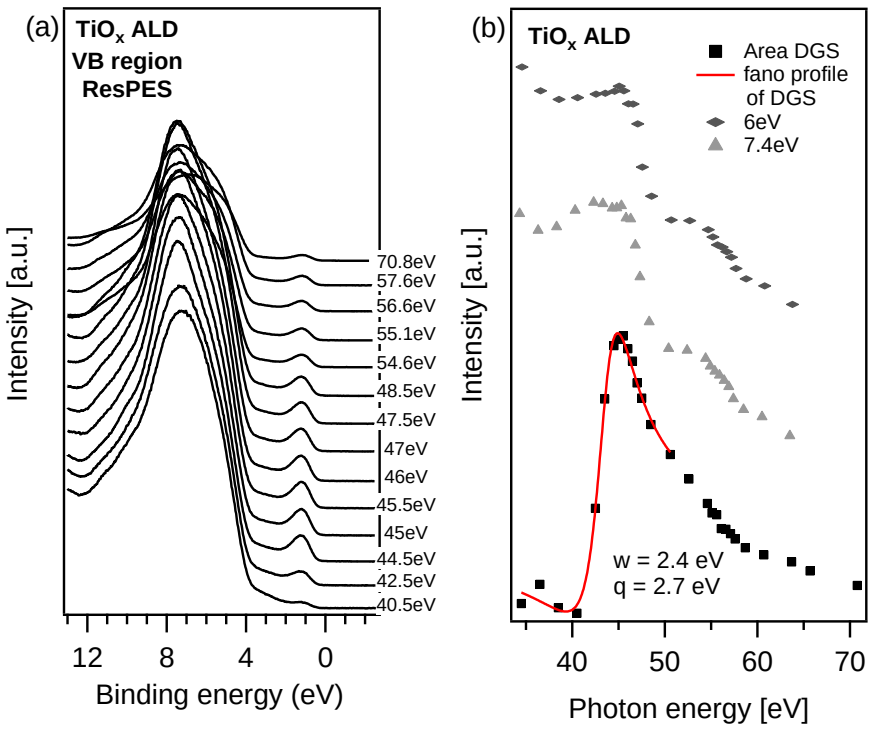

Figure 17.9. – (a): VB region spectra for photon energies between 40 and 70 eV. For the sake of clarity not all measured spectra are displayed. (b): CIS spectra of DGS, at 6 eV E_{Bin} and at 7.4 eV E_{Bin}. DGS have a maximum intensity at 45 eV, the intensities at 6 eV and 7.4 eV E_{Bin} have a maximum at 46.5 eV. A Fano profile (red) is added for the DGS CIS spectrum, where w describes the line width of the resonant energy and q the asymmetry of the Fano profile.

features as crystalline TiO_2. The CIS spectra of the VB have been taken at 6 eV and 7.4 eV binding energy, where crystalline samples show distinct features. Compared to the DGS emission, the maxima of the CIS spectra of the VB features are shifted to higher photon energies at around 46.5 eV. At the small photon energy side (40-45 eV) a decay of the VB emissions (6 eV and 7.4 eV E_{Bin} and DGS) intensity is expected as the spectra have been measured outside the resonance energy. Nevertheless there is no decay. The origin of the missing decay could be the presence of adsorbed species on the *ex situ* sample. Due to the adsorbates the valence band is a superposition of the TiO_x and the adsorbates. Assuming that the valence band of the adsorbed species does not resonate at the used photon energies, their contribution to the overall valence band emission is almost independent of the photon energy and relatively constant. Therefore the resonance behavior of the TiO_2 valence band emissions may is less pronounced in the CIS spectra. At ~1 eV binding energy, where DGS are, the emission of the adsorbed species may be less intense, and therefore the DGS CIS spectrum shows a decrease at lower photon energies. Hydroxyls and carbonates, occur on the ALD TiO_x sample (see Fig. 8.8) and have a valence band emission in the relevant binding energy region.[247,248] Another reason could be Urbach tails occurring in amorphous or polycrystalline materials. Urbach tails result from the disordered structure of materials and their DOS reaches from the band edges into the energy gap. If the Urbach tails do not resonate as well, this has the same effect as a non-resonating adsorbate.

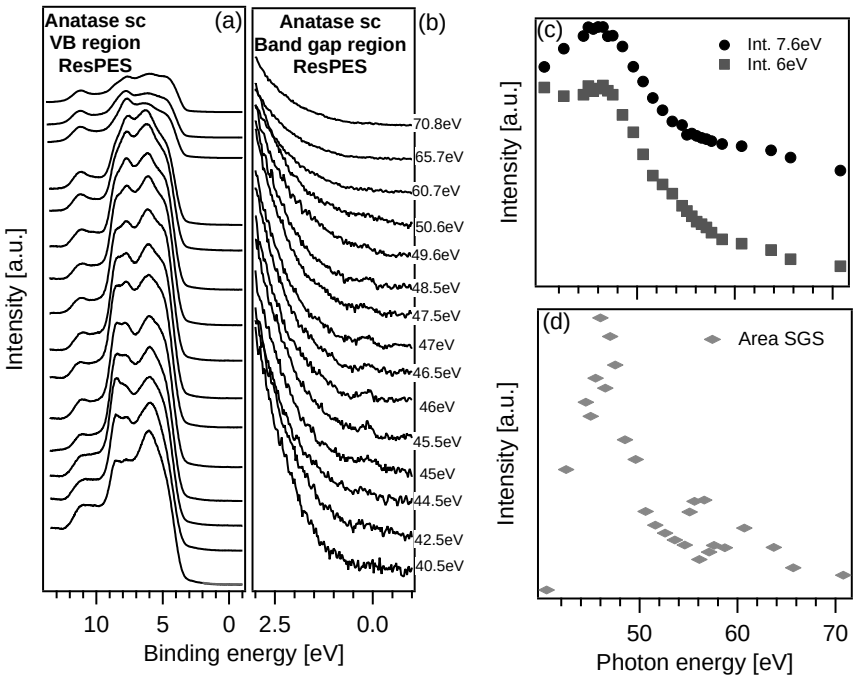

Figure 17.10. – (a): VB region spectra of *ex situ* cleaved sc-(101) surface at different photon energies. (b): Magnified band gap spectra. (c): CIS spectra of the VB region at 6 eV and 7.6 eV. (d): CIS spectra of the SGS emission.

RESPES of the *ex situ* cleaved sc-(101) anatase surface

Figure 17.10 left shows the band gap region of an *ex situ* cleaved anatase crystal. The stronger emission in the range below 10 eV binding energy is probably due to *ex situ* cleavage and may origin from adsorbed hydroxyls.[248] The O 2p derived VB shows several features: The high binding energy side of the main VB emission around 8 eV originates from O 2p-Ti 3d σ-bonding, whereas the low binding energy emission at around 5 eV is attributed to the O 2p-Ti 4sp π-bonding.[83] In the resonance spectra of the valence band region (Fig. 17.10 a) neither DGS nor SGS are visible, but a magnification of the band gap region (Fig. 17.10 b) clearly shows the appearance of SGS at the Fermi level at photon energies of 45 to 48 eV. But a DGS emission is not observed.

On the right of Fig. 17.9 the photon energy dependent measurements (CIS-spectra) of the VB region and the SGS emission of *ex situ* cleaved sc-(101) surface are displayed. The top spectra (c) show the course of the intensities at 6 eV and 7.6 eV binding energy. For the valence band features at 6 eV and at 7.6 eV binding energy a strong resonance between 45 and 47 eV is present. At higher photon binding energies (60 eV) a broad shoulder is observed at both CIS spectra, but for 7.6 eV this shoulder is more pronounced. The broad shoulder of the CIS spectra at 7.6 eV is in accordance with the calculated DOS by Ashasi et al.,[83] who predicted a 4sp characters for this part of the valence band. On the contrary the broad shoulder for the CIS spectra at 6 eV is not in accordance to the calculated DOS by Asahi et al. as they predicted no 4sp contribution in this part of the valence band. Thomas et al. reported such a broad shoulder on the sputter annealed sc-(101) surface as well and linked it to the reduced symmetry at the surface, which was stated to be the reason for a large resonance state around 55 eV on rutile (110).[80,234]

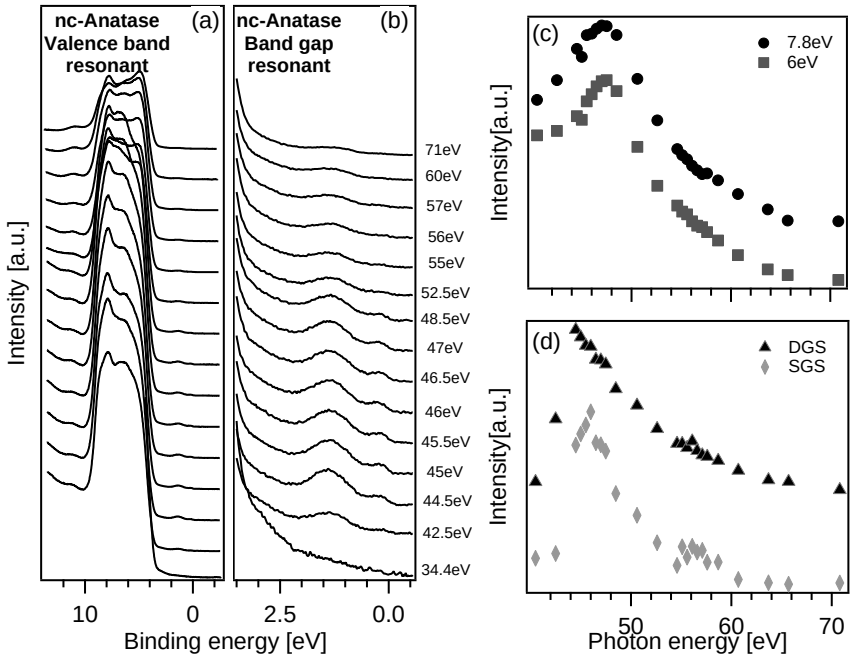

Figure 17.11. – (a): VB region spectra of nanocrystalline TiO_2. The band gap region (b) shows both band gap emissions, SGS and DGS. The CIS spectra of the VB features (c) at 6 eV and 7.8 eV E_{Bin} show a resonance at ∼47 eV photon energy. The CIS spectrum of the DGS emissions (d) has its maximum at 45 eV photon energy and SGS at 46.5 eV photon energy. Compared to the CIS spectra at 6 eV, 7.8 eV and DGS, the SGS display a stronger resonance at 55 to 60 eV, indicating a Ti 4sp character.

SGS of the cleaved anatase (101) surface (Fig. 17.9 right bottom) show strongest resonance between 46 eV and 47 eV. Due the low intensity of the SGS emission an exact position of maximum resonance cannot be determined. The decay of the intensity is steeper, than the one of the DGS of the ALD layer (see Fig. 17.9). Around 56 eV the relative intensity of SGS is increasing again. This suggest strong Ti 3d character of the SGS with some additional Ti 4sp character.[83,234] Nevertheless, due to the low intensity of the SGS on the *ex situ* cleaved sc-(101) surface, there remains some uncertainty, if there is a Ti 4sp contribution and how large it is.

RESPES of nanocrystalline anatase

Figure 17.11 shows the VB region and band gap spectra of nc-TiO_2. The VB structure resembles well the VB structure of the *ex situ* cleaved sc-(101) surface, what can be expected as nc-TiO_2 mainly exhibits (101) facets.[223] As for the *ex situ* sc-(101) surface, an emission above 10 eV E_{Bin} is observed, which is assigned again to hydroxyls. The band gap shows DGS and SGS emission and both resonate by exciting across the Ti 3p→Ti 3d/4sp transition.

The CIS spectra of the VB were determined for 6 eV and 7.8 eV binding energy. Compared to the *ex situ* cleaved sc-(101) surface, the resonance is sharper, as the intensity drop on the small photon energy side is stronger. At the same time the emission at 10 eV is smaller as well. The resonances of the indicated VB binding energies have both their maxima at 47 eV. CIS spectra of the DGS and SGS of the nc-TiO_2 show the same trends as DGS and SGS in the amorphous ALD, respectively the *ex situ* sc-TiO_2. DGS resonate strongest around 45 eV and then the intensity diminishes quiet slowly in the direction of

increasing photon energies, indicating some Ti 4sp character of the DGS, additionally to the evident Ti 3d character. As for the *ex situ* sc-(101) surface, the strongest SGS resonance is at 46.5 eV photon energy. Between 55 eV and 60 eV a strong resonance, compared to DGS and VB features, occurs, giving evidence of stronger Ti 4sp character of the SGS emission, than for DGS and the valence band.

17.2.2 Discussion of the resonant photoemission measurements of the Ti 3p→3d transition.

Resonant photoemission spectroscopy has been performed using the Ti 3p→3d transition for amorphous TiO_x, nc-anatase, and sc-(101) anatase. CIS spectra of the valence band feature around 6 eV and 7.5 eV were plotted for each titania sample. At the low photon energy side of the resonance excitation all VB CIS spectra show an unexpected low decay of the intensity, which is in contrast to former results on sputter annealed TiO_2 (101) surfaces.[84] The expected decay is lowest for the amorphous TiO_x and the *ex situ* cleaved anatase and highest for the nc-TiO_2. At the same time the intensity of the emission at ~10 eV, which is attributed to hydroxyls,[248] is highest for the amorphous and *ex situ* cleaved anatase and lowest for the nc-TiO_2. This indicates that adsorbates are the origin of the missing intensity drop on the small photon energy side of the CIS spectra of the VB region in Fig. 17.10. Either hydroxyls, carbonates or Urbach tails may cause an additional emission in the displayed valence band region.[248,249] As neither hydroxyl nor carbon do resonate at the specified photon energies, its impact becomes more pronounced in spectra measured off resonance. Therefore, the photon energy just before the intensity drop to higher photon energies is assumed as the maximum of the resonance. The maxima of the CIS spectra for all O 2p derived VB features are around 46.5 eV. This corresponds with the Ti 3p→3d resonance and is in good accordance with former results of Thomas et al. on *in situ* sputter annealed (101) anatase.[84] CIS spectra of the DGS of amorphous and nc-TiO_2 show similar behavior, but resonate at lower photon energies. DGS have their strongest resonance around 45 eV and then the intensity diminishes quiet slowly in the direction of increasing photon energies, indicating some Ti 4sp character of the DGS, additionally to the Ti 3d character.[84] SGS resonate strongest at 46.5 eV photon energy, as do the VB features and the enhanced resonance between 55 eV and 60 eV gives evidence of stronger Ti 4sp character of the SGS emission, than for DGS emission and the valence band. For SGS resonance, published results are scarce. Konrad Schwanitz investigated SGS of nc-TiO_2 by RESPES in his PhD thesis and found the maximum of the resonance at 44 eV.[81] Reasons for the difference to the presented results, could be that the photon energy step width was higher (here: 0.5 eV; Schwanitz: 1 eV) or a different evaluation of the DGS and SGS intensity. E.g. Schwanitz performed a normalization to the cross section of the Ti 3d orbital at the used photon energy, which was not done in this work. The cross section of the Ti 3d in dependence of the excitation energy is shown in Fig. B.2. The cross section of the Ti 3d orbital declines steeply in the range of 40 to 70 eV excitation energy. The decrease of the cross section with increasing excitation energy causes an amplification of the low excitation energy side of the CIS spectrum. Hence this could explain the lower excitation energy maximum of the SGS resonance determined by Schwanitz et al., but as this should also effect the DGS emission, the difference probably rather origins from the smaller step width in these experiments. Furthermore the course of Ti 3p cross section over the excitation energy span may influence the intensity of the resonant behavior of the gap state emission. The cross section of the Ti 3p orbital determines how many electrons from the Ti 3p orbital are excited to enable a resonant photoemission process. As the exact influence of both mechanisms on the emission intensity

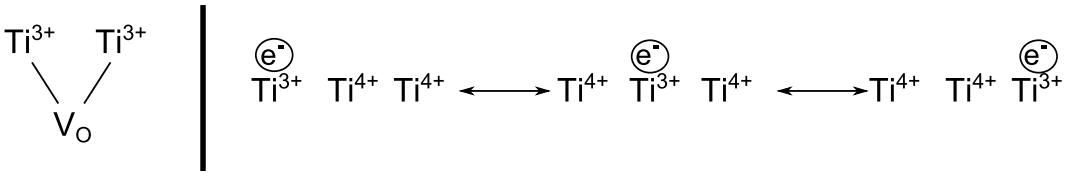

Figure 17.12. – Left: An oxygen vacancy, V_O, donating localized electrons to Ti^{4+} atoms, causing the formation of two Ti^{3+} atoms. Right: At step edges excess electrons are delocalized and the extra electron cannot be attributed to one specific Ti^{4+} atom.

is not known, CIS spectra were concluded from the as measured spectra after background subtraction. Thomas et al. observed the most intense DGS resonance at around 45 eV as well and attributed the lower peak position to the lower oxidation state of Ti^{3+}, compared to the VB features (oxidation state Ti^{4+}; CIS maxima at ∼47 eV). Such a shift of the CIS peak position with respect to the oxidation state has also been observed by Flavell et al. for mixed-valency oxide systems.[84,250] As SGS have their CIS spectrum maxima at 47 eV, as the VB features, this suggest that the partial charge of the Ti atoms at DGS and SGS is different. This could mean that the oxidation state of SGS is higher than the one of DGS. One interpretation is that the additional electrons due to V_O are localized at the neighboring Ti atoms causing Ti^{3+} formation (see Fig. 17.12 left), while the extra electrons due to steps are delocalized over several Ti^{4+} atoms causing a net increase of the oxidation state of several titanium atoms (see Fig. 17.12 right). Therefore smaller photon energies are needed to excite the resonant process and the position of the maximum intensity is shifted to lower photon energies compared to DGS. This is also in accordance with smaller photon energies of the maximal peak position of the SGS resonance.

17.2.3 RESPES of the Ti 2p→3d/4sp transition on the *in situ* cleaved sc-(101) anatase surface

In Fig. 17.13 the resonant photoemission spectra of the Ti 2p→Ti 3d/4sp resonance of an *in situ* cleaved sc-(101) surface are displayed. Photon energies between 450 eV and 478 eV were used. On the left the VB region is displayed and on the right the band gap region. Both, the VB region and band gap spectra, show that resonances occur at two photon energies with a difference of about 5 eV (∼460 eV and ∼465 eV). This difference corresponds well to core level splitting of 5.7 eV of the Ti 2p level into the Ti $2p_{3/2}$ and Ti $2p_{1/2}$ level.

Figure 17.14 shows CIS spectra of the bonding, high binding energy part (A; 8 eV) the non-bonding, low binding energy part (B; 5 eV), DGS (C) emission and SGS (D) emission. CIS spectra of features A and B were conducted by using the maximum intensity of the respective energy. CIS spectra for C and D were conducted by an overall fit of the band gap emission with two components, one for DGS and one for SGS, and then integrated over the respective area. As in some spectra DGS and SGS are difficult to discriminate from each other, at first fit parameters were determined by using a spectrum with distinguishable DGS and SGS emission. For all following fits, only the DGS/SGS ratio is varied. CIS spectra of the valence band feature A, B and D (SGS) show three resonant enhancements. In accordance to resonant photoemission data of the Ti 2p→Ti 3d/4sp transition by Prince et al. the maximum at 464 eV photon energy is assigned to the Ti $2p_{1/2}$ →Ti $3d(t_{2g})$ transition and the maximum at 466 eV photon energy to the Ti $2p_{1/2}$ →Ti $3d(e_g)$. The distance of about 2 eV is in good agreement with crystal-field interaction parameter of 1.7 eV, which splits the t_{2g} and the e_g level.[246] The resonance around

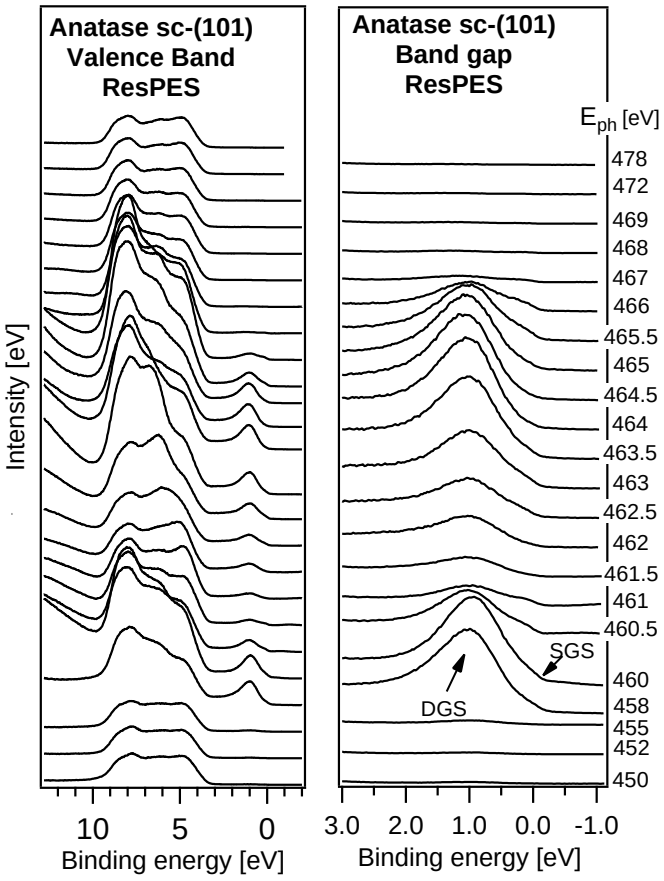

Figure 17.13 – Resonant photoemission spectra of an *in situ* cleaved sc-(101) surface. Displayed are spectra of the valence band region (left) and the band gap region (right) of the Ti 2p→3d/4sp transition. Two resonance occur, one is at ~460 eV photon energy, one at about ~465 eV photon energy. This is due to the core level splitting of the Ti $2p_{3/2}$ emission.

461 eV is attributed to the Ti $2p_{3/2}$ →Ti 3d(e_g) emission. This fits well to the spin-orbit splitting of 5.7 eV of the Ti 2p core level. At lower photon energies, about 2 eV below the Ti $2p_{3/2}$ →Ti 3d(e_g) transition, the Ti $2p_{3/2}$ →Ti 3d(t_{2g}) transition is expected according to Prince et al., but is not observed. The RESPES spectra of Prince et al. are shown in Fig. B.4. As the above mentioned three resonances are present and their energetic positions and distances among themselves coincide well with the data by Prince et al. it is assumed that a lack of data points is the reason for the missing Ti $2p_{3/2}$ →Ti 3d(t_{2g}) resonance. In the respective photon energy region, valence band spectra were only recorded for photon energies of 455, 458 and 460 eV and the width of Ti $2p_{3/2}$ →Ti 3d(t_{2g}) transition has a *fwhm* of about 1 eV.[246] Therefore the Ti $2p_{3/2}$ →Ti 3d(t_{2g}) transition is probably missing due to the too large energy step width of the recorded valence band spectra in this photon energy region.

In contrast to the CIS spectra at 5 and 8 eV the CIS spectrum of the DGS shows in Fig. 17.14 only two broad resonant enhancements. Prince et al. observed the same for the VB features and DGS and explained this with the loss of symmetry and due to V_O formation at the surface. Due to the loss of symmetry, the crystal field splitting at the surface disappears and so do the features in the DGS CIS spectrum. This interpretation was encouraged by the fact that NEXAFS spectra of Ti_2O_3 are rather similar to the CIS spectrum of DGS.[246] In contrast to DGS, SGS experience the same crystal field splitting as the VB at 5 eV and 8 eV. The peak positions of the SGS resonances is also in accordance with the VB resonance positions. Results by Schwanitz obtained on nc-TiO_2 for the Ti 2p→Ti 3d/4sp transition confirm results of DGS and SGS in the manner, that Schwanitz observed a minimum of the SGS intensity at 464 eV and a maximum of DGS intensity at 464 eV photon energy.

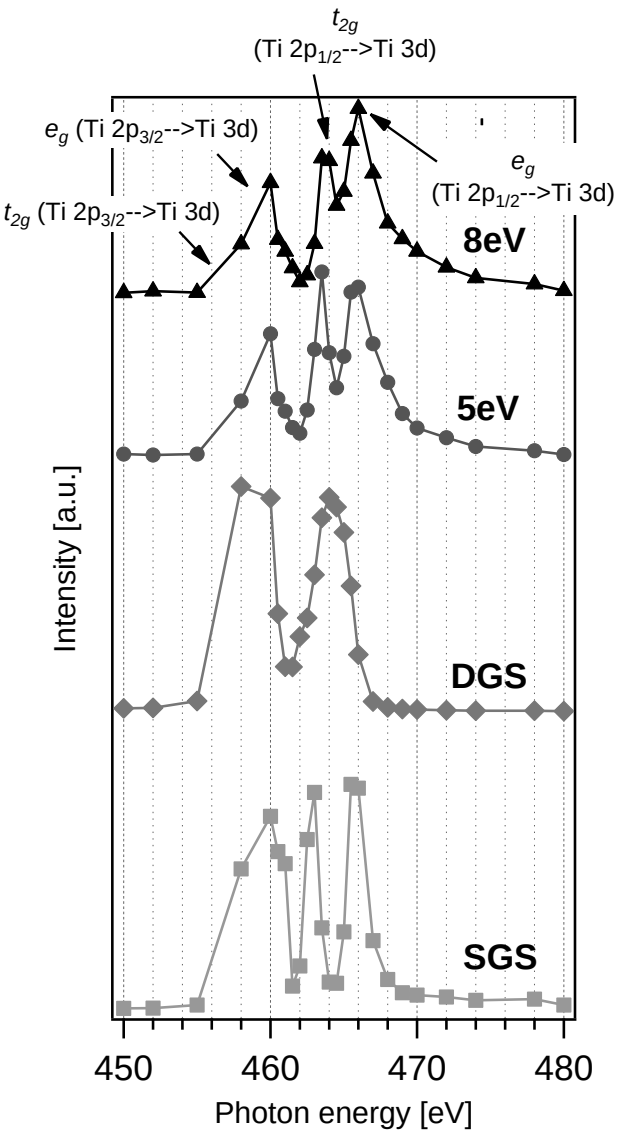

Figure 17.14 – CIS spectra of the Ti2p→3d transition of an *in situ* cleaved anatase (101) surface. CIS spectra at 8 eV, 5 eV and of the SGS show three features. The right one is attributed to the Ti $2p_{1/2}$ →Ti $3d(e_g)$ transition (466 eV), the middle on to the Ti $2p_{1/2}$ →Ti $3d(t_{2g})$ transition (464 eV) and the left one to the Ti $2p_{3/2}$ →Ti $3d(e_g)$ and Ti $2p_{3/2}$ →Ti $3d(t_{2g})$ transition. DGS show only two resonances as due to the missing oxygen, crystal field splitting does not occur.

17.2.4 Conclusion and summary of resonant photoemission measurements

Resonant photoemission spectra were recorded on amorphous, nanocrystalline and *ex situ* and *in situ* sc-(101) surfaces. For time constraints the first three were investigated by exciting the Ti 2p→3d transition and the *in situ* cleaved sc-(101) surface by exciting the Ti 3p→3d transition. For the first time a detailed resonant photoemission study of SGS, occurring just below the Fermi level was performed.

Resonant measurements of the Ti 3p→Ti 3d/4sp transition of the VB features and DGS of the sputter annealed anatase (101) surface and rutile (110) were already performed by Thomas et al. and Zhang et al.[84,85,234] The observed results in this work are in good agreement with their results. CIS spectra of the VB features have their maximum at around 46.5 eV and show all a clear Ti 3p→Ti 3d resonance. The DGS emission shows as well a clear Ti 3p→Ti 3d resonance and some weak Ti 3p→Ti 4sp contribution. The maximum of the resonance is at around 45 eV photon energy and hence 1.5 eV lower than for the VB features. The shift of the DGS resonance probably originates from the nature of the reduced Ti^{3+} species and was observed as well by Thomas et al.[84] The same behavior was monitored for mixed-valency oxide systems before.[250] Regarding the Ti 2p→Ti 3d/4sp transition, the presented results for the VB features and DGS are in good agreement with presented results by Prince et al. The VB emissions at 5 and 8 eV and SGS show crystal field splitting, while DGS do not. In contrast the DGS emission shows only two maxima, which is attributed to a lowering of the symmetry at the surface caused by oxygen vacancies.[246]

The observed resonant behavior of SGS is more similar to the VB features, than to the DGS. The Ti 3p→Ti 3d/4sp resonant measurements of SGS have their maximum around 46.5 eV as the VB features and not at lower photon energies as the DGS. This is in contrast to results by Schwanitz et al. on nc-TiO_2 published in his PhD thesis. Schwanitz observed a SGS and DGS resonances at 44 eV photon energy.[81] The origin of this difference could be the lower step width of the photon energies used in this work, a different determination method of the DGS/SGS intensity or the normalization to the Ti 3d cross section at the used respective photon energies performed by Schwanitz. Such a normalization was not performed for any of the presented RESPES spectra here. Regarding the Ti 2p→Ti 3d/4sp transition, SGS behave as the VB features and show crystal field splitting and peak maxima at the same photon energies as the VB features. Similar results to our experiments have been observed by Schwanitz on nc-TiO_2, who found the DGS maximum at 464 eV, while the SGS have a minimum at the same photon energy.[81] This was also observed at the presented measurements on the *in situ* sc-(101) surface (see Fig. 17.14).

Summarizing the results, the resonant behavior of SGS resemble the one of the VB features. The maxima of the Ti 3p→Ti 3d/4sp transition are at 46.5 eV for SGS and VB features and both show a crystal field splitting. This could indicate that:

1. SGS have not the same Ti^{3+} character as DGS. Extra electrons at the SGS sites due to under-coordinated Ti_{5c} at steps and edges are delocalized along the steps/edges causing a delocalized

charge over several Ti atoms causing a net oxidation of the Ti atoms. Extra electrons due to oxygen vacancies causing DGS are localized at Ti atoms, which results in Ti^{3+}.

2. SGS experience the same crystal field splitting as VB features, which consists of Ti^{4+} atoms. DGS do not show a crystal field splitting. This evidences on one hand the crystalline origin of SGS and on the other hand the lower partial charge at Ti atoms at edges and steps compared to oxygen vacancies.

17.3 Water on TiO_2 sc-(101) surface plane

Besides its application in organic solar cells and dye sensitized solar cells, TiO_2 may also be used in hydrogen production.[251] On the rutile (110) surface water dissociation in the presence of surface vacancies has been predicted theoretically by DFT calculations and observed experimentally by STM and PES.[16,252,253] The anatase (101) surface is far less investigated, but recently the interest increased, as the anatase (101) surface has a high photocatalytic activity and as nanocrystalline anatase TiO_2 exhibits the (101) surface for the most part.[205,235,254] Theoretical calculations and most experimental data showed, that water adsorbs molecularly on the (101) surface.[193,255,256] DFT calculation predicted water dissociation at V_O on the anatase (101) and the rutile (110) surface.[257] Such a water dissociation could not be shown by STM[205] or PES[193]. A reason might be the formation of subsurface defects on anatase (101), rather than surface defects as observed on rutile (110).[240,258] Aschauer et al. suggested by data from STM measurements and DFT calculations that the molecular water adsorption is favored at subsurface defects on the anatase (101) surface, while the dissociated state is not favorable in the presence of a vacancy.[205] In contrast to others, Walle et al. observed water dissociation on the anatase (101) surface by synchrotron induced PES experiments. The respective anatase (101) surface did not exhibit a Ti^{3+} emission in the Ti $2p_{3/2}$ core level, indicating no or little existence of oxygen vacancies.[195] ALD titania prepared at low temperatures was recently used to stabilize silicon photo anodes for efficient water oxidation.[230,259] Also an important application of the interaction of water with anatase are the photoinduced superhydrophilic effects for self-cleaning and antifogging.

17.3.1 Results and discussion: Water on LN-cooled sc-(101) surface

To investigate the process of water adsorption onto the TiO_2 (101) surface, an anatase crystal was cleaved *in situ* to obtain the (101) surface plane. For water adsorption the single crystal was cooled down to liquid nitrogen temperature and exposed to degassed ultrapure water evaporated from a liquid source. Exposure times and pressures to water were 40 s @ 10^{-8} mbar, 10 s @ 10^{-7} mbar, 26 s @ 10^{-7} mbar, 90 s @ 10^{-7} mbar and 60 s @ 10^{-6} mbar. Assuming a sticking coefficient of 1 for water on LN cooled anatase, the H_2O coverages should be 0.4 ML, 1.0 ML, 3.1 ML, 12.1 ML and 72.1 ML respectively. The nominal H_2O coverages in Fig. 17.15 are calculated by the damping of the Ti $2p_{3/2}$ emission after each adsorption step and are 0.1 Å, 1.0 Å, 1.7 Å and 9.2 Å. The average thickness of a water monolayer is about 2.5 Å.[260] This suggests, that either the calculation of the layer thickness is wrong, which could be caused by the growth of water islands or that the sticking coefficient was less than 1.

Figure 17.15 shows the evolution of the SE-edge (left) the O 1s (middle) and the Ti2p core level (right) upon adsorption of water onto an *in situ* cleaved sc-(101) surface. The SE-edge shifts from about 5 eV to 4 eV kinetic energies, with increasing water adsorption. The SE-edge of the third water adsorption was not measured (1.7 Å). Between the last two water adsorption steps the SE-edge does not shift anymore. The O 1s emission of the *as cleaved* crystal is symmetric and no indication of any oxygen containing contaminations is observed. Its binding energy is ~531 eV. Already after the first H_2O adsorption a small additional emission at around 534 eV binding energy can be observed. As for rutile, this emission can be attributed to molecular water.[193,261] Dissociated water, namely OH^-, has a lower binding energy

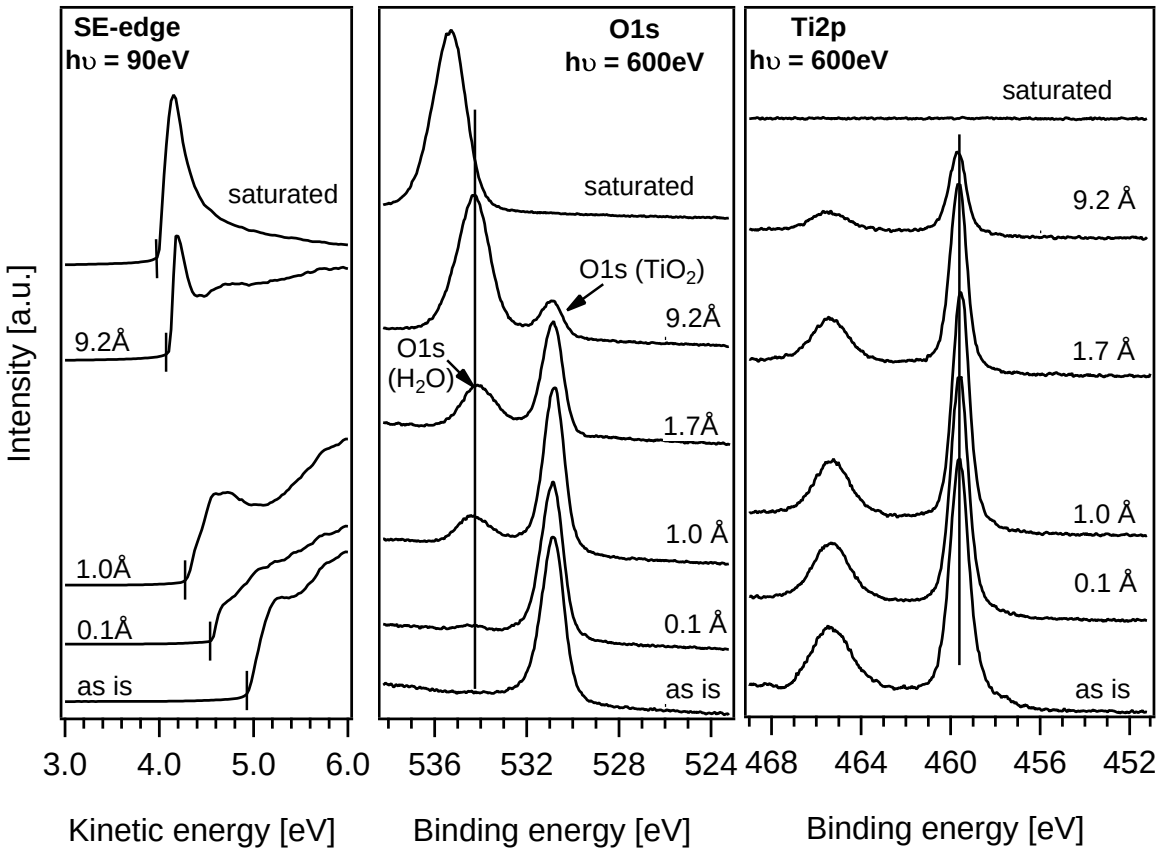

Figure 17.15. – SE-edge (left), O 1s core level (middle) and Ti $2p_{3/2}$ core level (right) evolution upon adsorption of water onto an *in situ* cleaved sc-(101) surface. The SE-edge shift continuously to lower kinetic energies with increasing C_{60} coverage. The O 1s emission displays the O^{2-} of TiO_2 (∼531 eV) and the oxygen emission of water (∼534 eV). The water O 1s emission is increasing with ongoing water adsorption. No emission of OH (∼532 eV) is observed. The Ti $2p_{3/2}$ emission of the sc-(101) substrate shows some Ti^{3+} emission, which decreases after the first water adsorption step. With progressive water dosage the Ti $2p_{3/2}$ emission is damped.

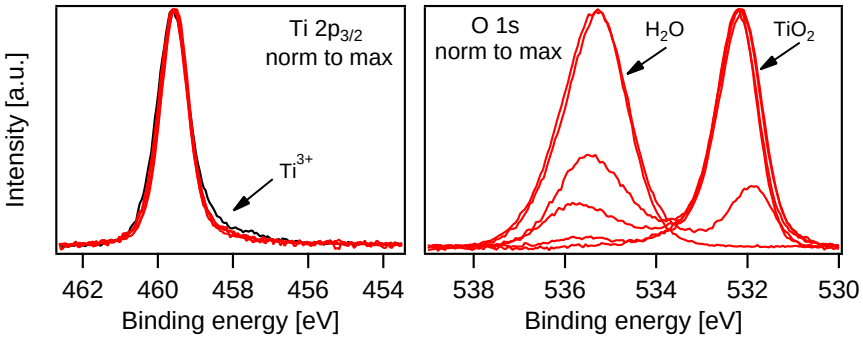

Figure 17.16. – Left: All Ti $2p_{3/2}$ emissions of the water adsorption experiment normalized to the maximum. The black emission is from the anatase crystal without any water adsorption. At the low binding energy side the Ti^{3+} emission is visible, which attenuates after water adsorption. Right: All O 1s emissions of the water adsorption experiment normalized to the maximum. On the high binding energy side is the O 1s emission of water on the low binding energy side, is the O 1s emission of TiO_2. Emissions from OH should appear around 534 eV E_{Bin}, but no emission can be found.

than molecular water (around 532 eV),[196,261,262] but no emission can be found there. In Fig. 17.16 normalized O 1s spectra are shown and no indication of an OH emission is observed. With increasing water exposure times, the TiO_2 O 1s emission diminishes, while the water O 1s emission increases. Till 10 Å H_2O coverage no shift of the O 1s emissions of the substrate and adsorbate is observed. At the highest H_2O coverage the substrate O 1s emission vanished and the water O 1s emission shifts about 1 eV to higher binding energies.

The Ti $2p_{3/2}$ emission of the *as is* cleaved sc-(101) surface shows an emission at the low binding energy onset, which is attributed to Ti^{3+} ions due to oxygen vacancies. The Ti^{3+} states disappear after the first water adsorption step, while the Ti^{4+} main component is damped only a little. With increasing H_2O coverage the Ti 2p emission decreases further and from 1.7 Å the emission shifts by 100 meV to higher binding energies.

Figure 17.17 shows the VB region (left) and the band gap region (right) upon adsorption of water. At 1.0 Å H_2O the typical valence band emission of molecular water can already by recognized. At ~13 eV E_{Bin} the bonding state $1b_2$ is appearing and at ~10 eV E_{Bin} the partly bonding $3a_1$ is observed as well. The nonbonding $1b_1$ state of water at ~8 eV E_{Bin} is only observed from 9 Å H_2O coverage on, cause of the overlap with the VB structure of TiO_2. As the water O 1s core level, the water VB shifts about 1 eV to higher binding energies, after the last water adsorption step. The origin could be either charging of the sample or the increase of binding energy due to the decreased screening of water from the surface.[193] A formation of OH cannot be concluded from the VB spectra nor from the O 1s emission. OH emission would be expected at ~7 (3π) and 11.4 eV (3σ), but is hard to recognize due to the overlapping TiO_2 and H_2O emissions. A difference spectrum of the VB gave no indication of the OH presences as well (see Fig. B.3). From the O 1s emission no indication is given that OH forms at the surface and hence no evidence is given, that water dissociates at the surface of sc-(101) anatase, as well. This is in good agreement with many previous result of water on anatase (101) investigated by STM, XPS and DFT calculations.[80,193,240,256,263] A more recent study of Walle et al. by surface sensitive synchrotron induced PES, indicated the formation of OH on a sputter annealed anatase sc-(101) surface. At a similar photon energy (Ti 2p: 610 eV; VB: 130 eV), Walle et al., did only observe little Ti^{3+} emission in the

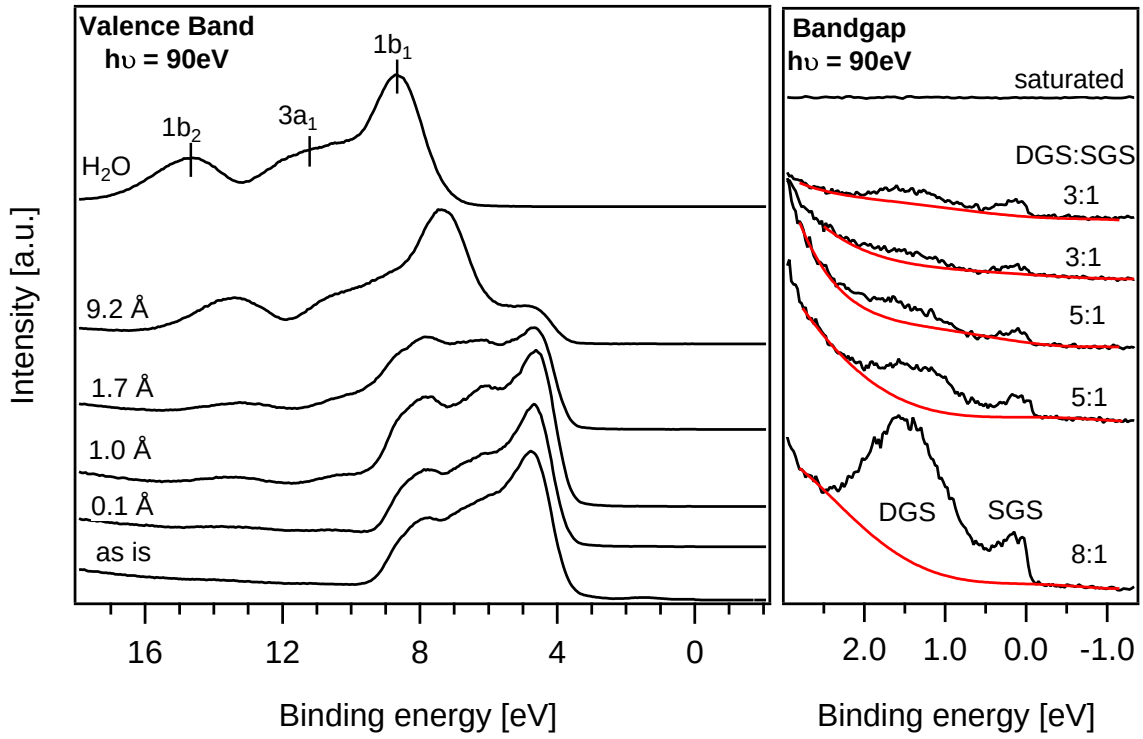

Figure 17.17. – Left: Valence band region spectra of the sc-(101) TiO_2 water adsorption. With increasing H_2O coverage, the water originating emissions $1b_2$, $3a_1$ and $1b_1$ increase steadily. At the top spectrum only water emissions are observed. Right: Bandgap region spectra with increasing H_2O coverage. DGS and SGS first decreases strongly after first water adsorption. After the forth adsorption an increase of the DGS and SGS emission is observed. At highest H_2O coverage no emission of the substrate is observed. Additionally the DGS:SGS ratio for each spectrum is shown on the very right. To obtain the ratio the area underneath the emission is used. Red lines indicate the background intensity, which was removed in order to obtain the values for the DGS and SGS intensity.

Ti $2p_{3/2}$ emission and only small DGS emission in VB spectrum.[195]
On the right of Fig. 17.17 the band gap region of the TiO_2/H_2O interface is displayed. The *in situ* cleaved TiO_2 spectrum has a DGS emission at around 1.5 eV and SGS emission just below E_F (0 eV binding energy). Both SGS and DGS diminish with water adsorption. As indicated by the DGS:SGS ratio on the very right, it seems that the DGS emission decreases more strongly, than the SGS emission. With ongoing water adsorption DGS seem to diminish more than SGS as well. At the last adsorption step (9.2 Å), DGS and SGS emission increase again even though water coverage clearly increases, as the core level and valence band spectra indicate. As DGS and SGS increase after the forth water adsorption step again, an increase of the Ti^{3+} emission in Ti $2p_{3/2}$ spectrum is expected. On the left of Fig. 17.16, no increase of the Ti^{3+} emission can be seen, which is probably due to the low intensity of the Ti^{3+} emission after the forth water adsorption step. The increase of the DGS emission after a certain amount of water adsorption was observed by Di Valentin at al. on rutile (110) before and they attributed the DGS increase to OH formation caused by water dissociation at the rutile (110) surface.[213,264] Feibelman et al. addressed the increase of DGS to hydrogen induced surface states on a PES study on titanium(0001).[265] Schwanitz observed the same DGS increase at higher H_2O coverages on nanocrystalline anatase and attributed it to hydrogen induced surface states. He observed no increase of also existent SGS emission.[81] In contrast to the cited studies, additional SGS emission is present in the PE spectra and SGS increase as the DGS emission. As OH formation is not observed in the respective valence band region and O 1s core level spectra and hydrogen induced surface states are located at around 1 eV E_{Bin} and not at E_F, an OH caused increase of DGS and SGS or hydrogen induced surface states at E_F are unlikely.

17.3.2 In detail analysis of valence band feature evolution upon water adsorption

In Section 17.1 a suggestion for the assignment of the different valence band emissions of a TiO_2 sc-(101) surface was made. The O 2p derived VB, which spans from about 3 to 10 eV E_{Bin}, originates from the perfect, unreconstructed surface, which are the (101) terraces on the cleaved surface. DGS emissions originate from oxygen vacancies (resp. Ti^{3+} ions) present on the surface or subsurface (of terraces). SGS stem from under coordinated Ti^{4+} ions at the intersections of (100) and (101) cleavage planes, which occur at step edges of cleaved surface and nanocrystalline TiO_2. The VB and band gap spectra in Fig. 17.17 already suggested that a preferential adsorption of H_2O on DGS surface sites takes place on the sc-(101) surface. To analyze the adsorption behavior of water on the *in situ* cleaved sc-(101) surface in more detail, the evolution of the VB intensity at 4.9 eV E_{Bin} and evolution of the DGS and SGS intensities are displayed in Fig. 17.18. As can be seen, the VB at 4.9 eV E_{Bin} emission stays constant after the first two H_2O adsorption steps, while DGS decrease strongly and SGS to a smaller extent. After the third adsorption step, the VB at 4.9 eV E_{Bin} starts decreasing, while SGS and DGS slightly increase even though the water coverage increases.

In Fig. 17.19 the VB spectra features were normalized and its relative intensity evolution was characterized. VB spectra were normalized to different E_{Bin} positions. As a measure for the VB emission (terraces), the intensity at E_{Bin} = 4.9 eV is used. For the DGS and the SGS emission, the respective area below the emission is integrated after subtracting a polynomial background (see Fig. 17.17). In

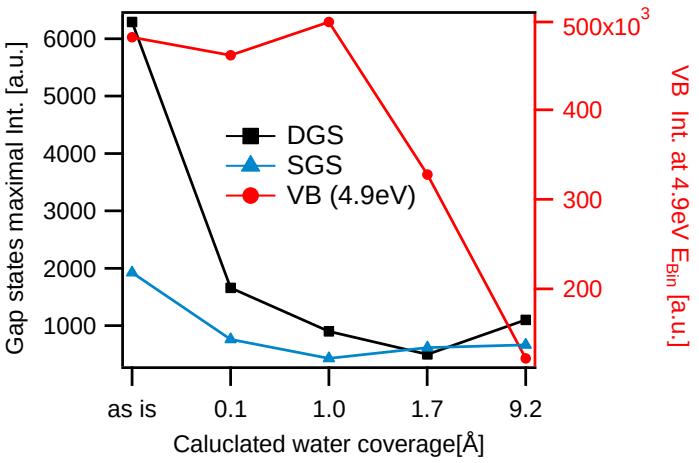

Figure 17.18. – Gap states (DGS and SGS) and VB (E_{Bin}: 4.9 eV) intensities for different water coverages on the *in situ* cleaved anatase (101) surface. While the VB intensity is constant for the first two water adsorption steps, the DGS and SGS intensities drop by factor of 2 to 3. With increasing water coverage (third and fourth adsorption step) the VB feature intensity drops, while the DGS and SGS intensity increases slightly again.

Fig. 17.19 (a) the valence band spectra were normalized to the VB emission of maximum intensity at around 4.9 eV E_{Bin}. Plotted is the DGS and SGS evolution with respect to increasing H_2O coverage. After the first H_2O adsorption (0.1 Å) DGS and SGS decrease, while the DGS emission decreases stronger. After the second adsorption (1.0 Å) SGS decrease more. From then on, DGS and SGS emission increase again, whereas the SGS emission increases faster, than the DGS emission. As DGS and SGS emissions decrease first upon H_2O adsorption and as DGS decrease faster, this suggest that H_2O adsorption at DGS is preferential to adsorption at SGS sites and that adsorption at DGS and SGS is preferred, compared to H_2O adsorption at terraces. With increasing H_2O adsorption DGS and SGS increase again, while the SGS intensity increases more rapidly than DGS intensity. The origin could be a rearrangement of water from DGS and SGS sites to terraces. As SGS intensity increases more rapidly, H_2O abandons SGS sites first. This is in good agreement, with the observed lower decrease of SGS emission after the first H_2O adsorption step.

Figure 17.19 (b) displays the evolution of SGS:DGS and DGS:SGS intensities after normalization to the DGS and SGS emission respectively. The SGS:DGS ratio is first low till it increases strongly after the third water adsorption step and decreases a little after the fourth adsorption. This indicates a preferential occupation of DGS first and an abandoning of DGS after the forth water adsorption step. The DGS:SGS ratio shows the expected contrary behavior. First the ratio decrease strongly and then it decreases less. This indicates as well a preferential adsorption of DGS compared to SGS.

The data in Fig. 17.19 (a) and (b) suggest that the adsorption energy at low water coverages (as a single molecules) decrease from DGS to SGS to terraces. At higher coverages the adsorption energy for water on terraces as bilayer (molecular-molecular interaction) appears highest.

17.3.3 Model of water adsorption onto the anatase sc-(101) surface plane

On defect free anatase sc-(101) water is assumed to adsorb first on Ti_{5c} atoms, followed by an adsorption on O_{2c} atoms.[193,266] So basically two submonolayers of water are formed, sometimes referred to as a

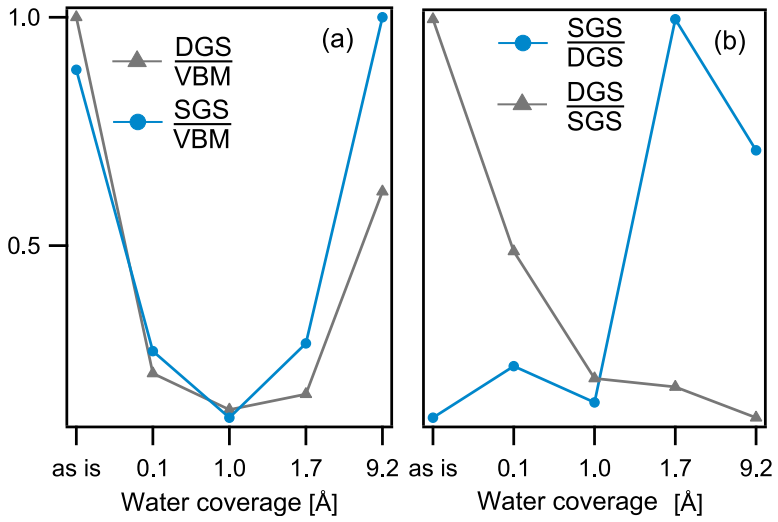

Figure 17.19. – Left (a): Evolution of the DGS (gray) and SGS (blue) emission evolution with respect to water coverage after normalization to the VB at 4.9 eV. Right (b): DGS:SGS (blue) and SGS:DGS (gray) evolution with respect to water coverage after normalization to SGS and DGS respectively.

buckled bilayer.[267] On top of that, a H_2O multilayer is formed. Temperature programmed desorption (TPD) by Herman et al. on the stoichiometric sputter annealed anatase (101) surface showed three desorption peaks. They proposed a multilayer water desorption at 160 K, desorption of water bound at twofold coordinated oxygen at 190 K and water desorption at 250 K from fivefold coordinated titanium.[193] Aschauer et al. showed by STM measurements that subsurface defects on anatase sc-(101) lead to higher desorption temperature of water, than on defect free anatase. This indicates an enhanced binding of water to the defects. They supported this assumption by DFT calculations, which showed that subsurface vacancies are very favorable for water adsorption.[205] Zhao et al. performed a detailed DFT analysis of the adsorption configuration and adsorption energy of water on anatase sc-(101). In the beginning ($d(H_2O) < 1/3$ ML) water-water interaction do not play a significant role and adsorption is mainly driven by the interface formation energy to TiO_2. H_2O attaches at Ti_{5c} atoms. Between 1/3 and 1 ML H_2O coverage water-water interaction becomes more attractive.[266] This coincides with the adsorption of water via hydrogen atoms on O_{2c} atoms and is equivalent to the formation of the second submonolayer.[266] At higher H_2O coverages, H_2O-H_2O multilayer coverage takes place, which is initially improbable.[193]

From the performed experiments and the informations from literature a model for the dynamic water adsorption is concluded. A sketch of the model is depicted in Fig. 17.20. Water molecules are sketched as "V". The upper terrace illustrates a surface with oxygen vacancies on the surface/subsurface. The middle terrace has step edges due to trapezoid shaped islands[86] and the lowest terrace is free of any defects. For a simplification each of the illustrated three steps only displays one surface modification. In reality each terrace can exhibit all three surface modifications. From the data derived in Fig. 17.19 it is assumed that oxygen vacancy sites (DGS) become occupied before step edges (SGS) and the stoichiometric surface (terraces) by water molecules (see Fig. 17.20 (I)). This is evidenced by the strong decrease of the DGS emission in Fig. 17.19 (a) and the decrease of DGS:SGS ratio in Fig. 17.19 (b). With increasing H_2O coverage SGS also become more and more occupied (see Fig. 17.20 (II)). Terraces seem to have the lowest adsorption energy for isolated molecules and become occupied last (III). The data in Fig. 17.19

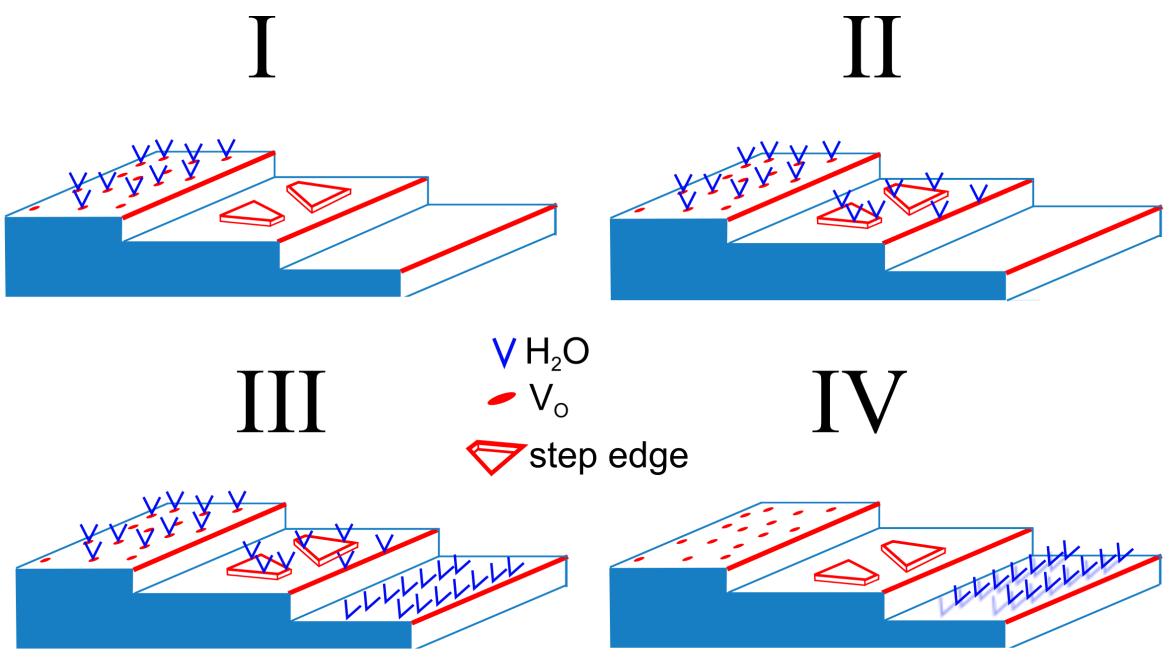

Figure 17.20. – Model of water adsorption on the sc-(101) surface. For simplification each of the illustrated three terraces only displays one surface modification (left: oxygen vacancies; middle: step edges; right: no defects). In reality each terrace can exhibit all three surface modifications. I: Water adsorbs on oxygen vacancies first; II: Water then adsorbs on step edges; III: Water adsorbs last on defect free terraces; IV: If a first submonolayer is adsorbed on the terrace, the formation of a second monolayer becomes energetically favorable. Water moves from DGS and SGS spots to form a second layer on top of the first H_2O layer. At last multilayer formation on the whole crystal surface takes place.

and the spectra in Fig. 17.17 show that despite additional water coverage the relative intensities of SGS and DGS emission increases again. This could be caused by a bilayer (or two submonolayers) formation of water after completion of the first submonolayer on the sc-(101) surface (see (IV)) due to a strongly increased adsorption energy due to H-bridge formation at high water coverage. A bilayer formation or formation of two submonolayers could happen, if at some point water occupies Ti_{5c} atoms on the terraces as DGS and SGS sites are already occupied. If all Ti_{5c} spots are occupied, water-water interaction becomes favorable and H_2O adsorption on the O_{2c} sites takes place.[266] Additionally a rearrangement of the water molecules from the DGS and SGS sites to the submonolayer (O_{2c} sites) of water happens. STM measurement at 190 K of water on sc-(101) surface by He et al. showed that hopping of H_2O molecules on the surface occurs.[240] After the bilayer (two submonolayers) formation multilayer, DGS and SGS become occupied again and H_2O-H_2O multilayer form.[193,266]

17.3.4 Conclusion and Summary

The adsorption energies in the different adsorption states are sketched in Fig. 17.21, where the principal adsorption energies of water molecules are sketched according to the findings. In the beginning the adsorption energy for DGS is lowest and DGS occupation is favored. SGS adsorption energy is slightly higher and takes place at higher H_2O coverages. The adsorption energy at the terraces is highest and therefore they become occupied last. Once terraces are occupied, the formation of two submonolayers

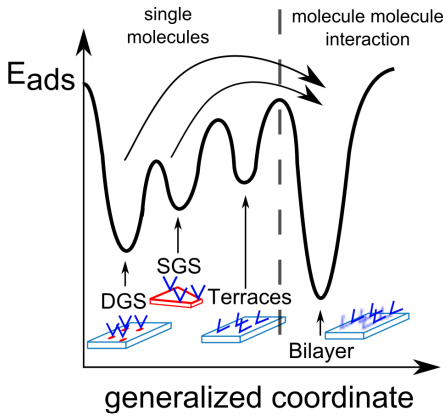

Figure 17.21 – Model for the adsorption energy (E_{ads}) of water vs. the nominal H_2O layer thickness. E_{ads} is first lowest for DGS, then SGS and then terraces. At a certain coverage, when terraces are already partly occupied, E_{ads} of the formation of a second monolayer becomes more favorable and hence water molecules move from DGS and SGS to form a water bilayer.

becomes more favorable (low adsorption energy) and water molecules from DGS and SGS move towards terraces, where they can form a H-bonded bilayer. As a result, DGS and SGS site become unoccupied again.

18 Summary of fundamental investigation on *in situ* and *ex situ* cleaved anatase (101) surfaces and outlook

In Section 17.1 gap states on differently prepared titania surfaces were investigated. While amorphous ALD TiO_x only exhibited deep gap states (DGS) at around 1.3 eV binding energy, nanocrystalline anatase, annealed TiO_x samples, and *in situ* and *ex situ* cleaved anatase (101) surfaces exhibit additional shallow gap states (SGS) starting at 0.5 eV binding energy and reaching up to E_F. SGS show a Gauss-Fermi line shape approaching E_F (0 eV). It was shown that DGS can be induced by synchrotron radiation, while SGS emission does not increase with synchrotron irradiation time. From the experiments it was concluded that SGS are a property of crystalline anatase (101) surfaces and origin from step edges either due to trapezoid shaped terraces on the (101) surface (existing on cleaved anatase) or at the intersection of the (101) planes on the single crystal (existing a lot on nanocrystalline anatase). DGS were attributed to point like oxygen defects as done before by many others.[16,84,138]

In Section 17.2 resonant photoemission was performed on the valence band structures of amorphous titania and crystalline anatase. CIS spectra for the Ti 3p→Ti 3d/Ti 4sp resonance and the Ti 2p→Ti 3d/Ti 4sp resonance were recorded. At the Ti 3p→Ti 3d/Ti 4sp resonance DGS have their strongest resonance at around 45 eV photon energy independent, if occurring on amorphous or crystalline titania. The resonances of VB features (determined at around 6 and 8 eV binding energy) have their maximum shifted by about 1.5 eV to higher photon energies at 46.5 eV. This shift is attributed to the lower oxidation state of Ti^{3+}, causing the shift of the resonance photon energy. In contrast to DGS, SGS resonate most at around 46.5 eV as do the VB features, this indicates a higher oxidation state of SGS compared to DGS.
The Ti 2p→Ti 3d/Ti 4sp resonance was recorded on an *in situ* cleaved anatase (101) surface. For the VB features, at 5 eV and 8 eV binding energy, and the SGS three maxima have been measured. The three maxima exist due to the crystal field splitting occurring in anatase. The fourth maxima is probably missing due to a low resolution at the low photon energy side. DGS show only two maxima, due to Ti $2p_{3/2}$ spin orbit coupling. The additional splitting due to crystal field splitting is missing, which is attributed to the loss in symmetry due to V_O formation at the surface.

In Section 17.3 water was adsorbed on the LN cooled *in situ* cleaved anatase (101) surface. The analyses of SGS, DGS and VB emissions upon increasing water coverages shows that individual areas of the crystal surface become occupied at different water coverages. From the experiments it is concluded that water first adsorbs at DGS, then on SGS and last on terraces, when SGS and DGS are already occupied. Once molecular-molecular interaction becomes effective, further water adsorption becomes

more favorable and water from DGS and SGS spots move to the terrace to form a water bilayer.

Outlook

The *in situ* cleavage of the anatase single crystal enables many other opportunities to investigate different surface of the anatase crystal. In the context of the SGS, a more detailed investigation of the intensity of SGS emission and the correlation to step edges on the (101) surface is desirable. To do this, a combined PES/STM study would be necessary to compare the step edge density on the surface with the SGS emission in PES. By varying the angle of cleavage, the step edge density on the surface may be de- or increased. Regarding the resonance measurements a repetition of the Ti 2p→Ti 3d/Ti 4sp resonance measurement on the *in situ* cleaved anatase crystal with a better resolution is necessary to confirm the crystal field splitting of the VB feature and the SGS. For the adsorption experiments also other adsorbates like methanol could be investigated. All the performed and suggested experiments could also be performed on an *in situ* cleaved (100) surface.

A Appendix of part II

A.1 TiO_2 sc-(101) O1s - *ex situ* and *in situ*

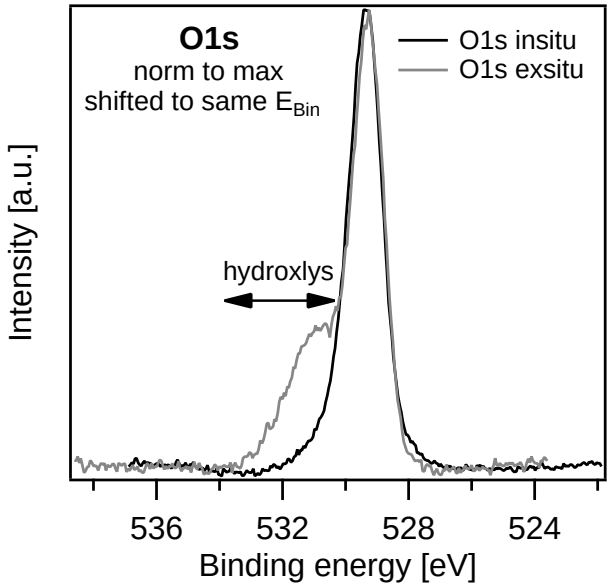

Figure A.1. – O 1s emission of an *in situ* (black) and *ex situ* (gray) cleaved anatase sc-(101) surface. The O 1s emission of the *ex situ* cleaved crystal shows an emission at the high binding energy side of the main emission due to hydroxyls. The O 1s emission of the *in situ* cleaved crystal shows only an emission of the oxygen of TiO_2.

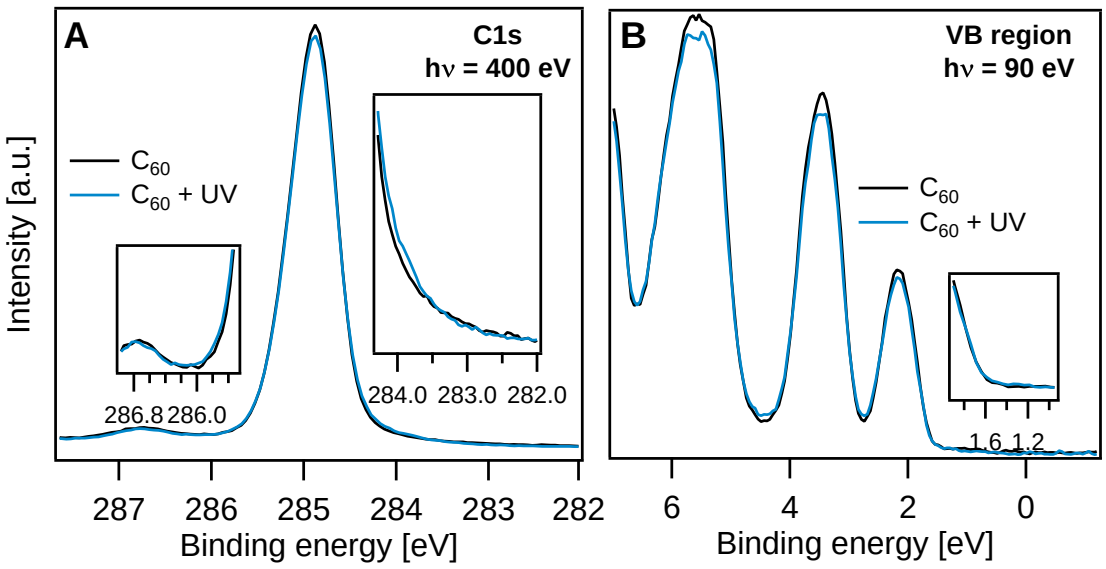

Figure A.2. – A: C 1s emission of C_{60}, which was deposited on a gold substrate. UV illumination induces no changes of the C 1s shape and its binding energy position. B: VB region spectrum of the C_{60} layer. No influence of UV illumination on the shape and the energetic position are observed as well.

Table A.1. – Work function (WF) and Ti $2p_{3/2}$ and C 1s level values of the 500 °C TiO_x samples with different C_{60} coverages.

	C_{60}	absolute values				with respect to initial			
	[Å]	initial	X-ray	UV	UV + X-ray	initial	X-ray	UV	UV + X-ray
WF [eV]		4.35	4.21	-	4.15	0	0.14	-	0.20
Ti $2p_{3/2}$ [eV]	0	459.36	459.47	-	459.59	0	-0.11	-	-0.23
C 1s [eV]		-	-	-	-	-	-	-	-
WF [eV]		4.21	4.21	4.16	4.15	0	0	0.05	0.06
Ti $2p_{3/2}$ [eV]	7	459.42	459.49	459.50	459.53	0	-0.07	-0.08	-0.11
C 1s [eV]		285.61	285.59	285.43	285.42	0	0.02	0.18	0.19
WF [eV]		4.21	4.26	4.30	4.30	0	-0.05	-0.09	-0.09
Ti $2p_{3/2}$ [eV]	30	459.47	459.52	459.51	459.53	0	-0.05	-0.04	-0.06
C 1s [eV]		285.59	285.51	285.39	285.39	0	0.08	0.20	0.20
WF [eV]		4.25	4.27	4.28	4.29	0	-0.02	-0.03	-0.04
Ti $2p_{3/2}$ [eV]	76	459.45	459.52	459.51	459.50	0	-0.05	-0.04	-0.06
C 1s [eV]		285.57	285.46	285.41	285.38	0	0.11	0.16	0.19
WF [eV]		4.41	4.40	4.40	4.41	0	0.01	0	0.01
Ti $2p_{3/2}$ [eV]	140	-	-	-	-	-	-	-	-
C 1s [eV]		285.20	285.22	285.20	285.19	0	-0.02	0	-0.01

A.2 The 500 °C TiO_x/C_{60} interface

To investigate the 500 °C TiO_x/C_{60} interface, amorphous, as deposited, 80 °C TiO_x was annealed on a hot plate for 60 min at 500 °C. Different C_{60} thicknesses were deposited onto the TiO_x substrate and subsequently irradiated with an UV source of 365 nm wave length. The experiments were performed at DAISY-FUN with monochromated $Al_{K\alpha}$ radiation. The influence of X-ray and UV radiation on the interface is investigated.

A.2.1 TiO_x 500 °C substrate

To analyze a possible influence of X-ray and/or UV radiation on the work function and the core level lines of the TiO_x substrate, spectra were recorded on sample spots, which were exposed different amount of times to X-rays and UV radiation. The indicated times in Fig. A.3 and Fig. A.4 represent the amount of X-ray or UV irradiation time the specific sample spot was exposed during recording the spectrum.

The measurement procedure was performed as for the amorphous TiO_x in Section 9.1. To gather a spectrum of a fresh spot, the sample was moved to a non X-ray exposed sample spot and the measurement started as fast as possible. In average it took about 5 s to start the measurement after sample movement and about 20 s for recording the spectrum. Overall it is difficult to determine and quantify the exact X-ray exposure already occurring during the measurement. The time designations for the first spectra (work function and Ti $2p_{3/2}$) in Fig. A.3 and Fig. A.4 are composed of 5 s to start the measurement plus the time to record the spectra (20 s). For the additional spectra the time between starting each measurement is added. Due to the limited amount of fresh spots on the sample (about four), time dependent spectra were not recorded for the oxygen and carbon emission lines. To keep the X-ray exposure as low as possible the margins of the recorded spectra were kept to a minimum. Therefore only the Ti $2p_{3/2}$ emission of the Ti 2p core level was measured. Subsequently, secondary electron and core level spectra were recorded until the shift of the energetic positions and the line shapes saturated (see Fig. A.4). Subsequently the sample was transferred *in situ* to a chamber, where a UV transparent MgF_2 window is attached and illuminated with UV light of 365 nm wavelength for 60 min.

Fig. A.3 shows the evolution of the work function (left) and the Ti $2p_{3/2}$ core level emission (right) in dependence of the exposure to X-rays and UV light. All black spectra are obtained on sample spots, which were not exposed to UV light before. All blue spectra were exposed to UV light. The first blue spectrum from below was illuminated for 60 min with UV light, and recorded on the same spot as all black spectra, hence it is X-ray and UV influenced. The third blue spectra from below (new spot 25 s) are recorded on a spot which was not exposed to X-rays before and only to UV light. Upon increase of X-rays exposure time the work function decreases from 4.36 eV (25 s X-ray) to 4.20 eV after 2800 s of X-ray illumination. The Ti $2p_{3/2}$ core level binding energy increases from 459.36 eV (25 s X-ray) to 459.47 eV after 2800 s X-ray exposure. At the start of the experiments the work function decreases by about 150 meV and the

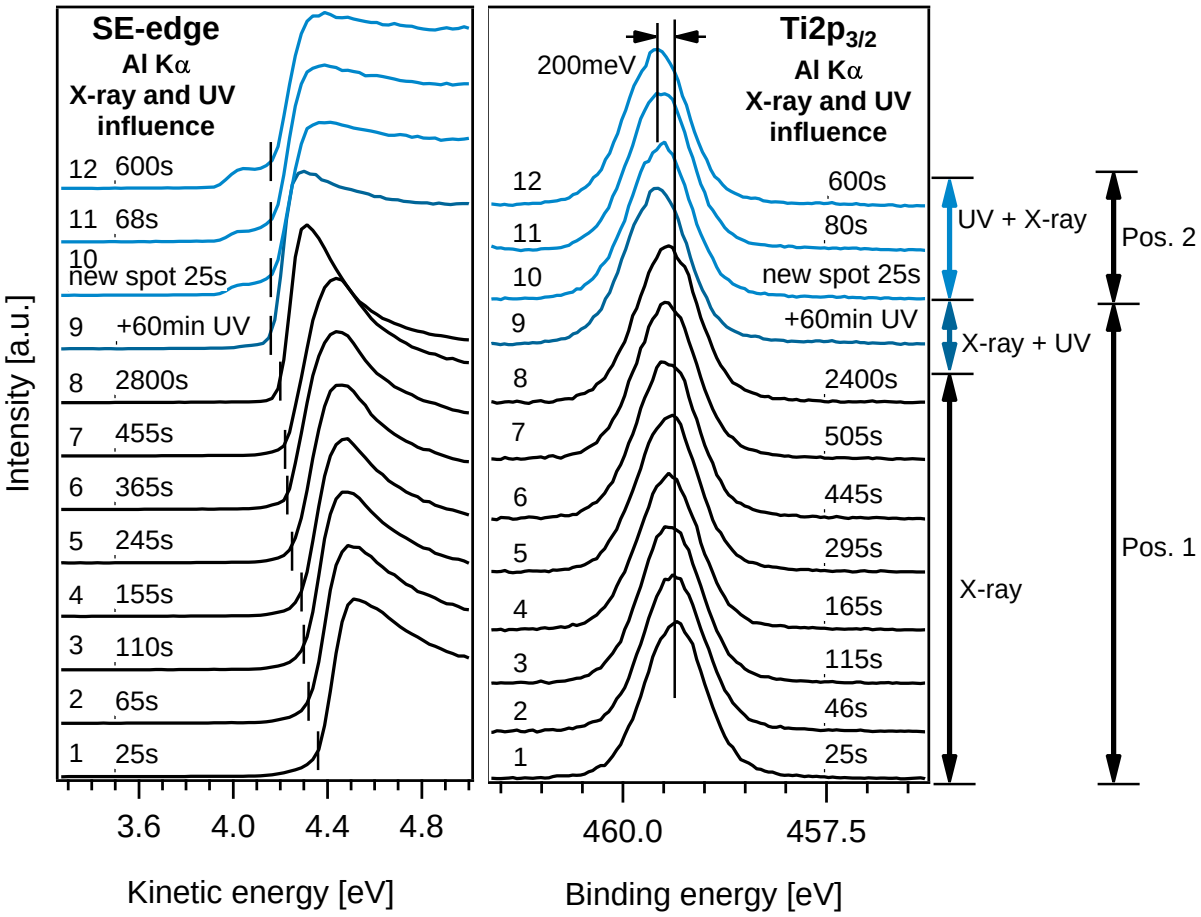

Figure A.3. – WF changes (left) and Ti $2p_{3/2}$ core level (right) changes with UV and X-rays are displayed. All black spectra are only exposed to $Al_{K\alpha}$ radiation, of the indicated time. Blue spectra are exposed additionally to 60 min UV light and different times of X-rays. While the first blue spectra from below are measured on the same spot as the previous black spectra, the upper three blue spectra are measured on a new, minimal X-ray exposed, sample spot.

Ti $2p_{3/2}$ core level increases by ~100 meV and saturates after around 500 s (see Fig. A.4). After UV light illumination for 60 min a further decrease of the work function (increase of the Ti $2p_{3/2}$ binding energy) is obtained. Whereas the work function decreases by 50 meV, the Ti $2p_{3/2}$ binding energy increases by 100 meV, which results for the Ti $2p_{3/2}$ level and the WF in a total shift (from the initial spectra (8 s) to the UV illuminated spectra (+60 min UV)) of 200 meV. To distinguish between X-ray and UV light influences, additional spectra on an only UV light, but not X-ray, exposed sample spot were recorded (upper three blue spectra in Fig. A.3). As Fig. A.3 and Fig. A.4 show neither the work function nor the Ti $2p_{3/2}$ binding energy defer significantly from the X-ray and UV radiation exposed spot. The slightly reduced Ti $2p_{3/2}$ binding energy (30 meV) on the new spot (see Fig. A.4), may e.g. have its origin in the rough, non-uniform surface of the post annealed surface (see Section 8.1.3).

In summary the time and light dependent measurements show, that X-rays and UV light have similar effects on the energetic position of the WF and Ti 2p core level. Nonetheless UV light has a stronger influence and shifts the emission lines further than X-rays.

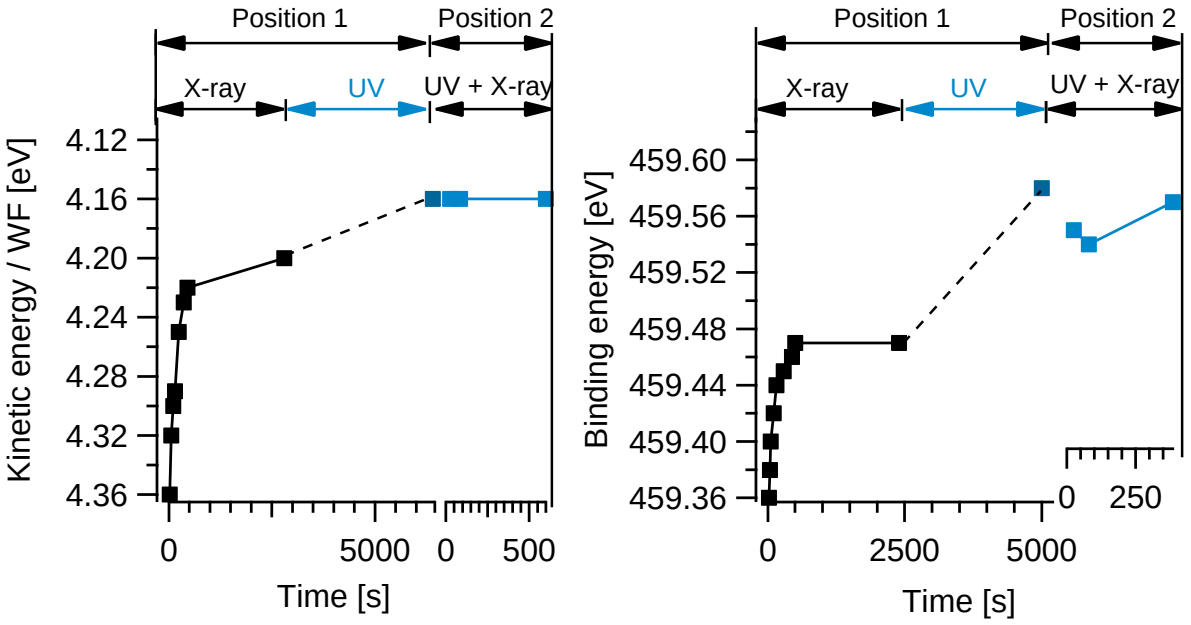

Figure A.4. – Separation of the X-ray and UV influence on 500 °C post annealed TiO_x. On the left, the WF evolution is shown upon X-ray and UV illumination and on the right the evolution of the Ti $2p_{3/2}$ core level. While the first spectra after 60 min UV irradiation are recorded on the X-ray exposed sample spot, the following measurements were performed on a new sample spot and hence are irradiated by less $Al_{K\alpha}$ radiation.

A.2.2 TiOx 500 °C/C_{60}: Influence of X-ray and UV radiation

To characterize the TiO_x/C_{60} interface a, 7, 30, 76 and 140 Å thick C_{60} layer was deposited on a 500 °C annealed TiO_x sample. To determine the influence of X-rays, Ti 2p, C 1s and the secondary electron edge spectra were recorded on a pristine sample spot first and successively spectra were recorded on a long time (min. 600 s) irradiated sample spot. Then the sample was illuminated for 60 min with UV light (365 nm). To determine the influence of UV only, Ti 2p, C 1s and the secondary electron edge spectra were recorded on a pristine sample spot first (not X-ray affected) (light blue). At last UV and X-ray affected spectra were recorded (dark blue).

Photoemission spectra

Figure A.5 shows the evolution of the SE-edge (left), the Ti $2p_{3/2}$ (middle) and the C 1s (right) core level emission with increasing nominal C_{60} coverage (as indicated) and the influence of UV radiation. The black spectra are the initial spectra and recorded with a minimum of X-ray exposure time. Blue spectra are recorded after 60 min of *in situ* UV illumination. For all C_{60} coverages a fresh TiO_x substrate was used and the post UV spectra were recorded on a new sample spot.

The SE-edge (Fig. A.5 left) of the TiO_x substrate shifts with UV light irradiation by 200 meV from 4.35 eV kinetic energy to 4.15 eV kinetic energy. At 6 Å C_{60} layer thickness, the UV induced decrease of the SE-edge shift decreases to 50 meV, while at 30 Å and 76 Å C_{60} coverage UV light causes an increase of the kinetic energy of the SE-edge by 100 meV and 50 meV respectively. At 140 Å C_{60} coverage no shift

of the SE-edge is observed after UV illumination. The Ti $2p_{3/2}$ signal (Fig. A.5 middle) is damped with increasing C_{60} coverage. Upon UV illumination the Ti $2p_{3/2}$ level of the TiO_x substrate shifts 200 meV to higher binding energies. As the secondary electron edge shift to lower kinetic energies, this means a downward band bending of the energy level at the surface. With increasing C_{60} coverage the UV induced Ti $2p_{3/2}$ binding energy shifts become smaller and are 100 meV for 7 Å C_{60}, and 50 meV for 30 and 76 Å C_{60}. The initial Ti $2p_{3/2}$ spectrum shifts 100 meV with increasing C_{60} coverage from 459.35 eV to 459.45 eV. After UV illumination the Ti $2p_{3/2}$ level shifts 100 meV to lower binding energies (459.6 eV to 459.5 eV). On the right of Fig. A.5, the C 1s core level spectra are depicted. The C 1s emission of the TiO_x substrate is attributed to carbon contamination due to *ex situ* handling of the sample. The C 1s emission of the substrate is subtracted from all other C 1s spectra. With increasing C_{60} coverage the C 1s signal increases. Before UV illumination the C 1s binding energy is at 285.6 eV for lower C_{60} coverages (7, 30 and 76 Å). At highest C_{60} coverage the C_{60} C 1s level is at 285.2 eV. Despite for the sample with 140 Å C_{60} coverage, the C_{60} C 1s level of all TiO_x/C_{60} samples shows a 200 meV decrease, from 285.6 eV to 285.4 eV, after UV illumination. The 140 Å C_{60} sample shows no shift of the C 1s level after UV and is constant at 285.2 eV. The energetic positions and shifts are summarized in Table A.1.

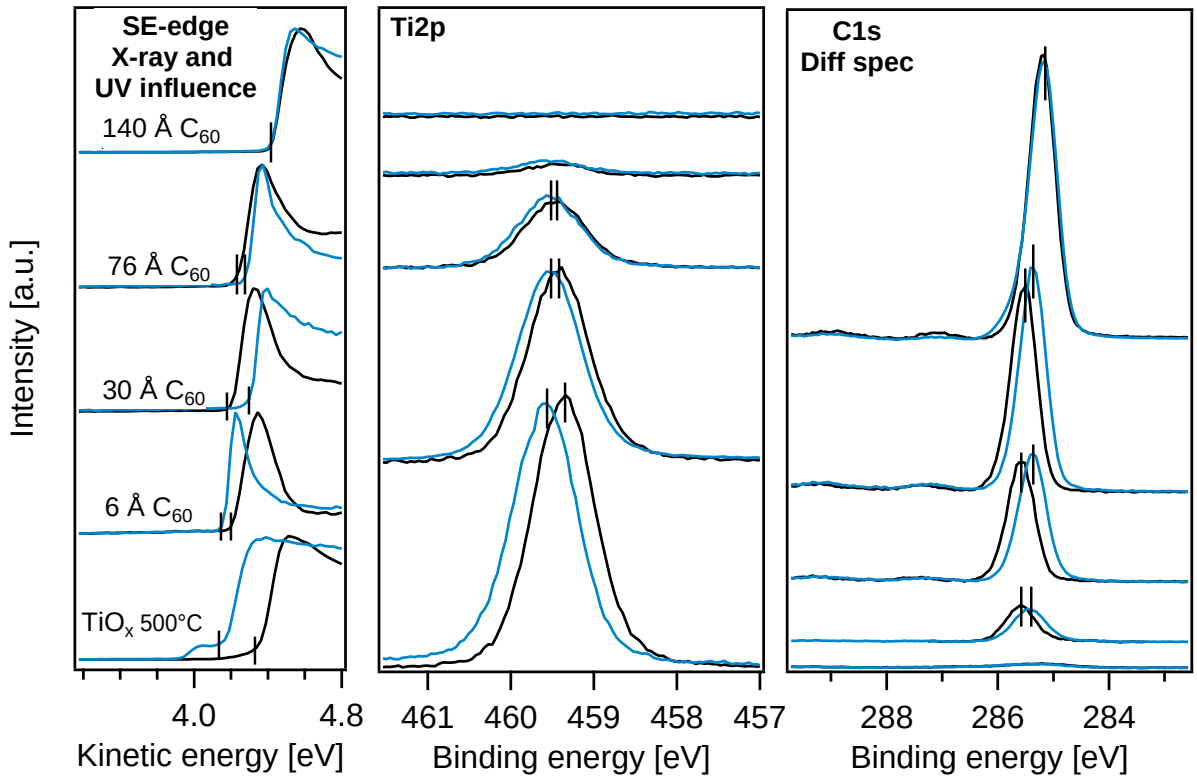

Figure A.5. – Photoemission spectra of TiO_x 500 °C/C_{60} interface before (black) and after UV illumination (blue). On the left is the SE-edge of the pristine TiO_x with increasing C_{60} layer thickness. While UV induces a lowering of the WF at the pristine TiO_x at low C_{60} coverages (6 Å C_{60}), the WF increases at 30 Å C_{60}. At higher C_{60} coverages no WF shift occurs upon UV. In the middle is the evolution of the Ti $2p_{3/2}$ emission upon increasing C_{60} coverage and UV irradiation. At all C_{60} coverages the Ti $2p_{3/2}$ binding energy increases after UV illumination. The increase is lower with increasing C_{60} coverage. On the right the C 1s emission is depicted. The bottom spectrum shows the carbon contamination of the TiO_x 500 °C sample and is subtracted from all other C 1s spectra. UV light induces a shift of the C 1s energy level to lower binding energies. At highest coverage no UV induced shift is observed. For all C_{60} coverages a fresh TiO_x substrate was used and the spectra after UV were recorded on a new sample spot.

Analysis of the Ti $2p_{3/2}$ and C 1s line shape

Figure A.6 shows the evolution of the Ti^{3+} percentage of the Ti 2p and the C 1s *fwhm* of the Ti^{3+} states upon C_{60} deposition and UV illumination. In general the Ti^{3+} content is low (only about 1 %) and hence the error of the Ti^{3+} content determination is higher, than compared to the 80 °C samples in Chapter 9. From the data points obtained of the Ti^{3+} content, it is not possible to identify a trend of a preferential adsorption of C_{60} on Ti^{3+} sites. Before UV illumination the C 1s *fwhm* decreases with increasing C_{60} coverage from 0.56 eV to 0.49 eV at highest C_{60} coverage. After UV illumination the C 1s *fwhm* increases up to 50 meV (for 7 Å C_{60}), but the increment becomes smaller for higher C_{60} coverages (20 meV for 7 Å C_{60}), till it almost zero at 140 Å (5 meV for 140 Å).

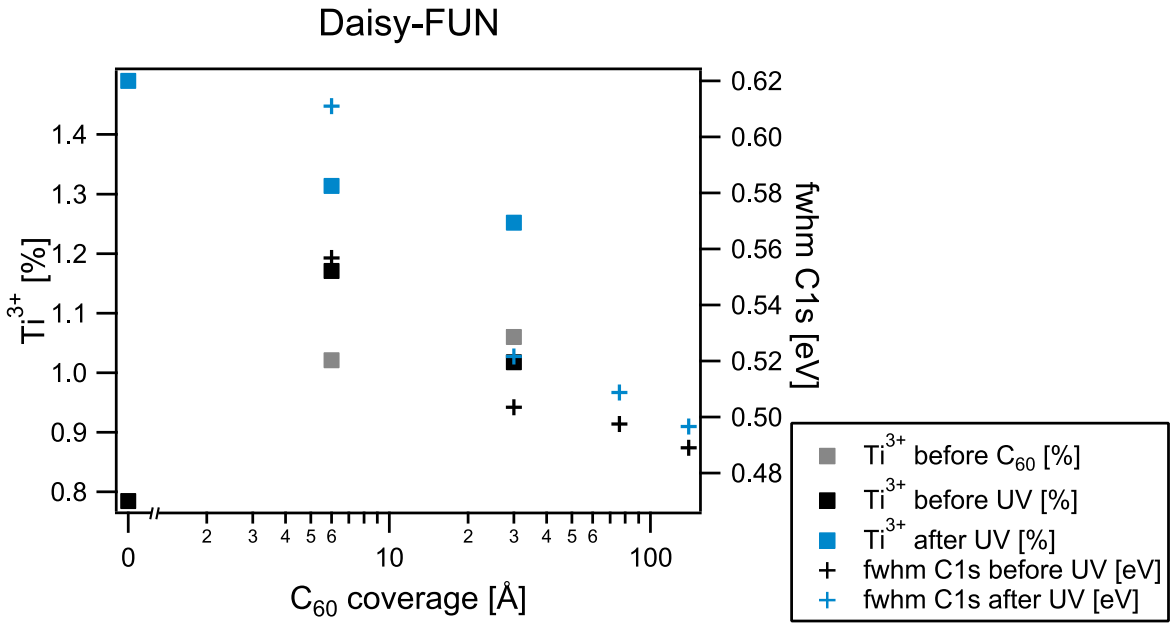

Figure A.6. – Ti^{3+} and C_{60} C 1s *fwhm* evolution with increasing C_{60} coverage and with respect to the influence of UV light. The Ti^{3+} content is low before (black squares) and after UV (blue squares) illumination but still increases with UV illumination. The C_{60} C 1s *fwhm* increases as well with UV irradiation (black and blue plus signs). The UV induced *fwhm* increase is lower with increasing C_{60} coverage and becomes almost 0 eV at the highest C_{60} coverage.

A.2.3 Energy diagram of the 500 °C TiO_x interface before and after UV

Figure A.7 shows the energy diagram deduced from the obtained photoemission spectra in Fig. A.5. Before UV illumination (on the left) the TiO_x Ti $2p_{3/2}$ emission shifts from 459.4 eV to 459.5 eV and therefore shows a downward band bending of 100 meV towards the interface. The C_{60} C 1s emission decreases from 285.2 eV to 285.7 eV binding energy towards the interface and hence shows a downward band bending of 500 meV. This results in a Ti $2p_{3/2}$/C 1s difference of 173.8 eV before UV and an interface dipole of 0.4 eV. The energy diagram after UV illumination was determined as for amorphous TiO_x/C_{60} and AZO/C_{60}. UV induced shifts of the energy levels of the substrate and of low C_{60} coverages are also assumed to occur at high C_{60} coverages close to the interface. After UV illumination the Ti $2p_{3/2}$ level is at 459.6 eV and decreases to 459.5 eV with increasing C_{60} coverage, hence an upward band bending of 100 meV towards the interface occurs. The C_{60} downward band bending decreases after UV illumination

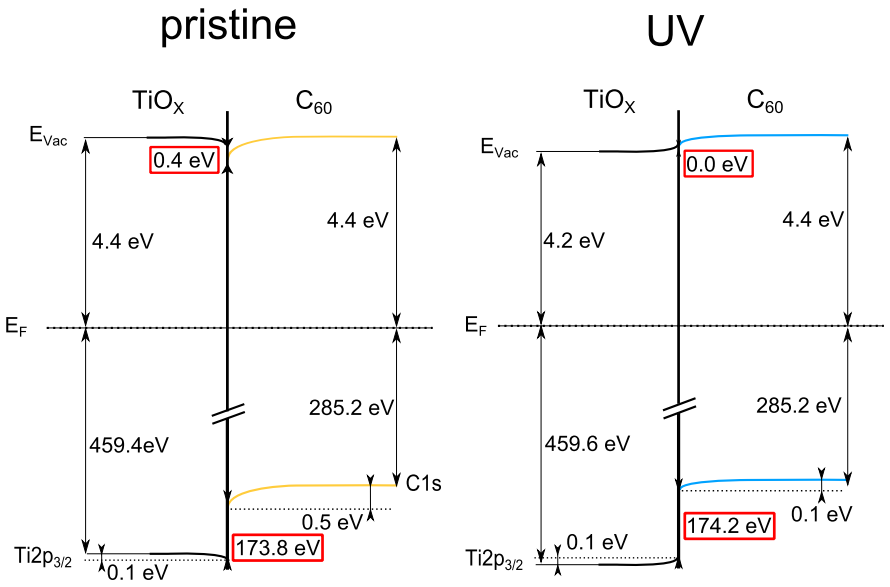

Figure A.7. – Energy diagram of the TiO_x 500 °C/C_{60} interface before (left) and after UV illumination (right). The interface dipole before UV illumination is 0.4 eV and the Ti $2p_{3/2}$-C 1s distance is 173.8 eV. After UV illumination the interface dipole is 0.0 eV and the Ti $2p_{3/2}$-C 1s difference increases by 0.4 eV to 174.2 eV. The Ti $2p_{3/2}$ core level shows 100 meV downward shift towards the interface before UV and 100 meV upward shift towards the interface after UV illumination. The C 1s downward band bending decreases from 0.5 eV before UV to 0.1 eV after UV illumination.

by 400 meV to 100 meV. This results in an increase of the Ti $2p_{3/2}$/C 1s difference to 174.2 eV, which is reflected by the disappearance of the interface dipole.

A.2.4 Influence of UV light on the 500 °C TiO_x/C_{60} interface after UV pretreatment of the TiO_x substrate

As for the 80 °C TiO_x an UV pretreatment of 24 h was performed on the 500 °C TiO_x. First the TiO_x sample was illuminated for 24 h with UV. Then C_{60} was evaporated with a rate of 0.5 Å/ s for 60 s, resulting in C_{60} coverage of ~15 Å. Finally the sample was irradiated again for 60 min with UV light (top blue spectra). After each sample treatment XPS spectra were recorded on a fresh spot. After the C_{60} deposition, X-ray time dependent measurements were performed to check if a X-ray influence is apparent (see Fig. A.8). The work function is at 3.9 eV after 24 h of UV illumination. After C_{60} deposition the WF increases to ~4.0 eV and after UV it increases further to ~4.1 eV. The course of the WF is similar to the one observed on the TiO_x/30 Å C_{60} sample in Fig. A.5. The Ti $2p_{3/2}$ core level shows no shift, neither upon C_{60} deposition nor after UV irradiation. The C 1s level of C_{60} shows a shift of ~100 meV to lower binding energies after UV illumination. Compared to the TiO_x/30 Å sample in Fig. A.5 the UV induced shift is 100 meV smaller. In Table A.2 the energetic shifts are summarized.

A.2.5 Summary: TiO_x 500 °C/C_{60} interface and the UV influence

Summarizing the results it is observed that the UV induced shifts at the TiO_x 500 °C/C_{60} interface are similar to the ones observed at the TiO_x 80 °C/C_{60} and the AZO/C_{60} interface in Sections 9.1 and 13.2.1.

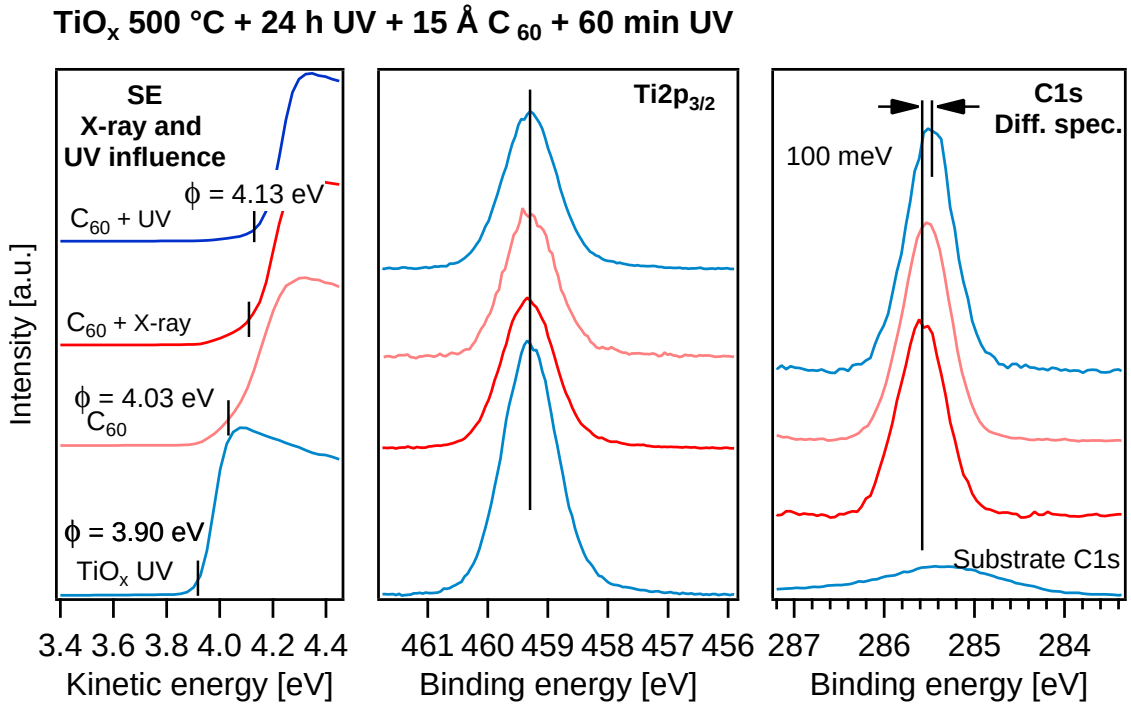

Figure A.8. – SE-edge(left), Ti $2p_{3/2}$ (middle) and C 1s spectra (right) of the UV pretreated TiO_x substrate (bottom blue), the TiO_x substrate + C_{60} (red) and the TiO_x substrate + C_{60} + UV (top blue). The SE-edge shifts from 3.9 eV (TiO_x substrate) to 4.0 eV (after C_{60} deposition) to 4.1 eV (after additional UV illumination). The TiO_2 Ti $2p_{3/2}$ core level shows no shifts. The C 1s level of C_{60} shifts 100 meV to lower binding energies after UV illumination. The substrate C 1s emission is subtracted from the C_{60} C 1s spectra.

The model for the UV induced changes at the 80 °C TiO_x/C_{60} interface derived in Chapter 12 is also applicable for the 500 °C TiO_x/C_{60} interface.

At the TiO_x 500 °C/C_{60} interface the Ti $2p_{3/2}$ emission shifts 200 meV to higher binding energies, while the C_{60} C 1s level shifts 200 meV to lower binding energies at low C_{60} coverages. This results in an increase of the Ti $2p_{3/2}$-C 1s distance after UV illumination of 400 meV, from 173.8 eV to 174.2 eV. In addition the C_{60} C 1s *fwhm* increases as well after UV illumination. Apparently neither the crystalline structure or the reduced amount V_O of the TiO_x 500 °C substrate do influence the UV induced changes at the titania/C_{60} interface. Furthermore the UV induced change can be reduced by a UV pretreatment, but the decrease of the C 1s core level shift is limited to a minimum of 100 meV.

Table A.2. – Work function, Ti $2p_{3/2}$, and C 1s values of the UV pretreated 500 °C TiO_x/C_{60} interface.

	absolute values				with respect to C_{60} initial			
	TiO_x substrate	C_{60} initial	C_{60} X-ray	C_{60} UV	TiO_x substrate	C_{60} initial	C_{60} X-ray	C_{60} UV
Work function [eV]	3.92	4.03	4.11	4.13	-	0	-0.08	-0.10
Ti $2p_{3/2}$ [eV]	459.30	459.30	459.32	459.30	-	0	-0.02	0
C 1s [eV]	-	285.58	285.53	285.49	-	0	0.05	0.09
fwhm C1s [eV]	0.66	0.68	0.74	0.74	0	-0.02	-0.08	-0.08

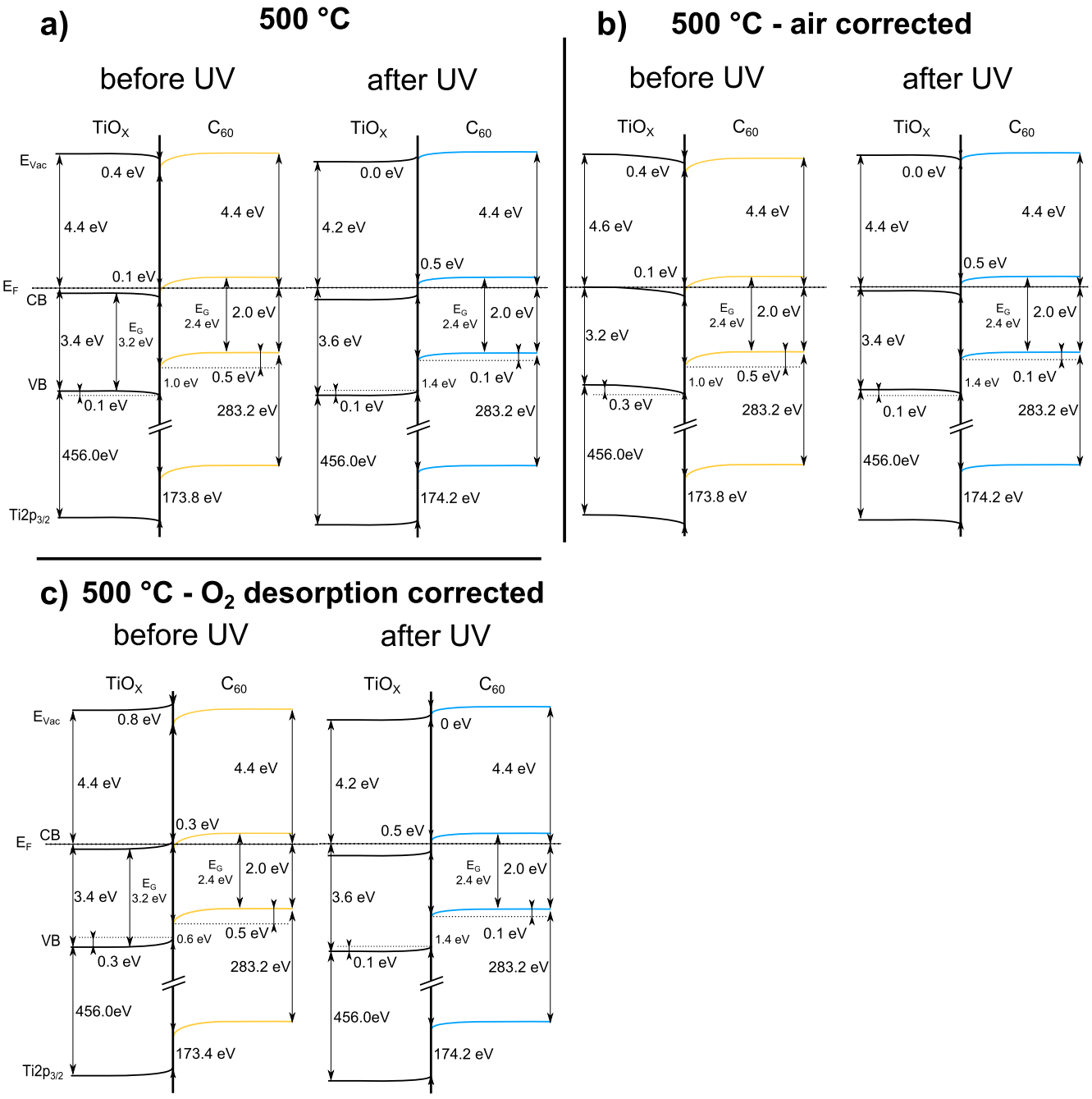

Figure A.9. – 500 °C TiO_x/C_{60} interface as measured (a), air corrected (b) and O_2 desorption corrected (c). The as measured energy diagram (a) shows no electron extraction barrier before and after UV illumination. Furthermore the E_{CB} position of the 500 °C TiO_x is below E_F, which indicates a good conductivity of the titania. The air corrected energy diagrams (b) show no electron extraction barrier as well before and after UV illumination. The oxygen desorption corrected energy diagrams (c) shows an electron extraction barrier of 0.1 eV before UV illumination (as E_{CB} of TiO_x is 0.1 eV above E_F and the C_{60} LUMO is below E_F) and no barrier after UV illumination.

Figure A.9a) shows the complete energy diagram of the as measured TiO_x 500 °C/C_{60} interface. In Section 8.1.1 XRD showed that 500 °C post annealed TiO_x is partly anatase and AFM images (see Section 8.1.3) showed a similarity of 500 °C annealed TiO_x and nanocrystalline anatase particles. Therefore the fundamental band gap of anatase, 3.2 eV, is assumed.[16] The VB position is calculated from the Ti $2p_{3/2}$-VBM distance of anatase determined in Section 8.2.2, which is 456.0 eV. Those values are added to the energy diagrams in Fig. A.9.
While Fig. A.9a) represents the as measured energy diagram, Fig. A.9b) includes the formation of an accumulation layer due to *ex situ* handling at the TiO_x surface and Fig. A.9c) displays the situation assuming oxygen adsorption at the TiO_x surface. In case b) an air caused downward band bending at the surface of 200 meV is assumed and in case c) an oxygen caused upward band bending of 400 meV (as in Section 15.1.1). In case a) and b), E_F of TiO_x is below or at the same level as the CBM at the interface and in the bulk, and hence no electron extraction barrier exists. The assumption of the formation of an accumulation layer at the surface leads to E_{CB} energy level position in bulk just at E_F, which is in good agreement with the observed good conductivity of nc-TiO_2 compared to amorphous TiO_x.[223] Assuming an oxygen caused depletion layer at the TiO_x surface of 0.4 eV as done for the TiO_x 80 °C, this leads to E_{CB}-LUMO offset of 0.3 eV and, as the CBM at the interface is 0.1 eV above E_F, to an electron extraction barrier of only 0.1 eV, which is significantly lower compared to 0.4 eV as in the case of IOSC with TiO_x 80 °C.

Kuwabara et al. showed that inverted organic solar cells with TiO_x ETL's prepared by a chemical bath method show S-shaped I-V characteristics, if the TiO_x layer is annealed to 150 °C and shows an amorphous XRD pattern. An annealing of the TiO_x layer to 450 °C and the transformation of the titania to anatase crystal structure, leaded to good I-V characteristics of the prepared inverted organic solar cells. Kuwabara et al. attributed the S-shape to charge recombination centers existing at the TiO_x 80 °C/P3HT:PC_{61}BM interface, which do not exist at the TiO_x 450 °C/P3HT:PC_{61}BM interface.[71] The determined energy band diagrams of the TiO_x 500 °C/C_{60} interface give evidence, that also different energetic barriers at the TiO_x/C_{60} interface could be the origin of the increased FF of inverted solar cells containing anatase TiO_2 ETL's.

B Appendix of part III

B.1 Resonant photoemission

Resonant photoemission of 500 °C annealed ALD TiO_x

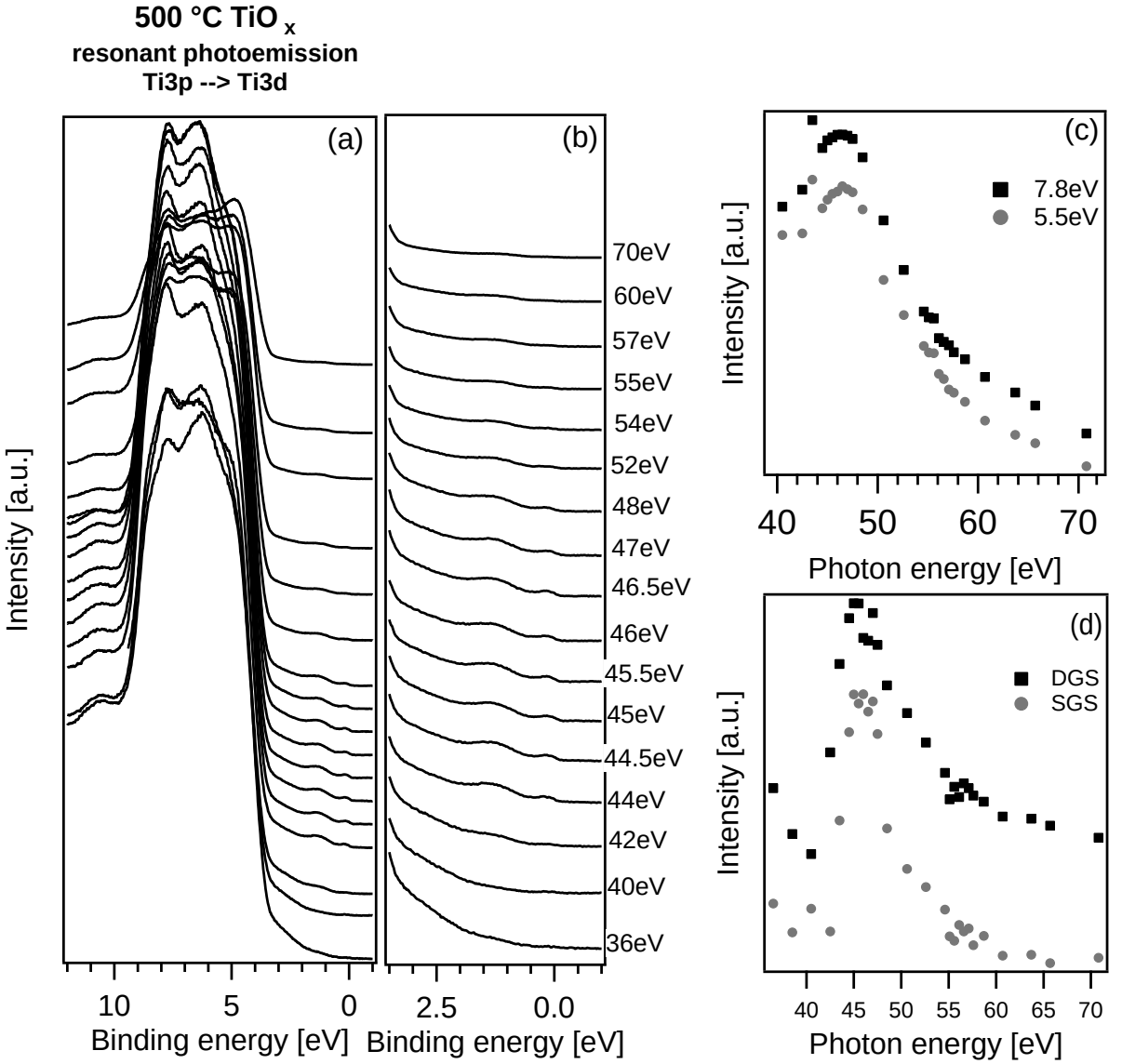

Figure B.1. – Left: Resonant photoemission spectra of the valence band (a) and the band gap region of 500 °C TiO_x. As for the nc-TiO_2 DGS and SGS emissions are observed, Right: CIS spectra of the valence band emissions at 5.5 eV and 7.8 eV (c) and CIS spectra of the DGS and SGS emission (d). All CIS spectra show a similar course to the ones of nc-TiO_2.

Cross section of the Ti 3p orbital

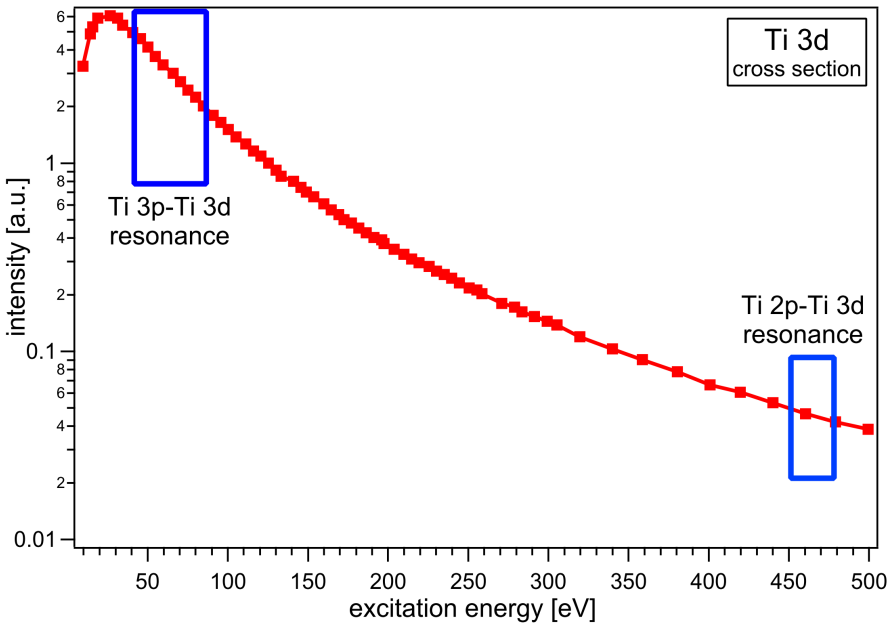

Figure B.2. – Cross section of the Ti 3d orbital in dependence of the excitation energy. Using different excitation energies with the Ti $2p_{3/2}$- Ti 3d resonance results in big variation of the cross section of the Ti 3d orbital and therefore may have an influence on the DGS and SGS intensity. Taken from Ref. [81].

Gaussian-Fermi Dirac fit of shallow gap states

In Figure 17.5 a Gaussian and Fermi Dirac distribution is used to fit the SGS. For the Gaussian distribution formula 1.1 is used and formula 1.2 describes the Fermi Dirac like distribution.

$$\text{Gauss}(E_{Bin}) = A\, exp\left[-\frac{1}{2}\left(\frac{E_{Bin}-x_0}{\sigma_G}\right)^2\right] \tag{1.1}$$

$$\text{Fermi}(E_{Bin}) = \left[\frac{1}{exp\left(\frac{(-E_{Bin}-E_F)}{B_{EF}}\right)}\right] + 1 \tag{1.2}$$

For the overall fit, the product (Eq. (1.3)) of both distributions is used.

$$f(E_{Bin}) = \left[A\, exp\left[-\frac{1}{2}\left(\frac{E_{Bin}-x_0}{\sigma_G}\right)^2\right]\right] \cdot \left[\left[\frac{1}{exp\left(\frac{(-E_{Bin}-E_F)}{B_{EF}}\right)}\right] + 1\right] \tag{1.3}$$

Here A is the maximum, x_0 is E_{Bin} at the position of maximum intensity, σ_G is the standard deviation of the Gaussian fit, E_F the Fermi energy and B_{EF} a measure for the broadening of the Fermi edge. B_{EF}

consist of the broadening due to Fermi Dirac statistics (k_BT) and additional broadening owed to the limited lifetime of the excited state, the energy width of the photon source and the resolution of the analyzer. B_{EF} for the Ag Fermi edge is 0.038 eV at 298 K. At room temperature k_BT is ~0.025 eV and at 90 K 0.008 eV. All used fitting parameters are displayed in Table B.1. The Fermi edge E_F is set to zero, as the spectra are calibrated to the Fermi edge of Ag. $fwhm_G$ (FWHM of the Gaussian distribution, Eq. (1.1)) is calculated by multiplying σ_G with $2\sqrt{2ln2}$. $fwhm_F$ is deduced from the Gaussian like first derivative of the Fermi fit, by using its standard deviation σ_F (inflection point of Gaussian distribution).[136]

Table B.1. – Work function, binding energy and valence band maximum position of the *in situ* and *ex situ* sc-anatase (101), in dependence of X-ray and UV illumination. *Calculated by the Ti $2p_{3/2}$ core level minus 456.00 eV (see Section 8.2.1).Taken from Ref. [136].

Sample	x_0	σ_G [eV]	$fwhm_G$	E_F	B_{EF}	σ_F	$fwhm_F$
nc-TiO_2 298 K	0.1354 ±0.015	0.2480 ±0.014	0.583	0 ±0	0.0670 ±0.011	0.115	0.271
sc-TiO_2 [eV] 298 K	0.1293 ±0.013	0.1995 ±0.013	0.470	0 ±0	0.0543 ±0.012	0.098	0.231
sc-TiO_2 [eV] 290 K	0.1501 ±0.0075	0.2014 ±0.010	0.474	0 ±0	0.0267 ±0.006	0.074	0.174

H_2O difference spectrum

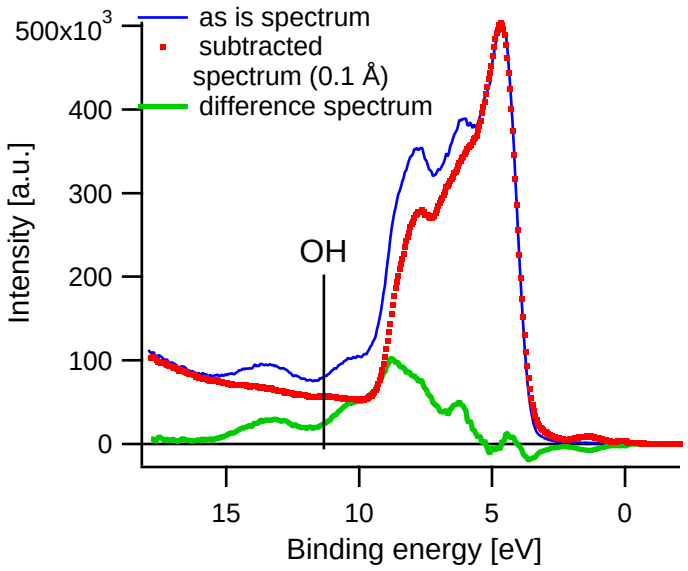

Figure B.3. – Difference spectrum (green) of the anatase (101) valence band before water adsorption (blue) and the sc-(101) plus 0.1 Å H_2O. The difference spectrum shows no emission of OH at ~11 eV.

Resonant photoemission of the Ti $2p_{3/2}$ →Ti 3d and the Ti $2p_{1/2}$ →Ti 3d transition by Prince et al.

Prince et al. recorded resonant photoemission of the Ti $2p_{3/2}$ →Ti 3d and the Ti $2p_{1/2}$ →Ti 3d transition. The CIS spectrum shows four maxima due to crystal field interaction of the final d state. The maxima are t_{2g} and e_g of the Ti $2p_{3/2}$ →Ti 3d and the t_{2g}, e_g of the Ti $2p_{1/2}$ →Ti 3d transition.

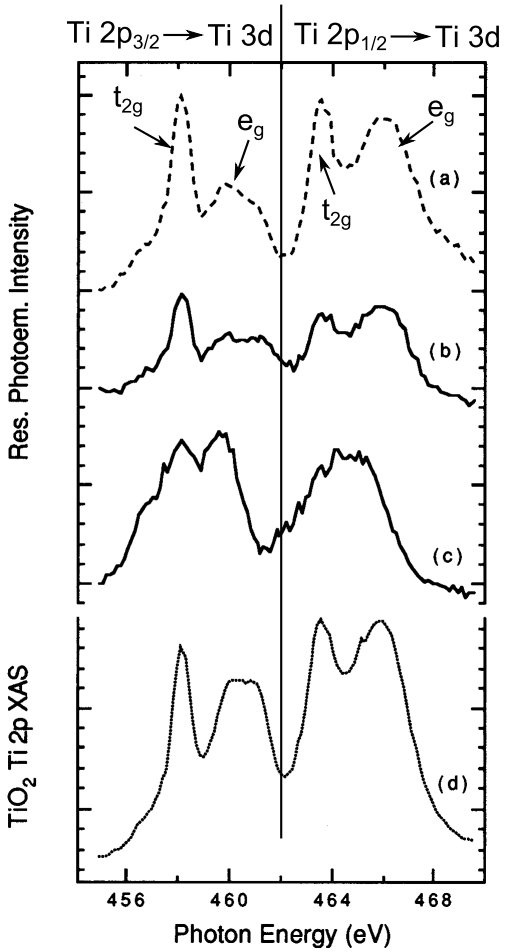

Figure B.4. – Resonant photoemission of a sputter annealed rutile (100) surface. (a) is the CIS spectrum at 8.2 eV E_{Bin}, (b) 4.6 eV E_{Bin}, (c) DGS emission and (d) XAS spectrum. Taken from Ref. [246].

Bibliography

[1] International Energy Agency. *Key world energy statictics 2015*. URL: http://www.webcitation.org/6fzEHL2Bz, visited on: Oct. 15, 2016.

[2] BP p.l.c. *BP Energy Outlook 2035*. URL: http://www.bp.com/content/dam/bp-country/de_de/PDFs/Sonstiges/Energy_Outlook_Energietrends_und_Daten_EU_2015.pdf, visited on: Oct. 15, 2016.

[3] REN21 Secretariat. *Renewables 2014 global status report*. URL: http://www.webcitation.org/6SKF06GAX, visited on: Apr. 3, 2016.

[4] Rajendra K Pachauri, Myles R Allen, VR Barros, J Broome, W Cramer, R Christ, JA Church, L Clarke, Q Dahe, P Dasgupta, et al. *Climate change 2014: synthesis Report. Contribution of working groups I, II and III to the fifth assessment report of the intergovernmental panel on climate change*. IPCC, 2014.

[5] Joeri Rogelj, Gunnar Luderer, Robert C Pietzcker, Elmar Kriegler, Michiel Schaeffer, Volker Krey, and Keywan Riahi. "Energy system transformations for limiting end-of-century warming to below 1.5 °C ". In: *Nature Climate Change* vol. 5, no. 6 (2015), pp. 519–527.

[6] Anja Schneikart. "Herstellung und Charakterisierung von SnS-Dünnschichtsolarzellen". PhD thesis. Technische Universität Darmstadt, 2014.

[7] Daryl M Chapin, CS Fuller, and GL Pearson. "A new silicon p-n junction photocell for converting solar radiation into electrical power". In: *Journal of Applied Physics* vol. 25, no. 5 (1954), pp. 676–677.

[8] ISE Fraunhofer. "Photovoltaics report". In: *Fraunhofer ISE, Freiburg* (2014).

[9] Albert Polman, Mark Knight, Erik C Garnett, Bruno Ehrler, and Wim C Sinke. "Photovoltaic materials: Present efficiencies and future challenges". In: *Science* vol. 352, no. 6283 (2016).

[10] Brian Oregan and M Grätzel. "Low cost and highly efficient solar cells based on the sensitization of colloidal titanium dioxide". In: *Nature* vol. 335, no. 24 (1991), pp. 737–740.

[11] A. J. Heeger. "Semiconducting and metallic polymers: The fourth generation of polymeric materials (Nobel lecture)". In: *Angewandte Chemie-International Edition* vol. 40, no. 14 (2001), pp. 2591–2611.

[12] C. W. Tang. "Two-layer organic photovoltaic cell". In: *Applied Physics Letters* vol. 48 (1986), pp. 183–185.

[13] Heliatek GmbH. *Heliatek Introduction*. URL: http://www.heliatek.com/de/presse/downloads?file=files/content/downloads/Heliatek%20Introduction_2015.pdf, visited on: Oct. 13, 2016.

[14] Markus Clark Scharber and Niyazi Serdar Sariciftci. “Efficiency of bulk-heterojunction organic solar cells”. In: *Progress in polymer science* vol. 38, no. 12 (2013), pp. 1929–1940.

[15] Sara Trost, Kirill Zilberberg, Andreas Behrendt, Andreas Polywka, Patrick Görrn, Philip Reckers, Julia Maibach, Thomas Mayer, and Thomas Riedl. “Overcoming the Light-Soaking Issue in Inverted Organic Solar Cells by the Use of Al:ZnO Electron Extraction Layers”. In: *Advanced Energy Materials* vol. 3, no. 11 (2013), pp. 1437–1444.

[16] Ulrike Diebold. “The surface science of titanium dioxide”. In: *Surface Science Reports* vol. 48, no. 5 (2003), pp. 53–229.

[17] Wolfgang Tress. “Device physics of organic solar cells”. PhD thesis. Technische Universität Dresden, 2011.

[18] RC Haddon, AS Perel, RC Morris, TTM Palstra, AF Hebard, and RM Fleming. “C_{60} thin film transistors”. In: *Applied Physics Letters* vol. 67, no. 1 (1995), pp. 121–123.

[19] Heinz Bässler and Anna Köhler. “Charge transport in organic semiconductors”. In: *Unimolecular and supramolecular electronics I*. Springer, 2011, pp. 1–65.

[20] Zachary B Henson, Klaus Müllen, and Guillermo C Bazan. “Design strategies for organic semiconductors beyond the molecular formula”. In: *Nature chemistry* vol. 4, no. 9 (2012), pp. 699–704.

[21] Dr. C. Melzer Prof. Dr. R. Schmechel. *Lecture notes* "*Organische Halbleiter*". Darmstadt: Technische Universität Darmstadt FB 11 Material- und Geowissenschaften Fachgebiet Elektronische Materialeigenschaften, 2008/2009.

[22] Brian A Gregg and Mark C Hanna. “Comparing organic to inorganic photovoltaic cells: Theory, experiment, and simulation”. In: *Journal of Applied Physics* vol. 93, no. 6 (2003), pp. 3605–3614.

[23] E. Mankel. “Elektronische Eigenschaften von Heterosystemen organischer und anorganischer Halbleiter: Praeparation, Modifikation und Charakterisierung von Grenzflächen und Kompositen”. PhD thesis. Technische Universität Darmstadt, 2010.

[24] Julia Maibach. “Preparation and Characterization of Solution Processed Organic Semiconductor Interfaces: Electronic Properties of Thiophene-Fullerene based Donor-Acceptor Systems”. PhD thesis. Darmstadt: Technische Universität, 2014.

[25] René Pekkola. “Electronic Structure of Solid-State Dye-Sensitized Solar Cells: Synchrotron Induced Photoelectron Spectroscopy on Nanocrystalline TiO_2, Newly Developed Dyes and Spiro-MeOTAD”. PhD thesis. Technische Universität Darmstadt, 2014.

[26] Ze-Lei Guan, Jong Bok Kim, He Wang, Cherno Jaye, Daniel A. Fischer, Yueh-Lin Loo, and Antoine Kahn. “Direct determination of the electronic structure of the poly(3-hexylthiophene):phenyl-[6,6]-C61 butyric acid methyl ester blend”. In: *ORGANIC ELECTRONICS* vol. 11, no. 11 (2010), 1779–1785.

[27] Walter Schottky. “Zur Halbleitertheorie der Sperrschicht-und Spitzengleichrichter”. In: *Zeitschrift für Physik* vol. 113, no. 5-6 (1939), pp. 367–414.

[28] Slawomir Braun, William R. Salaneck, and Mats Fahlman. "Energy-Level Alignment at Organic/Metal and Organic/Organic Interfaces". In: *Advanced Materials* vol. 21, no. 14-15 (2009), pp. 1450–1472.

[29] Harald Ibach and Hans Lüth. *Festkörperphysik: Einführung in die Grundlagen*. Springer-Verlag, 2009.

[30] Simon M Sze and Kwok K Ng. *Physics of semiconductor devices*. John Wiley & Sons, 2006.

[31] Andreas Klein. "Halbleitergrenzflächen". In: *lecture notes Technische Universität Darmstadt* vol. 11 (2000).

[32] J Maibach, E Mankel, T Mayer, and W Jaegermann. "The band energy diagram of PCBM–DH6T bulk heterojunction solar cells: synchrotron-induced photoelectron spectroscopy on solution processed DH6T: PCBM blends and in situ prepared PCBM/DH6T interfaces". In: *Journal of Materials Chemistry C* vol. 1, no. 45 (2013), pp. 7635–7642.

[33] Martin A Green, Keith Emery, Yoshihiro Hishikawa, Wilhelm Warta, and Ewan D Dunlop. "Solar cell efficiency tables (Version 45)". In: *Progress in photovoltaics: research and applications* vol. 23, no. 1 (2015), pp. 1–9.

[34] Steven K Hau, Hin-Lap Yip, Orb Acton, Nam Seob Baek, Hong Ma, and Alex K-Y Jen. "Interfacial modification to improve inverted polymer solar cells". In: *Journal of Materials Chemistry* vol. 18, no. 42 (2008), pp. 5113–5119.

[35] Frederik C Krebs. "Polymer solar cell modules prepared using roll-to-roll methods: knife-over-edge coating, slot-die coating and screen printing". In: *Solar Energy Materials and Solar Cells* vol. 93, no. 4 (2009), pp. 465–475.

[36] Harald Hoppea and Niyazi Serdar Sariciftci. "Organic solar cells: An overview". In: *J. Mater. Res* vol. 19, no. 7 (2004), p. 1925.

[37] Roland Steim, F René Kogler, and Christoph J Brabec. "Interface materials for organic solar cells". In: *Journal of Materials Chemistry* vol. 20, no. 13 (2010), pp. 2499–2512.

[38] Jeihyun Lee, Soohyung Park, Younjoo Lee, Hyein Kim, Dongguen Shin, Junkyeong Jeong, Kwangho Jeong, Sang Wan Cho, Hyunbok Lee, and Yeonjin Yi. "Electron transport mechanism of bathocuproine exciton blocking layer in organic photovoltaics". In: *Physical Chemistry Chemical Physics* vol. 18, no. 7 (2016), pp. 5444–5452.

[39] Sara Trost, Tim Becker, Andreas Polywka, Patrick Görrn, Marek F Oszajca, Norman A Luechinger, Detlef Rogalla, Mirko Weidner, Philip Reckers, Thomas Mayer, et al. "Avoiding Photoinduced Shunts in Organic Solar Cells by the Use of Tin Oxide (SnO_x) as Electron Extraction Material Instead of ZnO". In: *Advanced Energy Materials* (2016).

[40] Sara Trost, Andreas Behrendt, Tim Becker, Andreas Polywka, Patrick Görrn, and Thomas Riedl. "Tin Oxide (SnO_x) as Universal Light-Soaking Free Electron Extraction Material for Organic Solar Cells". In: *Advanced Energy Materials* vol. 5, no. 17 (2015).

[41] Hui Huang and Jinsong Huang. *Organic and Hybrid Solar Cells*. Springer, 2014.

[42] Kwanghee Lee, Jin Young Kim, Sung Heum Park, Sun Hee Kim, Shinuk Cho, and Alan J Heeger. “Air-Stable Polymer Electronic Devices”. In: *Advanced Materials* vol. 19, no. 18 (2007), pp. 2445–2449.

[43] AKK Kyaw, XW Sun, CY Jiang, GQ Lo, DW Zhao, and DL Kwong. “An inverted organic solar cell employing a sol-gel derived ZnO electron selective layer and thermal evaporated MoO_3 hole selective layer”. In: *Appl. Phys. Lett* vol. 93, no. 22 (2008), p. 221107.

[44] Chen Tao, Shengping Ruan, Guohua Xie, Xiangzi Kong, Liang Shen, Fanxu Meng, Caixia Liu, Xindong Zhang, Wei Dong, and Weiyou Chen. “Role of tungsten oxide in inverted polymer solar cells”. In: *Applied Physics Letters* vol. 94, no. 4 (2009), pp. 043311–1.

[45] Jonas Weickert, Haiyan Sun, Claudia Palumbiny, Holger Christian Hesse, and Lukas Schmidt-Mende. “Spray-deposited PEDOT: PSS for inverted organic solar cells”. In: *Solar Energy Materials and Solar Cells* vol. 94, no. 12 (2010), pp. 2371–2374.

[46] William J Potscavage Jr, Asha Sharma, and Bernard Kippelen. “Critical interfaces in organic solar cells and their influence on the open-circuit voltage”. In: *Accounts of chemical research* vol. 42, no. 11 (2009), pp. 1758–1767.

[47] A. Sharma, A. Haldi, W. J. Jr. Potscavage, P. J. Hotchkiss, S. R. Marder, and B. Kippelen. “Effects of surface modification of indium tin oxide electrodes on the performance of molecular multilayer organic photovoltaic devices”. In: *Journal of Materials Chemistry* (2009), pp. 5298–302.

[48] Markus C Scharber, David Mühlbacher, Markus Koppe, Patrick Denk, Christoph Waldauf, Alan J Heeger, and Christoph J Brabec. “Design rules for donors in bulk-heterojunction solar cells - Towards 10% energy-conversion efficiency”. In: *Advanced materials* vol. 18, no. 6 (2006), pp. 789–794.

[49] Peter Würfel. *Physik der Solarzellen*. Spektrum, Akad. Verlag, 1995.

[50] Bettina Späth. “Rückkontaktbildung von CdTe-Solarzellen”. PhD thesis. Technische Universität Darmstadt, 2007.

[51] Wolfgang Tress and Olle Inganäs. “Simple experimental test to distinguish extraction and injection barriers at the electrodes of (organic) solar cells with S-shaped current–voltage characteristics”. In: *Solar Energy Materials and Solar Cells* vol. 117 (2013), pp. 599–603.

[52] SH Demtsu and JR Sites. “Effect of back-contact barrier on thin-film CdTe solar cells”. In: *Thin Solid Films* vol. 510, no. 1 (2006), pp. 320–324.

[53] A. Wagenpfahl, D. Rauh, M. Binder, C. Deibel, and V. Dyakonov. “S-shaped current-voltage characteristics of organic solar devices”. In: *PHYSICAL REVIEW B* vol. 82, no. 11 (2010).

[54] Bernhard Ecker, Hans-Joachim Egelhaaf, Roland Steim, Jürgen Parisi, and Elizabeth von Hauff. “Understanding S-Shaped Current Voltage Characteristics in Organic Solar Cells Containing a TiO_x Interlayer with Impedance Spectroscopy and Equivalent Circuit Analysis”. In: *The Journal of Physical Chemistry C* vol. 116, no. 31 (2012), pp. 16333–16337.

[55] Wolfgang Tress, Karl Leo, and Moritz Riede. “Influence of Hole-Transport Layers and Donor Materials on Open-Circuit Voltage and Shape of I–V Curves of Organic Solar Cells”. In: *Advanced Functional Materials* vol. 21, no. 11 (2011), pp. 2140–2149.

[56] Marc Burgelman, Peter Nollet, and Stefaan Degrave. “Modelling polycrystalline semiconductor solar cells”. In: *Thin Solid Films* vol. 361 (2000), pp. 527–532.

[57] J. C. Wang, X. C. Ren, S. Q. Shi, C. W. Leung, and Paddy K. L. Chan. “Charge accumulation induced S-shape J-V curves in bilayer heterojunction organic solar cells”. In: *ORGANIC ELECTRONICS* vol. 12, no. 6 (2011), 880–885.

[58] Jen-Chun Wang, Wei-Tse Weng, Meng-Yen Tsai, Ming-Kun Lee, Sheng-Fu Horng, Tsong-Pyng Perng, Chi-Chung Kei, Chih-Chieh Yu, and Hsin-Fei Meng. “Highly efficient flexible inverted organic solar cells using atomic layer deposited ZnO as electron selective layer”. In: *Journal of Materials Chemistry* vol. 20, no. 5 (2010), pp. 862–866.

[59] Zhenhua Lin, Changyun Jiang, Chunxiang Zhu, and Jie Zhang. “Development of inverted organic solar cells with TiO_2 interface layer by using low-temperature atomic layer deposition”. In: *ACS applied materials & interfaces* vol. 5, no. 3 (2013), pp. 713–718.

[60] Chen-Yan Li, Ten-Chin Wen, Tsung-Hsun Lee, Tzung-Fang Guo, Ying-Chang Lin, Yao-Jane Hsu, et al. “An inverted polymer photovoltaic cell with increased air stability obtained by employing novel hole/electron collecting layers”. In: *Journal of Materials Chemistry* vol. 19, no. 11 (2009), pp. 1643–1647.

[61] Roland Steim, Stelios A Choulis, Pavel Schilinsky, and Christoph J Brabec. “Interface modification for highly efficient organic photovoltaics”. In: *Applied Physics Letters* vol. 92, no. 9 (2008), p. 093303.

[62] Anton Sundqvist, Oskar J Sandberg, Mathias Nyman, Jan-Henrik Smått, and Ronald Österbacka. “Origin of the S-Shaped JV Curve and the Light-Soaking Issue in Inverted Organic Solar Cells”. In: *Advanced Energy Materials* (2016).

[63] Sylvain Chambon, Elodie Destouesse, Bertrand Pavageau, Lionel Hirsch, and Guillaume Wantz. “Towards an understanding of light activation processes in titanium oxide based inverted organic solar cells”. In: *Journal of Applied Physics* vol. 112, no. 9 (2012), p. 094503.

[64] Wolfgang Tress, Annette Petrich, Markus Hummert, Moritz Hein, Karl Leo, and Moritz Riede. “Imbalanced mobilities causing S-shaped IV curves in planar heterojunction organic solar cells”. In: *Applied Physics Letters* vol. 98, no. 6 (2011), p. 063301.

[65] Wolfgang Tress, Karl Leo, and Moritz Riede. “Optimum mobility, contact properties, and open-circuit voltage of organic solar cells: A drift-diffusion simulation study”. In: *Physical Review B* vol. 85, no. 15 (2012), p. 155201.

[66] Jenny Nelson, James Kirkpatrick, and P Ravirajan. “Factors limiting the efficiency of molecular photovoltaic devices”. In: *Physical Review B* vol. 69, no. 3 (2004), p. 035337.

[67] Benjamin Y Finck and Benjamin J Schwartz. “Drift-Diffusion Modeling of the Effects of Structural Disorder and Carrier Mobility on the Performance of Organic Photovoltaic Devices”. In: *Physical Review Applied* vol. 4, no. 3 (2015), p. 034006.

[68] Oskar J Sandberg, Mathias Nyman, and Ronald Österbacka. “Effect of contacts in organic bulk heterojunction solar cells”. In: *Physical Review Applied* vol. 1, no. 2 (2014), p. 024003.

[69] Ankit Kumar, Srinivas Sista, and Yang Yang. “Dipole induced anomalous S-shape IV curves in polymer solar cells”. In: *J. Appl. Phys* vol. 105, no. 9 (2009), p. 094512.

[70] Junghwan Kim, Geunjin Kim, Youna Choi, Jongjin Lee, Sung Heum Park, and Kwanghee Lee. “Light-soaking issue in polymer solar cells: Photoinduced energy level alignment at the sol-gel processed metal oxide and indium tin oxide interface”. In: *Journal of Applied Physics* vol. 111, no. 11 (2012).

[71] Takayuki Kuwabara, Katsuhiro Yano, Takahiro Yamaguchi, Tetsuya Taima, Kohshin Takahashi, Donghyun Son, and Kazuhiro Marumoto. “Mechanistic Investigation into the Light Soaking Effect Observed in Inverted Polymer Solar Cells Containing Chemical Bath Deposited Titanium Oxide”. In: *The Journal of Physical Chemistry C* vol. 119, no. 10 (2015), pp. 5274–5280.

[72] Markus Glatthaar, Moritz Riede, Nicholas Keegan, Kristian Sylvester-Hvid, Birger Zimmermann, Michael Niggemann, Andreas Hinsch, and Andreas Gombert. “Efficiency limiting factors of organic bulk heterojunction solar cells identified by electrical impedance spectroscopy”. In: *Solar Energy Materials and Solar Cells* vol. 91, no. 5 (2007), pp. 390–393.

[73] K Pomoni, A Vomvas, and Chr Trapalis. “Transient photoconductivity of nanocrystalline TiO_2 sol–gel thin films”. In: *Thin Solid Films* vol. 479, no. 1 (2005), pp. 160–165.

[74] Shang-Di Mo and WY Ching. “Electronic and optical properties of three phases of titanium dioxide: rutile, anatase, and brookite”. In: *Physical Review B* vol. 51, no. 19 (1995), p. 13023.

[75] Krizu. *Eigenes Werk, CC BY-SA 3.0, Anatase crystal structure*. URL: `https://commons.wikimedia.org/w/index.php?curid=19058518`, visited on: Sept. 4, 2017.

[76] Solid State. *Eigenes Werk, CC BY-SA 3.0, Rutile crystal structure*. URL: `https://commons.wikimedia.org/w/index.php?curid=20586067`, visited on: Sept. 4, 2017.

[77] Ulrike Diebold, Nancy Ruzycki, Gregory S Herman, and Annabella Selloni. “One step towards bridging the materials gap: surface studies of TiO_2 anatase”. In: *Catalysis Today* vol. 85, no. 2 (2003), pp. 93–100.

[78] Francesca Nunzi, Edoardo Mosconi, Loriano Storchi, Enrico Ronca, Annabella Selloni, Michael Gratzel, and Filippo De Angelis. “Inherent electronic trap states in TiO_2 nanocrystals: effect of saturation and sintering”. In: *Energy & Environmental Science* vol. 6, no. 4 (2013), pp. 1221–1229.

[79] Rob Lavinsky. *iRocks.com CC-BY-SA-3.0*. URL: `https://upload.wikimedia.org/wikipedia/commons/e/ef/Anatase-238983.jpg`, visited on:

[80] Wilhelm Hebenstreit, Nancy Ruzycki, Gregory S Herman, Yufei Gao, and Ulrike Diebold. “Scanning tunneling microscopy investigation of the TiO_2 anatase (101) surface”. In: *Physical Review B* vol. 62, no. 24 (2000), R16334.

[81] Konrad Christian Norbert Schwanitz. “The TiO_2/Dye/Electrolyte Interface in the Dye Sensitized Solar Cell: A Synchrotron Induced Photoelectron Spectroscopy Study”. PhD thesis. Darmstadt: Technische Universität Darmstadt, 2008.

[82] Xue-Qing Gong, Annabella Selloni, Matthias Batzill, and Ulrike Diebold. “Steps on anatase TiO2 (101)”. In: *Nature materials* vol. 5, no. 8 (2006), pp. 665–670.

[83] R. Asahi, Y. Taga, W. Mannstadt, and A. J. Freeman. “Electronic and optical properties of anatase TiO_2 ”. In: *Phys. Rev. B* vol. 61 (11 2000), pp. 7459–7465.

[84] A. G. Thomas, W. R. Flavell, A. R. Kumarasinghe, A. K. Mallick, D. Tsoutsou, G. C. Smith, R. Stockbauer, S. Patel, M. Grätzel, and R. Hengerer. “Resonant photoemission of anatase TiO_2 (101) and (001) single crystals”. In: *Physical Review B* vol. 67, no. 3 (2003), p. 035110.

[85] AG Thomas, WR Flavell, AK Mallick, AR Kumarasinghe, D Tsoutsou, N Khan, C Chatwin, S Rayner, GC Smith, RL Stockbauer, et al. “Comparison of the electronic structure of anatase and rutile TiO_2 single-crystal surfaces using resonant photoemission and X-ray absorption spectroscopy”. In: *Physical Review B* vol. 75, no. 3 (2007), p. 035105.

[86] Martin Setvín, Cesare Franchini, Xianfeng Hao, Michael Schmid, Anderson Janotti, Merzuk Kaltak, Chris G Van de Walle, Georg Kresse, and Ulrike Diebold. “Direct view at excess electrons in TiO_2 rutile and anatase”. In: *Physical review letters* ().

[87] Tara Dhakal, Daniel Vanhart, Rachel Christian, Abhishek Nandur, Anju Sharma, and Charles R. Westgate. “Growth morphology and electrical/optical properties of Al-doped ZnO thin films grown by atomic layer deposition”. In: *Journal of Vacuum Science & Technology A: Vacuum, Surfaces, and Films* vol. 30, no. 2 (2012), pp. 021202–10.

[88] Do-Joong Lee, Hyun-Mi Kim, Jang-Yeon Kwon, Hyoji Choi, Soo-Hyun Kim, and Ki-Bum Kim. “Structural and Electrical Properties of Atomic Layer Deposited Al-Doped ZnO Films”. In: *Advanced Functional Materials* vol. 21, no. 3 (2011), pp. 448–455.

[89] Parag Banerjee, Won-Jae Lee, Ki-Ryeol Bae, Sang Bok Lee, and Gary W Rubloff. “Structural, electrical, and optical properties of atomic layer deposition Al-doped ZnO films”. In: *Journal of Applied Physics* vol. 108, no. 4 (2010), p. 043504.

[90] Tao Liu and Alessandro Troisi. “What makes fullerene acceptors special as electron acceptors in organic solar cells and how to replace them”. In: *Advanced Materials* vol. 25, no. 7 (2013), pp. 1038–1041.

[91] Ryan D Pensack, Changhe Guo, Kiarash Vakhshouri, Enrique D Gomez, and John B Asbury. “Influence of acceptor structure on barriers to charge separation in organic photovoltaic materials”. In: *The Journal of Physical Chemistry C* vol. 116, no. 7 (2012), pp. 4824–4831.

[92] Donald B Boyd and Zdeněk Slanina. “Introduction and foreword to the special issue commemorating the 30th anniversary of Eiji Osawas C_{60} paper”. In: *Journal of Molecular Graphics and Modelling* vol. 19, no. 2 (2001), pp. 181–184.

[93] Harold W Kroto, James R Heath, Sean C O’Brien, Robert F Curl, Richard E Smalley, et al. “C_{60}: buckminsterfullerene”. In: *Nature* vol. 318, no. 6042 (1985), pp. 162–163.

[94] Jan C Hummelen, Brian W Knight, F LePeq, Fred Wudl, Jie Yao, and Charles L Wilkins. “Preparation and characterization of fulleroid and methanofullerene derivatives”. In: *The Journal of Organic Chemistry* vol. 60, no. 3 (1995), pp. 532–538.

[95] Julia Maibach, Torben Adermann, Tobias Glaser, Ralph Eckstein, Eric Mankel, Annemarie Pucci, Klaus Müllen, Uli Lemmer, Manuel Hamburger, Thomas Mayer, et al. "Impact of processing on the chemical and electronic properties of phenyl-C61-butyric acid methyl ester". In: *Journal of Materials Chemistry C* vol. 2, no. 37 (2014), pp. 7934–7942.

[96] Th Mayer, A Klein, O Lang, C Pettenkofer, and W Jaegermann. "H_2O adsorption on the layered chalcogenide semiconductors WSe_2, InSe and GaSe". In: *Surface science* vol. 269 (1992), pp. 909–914.

[97] O. Bondarchuk and I. Lyubinetsky. "Preparation of TiO_2 (110)-(1x1) surface via UHV cleavage: An scanning tunneling microscopy study". In: *Review of Scientific Instruments* vol. 78, no. 11 (2007), pp. 113907–3.

[98] Olga Dulub and Ulrike Diebold. "Preparation of a pristine TiO_2 anatase (101) surface by cleaving". In: *Journal of Physics: Condensed Matter* vol. 22, no. 8 (2010), p. 084014.

[99] Tommi Kääriäinen, David Cameron, Marja-Leena Kääriäinen, and Arthur Sherman. *Atomic Layer Deposition: Principles, Characteristics, and Nanotechnology Applications*. John Wiley & Sons, 2013.

[100] Tuomo Suntola. "Atomic layer epitaxy". In: *Materials Science Reports* vol. 4, no. 5 (1989), pp. 261–312.

[101] Arthur Sherman. *Chemical vapor deposition for microelectronics: principles, technology, and applications*. Noyes Publications, Park Ridge, NJ, 1987.

[102] Cepheiden. *Schematische Darstellung eines ALD-Reaktionszyklus für ein ALD-System aus zwei Komponenten*. URL: https://de.wikipedia.org/wiki/Atomlagenabscheidung#/media/File:Atomic_layer_deposition_-_schematic_cycle_DE.svg, visited on: May 5, 2015.

[103] L. Holland. *Vacuum deposition of thin films*. Wiley, 1956.

[104] Corinna Hein. "Anpassung der elektronischen Struktur an organischen Heterokontakten". PhD thesis. Technische Universität Darmstadt, 2012.

[105] Germany ROSCHWEGE GmbH. *Datasheet -High Efficacy UV LED Emitter 365nm / 11W RSW-P11-365-0*. URL: http://www.produktinfo.conrad.com/datenblaetter/475000-499999/491253-da-01-en-ALU_STAR_LZ_ML_LED_UV_365NM_11W.pdf, visited on: Jan. 8, 2016.

[106] P.Hoffmann. *Datenblatt zum Strahlrohr U49-PGM/2 am BESSY II in Berlin*. URL: https://www.helmholtz-berlin.de/pubbin/igama_output?modus=einzel&sprache=de&gid=1656&typoid=37587, visited on: May 3, 2017.

[107] P.Hoffmann. *Datenblatt zum Strahlrohr TGM-7 am BESSY II in Berlin*. URL: http://www.helmholtz-berlin.de/pubbin/igama_output?modus=einzel&sprache=de&gid=1622&typoid=, visited on: May 3, 2017.

[108] Heinrich Hertz. "Über einen Einfluss des ultravioletten Lichtes auf die electrische Entladung". In: *Annalen der Physik* vol. 267, no. 8 (1887), pp. 983–1000.

[109] Albert Einstein. "Über einen die Erzeugung und Verwandlung des Lichtes betreffenden heuristischen Gesichtspunkt". In: *Annalen der physik* vol. 322, no. 6 (1905), pp. 132–148.

[110] D. Briggs. “Handbook of X-ray Photoelectron Spectroscopy C. D. Wanger, W. M. Riggs, L. E. Davis, J. F. Moulder and G. E.Muilenberg Perkin-Elmer Corp., Physical Electronics Division, Eden Prairie, Minnesota, USA, 1979. 190 pp. 195”. In: *Surface and Interface Analysis* vol. 3, no. 4 (1981).

[111] Kenjiro Oura, VG Lifshits, Alexander Saranin, AV Zotov, and M Katayama. *Surface science: An introduction*. Springer Science & Business Media, 2013.

[112] Andreas Decker. “Farbstoffsensibilisierung von Dünnschichtsilizium für photovoltaische Anwendungen”. PhD thesis. Technische Universität Darmstadt, 2012.

[113] Andreas Klein, Thomas Mayer, Andreas Thissen, and Wolfram Jaegermann. “Photoelectron spectroscopy in materials science and physical chemistry”. In: *Bunsen-Magazin* vol. 10, no. 4 (2008), pp. 124–139.

[114] J. J. Yeh and I. Lindau. “Atomic subshell photoionization cross sections and asymmetry parameters: $1 \leq Z \leq 103$”. In: *Atomic Data and Nuclear Data Tables* vol. 32, no. 1 (1985), pp. 1–155.

[115] CJ Powell and A Jablonski. *NIST Electron Inelastic-Mean-Free-Path Database, Version 1.2, Standard Reference Data Program Database 71*. 2010.

[116] W. H. Gries. “A Universal Predictive Equation for the Inelastic Mean Free Pathlengths of X-ray Photoelectrons and Auger Electrons”. In: *Surface and Interface Analysis* vol. 24, no. 1 (1996), pp. 38–50.

[117] Mirko Weidner. “Fermi Level Determination in Tin Oxide by Photoelectron Spectroscopy: Relation to Optoelectronic Properties; Band Bending at Surfaces and Interfaces; Modulation Doping”. PhD thesis. Darmstadt: Technische Universität, 2016.

[118] Stephan Hüfner. *Photoelectron spectroscopy: principles and applications*. Springer Science & Business Media, 2013.

[119] Clinton Davisson and Lester H Germer. “Diffraction of electrons by a crystal of nickel”. In: *Physical review* vol. 30, no. 6 (1927), p. 705.

[120] Gerhard Ertl and Jürgen Küppers. *Low energy electrons and surface chemistry*. VCH Verlagsgellschaft. Distribution, USA and Canada, VCH Publishers, 1985.

[121] Louis de Broglie. “XXXV. A tentative theory of light quanta”. In: *Philosophical Magazine Series 6* vol. 47, no. 278 (1924), pp. 446–458.

[122] Michel André Van Hove and Shuk Yin Tong. *Surface crystallography by LEED: theory, computation and structural results*. Vol. 2. Springer Science & Business Media, 2012.

[123] Ron Jenkins and Robert L. Snyder. “Diffraction Theory”. In: *Introduction to X-ray Powder Diffractometry*. John Wiley & Sons, Inc., 1996, pp. 47–95.

[124] William Henry Bragg and William Lawrence Bragg. “The reflection of X-rays by crystals”. In: *Proceedings of the Royal Society of London. Series A, Containing Papers of a Mathematical and Physical Character* vol. 88, no. 605 (1913), pp. 428–438.

[125] Wikimedia Commons by Dipl.-Phys. Matthias M. *Bragg diffraction*. URL: https://commons.wikimedia.org/w/index.php?curid=3528588, visited on: July 25, 2016.

[126] Olaf J. Schumann. URL: http://clip4.sourceforge.net/, visited on: 2009.

[127] Bertram Eugene Warren. *X-ray Diffraction*. Courier Corporation, 1969.

[128] Paul Scherrer. "Bestimmung der inneren Struktur und der Größe von Kolloidteilchen mittels Röntgenstrahlen". In: *Kolloidchemie Ein Lehrbuch*. Springer, 1912, pp. 387–409.

[129] Joseph Goldstein. *Scanning electron microscopy and x-ray microanalysis*. 3. ed. New York, NY: Springer, 2003.

[130] Wikimedia Commons by Freundchen. *Pear interaction SEM*. URL: https://commons.wikimedia.org/wiki/File:Pear_interaction_SEM_german.svg, visited on: July 25, 2016.

[131] V. J. Morris, A. R. Kirby, and A. P. Gunning. *Atomic force microscopy for biologists*. 2. ed. London: Imperial College Press, 2010.

[132] J Tauc, R Grigorovici, and A Vancu. "Optical properties and electronic structure of amorphous germanium". In: *physica status solidi (b)* vol. 15, no. 2 (1966), pp. 627–637.

[133] Sebastian Wilken, Jürgen Parisi, and Holger Borchert. "Role of Oxygen Adsorption in Nanocrystalline ZnO Interfacial Layers for Polymer–Fullerene Bulk Heterojunction Solar Cells". In: *The Journal of Physical Chemistry C* vol. 118, no. 34 (2014), pp. 19672–19682.

[134] Zheng Xu, Li-Min Chen, Guanwen Yang, Chun-Hao Huang, Jianhui Hou, Yue Wu, Gang Li, Chain-Shu Hsu, and Yang Yang. "Vertical phase separation in Poly (3-hexylthiophene): fullerene derivative blends and its advantage for inverted structure solar cells". In: *Advanced Functional Materials* vol. 19, no. 8 (2009), pp. 1227–1234.

[135] Ken Onda, Bin Li, and Hrvoje Petek. "Two-photon photoemission spectroscopy of TiO_2 (110) surfaces modified by defects and O_2 or H_2O adsorbates". In: *Phys. Rev. B* vol. 70 (4 2004), p. 045415.

[136] Philip Reckers, Mariel Dimamay, Joachim Klett, Sara Trost, Kirill Zilberberg, Thomas Riedl, Bruce A. Parkinson, Joachim Brötz, Wolfram Jaegermann, and Thomas Mayer. "Deep and Shallow TiO_2 Gap States on Cleaved Anatase Single Crystal (101) Surfaces, Nanocrystalline Anatase Films, and ALD Titania Ante and Post Annealing". In: *The Journal of Physical Chemistry C* vol. 119, no. 18 (2015), pp. 9890–9898.

[137] R Hengerer, B Bolliger, M Erbudak, and M Grätzel. "Structure and stability of the anatase TiO_2 (101) and (001) surfaces". In: *Surface science* vol. 460, no. 1 (2000), pp. 162–169.

[138] GS Herman and Y Gao. "Growth of epitaxial anatase (001) and (101) films". In: *Thin Solid Films* vol. 397, no. 1 (2001), pp. 157–161.

[139] Geert Silversmit, Geert De Doncker, and Roger De Gryse. "A Mineral TiO_2 (001) Anatase Crystal Examined by XPS". In: *Surface Science Spectra* vol. 9, no. 1 (2002), pp. 21–29.

[140] D. A. Shirley. "High-Resolution X-Ray Photoemission Spectrum of the Valence Bands of Gold". In: *Physical Review B* vol. 5, no. 12 (1972). PRB, pp. 4709–4714.

[141] Kai-Lin Ou, Delvin Tadytin, K. Xerxes Steirer, Diogenes Placencia, Mike Nguyen, Paul Lee, and Neal R. Armstrong. "Titanium dioxide electron-selective interlayers created by chemical vapor deposition for inverted configuration organic solar cells". In: *Journal of Materials Chemistry A* vol. 1, no. 23 (2013), pp. 6794–6803.

[142] R. Sanjines, H. Tang, H. Berger, F. Gozzo, G. Margaritondo, and F. Levy. "Electronic structure of anatase TiO_2 oxide". In: *Journal of Applied Physics* vol. 75, no. 6 (1994), pp. 2945–2951.

[143] Konrad Schwanitz, Ulrich Weiler, Ralf Hunger, Thomas Mayer, and Wolfram Jaegermann. "Synchrotron-Induced Photoelectron Spectroscopy of the Dye-Sensitized Nanocrystalline TiO_2/ Electrolyte Interface:Band Gap States and Their Interaction with Dye and Solvent Molecules". In: *The Journal of Physical Chemistry C* vol. 111, no. 2 (2006), pp. 849–854.

[144] Cristiana Di Valentin, Gianfranco Pacchioni, and Annabella Selloni. "Reduced and n-Type Doped TiO_2: Nature of Ti^{3+} Species". In: *The Journal of Physical Chemistry C* vol. 113, no. 48 (2009), pp. 20543–20552.

[145] Verena Pfeifer. "Interface Properties of Anatase and Rutile". Masterthesis. Technical University of Darmstadt - Surface Science Division, 2013.

[146] J.-M. Pan, B. L. Maschhoff, U. Diebold, and T. E. Madey. "Interaction of water, oxygen, and hydrogen with TiO_2 (110) surfaces having different defect densities". In: *Journal of Vacuum Science & Technology A* vol. 10, no. 4 (1992), pp. 2470–2476.

[147] ML Knotek, VO Jones, and Victor Rehn. "Photon-stimulated desorption of ions". In: *Physical Review Letters* vol. 43, no. 4 (1979), p. 300.

[148] Masakazu Anpo, Katsuichi Chiba, Masanori Tomonari, Salvatore Coluccia, Michel Che, and Marye Anne Fox. "Photocatalysis on Native and Platinum-Loaded TiO_2 and ZnO Catalysts. Origin of Different Reactivities on Wet and Dry Metal Oxides". In: *Bulletin of the Chemical Society of Japan* vol. 64, no. 2 (1991), pp. 543–551.

[149] Verena Pfeifer, Paul Erhart, Shunyi Li, Karsten Rachut, Jan Morasch, Joachim Brötz, Philip Reckers, Thomas Mayer, Sven Rühle, Arie Zaban, Ivan Mora Sero, Juan Bisquert, Wolfram Jaegermann, and Andreas Klein. "Energy Band Alignment between Anatase and Rutile TiO_2 ". In: *The Journal of Physical Chemistry Letters* (2013), pp. 4182–4187.

[150] E. A. Kraut, R. W. Grant, J. R. Waldrop, and S. P. Kowalczyk. "Semiconductor core-level to valence-band maximum binding-energy differences: Precise determination by x-ray photoelectron spectroscopy". In: *Phys. Rev. B* vol. 28 (4 1983), pp. 1965–1977.

[151] Specs. *Quantification in XPS using SpecsLab and CasaXPS*. Ed. by Specs. 2009.

[152] G Priebe, B Pietzak, and R Könenkamp. "Determination of transport parameters in fullerene films". In: *Applied physics letters* vol. 71 (1997), pp. 2160–2162.

[153] TW Ng, MF Lo, ZT Liu, FL Wong, SL Lai, MK Fung, CS Lee, and ST Lee. "Substrate effects on the interface electronic properties of organic photovoltaic devices with an inverted C_{60}/CuPc junction". In: *Journal of Applied Physics* vol. 106, no. 11 (2009), p. 4501.

[154] SKM Jönsson, Elin Carlegrim, Fengling Zhang, William R Salaneck, and Mats Fahlman. "Photoelectron spectroscopy of the contact between the cathode and the active layers in plastic solar cells: the role of LiF". In: *Japanese journal of applied physics* vol. 44, no. 6R (2005), p. 3695.

[155] PJ Benning, DM Poirier, TR Ohno, Y Chen, MB Jost, F Stepniak, GH Kroll, JH Weaver, J Fure, and RE Smalley. "C_{60} and C_{70} fullerenes and potassium fullerides". In: *Physical Review B* vol. 45, no. 12 (1992), p. 6899.

[156] OV Molodtsova and M Knupfer. "Electronic properties of the organic semiconductor interfaces CuPc/C_{60} and C_{60}/CuPc". In: *Journal of applied physics* vol. 99, no. 5 (2006), p. 3704.

[157] YC Zhou, ZT Liu, JX Tang, Chun Sing Lee, and Shuit Tong Lee. "Substrate dependence of energy level alignment at the donor–acceptor interface in organic photovoltaic devices". In: *Journal of Electron Spectroscopy and Related Phenomena* vol. 174, no. 1 (2009), pp. 35–39.

[158] JX Tang, YC Zhou, ZT Liu, Chun Sing Lee, and Shuit Tong Lee. "Interfacial electronic structures in an organic double-heterostructure photovoltaic cell". In: *Applied Physics Letters* vol. 93, no. 4 (2008), p. 043512.

[159] SC Veenstra, A Heeres, G Hadziioannou, GA Sawatzky, and HT Jonkman. "On interface dipole layers between C_{60} and Ag or Au". In: *Applied Physics A* vol. 75, no. 6 (2002), pp. 661–666.

[160] Corinna Hein, Eric Mankel, Thomas Mayer, and Wolfram Jaegermann. "Engineering the electronic structure of the ZnPc/C_{60} heterojunction by temperature treatment". In: *Solar Energy Materials and Solar Cells* vol. 94, no. 4 (2010), pp. 662–667.

[161] P Reinke and P Oelhafen. "In situ photoelectron spectroscopy investigation of silicon cluster growth on fullerene surfaces". In: *Physical Review B* vol. 71, no. 4 (2005), p. 045420.

[162] R. W. Lof, M. A. van Veenendaal, B. Koopmans, H. T. Jonkman, and G. A. Sawatzky. "Band gap, excitons, and Coulomb interaction in solid C_{60}". In: *Physical Review Letters* vol. 68, no. 26 (1992), pp. 3924–3927.

[163] Hiroyuki Yoshida. "Low-energy inverse photoemission study on the electron affinities of fullerene derivatives for organic photovoltaic cells". In: *The Journal of Physical Chemistry C* vol. 118, no. 42 (2014), pp. 24377–24382.

[164] Kaname Kanai, Kouki Akaike, Kiichirou Koyasu, Kentaro Sakai, Toshio Nishi, Yasunori Kamizuru, Tatsuhiko Nishi, Yukio Ouchi, and Kazuhiko Seki. "Determination of electron affinity of electron accepting molecules". In: *Applied Physics A: Materials Science & Processing* vol. 95 (2009), pp. 309–313.

[165] Wolfgang Brütting. *Physics of organic semiconductors*. John Wiley & Sons, 2006.

[166] Gabriel P López, David G Castner, and Buddy D Ratner. "XPS O 1s binding energies for polymers containing hydroxyl, ether, ketone and ester groups". In: *Surface and interface analysis* vol. 17, no. 5 (1991), pp. 267–272.

[167] Youjun He, Guangjin Zhao, Bo Peng, and Yongfang Li. "High-Yield Synthesis and Electrochemical and Photovoltaic Properties of Indene-C_{70}*Bisadduct*". In: *Advanced Functional Materials* vol. 20, no. 19 (2010), pp. 3383–3389.

[168] Matthias H Richter, Daniel Friedrich, and Dieter Schmeißer. “Valence and Conduction band states of PCBM as probed by photoelectron spectroscopy at resonant excitation”. In: *BioNanoScience* vol. 2, no. 1 (2012), pp. 59–65.

[169] H Schmidt, K Zilberberg, S Schmale, H Flügge, T Riedl, and W Kowalsky. “Transient characteristics of inverted polymer solar cells using titaniumoxide interlayers”. In: *Applied Physics Letters* vol. 96, no. 24 (2010), p. 243305.

[170] S. Gutmann, M. A. Wolak, M. Conrad, M. M. Beerbom, and R. Schlaf. “Effect of ultraviolet and x-ray radiation on the work function of TiO_2 surfaces”. In: *Journal of Applied Physics* vol. 107, no. 10 (2010).

[171] Soeren Porsgaard, Peng Jiang, Ferenc Borondics, Stefan Wendt, Zhi Liu, Hendrik Bluhm, Flemming Besenbacher, and Miquel Salmeron. “Charge state of gold nanoparticles supported on titania under oxygen pressure”. In: *Angewandte Chemie International Edition* vol. 50, no. 10 (2011), pp. 2266–2269.

[172] Nickolay Golego, SA Studenikin, and Michael Cocivera. “Effect of oxygen on transient photoconductivity in thin-film $Nb_xTi_{1-x}O_2$”. In: *Physical Review B* vol. 61, no. 12 (2000), p. 8262.

[173] Russell F Howe and Michael Gratzel. “EPR study of hydrated anatase under UV irradiation”. In: *Journal of Physical Chemistry* vol. 91, no. 14 (1987), pp. 3906–3909.

[174] Sergej Mezhenny, Petro Maksymovych, TL Thompson, Oliver Diwald, Dirk Stahl, SD Walck, and JT Yates. “STM studies of defect production on the TiO_2 (110)-(1×1) and TiO_2 (110)-(1×2) surfaces induced by UV irradiation”. In: *Chemical physics letters* vol. 369, no. 1 (2003), pp. 152–158.

[175] Jacques Jupille and Geoff Thornton. *Defects at Oxide Surfaces*. Springer, 2015.

[176] S Sato and JM White. “Photoassisted hydrogen production from titania and water”. In: *The Journal of Physical Chemistry* vol. 85, no. 5 (1981), pp. 592–594.

[177] H Van Damme and W Keith Hall. “Photoassisted decomposition of water at the gas-solid interface on titanium dioxide”. In: *Journal of the American Chemical Society* vol. 101, no. 15 (1979), pp. 4373–4374.

[178] Michael A. Henderson, Mingmin Shen, Zhi-Tao Wang, and Igor Lyubinetsky. “Characterization of the Active Surface Species Responsible for UV-Induced Desorption of O_2 from the Rutile TiO_2 (110) Surface”. In: *The Journal of Physical Chemistry C* vol. 117, no. 11 (2013), pp. 5774–5784.

[179] M. P. de Lara-Castells and Jeffrey L. Krause. “Theoretical study of the UV-induced desorption of molecular oxygen from the reduced TiO_2 (110) surface”. In: *The Journal of Chemical Physics* vol. 118, no. 11 (2003), pp. 5098–5105.

[180] Prashant V. Kamat, Idris Bedja, and Surat Hotchandani. “Photoinduced Charge Transfer between Carbon and Semiconductor Clusters. One-Electron Reduction of C_{60} in Colloidal TiO_2 Semiconductor Suspensions”. In: *The Journal of Physical Chemistry* vol. 98, no. 37 (1994), pp. 9137–9142.

[181] Prashant V Kamat, Matt Gevaert, and K Vinodgopal. “Photochemistry on semiconductor surfaces. Visible light induced oxidation of C_{60} on TiO_2 nanoparticles”. In: *The Journal of Physical Chemistry B* vol. 101, no. 22 (1997), pp. 4422–4427.

[182] Jaesang Lee, John D Fortner, Joseph B Hughes, and Jae-Hong Kim. “Photochemical production of reactive oxygen species by C_{60} in the aqueous phase during UV irradiation”. In: *Environmental science & technology* vol. 41, no. 7 (2007), pp. 2529–2535.

[183] Jaesang Lee, Min Cho, John D Fortner, Joseph B Hughes, and Jae-Hong Kim. “Transformation of aggregated C_{60} in the aqueous phase by UV irradiation”. In: *Environmental science & technology* vol. 43, no. 13 (2009), pp. 4878–4883.

[184] Yusuke Tanaka, Kaname Kanai, Yukio Ouchi, and Kazuhiko Seki. “Oxygen effect on the interfacial electronic structure of C_{60} film studied by ultraviolet photoelectron spectroscopy”. In: *Chemical physics letters* vol. 441, no. 1 (2007), pp. 63–67.

[185] A Hamed, YY Sun, YK Tao, RL Meng, and PH Hor. “Effects of oxygen and illumination on the in situ conductivity of C_{60} thin films”. In: *Physical Review B* vol. 47, no. 16 (1993), p. 10873.

[186] Chih-Ming Yang, Jian-Liang Liao, and Kuan-Cheng Chiu. “Diffusion of O_2 in C_{60} crystal by measuring the decay of electrical conductivity”. In: *Journal of applied physics* vol. 96 (2004), pp. 1934–1938.

[187] B. Pevzner, A. F. Hebard, and M. S. Dresselhaus. “Role of molecular oxygen and other impurities in the electrical transportand dielectric properties of C_{60} films”. In: *Phys. Rev. B* vol. 55 (24 1997), pp. 16439–16449.

[188] Roger Taylor, Jonathan P Parsons, Anthony G Avent, Steven P Rannard, T John Dennis, Jonathan P Hare, Harold W Kroto, and David RM Walton. “Degradation of C_{60} by light”. In: *Nature* vol. 351 (1991), p. 277.

[189] M. A. Henderson, W. S. Epling, C. H. F. Peden, and C. L. Perkins. “Insights into photoexcited electron scavenging processes on TiO_2 obtained from studies of the reaction of O_2 with OH groups adsorbed at electronic defects on TiO_2 (110)”. In: *Journal of Physical Chemistry B* vol. 107, no. 2 (2003), pp. 534–545.

[190] S. Moser, L. Moreschini, J. Jacimovic, O. S. Barisic, H. Berger, A. Magrez, Y. J. Chang, K. S. Kim, A. Bostwick, E. Rotenberg, L. Forro, and M. Grioni. “Tunable Polaronic Conduction in Anatase TiO_2 ”. In: *Physical Review Letters* vol. 110, no. 19 (2013), p. 5.

[191] Ashley N. Shultz, Winyann Jang, W.M. Hetherington III, D.R. Baer, Li-Qiong Wang, and M.H. Engelhard. “Comparative second harmonic generation and X-ray photoelectron spectroscopy studies of the UV creation and O_2 healing of Ti^{3+} defects on (110) rutile TiO_2 surfaces”. In: *Surface Science* vol. 339, no. 12 (1995), pp. 114 –124.

[192] Andriy Borodin and Michael Reichling. “Characterizing TiO_2 (110) surface states by their work function”. In: *Phys. Chem. Chem. Phys.* Vol. 13 (34 2011), pp. 15442–15447.

[193] G. S. Herman, Z. Dohnalek, N. Ruzycki, and U. Diebold. “Experimental Investigation of the Interaction of Water and Methanol with Anatase TiO_2 (101)”. In: *The Journal of Physical Chemistry B* vol. 107, no. 12 (2003), pp. 2788–2795.

[194] J. Blomquist, L. E. Walle, P. Uvdal, A. Borg, and A. Sandell. "Water Dissociation on Single Crystalline Anatase TiO_2 (001) Studied by Photoelectron Spectroscopy". In: *The Journal of Physical Chemistry C* vol. 112, no. 42 (2008), pp. 16616–16621.

[195] Lars Erik Walle, Anne Borg, EMJ Johansson, Stefan Plogmaker, Håkan Rensmo, Per Uvdal, and Anders Sandell. "Mixed dissociative and molecular water adsorption on anatase TiO_2 (101)". In: *The Journal of Physical Chemistry C* vol. 115, no. 19 (2011), pp. 9545–9550.

[196] Markus B Hugenschmidt, Lara Gamble, and Charles T Campbell. "The interaction of H_2O with a TiO_2 (110) surface". In: *Surface Science* vol. 302, no. 3 (1994), pp. 329–340.

[197] H.P. Marques, A.R. Canario, A.M.C. Moutinho, and O.M.N.D. Teodoro. "Tracking hydroxyl adsorption on TiO_2 (110) through secondary emission changes". In: *Applied Surface Science* vol. 255, no. 16 (2009), pp. 7389 –7393.

[198] Ken Onda, Bin Li, Jin Zhao, Kenneth D Jordan, Jinlong Yang, and Hrvoje Petek. "Wet electrons at the H_2O/TiO_2 (110) surface". In: *Science* vol. 308, no. 5725 (2005), pp. 1154–1158.

[199] Amy L. Linsebigler, Guangquan. Lu, and John T. Yates. "Photocatalysis on TiO_2 Surfaces: Principles, Mechanisms, and Selected Results". In: *Chemical Reviews* vol. 95, no. 3 (1995), pp. 735–758.

[200] W. Jaegermann and T. Mayer. "H_2O and OH on semiconductors - Figures 14 to 25". In: *Adsorbed Layers on Surfaces: Adsorbed Species on Surfaces and Adsorbate-Induced Surface Core Level Shifts*. Ed. by H.P. Bonzel. Berlin, Heidelberg: Springer Berlin Heidelberg, 2005, pp. 284–288.

[201] Th Mayer, C Pettenkofer, and W Jaegermann. "Synchrotron-induced photoelectron spectroscopy of semiconductor/electrolyte model interfaces: coadsorption of Br_2 and H_2O on WSe_2 (0001)". In: *The Journal of Physical Chemistry* vol. 100, no. 42 (1996), pp. 16966–16977.

[202] Estephania Lira, Jonas Ø Hansen, Peipei Huo, Ralf Bechstein, Patrick Galliker, Erik Lægsgaard, Bjørk Hammer, Stefan Wendt, and Flemming Besenbacher. "Dissociative and molecular oxygen chemisorption channels on reduced rutile TiO_2 (110): an STM and TPD study". In: *Surface Science* vol. 604, no. 21 (2010), pp. 1945–1960.

[203] Nikolay G. Petrik and Greg A. Kimmel. "Electron- and Hole-Mediated Reactions in UV-Irradiated O_2 Adsorbed on Reduced Rutile TiO_2 (110)". In: *The Journal of Physical Chemistry C* vol. 115, no. 1 (2011), pp. 152–164.

[204] Martin Setvín, Ulrich Aschauer, Philipp Scheiber, Ye-Fei Li, Weiyi Hou, Michael Schmid, Annabella Selloni, and Ulrike Diebold. "Reaction of O_2 with Subsurface Oxygen Vacancies on TiO_2 Anatase (101)". In: *Science* vol. 341, no. 6149 (2013), pp. 988–991.

[205] Ulrich Aschauer, Jia Chen, and Annabella Selloni. "Peroxide and superoxide states of adsorbed O_2 on anatase TiO_2 (101) with subsurface defects". In: *Phys. Chem. Chem. Phys.* Vol. 12 (40 2010), pp. 12956–12960.

[206] Michael A Henderson, William S Epling, Craig L Perkins, Charles HF Peden, and Ulrike Diebold. "Interaction of molecular oxygen with the vacuum-annealed TiO_2 (110) surface: molecular and dissociative channels". In: *The Journal of Physical Chemistry B* vol. 103, no. 25 (1999), pp. 5328–5337.

[207] Greg A. Kimmel and Nikolay G. Petrik. “Tetraoxygen on Reduced TiO_2 (110): Oxygen Adsorption and Reactions with Bridging Oxygen Vacancies”. In: *Phys. Rev. Lett.* Vol. 100 (19 2008), p. 196102.

[208] Karsten Reuter and Matthias Scheffler. “Composition, structure, and stability of RuO_2(110) as a function of oxygen pressure”. In: *Phys. Rev. B* vol. 65 (3 2001), p. 035406.

[209] Keith T. Butler, John Buckeridge, C. Richard A. Catlow, and Aron Walsh. “Crystal electron binding energy and surface work function control of tin dioxide”. In: *Phys. Rev. B* vol. 89 (11 2014), p. 115320.

[210] Haichao Liu, Alexander I Kozlov, Anguelina P Kozlova, Takafumi Shido, Kiyotaka Asakura, and Yasuhiro Iwasawa. “Active oxygen species and mechanism for low-temperature CO oxidation reaction on a TiO_2-supported Au catalyst prepared from Au (PPh3)(NO_3) and as-precipitated titanium hydroxide”. In: *Journal of Catalysis* vol. 185, no. 2 (1999), pp. 252–264.

[211] Michael A. Henderson. “A surface science perspective on photocatalysis”. In: *Surface Science Reports* vol. 66, no. 67 (2011), pp. 185 –297.

[212] Stefan Wendt, Phillip T Sprunger, Estephania Lira, Georg KH Madsen, Zheshen Li, Jonas Ø Hansen, Jesper Matthiesen, Asger Blekinge-Rasmussen, Erik Lægsgaard, Bjørk Hammer, et al. “The role of interstitial sites in the Ti 3d defect state in the band gap of titania”. In: *Science* vol. 320, no. 5884 (2008), pp. 1755–1759.

[213] N Aaron Deskins, Roger Rousseau, and Michel Dupuis. “Defining the role of excess electrons in the surface chemistry of TiO_2 ”. In: *The Journal of Physical Chemistry C* vol. 114, no. 13 (2010), pp. 5891–5897.

[214] J Meyer, P Görrn, S Hamwi, H-H Johannes, T Riedl, and W Kowalsky. “Indium-free transparent organic light emitting diodes with Al doped ZnO electrodes grown by atomic layer and pulsed laser deposition”. In: *Applied Physics Letters* vol. 93, no. 7 (2008), p. 073308.

[215] Nirton Cristi Silva Vieira, Edson Giuliani Ramos Fernandes, Alvaro Antonio Alencar de Queiroz, Francisco Eduardo Gontijo Guimarães, and Valtencir Zucolotto. “Indium tin oxide synthesized by a low cost route as SEGFET pH sensor”. In: *Materials Research* vol. 16, no. 5 (2013), pp. 1156–1160.

[216] Jongmin Lim and Chongmu Lee. “Effects of substrate temperature on the microstructure and photoluminescence properties of ZnO thin films prepared by atomic layer deposition”. In: *Thin Solid Films* vol. 515, no. 7 (2007), pp. 3335–3338.

[217] Klaus Ellmer, Andreas Klein, and Bernd Rech. *Transparent conductive zinc oxide: basics and applications in thin film solar cells*. Vol. 104. Springer Science & Business Media, 2007.

[218] AR Kumarasinghe, WR Flavell, AG Thomas, AK Mallick, D Tsoutsou, C Chatwin, S Rayner, P Kirkham, S Warren, S Patel, et al. “Electronic properties of the interface between p-CuI and anatase-phase n-TiO_2 single crystal and nanoparticulate surfaces: A photoemission study”. In: *The Journal of chemical physics* vol. 127, no. 11 (2007), p. 114703.

[219] W. Jaegermann, A. Klein, and T. Mayer. “Interface Engineering of Inorganic Thin-Film Solar Cells - Materials-Science Challenges for Advanced Physical Concepts”. In: *Advanced Materials* vol. 21, no. 42 (2009), pp. 4196–4206.

[220] Guangming Liu, W Jaegermann, Jianjun He, Villy Sundström, and Licheng Sun. “XPS and UPS characterization of the TiO_2/ZnPcGly heterointerface: Alignment of energy levels”. In: *The Journal of Physical Chemistry B* vol. 106, no. 23 (2002), pp. 5814–5819.

[221] Andreas Opitz, Johannes Frisch, Raphael Schlesinger, Andreas Wilke, and Norbert Koch. “Energy level alignment at interfaces in organic photovoltaic devices”. In: *Journal of Electron Spectroscopy and Related Phenomena* vol. 190 (2013), pp. 12–24.

[222] DRT Zahn, GN Gavrila, and M Gorgoi. “The transport gap of organic semiconductors studied using the combination of direct and inverse photoemission”. In: *CHEMICAL PHYSICS* vol. 325, no. 1 (2006), 99–112.

[223] Hua Gui Yang, Cheng Hua Sun, Shi Zhang Qiao, Jin Zou, Gang Liu, Sean Campbell Smith, Hui Ming Cheng, and Gao Qing Lu. “Anatase TiO_2 single crystals with a large percentage of reactive facets”. In: *Nature* vol. 453, no. 7195 (2008), pp. 638–641.

[224] Karin Westermark, Anders Henningsson, Håkan Rensmo, Sven Södergren, Hans Siegbahn, and Anders Hagfeldt. “Determination of the electronic density of states at a nanostructured TiO_2/Ru-dye/electrolyte interface by means of photoelectron spectroscopy”. In: *Chemical physics* vol. 285, no. 1 (2002), pp. 157–165.

[225] Laurence Peter. “Sticky electrons transport and interfacial transfer of electrons in the dye-sensitized solar cell”. In: *Accounts of chemical research* vol. 42, no. 11 (2009), pp. 1839–1847.

[226] Fei Cao, Gerko Oskam, Gerald J. Meyer, and Peter C. Searson*. “Electron Transport in Porous Nanocrystalline TiO_2 Photoelectrochemical Cells”. In: *J. Phys. Chem.* (1996).

[227] Anita Solbrand, Henrik Lindström, Håkan Rensmo, Anders Hagfeldt, Sten-Eric Lindquist, and Sven Södergren. “Electron transport in the nanostructured TiO_2-electrolyte system studied with time-resolved photocurrents”. In: *The Journal of Physical Chemistry B* vol. 101, no. 14 (1997), pp. 2514–2518.

[228] L. Dloczik, O. Ileperuma, I. Lauermann, L. M. Peter, E. A. Ponomarev, G. Redmond, N. J. Shaw, and I. Uhlendorf. “Dynamic Response of Dye-Sensitized Nanocrystalline Solar Cells: Characterization by Intensity-Modulated Photocurrent Spectroscopy”. In: *The Journal of Physical Chemistry B* vol. 101, no. 49 (1997), pp. 10281–10289.

[229] Anders Hagfeldt and Michael Graetzel. “Light-Induced Redox Reactions in Nanocrystalline Systems”. In: *Chemical Reviews* vol. 95, no. 1 (1995), pp. 49–68.

[230] Shu Hu, Matthew R. Shaner, Joseph A. Beardslee, Michael Lichterman, Bruce S. Brunschwig, and Nathan S. Lewis. “Amorphous TiO_2 coatings stabilize Si, GaAs, and GaP photoanodes for efficient water oxidation”. In: *Science* vol. 344, no. 6187 (2014), pp. 1005–1009.

[231] Juan Bisquert, Francisco Fabregat-Santiago, Iván Mora-Seró, Germà Garcia-Belmonte, Eva M Barea, and Emilio Palomares. "A review of recent results on electrochemical determination of the density of electronic states of nanostructured metal-oxide semiconductors and organic hole conductors". In: *Inorganica Chimica Acta* vol. 361, no. 3 (2008), pp. 684–698.

[232] Francisco Fabregat-Santiago, Juan Bisquert, Germà Garcia-Belmonte, Gerrit Boschloo, and Anders Hagfeldt. "Influence of electrolyte in transport and recombination in dye-sensitized solar cells studied by impedance spectroscopy". In: *Solar Energy Materials and Solar Cells* vol. 87, no. 1 (2005), pp. 117–131.

[233] W. C. Mackrodt, E. A. Simson, and N. M. Harrison. "An ab initio Hartree-Fock study of the electron-excess gap states in oxygen-deficient rutile TiO_2 ". In: *Surface Science* vol. 384, no. 13 (1997), pp. 192–200.

[234] Zhaoming Zhang, Shin-Puu Jeng, and Victor E. Henrich. "Cation-ligand hybridization for stoichiometric and reduced TiO_2 (110) surfaces determined by resonant photoemission". In: *Physical Review B* vol. 43, no. 14 (1991), pp. 12004–12011.

[235] Hengzhong Zhang and Jillian F. Banfield. "Thermodynamic analysis of phase stability of nanocrystalline titania". In: *J. Mater. Chem.* Vol. 8 (9 1998), pp. 2073–2076.

[236] Konrad Schwanitz, Eric Mankel, Ralf Hunger, Thomas Mayer, and Wolfram Jaegermann. "Photoelectron Spectroscopy at the Solid–Liquid Interface of Dye–Sensitized Solar Cells: Unique Experiments with the Solid–Liquid Interface Analysis System SoLiAS at BESSY". In: *CHIMIA International Journal for Chemistry* vol. 61, no. 12 (2007), pp. 796–800.

[237] N. F. Mott and L. Friedman. "Metal-insulator transitions in VO_2, Ti_2O_3 and Ti_{2-x} V_xO_3". In: *Philosophical Magazine* vol. 30, no. 2 (1974), pp. 389–402.

[238] Martin Setvín, Benjamin Daniel, Vera Mansfeldova, Ladislav Kavan, Philipp Scheiber, Martin Fidler, Michael Schmid, and Ulrike Diebold. "Surface preparation of TiO_2 anatase (101): pitfalls and how to avoid them". In: *Surface Science* vol. 626 (2014), pp. 61–67.

[239] H. Tang, H. Berger, P. E. Schmid, F. Levy, and G. Burri. "Photoluminescence in TiO_2 anatase single crystals". In: *Solid State Communications* vol. 87, no. 9 (1993), pp. 847–850.

[240] Yunbin He, Olga Dulub, Hongzhi Cheng, Annabella Selloni, and Ulrike Diebold. "Evidence for the Predominance of Subsurface Defects on Reduced Anatase TiO_2 (101)". In: *Physical Review Letters* vol. 102, no. 10 (2009). PRL, p. 106105.

[241] Philipp Scheiber, Martin Fidler, Olga Dulub, Michael Schmid, Ulrike Diebold, Weiyi Hou, Ulrich Aschauer, and Annabella Selloni. "(Sub)Surface Mobility of Oxygen Vacancies at the TiO_2 Anatase (101) Surface". In: *Physical Review Letters* vol. 109, no. 13 (2012), p. 136103.

[242] Michele Lazzeri, Andrea Vittadini, and Annabella Selloni. "Structure and energetics of stoichiometric TiO_2 anatase surfaces". In: *Physical Review B* vol. 63, no. 15 (2001), p. 155409.

[243] Peter J. Feibelman and M. L. Knotek. "Reinterpretation of electron-stimulated desorption data from chemisorption systems". In: *Phys. Rev. B* vol. 18 (12 1978), pp. 6531–6539.

[244] L. Gregoratti, T.O. Mentes, A. Locatelli, and M. Kiskinova. “Beam-induced effects in soft X-ray photoelectron emission microscopy experiments”. In: *Journal of Electron Spectroscopy and Related Phenomena* vol. 170, no. 13 (2009). Radiation Damage, pp. 13 –18.

[245] TO Menteş, A Locatelli, L Aballe, A Pavlovska, E Bauer, T Pabisiak, and A Kiejna. “Surface modification of oxides by electron-stimulated desorption for growth-mode control of metal films: Experiment and density-functional calculations”. In: *Physical Review B* vol. 76, no. 15 (2007), p. 155413.

[246] KC Prince, VR Dhanak, P Finetti, JF Walsh, R Davis, CA Muryn, HS Dhariwal, G Thornton, and G Van der Laan. “2p resonant photoemission study of TiO_2 ”. In: *Physical Review B* vol. 55, no. 15 (1997), p. 9520.

[247] Sajan Thomas and Peter Sherwood. “Valence band x-ray photoelectron spectroscopic studies of carbonate, bicarbonate and formate interpreted by Xα calculations”. In: *Surface and interface analysis* vol. 20, no. 7 (1993), pp. 595–599.

[248] W. Jaegermann and T. Mayer. “H_2O and OH on semiconductors”. In: *Adsorbed Layers on Surfaces*. Ed. by H. P. Bonzel. Vol. 42A4. Landolt-Börnstein - Group III Condensed Matter. Springer Berlin Heidelberg, 2005. Chap. 3.8.2, pp. 226–298.

[249] P Reinke and P Oelhafen. “Thermally induced structural changes in amorphous carbon films observed with ultraviolet photoelectron spectroscopy”. In: *Journal of applied physics* vol. 81, no. 5 (1997), pp. 2396–2399.

[250] WR Flavell, J Hollingworth, JF Howlett, AG Thomas, Md M Sarker, S Squire, Z Hashim, M Mian, PL Wincott, D Teehan, et al. “Resonant photoemission from complex cuprates and nickelates”. In: *Journal of synchrotron radiation* vol. 2, no. 5 (1995), pp. 264–271.

[251] Akira Fujishima. “Electrochemical photolysis of water at a semiconductor electrode”. In: *nature* vol. 238 (1972), pp. 37–38.

[252] I. M. Brookes, C. A. Muryn, and G. Thornton. “Imaging Water Dissociation on TiO_2 (110)”. In: *Phys. Rev. Lett.* Vol. 87 (26 2001), p. 266103.

[253] R. Schaub, P. Thostrup, N. Lopez, E. Lægsgaard, I. Stensgaard, J. K. Nørskov, and F. Besenbacher. “Oxygen Vacancies as Active Sites for Water Dissociation on Rutile TiO_2(110)”. In: *Phys. Rev. Lett.* Vol. 87 (26 2001), p. 266104.

[254] Kavan, M. Grätzel, S. E. Gilbert, C. Klemenz, and H. J. Scheel. “Electrochemical and Photoelectrochemical Investigation of Single-Crystal Anatase”. In: *Journal of the American Chemical Society* vol. 118, no. 28 (1996), pp. 6716–6723.

[255] Antonio Tilocca and Annabella Selloni. “Structure and Reactivity of Water Layers on Defect-Free and Defective Anatase TiO_2 (101) Surfaces”. In: *The Journal of Physical Chemistry B* vol. 108, no. 15 (2004), pp. 4743–4751.

[256] A. Vittadini, A. Selloni, F. P. Rotzinger, and M. Grätzel. “Structure and Energetics of Water Adsorbed at TiO_2 Anatase (101) and (001) Surfaces”. In: *Physical Review Letters* vol. 81, no. 14 (1998), pp. 2954–2957.

[257] Antonio Tilocca and Annabella Selloni. “Reaction pathway and free energy barrier for defect-induced water dissociation on the (101) surface of TiO_2-anatase”. In: *The Journal of Chemical Physics* vol. 119, no. 14 (2003), pp. 7445–7450.

[258] Hongzhi Cheng and Annabella Selloni. “Surface and subsurface oxygen vacancies in anatase TiO_2 and differences with rutile”. In: *Physical Review B* vol. 79, no. 9 (2009). PRB, p. 092101.

[259] Y. W. Chen, J. D. Prange, S. Duhnen, Y. Park, M. Gunji, C. E. D. Chidsey, and P. C. McIntyre. “Atomic layer-deposited tunnel oxide stabilizes silicon photoanodes for water oxidation”. In: *Nature Materials* vol. 10, no. 7 (2011), pp. 539–544.

[260] A Opitz, M Scherge, SI-U Ahmed, and JA Schaefer. “A comparative investigation of thickness measurements of ultra-thin water films by scanning probe techniques”. In: *Journal of applied physics* vol. 101, no. 6 (2007), p. 064310.

[261] LE Walle, Anne Borg, Per Uvdal, and Anders Sandell. “Experimental evidence for mixed dissociative and molecular adsorption of water on a rutile TiO_2 (110) surface without oxygen vacancies”. In: *Physical Review B* vol. 80, no. 23 (2009), p. 235436.

[262] Guido Ketteler, Susumu Yamamoto, Hendrik Bluhm, Klas Andersson, David E Starr, D Frank Ogletree, Hirohito Ogasawara, Anders Nilsson, and Miquel Salmeron. “The nature of water nucleation sites on TiO_2 (110) surfaces revealed by ambient pressure X-ray photoelectron spectroscopy”. In: *The Journal of Physical Chemistry C* vol. 111, no. 23 (2007), pp. 8278–8282.

[263] Antonio Tilocca and Annabella Selloni. “Vertical and Lateral Order in Adsorbed Water Layers on Anatase TiO_2 (101)”. In: *Langmuir* vol. 20, no. 19 (2004), pp. 8379–8384.

[264] Cristiana Di Valentin, Antonio Tilocca, Annabella Selloni, TJ Beck, Andreas Klust, Matthias Batzill, Yaroslav Losovyj, and Ulrike Diebold. “Adsorption of Water on Reconstructed Rutile TiO_2 (011)-(2×1): Ti-O Double Bonds and Surface Reactivity”. In: *Journal of the American Chemical Society* vol. 127, no. 27 (2005), pp. 9895–9903.

[265] Peter J Feibelman, DR Hamann, and FJ Himpsel. “Site and nature of H bonding on Ti (0001)”. In: *Physical Review B* vol. 22, no. 4 (1980), p. 1734.

[266] Zongyan Zhao, Zhaosheng Li, and Zhigang Zou. “Structure and properties of water on the anatase TiO_2 (101) surface: from single-molecule adsorption to interface formation”. In: *The Journal of Physical Chemistry C* vol. 116, no. 20 (2012), pp. 11054–11061.

[267] PB Miranda, Lei Xu, YR Shen, and Miquel Salmeron. “Icelike water monolayer adsorbed on mica at room temperature”. In: *Physical review letters* vol. 81, no. 26 (1998), p. 5876.

List of Figures

Fig. 2.1 Electronic band structure of a metal, a semiconductor and an insulator 19
Fig. 2.2 Energy gaps in organic semiconductors 22
Fig. 2.3 Band diagram of a metal and a semiconductor. 23
Fig. 2.4 Band structure of a p-n interface 25
Fig. 2.5 Contact formation of metals and semiconductors 26
Fig. 2.6 Interface dipole formation at the metal/semiconductor interfaces 28
Fig. 2.7 Device structures of organic solar cells 29
Fig. 2.8 Charge transfer exciton (CT-Exciton) formation at a donor/acceptor interface 31
Fig. 2.9 I-V characteristic of a solar cell in the dark and under illumination 33
Fig. 2.10 Equivalent circuit diagrams of solar cells 34
Fig. 2.11 Injection and extraction barrier for electrons. 34

Fig. 3.1 Unit cell of anatase and rutile 38
Fig. 3.2 Left: Sketch of the equilibrium-shape of an anatase single crystal (adapted from Ref. [78]). Right: Natural anatase single crystal similar to the used ones in this work. Taken from Ref. [79]. 38
Fig. 3.3 a) Model of the autocompensated anatase (101) surface. b) STM image of a sputter annealed anatase (101) surface. c) Sketch of possible island shapes on the anatase (101) surface. 39
Fig. 3.4 Photoemission spectrum of the valence band of a sputter annealed anatase (101) surface and the calculated band structure and molecular orbital diagram 40
Fig. 3.5 Chemical structure of C_{60}, $PC_{61}BM$ and P3HT 42

Fig. 4.1 Sketch of the newly developed single crystal cleavage techniques 44
Fig. 4.2 Sketch of the atomic layer deposition (ALD) cycles. 45
Fig. 4.3 Left: Sketch of the Daisy-Fun system in Darmstadt. Right: Sketch of the SoLiAS system situated at the synchrotron Bessy II in Berlin. 47

Fig. 5.1 Schematic setup for photoemission experiments including a radiation source, a sample, a system of focusing lenses (including a retarding voltage), an analyzer and a detector. 49
Fig. 5.2 Schematic illustration of the photoemission process within the sample and the transfer of the photoelectron to the detector 50
Fig. 5.3 Experimental data of the inelastic mean free path of electrons in dependence of their kinetic energy. The curve is a fit and is also called *bathtub curve*. 52

Fig. 5.4 Resonant photoemission process using the example of the $Ti\,3p \rightarrow Ti\,3d$ 55
Fig. 5.5 Resonant photoemission of amorphous ALD prepared TiO_x 55
Fig. 5.6 Left: Schematic diagram of a standard four-grid LEED set-up (left) and LEED pattern of a Si(111)7×7 surface. 56
Fig. 5.7 Geometric illustration of the Bragg law 57
Fig. 5.8 Pear interaction of electrons 59
Fig. 5.9 Sketch of the working principle of an AFM 60

Fig. 7.1 Typical stack of IOSC devices used in this work to conduct I-V measurements. 67
Fig. 7.2 I-V curves of IOSC with 80 nm thick TiO_x or AZO as ETL 68
Fig. 7.3 I-V curves of IOSC with a TiO_x/AZO bilayer structure as ETL 69
Fig. 7.4 Unipolar devices with TiO_x/C_{60}, $TiO_x/PC_{61}BM$, AZO/C_{60} and AZO/$PC_{61}BM$ 71

Fig. 8.1 Photograph of a cleaved naturally grown anatase single crystal as used in this work. Facing the camera is the (101) surface plane 73
Fig. 8.2 Laue and XRD diffraction patterns of different titania samples 74
Fig. 8.3 Left: Amorphous ALD TiO_x on ITO/glass. Right: 500 °C annealed ALD TiO_x on ITO/glass. 75
Fig. 8.4 AFM images of different titania samples and surfaces 76
Fig. 8.5 LEED image of an *in situ* cleaved anatase sc-(101) surface 77
Fig. 8.6 Tauc plot of TiO_x 80 °C for the determination of the optical gap 77
Fig. 8.7 TiO_x survey spectra of all investigated titania samples: as is TiO_x ALD 80 °C, TiO_x annealed for 60 min at 300 °C, TiO_x annealed for 60 min at 500 °C and *in situ* cleaved 101-anatase single crystal 78
Fig. 8.8 Deconvoluted O 1s, Ti $2p_{3/2}$ and C 1s spectra of 300 °C TiO_x 79
Fig. 8.9 O 1s, Ti $2p_{3/2}$ and VBM distances for *in situ* sc-(101), 80 °C, 300 °C, and 500 °C TiO_x 80
Fig. 8.10 Evolution of the Ti $2p_{3/2}$ and VBM position with respect to preparation method and X-ray influence 83
Fig. 8.11 Fit of the O 1s and Ti $2p_{3/2}$ spectra of various TiO_x samples 84
Fig. 8.12 Evolution of the Ti^{3+}/Ti^{4+} ratio, the Ti^{4+} *fwhm*, the OH^-/O^{2-} ratio and the stoichiometry of the different TiO_x 85
Fig. 8.13 XP spectra of C_{60} 88
Fig. 8.14 O 1s (left), Ti $2p_{3/2}$ (middle) and C 1s photoemission spectra of drop-casted $PC_{61}BM$ on 80 °C TiO_x. 89
Fig. 8.15 Energy level positions of $PC_{61}BM$ and C_{60} 90

Fig. 9.1 Layer sequence and I-V characteristics of an IOSC device with TiO_x as ETL 91
Fig. 9.2 Influence of X-ray and UV illumination on 80 °C TiO_x 93
Fig. 9.3 Influence of X-ray and UV illumination on 80 °C TiO_x + 3 Å C_{60} 94
Fig. 9.4 XP spectra of the TiO_x/C_{60} interface before and after UV illumination 96
Fig. 9.5 Evolution of the TiO_x and C_{60} energy levels with increasing C_{60} coverage before and after UV illumination 96
Fig. 9.6 Energy diagram of the TiO_x/C_{60} interface before and after UV illumination 98

Fig. 9.7 Evolution of the TiO_x Ti^{3+} and C 1s *fwhm* with increasing C_{60} coverage and in dependence of UV illumination . . . 99
Fig. 9.8 Influence of UV light on the UV pretreated TiO_x/C_{60} interface . . . 100
Fig. 9.9 TiO_x/C_{60} energy diagram with and w/o UV pretreatment of the TiO_x substrate . . . 101
Fig. 9.10 Comparison of the Ti $2p_{3/2}$ Ti^{3+} and C 1s *fwhm* evolution with and w/o UV pretreatment of the TiO_x substrate . . . 102

Fig. 10.1 Survey spectrum of the *in situ* cleaved (101) surface plane prior to C_{60} deposition . 105
Fig. 10.2 Anatase (101) *in situ* cleaved C_{60} interface experiment . . . 106
Fig. 10.3 Influence of UV light on the *in situ* cleaved anatase (101)/C_{60} interface . . . 108
Fig. 10.4 Anatase *ex situ* cleaved C_{60} interface experiment . . . 109
Fig. 10.5 Influence of UV light on the *ex situ* cleaved anatase (101)/C_{60} interface . . . 110
Fig. 10.6 Evolution of Ti^{3+} emission and C_{60} C 1s *fwhm* in the course of the C_{60} deposition onto an *in situ* cleaved TiO_2 sc-(101) surface . . . 112
Fig. 10.7 Energy diagrams of the *in situ* TiO_2/C_{60} interface (left), the *ex situ* TiO_2/C_{60} interface (middle) and the TiO_x 80 °C/C_{60} interface (right) . . . 113

Fig. 11.1 Influence of air exposure and subsequent UV illumination on an *in situ* cleaved (101) surface . . . 118
Fig. 11.2 Surface potential energy diagram of the *in situ* cleaved anatase (101) surface (left) upon exposure to air (middle) and subsequent UV irradiation (right) . . . 118
Fig. 11.3 SE-edge, O 1s, Ti $2p_{3/2}$ and valence band spectra of an *in situ* and *ex situ* cleaved anatase crystal . . . 119
Fig. 11.4 Detail spectra of the O 1s (A), the Ti $2p_{3/2}$ (B), and the C 1s (C) emission lines for the *in situ* (red) and *ex situ* (black) cleaved single crystal . . . 120
Fig. 11.5 Derived surface potential diagrams for the *in situ* and *ex situ* cleaved sc-anatase. . . 122
Fig. 11.6 Secondary electron edge (left), O 1s core level (middle), and Ti $2p_{3/2}$ core level (right) of the oxygen plasma treated *in situ* cleaved TiO_2 sc-(101). . . . 123
Fig. 11.7 Binding energy and work function shifts upon O_2 plasma and subsequent X-ray/UV treatment. . . . 124
Fig. 11.8 Schematic surface potential diagrams for the *in situ* sc-(101) surface exposed to a soft oxygen plasma. . . . 124
Fig. 11.9 Model for H_2O induced accumulation layer formation on TiO_2 surfaces. . . . 127
Fig. 11.10 a) Oxygen adsorbs as O_2^- at the TiO_2 surface inducing a depletion layer at the surface and a surface dipole. b) Upon irradiation with UV light, electrons are excited above the energy gap and O_2^- desorbs as O_2 by scavenging a hole. . . . 128
Fig. 11.11 Model of H_2O and O_2 adsorption/desorption on a defect free sc-anatase (101) surface and the respective band diagrams. . . . 130
Fig. 11.12 Energy diagram of TiO_x 80 °C as measured after introduction into UHV (left) and after 60 min UV illumination(right). . . . 131
Fig. 11.13 Ti^{4+} *fwhm* evolution of all *ex situ* samples and the *in situ* cleaved TiO_2 sc-(101) upon X-ray and UV illumination. . . . 132

Fig. 11.14 X-ray and UV induced Ti^{3+} emission intensity ratio of as deposited 80 °C, 300 °C and 500 °C post annealed TiO_x. 134
Fig. 11.15 Evolution of the SE-edge, the O1s emission and the Ti $2p_{3/2}$ emission upon X-ray and UV irradiation, subsequent O_2 treatment and a last UV illumination. 135
Fig. 11.16 Progression of the SE-edge, the O1s emission and the Ti $2p_{3/2}$ emission upon O_2/UV treatment and progression of the Ti^{3+} states upon O_2/UV treatment. 136
Fig. 11.17 Effect of surface states on a n-type semiconductor. 137
Fig. 11.18 Model of *ex situ* amorphous ALD prepared samples upon UV illumination. 139

Fig. 12.1 Model I of the UV influence on the TiO_2/C_{60} interface. 143
Fig. 12.2 Model II of the UV influence on the TiO_2/C_{60} interface. 145

Fig. 13.1 I-V characteristic from IOSC with AZO and TiO_x as ETL. 147
Fig. 13.2 SEM images of 80 nm ALD ZnO and AZO layers on ITO. 148
Fig. 13.3 XRD spectra of ITO, ITO/ZnO and ITO/AZO and a Tauc plot of ALD AZO. 149
Fig. 13.4 Survey and detail spectra of Al:ZnO (AZO) 150
Fig. 13.5 Photoemission spectra of the AZO substrate and AZO/C_{60} interface before (black) and after UV illumination (blue) 152
Fig. 13.6 Evolution of the C_{60} C 1s *fwhm* with increasing C_{60} coverage before UV illumination and after UV illumination. 152
Fig. 13.7 Energy diagram of the AZO/C_{60} interface before UV illumination (left) and after UV illumination (right). 154

Fig. 14.1 PES spectra of TiO_x/C_{60} interface obtained at synchrotron Bessy II 156
Fig. 14.2 PES spectra of AZO/C_{60} interface obtained at synchrotron Bessy II 157
Fig. 14.3 Energy diagrams of the TiO_x/C_{60} and AZO/C_{60} interface directly derived from the photoemission measurements. 158

Fig. 15.1 I-V characteristic of different inverted organic solar cells. 160
Fig. 15.2 Energy band diagrams of 80 °C TiO_x/C_{60} interface derived at Bessy before UV, derived at Daisy-Fun before UV (middle) and after derived at Daisy-Fun after UV. . . . 161
Fig. 15.3 Energy diagram with an assumed accumulation layer at the TiO_x surface due to the adsorption of hydroxyls and oxygen at the surface. 162
Fig. 15.4 Logarithmic plot of the dark I-V curves of IOSC with TiO_x as ETL. 163
Fig. 15.5 TiO_x/C_{60} energy diagram with an assumed upward shift of the energy levels by 0.4 eV due to adsorbed oxygen species. 164
Fig. 15.6 Energy diagram of the ALD AZO/C_{60} interface derived at Bessy without UV illumination and as measured energy diagram of the AZO/C_{60} interface derived from Daisy-Fun experiments. 165

Fig. 17.1 Different valence band and band gap spectra of *in situ* and *ex situ* cleaved anatase sc-(101) surfaces. 175

Fig. 17.2 Valence band region and band gap spectra of ALD prepared amorphous TiO_x, 500 °C post annealed ALD TiO_x, nanocrystalline anatase out of a slurry and *in situ* cleaved anatase sc-(101) surface. 176
Fig. 17.3 Synchrotron influenced amorphous TiO_x ALD spectra and sc-(101) surface. 177
Fig. 17.4 Ti^{3+} increase of an as deposited ALD prepared TiO_x sample upon synchrotron irradiation. 178
Fig. 17.5 Fit of the SGS emission of the *in situ* cleaved sc-(101) surface at 90 K sample temperature, at 298 K and a nc-TiO_2 at 298 K. 179
Fig. 17.6 Background treatment of the nc-TiO_2 and the sc-(101) anatase band gap region. . . 179
Fig. 17.7 Model of band gap emissions and morphology of the investigated titania samples. . 181
Fig. 17.8 Band gap region of ALD prepared TiO_x, nanocrystalline TiO_2, *ex situ* cleaved sc-(101) surface and the *in situ* cleaved sc-(101) surface. 184
Fig. 17.9 VB region spectra and CIS spectra for photon energies between 40 and 70 eV. 185
Fig. 17.10 VB region spectra and CIS spectra of *ex situ* cleaved sc-(101) surface at different photon energies. 186
Fig. 17.11 VB region spectra and CIS spectra of nanocrystalline TiO_2 187
Fig. 17.12 Left: An oxygen vacancy, V_O, donating localized electrons to Ti^{4+} atoms, causing the formation of two Ti^{3+} atoms. Right: At step edges excess electrons are delocalized and the extra electron cannot be attributed to one specific Ti^{4+} atom. 189
Fig. 17.13 Resonant photoemission spectra of an *in situ* cleaved sc-(101) surface. 190
Fig. 17.14 CIS spectra of the Ti2p→3d transition of an *in situ* cleaved anatase (101) surface. . 191
Fig. 17.15 PES of the sc-(101)/water interface. 195
Fig. 17.16 Ti $2p_{3/2}$ and O 1s emissions of the water adsorption experiment normalized to the maximum. 196
Fig. 17.17 Valence band and bandgap region spectra of the sc-(101) TiO_2 water adsorption. . . 197
Fig. 17.18 Gap states (DGS and SGS) and VB intensities for different water coverages on the *in situ* cleaved anatase (101) surface. 199
Fig. 17.19 Evolution of the DGS and SGS emission with respect to water coverage after normalization to the VB. 200
Fig. 17.20 Model of water adsorption on the sc-(101) surface. 201
Fig. 17.21 Model for the adsorption energy (E_{ads}) of water vs. the nominal H_2O layer thickness.202

Fig. A.1 O 1s emission of an *in situ* and *ex situ* cleaved anatase sc-(101) surface. 205
Fig. A.2 C 1s emission of C_{60}, which was deposited on a gold substrate and VB region spectrum of the C_{60} layer. 206
Fig. A.3 WF and Ti $2p_{3/2}$ core level changes of 500 °C TiO_x with UV and X-rays. 208
Fig. A.4 Separation of the X-ray and UV influence on 500 °C post annealed TiO_x. 209
Fig. A.5 Photoemission spectra of TiO_x 500 °C/C_{60} interface before and after UV illumination.210
Fig. A.6 Ti^{3+} and C_{60} C 1s *fwhm* evolution with increasing C_{60} coverage and with respect to the influence of UV light. 211
Fig. A.7 Energy diagram of the TiO_x 500 °C/C_{60} interface before and after UV illumination. . 212

Fig. A.8 XPS spectra of the influence of UV light on the 500 °C TiO_x/C_{60} interface after UV pretreatment of the TiO_x substrate. . . . 213
Fig. A.9 500 °C TiO_x/C_{60} interface as measured, air corrected and O_2 desorption corrected. . 214

Fig. B.1 Resonant photoemission spectra of the valence band and the band gap region of 500 °C TiO_x. . . . 217
Fig. B.2 Cross section of the Ti 3d orbital in dependence of the excitation energy. . . . 218
Fig. B.3 Difference spectrum of the anatase (101) valence band before water adsorption and the sc-(101) plus 0.1 Å H_2O. . . . 219
Fig. B.4 Resonant photoemission of a sputter annealed rutile (100) surface. Taken from Ref. [246]. . . . 220

List of Tables

Tab. 8.1 Energetic positions and distances of the O 1s, the Ti $2p_{3/2}$ and the valence band maximum. . . . 82
Tab. 8.2 VBM positions of all ALD prepared *ex situ* samples and *in situ* cleaved sc-anatase (101). . . . 83

Tab. 9.1 Work function (WF) and Ti $2p_{3/2}$ and C 1s level values of the 60 °C TiO_x samples with different C_{60} coverages. . . . 97
Tab. 9.2 Work function and binding energy positions of the Ti $2p_{3/2}$ and C 1s core level for UV pretreated and a non UV pretreated TiO_x/C_{60} interface. . . . 101

Tab. 10.1 SE-edge, Ti $2p_{3/2}$, C 1s energy emission values and *fwhm* of C 1s, obtained from the *in situ*/C_{60} + UV light and the *ex situ*/C_{60} + UV light experiment. . . . 111
Tab. 10.2 Ti $2p_{3/2}$-C 1s distance of the differently prepared TiO_2/C_{60} interfaces and the influence of UV light. . . . 114

Tab. 11.1 Work function, core level binding energy and valence band maximum position of the *in situ* and *ex situ* clevaed TiO_2 sc-anatase (101), in dependence of X-ray and UV illumination. . . . 120
Tab. 11.2 Work function and binding energy (O 1s and Ti $2p_{3/2}$) of the *in situ* and O_2 plasma treated sc-anatase (101) in dependence of X-ray and UV illumination. . . . 122
Tab. 11.3 Work function, binding energy (O1s,Ti $2p_{3/2}$) and Ti^{3+} states evolution upon X-ray, UV and O_2 exposure on 300 °C TiO_x. . . . 136

Tab. 13.1 Work function (WF) and Zn $2p_{3/2}$ and C 1s level values of the ALD AZO samples with different C_{60} coverages. . . . 153

Tab. 13.2 Ti $2p_{3/2}$-C 1s and Zn $2p_{3/2}$-C 1s distances of the differently prepared TiO_2/C_{60} and AZO/C_{60} interfaces and influence of UV light. 154

Tab. A.1 Work function (WF) and Ti $2p_{3/2}$ and C 1s level values of the 500 °C TiO_x samples with different C_{60} coverages. 206

Tab. A.2 Work function, Ti $2p_{3/2}$, and C 1s values of the UV pretreated 500 °C TiO_x/C_{60} interface. 213

Tab. B.1 Work function, binding energy and valence band maximum position of the *in situ* and *ex situ* sc-anatase (101), in dependence of X-ray and UV illumination. 219

Publications and conference contributions

Publications

Philip Reckers, Mariel Dimamay, Joachim Klett, Sara Trost, Kirill Zilberberg, Thomas Riedl, Bruce A. Parkinson, Joachim Brötz, Wolfram Jaegermann and Thomas Mayer, *Deep and Shallow TiO_2 Gap States on Cleaved Anatase Single Crystal (101) Surfaces, Nanocrystalline Anatase Films, and ALD Titania Ante and Post Annealing* The Journal of Physical Chemistry C 119 (2015), 9890-9898

Sara Trost, Tim Becker, Andreas Polywka, Patrick Görrn, Marek F. Oszajca, Norman A. Luechinger, Detlef Rogalla, Mirko Weidner, Philip Reckers, Thomas Mayer and Thomas Riedl *Avoiding Photoinduced Shunts in Organic Solar Cells by the Use of Tin Oxide (SnO_x) as Electron Extraction Material Instead of ZnO* Advanced Energy Materials (2016), 1600347

Sara Trost, Krill Zilberberg, Andreas Behrendt, Andreas Polywka, Patrick Görrn, Philip Reckers, Julia Maibach, Thomas Mayer and Thomas Riedl,*Overcoming the Light-Soaking Issue in Inverted Organic Solar Cells by the Use of Al:ZnO Electron Extraction Layers* Advanced Energy Materials (2013) WILEY-VCH Verlag, 3, 1437-1444

Verena Pfeifer, Paul Erhart, Shunyi Li, Karsten Rachut, Jan Morasch, Joachim Brötz, Philip Reckers, Thomas Mayer, Sven Rühle, Arie Zaban, Ivan Mora Sero, Juan Bisquert, Wolfram Jaegermann and Andreas Klein, *Energy Band Alignment between Anatase and Rutile TiO_2* The Journal of Physical Chemistry Letters (2013), 4182-4187

Conference contributions - selection

Talk: Philip Reckers, Sara Trost, Kirill Zilberberg, Thomas Riedl and Thomas Mayer, *Photoemission study of the origin of S-shape in inverted OSC: Defect states in TiO_x and band structure of TiO_x/C_{60} and AZO/C_{60} from RESPES and SXPS*, International Symposium for Organic Electronics 2013 (ISFOE13), Thessaloniki, Greece

Talk: Philip Reckers, Mariel Dimamay, Sara Trost, Thomas Riedl, Thomas Mayer and Wolfram Jaegermann *The origin of TiO_2 shallow gap states evidenced from resonant photoelectron spectroscopy (RESPES) and AFM on anatase single crystal (101) surface, nanocrystalline anatase films and ALD titania ante and post annealing*, Frühjahrtagung der Deutschen Physikalischen Gesellschaft 2014, Dresden, Germany

Poster: Philip Reckers, Sara Trost, Thomas Riedl, Thomas Mayer and Wolfram Jaegermann *The electronic structure of the TiO_x/C_{60} interface before and after UV illumination: On track of the origin of S-shaped IV-curves by photoemission spectroscopy*, 6th International Conference on Hybrid and Organic Photovoltaics 2014 (HOPV14), Lausanne, Switzerland

Poster: Philip Reckers, Thomas Mayer and Wolfram Jaegermann *Water adsorption on an in-situ cleaved Anatase TiO_2 (101) surface*, 6th joint BER II and BESSY II User Meeting 2014, Berlin, Germany

Curriculum Vitae

Entfällt aus datenschutzrechtlichen Gründen.

Danksagung

An dieser Stelle möchte ich mich bei allen bedanken, die zum Gelingen dieser Arbeit beigetragen haben. Herzlichen Dank an

Prof. Dr. Wolfram Jaegermann für die die Ermöglichung der Dissertation im Fachgebiet Oberflächenforschung, die freundliche Aufnahme in die Arbeitsgruppe und die sehr interessante Aufgabenstellung.

Prof. Dr. Thomas Riedl für die freundlichen Übernahme des Zweitgutachtens und die wissenschaftlichen Diskussionen bezüglich invertierter organischer Solarzellen.

Meinem Betreuer Dr. Thomas Mayer für die Ermöglichung der Dissertation im Rahmen des von Ihm eingeworbenen DFG Projekts. Insbesondere danke ich für die vielen anregenden Diskussionen, die Ideen für Experimente und für die anschließende Diskussion der Ergebnisse.

Dr. Sara Trost für die gemeinsame Bearbeitung des Projekts über invertierte organische Solarzellen, sowie die zur Verfügung Stellung verschiedenster Proben zur Analyse.

Dr. Eric Mankel dafür, dass er jederzeit für wissenschaftliche Diskussionen zur Verfügung stand und seine Bereitschaft Wetten einzugehen. Weiterhin danke ich ihm für die gute Zusammenarbeit als Kopf des Admin-Teams.

Weiterhin danke ich allen Mitgliedern der Oberflächenforschungsgruppe für das angenehme Arbeitsklima in der Arbeitsgruppe. Die gemeinsamen Kaffee- und Zopfrunden mit sowohl wissenschaftlichen also auch nicht wissenschaftlichen Themen waren immer eine Freude.

Wolfram Calvet, Wolfgang Bremsteller, Herbert Sehnert und Prof. Christian Pettenkofer für ihre technische und wissenschaftliche Unterstützung während unserer Messzeiten am Synchrotron Bessy II in Berlin.

Meiner Familie, meinen Eltern und meinem Bruder, danke ich für die Ermöglichung des Studiums und die Unterstützung während der Dissertation.

Zum Schluss danke ich allen meinen Freunden und meiner Freundin, die meine gesamte Zeit an der Universität zu einer sehr angenehmen Zeit gemacht haben.

Erklärung zur Dissertation

Hiermit versichere ich, die vorliegende Dissertation ohne Hilfe Dritter nur mit den angegebenen Quellen und Hilfsmitteln angefertigt zu haben. Alle Stellen, die aus Quellen entnommen wurden, sind als solche kenntlich gemacht. Diese Arbeit hat in gleicher oder ähnlicher Form noch keiner Prüfungsbehörde vorgelegen.

Darmstadt, den April 19, 2019

(P. Reckers)